

Efficient Laser Ranging to Space Debris

Inauguraldissertation
der Philosophisch-naturwissenschaftlichen Fakultät
der Universität Bern

vorgelegt von

Julian Rodriguez-Villamizar

aus Kolumbien

Leiter der Arbeit
Prof. Dr. Thomas Schildknecht
Astronomisches Institut der Universität Bern

Efficient Laser Ranging to Space Debris

Inauguraldissertation
der Philosophisch-naturwissenschaftlichen Fakultät
der Universität Bern

vorgelegt von

Julian Rodriguez-Villamizar

aus Kolumbien

Leiter der Arbeit

Prof. Dr. Thomas Schildknecht
Astronomisches Institut der Universität Bern

Von der Philosophisch-naturwissenschaftlichen Fakultät angenommen.

Bern, 20 May 2022

Der Dekan:
Prof. Dr. Zoltán Balogh

Acknowledgments

The present work could not have been possible to do without the help of many people. I would like to express my deepest gratitude to:

- The Swiss Science National Foundation for providing the financial support.
- Prof. Dr. Adrian Jäggi and Prof. Dr. Thomas Schildknecht for giving me the opportunity of conducting the PhD at the Astronomical Institute of the University of Bern.
- Prof. Dr. Thomas Schildknecht for providing me such an interesting topic and framework, which has contributed to my education, both personal and professional.
- All the SwissOGS team including former and current members. I did learn many things from you.
- Dr. Alessandro Vananti for always being available to me.
- Family and Friends: for your support and for all special moments spent together.

Abstract

The increasing population of resident space objects (RSOs), in already congested specific regions of the outer space, leads to a growing number of close encounters between RSOs. Coping with this unprecedented amount of space-traffic, which only seems to worsen if e.g. one considers current plans for the deployment of mega-constellations in the Low Earth Orbit region, calls for new approaches to mitigate collisions between RSOs. Innovative concepts to avoid collisions involving active spacecraft, but also collisions among debris, including e.g. just-in-time collision avoidance techniques, will all require much better knowledge about the trajectories of the involved objects. Within this context, active electro-optical systems using lasers are attractive since they provide precise and accurate range measurements for the improvement of RSOs orbits. The latter have a direct impact on catalogue maintenance, as well as on the estimation of close conjunctions and efficient collision avoidance manoeuvres. In addition, laser systems may transfer a defined amount of optical electromagnetic radiation transforming it into mechanical energy, with the final aim of changing the trajectory of a non-manoeuverable RSO that is predicted to collide with another RSO on short notice. One of the drawbacks of the laser systems stems from the rather small field of view of the laser beam; to overcome the latter, laser systems may be equipped with a target acquisition and tracking passive electro-optical subsystem. In this work, we present our last achievements, which comprise the implementation of a target acquisition and tracking subsystem, selected examples of daylight observations with passive or active electro-optical systems, and the status of the operational implementation of the fundamental 1064 nm wavelength of the laser system, which was needed to increase the emitted pulse energy, thus increasing the likelihood of having returns with a focus on objects that do not carry any highly reflective element on board. We conducted all experiments and implementations in the Zimmerwald Laser and Astrometric Telescope (ZIMLAT), being a sensor of the Swiss Optical Ground Station and Geodynamics Observatory Zimmerwald (SwissOGS), located 10 km from Bern, Switzerland, operated by the Astronomical Institute of the University of Bern.

Contents

Acknowledgments	i
Abstract	iii
1 Introduction	1
1.1 Towards a Sustainable Use of the Outer Space	1
1.1.1 Mitigation Guidelines and International Recommendations	3
1.1.2 Space Debris Removal and In-Orbit Servicing	4
1.1.3 Just-in-Time Collision Avoidance	7
1.2 Sensing Resident Space Objects	13
1.2.1 Passive and Active Electro-Optical Systems	15
1.2.2 New Developments and Current Challenges	23
1.3 Outline	32
2 Employed Systems and Instrumentation	35
2.1 Telescope	35
2.2 Telescope Control	37
2.3 Passive Electro-Optical System	38
2.3.1 Novelties and Contribution	38
2.4 Active Electro-Optical System	39
2.4.1 Novelties and Contribution	39
3 Target Acquisition and Tracking	41
3.1 Introduction: the State of the Art	41
3.2 Validation of Measurements	44
3.2.1 Methodology	49
3.3 Object Recognition	51
3.3.1 Fitting of a Point Spread Function	51
3.3.2 Template Matching	54

Contents

3.3.3	Aperture Photometry	54
3.3.4	Centroiding and Light Curve Validation	56
3.4	Tracking	58
3.4.1	Initial Orbit Determination	58
3.4.2	Active Tracking	62
3.5	Implementation in a Real-Time System	65
3.5.1	Optimization of the Object Recognition Procedure	65
3.5.2	Statistical and Geometrical Considerations	66
3.6	Results: Algorithm Implementation	73
3.7	Summary and Outlook	76
4	Analysis of a Dual-Wavelength Laser Ranging System	79
4.1	Optical Link Equation	79
4.1.1	Free-Space Loss, Gain, Transmitting and Receiving Efficiencies	80
4.1.2	Atmospheric Transmittance	81
4.1.3	Target Cross-Section	85
4.1.4	Proposed Taxonomy According to Optical Cross-Section	88
4.2	Theoretical vs. Estimated Return Rates	89
4.2.1	Analysis of the Current Performance at 532 nm	103
4.2.2	Operational Implementation of the 1,064 nm Wavelength	105
4.3	Comparison Between System Performance at 532 and 1,064 nm	106
4.3.1	Theoretical Link at 1,064 nm	107
4.3.2	Single-Shot Root-Mean-Square to Calibration Target 3	108
4.3.3	Experimental Observations to International Laser Ranging Service (ILRS) Targets	111
4.4	Summary and Outlook	119
5	Daylight Optical Observations	121
5.1	Introduction: the State of the Art	121
5.2	Impact of Daylight Observations in the Monitoring of defunct RSOs	123
5.2.1	Length of Day	124
5.2.2	Attitude Determination	124
5.2.3	Observation Geometry and Orbital Arc	128
5.3	Background Noise	131
5.3.1	Solar Photon Budget	131
5.3.2	Mitigation of Background Noise in Passive Electro-Optical Systems	134
5.3.3	Mitigation of Background Noise in Active Electro-Optical Systems	138
5.4	Signal	139
5.4.1	Minimum Observable RSO	139
5.4.2	Signal Strengthening	142
5.5	Observation: Signal-to-Noise Ratio	143
5.5.1	Passive Observations	143
5.5.2	Active Observations	147
5.5.3	Simultaneous Combined Observations	150

Contents

5.6	Discussion	152
5.7	Summary and Outlook	154
6	Conclusion	157
6.1	Achievements	157
6.2	Follow-on Work	159

List of Figures

1.1	Instantaneous snapshot geometry of the active segment consisting of a ground-based laser system transferring a $\Delta\mathbf{V}$, at an elevation angle ε from the local horizon, onto a resident space object (RSO) whose flying direction is represented by \mathbf{F}_T and its normal vector \mathbf{F}_N pointing inwards the described trajectory. The horizontal RSO reference frame (dashed line) is perpendicular to the geocentric radius vector of the target and relates to the body-fixed frame by the flight path angle γ . The geocentric angle φ subtends the angular distance between the RSO and the local zenith at the station for a spherical Earth. The resulting vector \mathbf{V}_R shows a deceleration of the RSO to change its initial trajectory.	10
1.2	Left: Observation of a star during daylight using a sensor with a radiometric resolution of 16-bit and an exposure time of 0.05 seconds. Right: Acquired frame corresponding to a star observed during daylight using a sensor with a radiometric resolution of 16-bit and an exposure time of 0.1 seconds. The scale on the top of both images is provided for comparison of the different properties of the observed stars under nearly same observation conditions.	19
1.3	Comparison of the Single Photoavalanche Diode (SPAD) C11202-100 against the Photomultiplier Tube (PMT) H7421-40, both working in photon detection mode.	23
1.4	Comparison of calibration measurements acquired using the laser source Ekspla-NL317 (left) and Ekspla-PL2250 (right), corresponding to laser sources with pulse lengths of 5 nanoseconds and 30 nanoseconds, respectively. In addition, the round-trip time travel to the calibration target was recorded using two different timers: the Stanford counter SR620 and the Riga event timer A032. The statistical descriptors of the presented data are provided in Table 1.1 and Table 1.2.	24

List of Figures

2.1	The Zimmerwald Laser and Astrometry Telescope.	35
2.2	Technical drawing of ZIMLAT depicting active and passive optical paths. At the right-hand side, the Nasmyth platform depicts the position for using the tracking camera as passive electro-optical sensor with its respective focal reducer.	36
2.3	Control architecture for azimuth and elevation axis for ZIMLAT.	37
3.1	Left plots: differences of the estimated pointing position per image with respect to the reference point in azimuth (top) and elevation (bottom) as a function of observed azimuth and elevation. Right plots: modelled error of the reference point in azimuth (top) and elevation (bottom) as a function of observed azimuth and elevation. Units of colorbars: arcseconds.	46
3.2	Angular residuals in arcseconds after orbit determination.	48
3.3	Differences in azimuth (top) and elevation (bottom) between angular measurements acquired by the tracking camera and interpolated CPF predictions at the observation epoch. Units of differences: arcseconds.	49
3.4	Flowchart of the stare and chase observation strategy. PSF: point spread function. IOD: initial orbit determination. FoV: field of view.	50
3.5	Case study of fitting a Gaussian point spread function given a raw image acquired by the tracking camera. Units of colorbars: Analog-To-Digital unit (ADU).	53
3.6	Radial PSF profile showing normalized intensity values against distance from the peak of the object image. A: radius of the inner aperture. B: radius of the outer aperture.	55
3.7	Validation of the algorithm for centroiding and light curve determination. Top-left: raw image with estimated inner and outer rings. Top-right: comparison of source-minus-background between AIJ and our solution (ZIM). Bottom: comparison between centroid estimates using AIJ (\mathbf{X}_{aij}), object recognition (\mathbf{X}_{objrec}) and predicted values (\mathbf{X}_{track}).	57
3.8	Comparison of orbit solutions using a different set of observations within different parts of the observed arc against precise ephemerides in form of CPF. The solutions available for the same pass are an initial orbit determination under a circular orbit assumption (IOD), and two subsequent circular orbit improvements (OI* and OI**). The solutions available for the subsequent pass show a full orbit improvement (six Keplerian elements) adding only angular observations in the middle of the arc (Ang Mid), adding merged observations in the middle of the arc (Mer Mid), adding only angular observations at the middle and end of the arc (Ang Mid-End), adding only angular in the middle and merged observations at the end of the arc (Ang Mid Mer End) and finally merged observations in the middle and at the end of the arc (Mer Mid-End).	61
3.9	Differences in the horizon reference system of ephemerides generated by TLE and CPF for AJISAI (left) for a high culmination pass over Zimmerwald (right).	63

List of Figures

3.10 OmC terms in arcseconds for azimuth (top) and elevation (bottom), using a linear (left) and a quadratic (right) polynomial for the prediction of the coordinates of the target. Each solution depicts the number of measurements within the sliding window (NumMeas SW) that were used for the tracking.	64
3.11 Sequence of steps performed for the estimation of the centroid. The first image to the left shows a portion of the original frame. The second shows the result after convolving the subframe against a median filter using a kernel of 9x9 pixels and a step size of 5 pixels. The third shows the result after subtracting the estimated background. Finally, the last image shows all non-positive values masked to zero. Units colorbars: ADU. The X and Y axes correspond to the pixel position on the subframe.	66
3.12 Cost (top-left) and influence function (top-right) of the the sample mean. Cost (bottom-left) and influence function (bottom-right) of the sample median.	68
3.13 Top: estimation of the background using the entire subframe vs. circular apertures using the mean, with its standard deviation, and the median with its median absolute deviation. Middle: estimation of the background with the median and its associated median absolute deviation using circles and squares. Bottom: execution time for the estimation of the background using circles and squares.	70
3.14 Subframe of original image centered on the object image (left). Area of the subframe defined by the difference between outer and inner background radii (middle). Area of the subframe taking the circumscribed square of the difference between outer and inner background radii (right). Unit colobars: Analog-To-Digital (ADU) units.	71
3.15 Profiles of two frames acquired during the observation of a Topex-Poseidon pass using the tracking camera. The top plot shows that there is enough contrast to distinguish the object image compared to the bottom one. The figure highlights the impact of choosing a specific threshold for the removal of the background.	72
3.16 ENVISAT pass over Zimmerwald on the 11th of March 2020 at 17:24 UTC.	74
3.17 Time series of the object image centroid after its estimation with the object recognition procedure and predicted values by active tracking for the decommissioned satellite ENVISAT on the 11th of March 2020. Left: complete pass. Right: detail in the Y (Top) and X (bottom) components. The results were acquired in real time.	75
3.18 Apparent brightness changes acquired in real time by the tracking camera for the decommissioned satellite ENVISAT on the 11th of March 2020. .	75
3.19 Real time detections by our SLR system for the decommissioned satellite ENVISAT on the 11th of March 2020.	76

List of Figures

4.1	Examples of temperature and pressure vertical profiles used in the computation of the atmospheric transmission by Low Resolution Atmospheric Transmission (LOWTRAN) at the Swiss Optical Ground Station and Geodynamics Observatory Zimmerwald (SwissOGS).	83
4.2	Examples of season dependent vertical profiles depicting the concentration of molecules used in the computation of the atmospheric transmission by LOWTRAN at the SwissOGS.	83
4.3	One-way transmission curve as a function of the wavelength retrieved using LOWTRAN at different zenith angles. The green and red vertical lines depict the wavelengths available at the SwissOGS, i.e. 1,064 and 532 nm after frequency doubling. The models used include the midlatitude winter profiles, a rural aerosol model, a ground elevation of 950 m and a visibility of 23 km.	84
4.4	Atmospheric transmittance using the simplified model proposed by [27] for an elevation angle of 45 ° and different visibility conditions.	85
4.5	Schematic examples of cross-sections. A: dihedral reflector. B: trihedral reflector, also known as corner-cube reflector. D: Intersection between a beam and a cylinder. C: Intersection between a beam an a truncated cone.	86
4.6	Output optical link considering the technical specifications of the laser system at the SwissOGS and Laser Geodynamic Satellite (LAGEOS) -1. In red it is highlighted all losses while in green all gains.	90
4.7	Examples of theoretical return rates for target objects at different orbital regimes using as cross-sections parameters the values provided by the ILRS.	91
4.8	Comparison of different binning sizes for the retrieval of estimated return rates for LAGEOS-1 observed on March 2020 at the SwissOGS with its laser ranging system. Units of colorbars: photoelectrons/bin.	93
4.9	Observed and fitted return rates for LAGEOS-1 during the years 2019 and 2020. Units of colorbars in photoelectrons/second.	102
4.10	Box plot depicting monthly estimated return rates for LAGEOS-1 observed on 2019 and 2020 at the SwissOGS with its laser ranging system.	103
4.11	Box plot depicting monthly estimated return rates for LAGEOS-1 observed on 2019 and 2020 at the SwissOGS with its laser ranging system after filtering the raw data using the real-time and screening flags.	104
4.12	Examples of theoretical return rates for target objects at different orbital regimes using as cross-sections parameters the values provided by the ILRS using the 1,064 nm wavelength.	108
4.13	Calibration measurement estimates and precision ($\pm 1\sigma$) using observations at 532 nm collected in one minute through the 25th of November 2020. The dashed blue line represents the difference in estimates between the i th and i th + 1 estimated calibration value.	109
4.14	Calibration measurement estimates and precision ($\pm 1\sigma$) using observations at 1,064 nm collected in one minute through the 25th of November 2020. The dashed blue line represents the difference in estimates between the i th and i th + 1 estimated calibration value.	109

List of Figures

4.15	Detail of the first measurement set at 532 (left) and 1,064 nm (right) to the external calibration target. Both top histogram depict the counts/bin with a bin size of 6.5 seconds. The right vertical histogram depict the empirical distribution of the calibration measurements. Note the different spacing y-ticks magnitude values for both measurement sets.	110
4.16	Observations to the external calibration target employing the 1,064 nm wavelength. The different discontinuities depicted in the plot correspond to changes in the emitted power, which was adjusted manually. The discontinuities at 1268.5 and 1274 min correspond to an attenuation of 99 % of the total energy, while for the rest only 60 % attenuation was used. After 1268.5 the attenuation was performed gradually, while for the other cases it was set up instantaneously.	113
4.17	Experimental observations to ILRS targets using the 532 (left plots from <i>a</i> to <i>e</i>) and 1,064 (right plots from <i>a</i> to <i>e</i>) nm wavelengths available at the SwissOGS. The gaps within the displayed measurements occur as a consequence of local air-traffic safety measures. Likewise in orange it is shown the detected photoelectrons being triggered presumably by reflected photons from the target, while in blue photoelectrons classified as noise.	117
5.1	Length of day as a function of latitude and day of the year starting from winter solstice. The contour lines indicate the length of day, i.e. the elapsed time between the rise and set of the Sun.	125
5.2	Light curve of ENVISAT observed on April 15, 2021, during daylight. The elevation of the Sun was 2.4 ° at the beginning of the observation time, i.e. at 5:02 UTC. The left plot shows the brightness variations of the RSO while crossing the SwissOGS. The geometry of the pass with respect to the observing station is shown in the right plot as azimuth and elevation in the horizon system centred at the SwissOGS.	126
5.3	Light curve of ENVISAT observed on April 24, 2021, during daylight. The elevation of the Sun was 26.9 ° at the beginning of the observation time, i.e. at 15:46 UTC. The left plot shows the brightness variations of the RSO while crossing the SwissOGS. The geometry of the pass with respect to the observing station is shown in the right plot as azimuth and elevation in the horizon system centred at the SwissOGS.	127
5.4	Ground track of ENVISAT starting on July 28, 2021, at 10:00 UTC until July 29, 2021, at 22:00 UTC. The orbital elements were extracted from the latest TLE available from space-track at starting date. The segments of the track represented in magenta represent the portion of the orbit observed from the SwissOGS using an elevation mask of 20 °.	129

List of Figures

5.5	Sky plot centred at the SwissOGS for ENVISAT starting on July 28, 2021, at 10:00 UTC until July 29, 2021, at 22:00 UTC. The hours of each pass are shown at the bottom-right of the plot in UTC. The beginning and end of the pass are marked with a cross and a dot respectively to indicate the flight direction.	130
5.6	Observed orbital arc in Figure 5.5 represented in the orbit reference frame. Colours match with the passes displayed in Figure 5.5.	131
5.7	Distribution of the direct solar spectral flux density according to a black-body radiator, on top of the atmosphere (TOA) and on ground. The last two curves were extracted using the LOWTRAN7 software package [45]. The filled area under the curve represents the total amount of direct solar intensity in the visible domain [400 nm, 800 nm] yielding a total integrated value of 366 W/m ²	133
5.8	Distribution of the diffuse solar spectral flux density on ground at an angular distance of 45 °. The filled area under the curve represents the total amount of diffuse solar intensity in the visible domain [400 nm, 800 nm] yielding a value of 40 W/m ² sr after numerical integration.	134
5.9	Count of triggered photoelectrons after incident solar diffuse spectral radiance on the receiver using an integration time of 0.01 seconds. The plot shows the area removed by using a spectral broadband rectangular filter from 400 nm to 500 nm, and the remaining portion of the visible spectrum. The diffuse solar radiation direction is that of 45 ° away from the direct incidence.	136
5.10	Percentage of incoming starlight as a function of the daylight sky background with surface brightness ranging from 2 to 8 magnitudes per square arcsecond and stars within a surface brightness range from -2 to 10 magnitudes per square arcsecond. The dashed red lines indicate the limiting surface brightness for a daylight sky background of 2.9 magnitudes per square arcsecond; it shows that up to stars with a magnitude per square arcsecond of 7 , the percentage of incoming starlight is larger than 1 % . .	137
5.11	Minimum observable cross section as a function of altitude for a expected return rate of 2 photoelectrons/second derived relative to the measured return rates of 7 photoelectrons/second using one year of observations to the LAGEOS-1 satellite.	141
5.12	Antenna gain as a function of beam divergence and pointing accuracy with respect to a unit power isotropic radiator.	143
5.13	Examples of subframes acquired during daylight for TanDEM-X and TerraSAR-X (top plot) and the second stage Zenit-2 (bottom plot). The RSOs were observed on August 28, 2019, at 16:52 UTC (top) and on October 16, 2019, at 10:49 UTC (bottom). For both days the apparent position of the Sun was that of 244 °, 33 °, and 139 °, 25 ° in azimuth and elevation respectively. Units of colorbars: Analog-Digital Units (ADU).	144

List of Figures

5.14	Left plot: RSO image and estimated apertures on the image plane; the green circle represents the aperture for the source TerraSAR-X, while the red annulus represents the area sampled to estimate the background. The unit of the colorbar is given in ADU. Right plot: normalized intensity profile as a function of the estimated centroid with the resulting estimated point spread function.	145
5.15	Left plot: RSO image and estimated apertures on the image plane; the green circle represents the aperture for the source TanDEM-X, while the red annulus represents the area sampled to estimate the background. The unit of the colorbar is given in ADU. Right plot: normalized intensity profile as a function of the estimated centroid with the resulting estimated point spread function.	146
5.16	Left plot: RSO image and estimated apertures on the image plane; the green circle represents the aperture for the source Zenit-2M, while the red annulus represents the area sampled to estimate the background. The unit of the colorbar is given in ADU. Right plot: normalized intensity profile as a function of the estimated centroid with the resulting estimated point spread function.	146
5.17	Examples of laser ranging measurements to two pseudo-cooperative RSOs being the left plot measurements to the decommissioned RSO Topex/Poseidon observed on August 18, 2021, at 16:18 UTC, and the right plot for the rocket body L-55 (YF24) (Long March (CZ) 2C) observed on August 15, 2020, at 18:47 UTC. Both passes were observed during daytime and show different widths for the range gate at observation epochs.	148
5.18	Left: detail of triggered photoelectrons on receiver showing the entries classified by noise (blue) and the entries classified as signal (orange) by the real-time filter to the decommissioned satellite Topex/Poseidon on the 18th of August at 16:18 UTC. The sinusoidal pattern reflects the rotation of the retroreflector with respect to the centre of mass of the RSO. This plot exemplifies how the tumbling motion of a RSO can pose a difficulty for the real-time laser ranging filter detector. Right: detail of classified photoelectrons in spite of a trace showing a significant slope, about $\Delta OBS - COM = 200$ nsec per 5 seconds, due to the quality of the used ephemerides for the rocket body L-55 (YF24) (Long March (CZ) 2C) observed on August 15, 2020, at 18:47 UTC.	148
5.19	Residuals after a constraint-less orbit improvement using one observing station and an ultra-short arc. The bottom trace might correspond to the backscattered signal by a highly reflective element on board of the rocket body, which is a hypothesis supported by the relatively high return rate, while the upper trace might correspond to reflections from either the remaining irradiated portion of the body or a contribution provided by diffuse reflection of another highly reflective element on board of the rocket body.	150

List of Figures

5.20 Top: resulting tracking measurements in the camera reference system for both X and Y after the RSO recognition on the acquired frames by the passive system *ObjRec* and the prediction *ObjPred* step estimated by the active tracking module. Bottom left: resulting light curve for the RSO of interest extracted in real time while tracking the RSO. The lack of scattering suggest a good signal to noise ratio between source and background. Bottom right: resulting active observations after a binning of 30 nanoseconds in the Y -axis and 1 sec in the X -axis to infer the concentration of photoelectrons in both domains. 152

5.21 Top: real-time extracted light curve as a by-product of the active tracking; note that the signature shows a significant scatter coming from a suboptimal signal to noise ratio, however, the presence of relative critical points may add information to the understanding of the attitude and attitude motion of the RSO. Bottom: one-way laser ranges residuals after a constraint-less orbit improvement using all detected hits by our laser ranging real-time filter. 154

List of Tables

1.1	Statistical descriptors corresponding to the data presented on the left plot in Figure 1.4.	25
1.2	Statistical descriptors corresponding to the data presented on the right plot in Figure 1.4.	25
3.1	Results for the orbit determination of LAGEOS-1 using five days of normal points gathered from the ILRS network plus 35 minutes of angular observations acquired by the tracking camera. Results are shown in the satellite-fixed reference frame. σ stands for the standard deviation of the estimated component at a 68% of confidence for a normally distributed data set.	47
3.2	Estimated Gaussian point spread function parameters. Units of estimated values and their corresponding precision are given by the unit of the parameter (first column).	53
3.3	Orbit solutions using a different set of observations within different parts of the observed arc. Case study for AJISAI observed the 8th of September by ZIMLAT and tracking camera.	59
3.4	Estimation of the background varying the geometrical pattern from where samples of the background are extracted. Std: standard deviation. Mad: median absolute deviation. We highlight in gray the combination of estimators that minimize the impact of the source in the estimation of the background.	72

List of Tables

4.1	Summary of observations presented in Figure 4.17 per each target object observed employing either the 532 or 1,064 nm wavelength. The attributes correspond to the pass identifier, the observation date, the beginning of the pass (T0) in Coordinated Universal Time (UTC), the end of the pass (TE) in UTC, the wavelength (λ) in nm, the bearing of the pass, the culmination of the pass in degrees, the maximum photoelectron rate in photoelectrons/second (Max Re. Ra.) and the maximum of photoelectrons identified as signal by the real-time filter of the laser ranging system at the SwissOGS (Num. Hits).	118
5.1	Estimated synodic spin periods of ENVISAT during daylight passes after detrending the light curves depicted in Figure 5.2 and Figure 5.3.	127
5.2	Horizontal coordinates of the Sun at the starting epoch of visible passes for ENVISAT over the SwissOGS.	130
5.3	On-receiver diffuse solar radiance at 532 nm.	138

List of Abbreviations and Acronyms

ADU Analog-to-Digital units.

COPUOS Committee on the Peaceful Uses of Outer Space.

CPF Consolidated Prediction Format.

DISCOS Database and Information System Characterizing Objects in Space.

ESA European Space Agency.

GEO Geostationary Orbit.

GNSS Global Navigation Satellite System.

GPS Global Positioning System.

GTO Geostationary Transfer Orbit.

HEO Highly Elliptical Orbit.

IADC Inter-Agency Space Debris Coordination Committee.

ILRS International Laser Ranging Service.

ISO International Organization for Standardization.

ITU International Telecommunication Union.

JCA Just-in-Time Collision Avoidance.

LAGEOS Laser Geodynamic Satellite.

List of terms

LEO Low Earth Orbit.

LOWTRAN Low Resolution Atmospheric Transmission.

MEO Medium Earth Orbit.

PID Proportional Integral Derivative.

PMT Photomultiplier Tube.

RSO resident space object.

SPAD Single Photoavalanche Diode.

SwissOGS Swiss Optical Ground Station and Geodynamics Observatory Zimmerwald.

TLE Two-Line-Element set.

UTC Coordinated Universal Time.

1.1 Towards a Sustainable Use of the Outer Space

IN this section, we will define certain terms that will have a relevance in the development and contextualization of the contribution provided by this dissertation. In first place, the outer space is defined as all space above an altitude of 100 km with respect to the surface of the Earth according to the Fédération Aéronautique Internationale. Furthermore, from the Outer Space Treaty signed back in 1967 it is stated that there is no claim for sovereignty in space, i.e. no nation can own space, the Moon or any other extra-terrestrial body [76]. It is important to keep in mind that not all existing countries have signed the treaty on the use of the outer space, but the number of signatories is increasing in time¹. The previous treaty defines the legal framework on the use and exploitation of the space and all liabilities that may rise thereof. Likewise, in spite of its vastness, and, as with any other limited resource, we must use it in a responsible manner to ensure that the next generations will inherit the space, together with its potential for exploration and exploitation, as we did. Following the previous line of reasoning, the use of the outer space in a responsible fashion implies its use in the long term, and therefore its sustainability. Now, the question to be addressed might be: how has our usage of the outer space been since the beginning of the Space Age? For assessing our up-to-date footprint in the outer space, we peruse the most recent space environmental report provided by the European Space Agency (ESA)² as of 1 January, 2021.

After the filtering of all information available to only count and type of target object in space per year (see Figure 2.1 subplot *a*) in ESA's report), there is clear evidence of a continuous incremental growth on the population of RSOs with respect to time. The count of number of objects reached a value larger than 25,000 objects by 1 January, 2021, using all cataloged objects from the United States Strategic Command (USSTRATCOM) Two-Line Elements catalog, i.e. all data collected by the United States Space Surveillance Network, the Vimpel data set maintained by the JSC Vimpel Interstate

¹<https://2009-2017.state.gov/t/isn/5181.htm>

²https://www.esa.int/Safety_Security/Space_Debris/ESA_s_Space_Environment_Report_2021

Corporation and Keldysh Institute of Applied Mathematics (KIAM), and the Royal Aircraft Establishment (RAE) Tables of artificial satellites. Orbital information on asserted objects, i.e. information retrieved from technical specifications before launch, as well as the justification for their assertion, is taken from the Database and Information System Characterizing Objects in Space (DISCOS). According to ESA's report, the counting was conducted considering the fact that certain objects could appear in more than one catalog. Note that the multiplicity of entries might be solved through the use of normal forms associated to the design, implementation and merge of databases from either one or different catalogs. The merge of different catalogs into one provides a larger sample of the population for RSOs if compared e.g. to the one provided only by the United States Space Surveillance Network catalog³. In addition, the contribution of amateur observations is growing and is used in current catalogs such as the one used and maintained by AstriaGraph⁴. After comparing the results given by different sources, there are other striking features depicted by the growth of RSOs. From 1957 until 2006, the count of the different RSOs categories depict a general linear trend with punctual fluctuations in the years 1978, 1979, 1986, 1987, 1988 and 1989. The general behavior changes for the subsequent year onward, depicting a significantly non-linear complex behavior with a growth from about 15000 RSOs to 28000 in a time span of 11 years. This singularity within the analyzed time series was noticed and attributed to the commercial utilization of low and geosynchronous orbits, science missions into the Solar System, and expansion of human presence in space toward exploration further outward from Earth's boundaries⁵. The same source presents tables, qualitative and quantitative description of the geographically-wise developed space activities within each particular year. Additionally, by inspecting figures related to the growth of objects according to specific orbital regions (see e.g. Figure 2.2 *a*) in ESA's report), it is possible to infer that the most crowded areas, and its growth over time, are more critical for the Low Earth Orbit (LEO) and Geostationary Orbit (GEO) orbital regimes.

The presented evidence shows a worrisome growing number of RSOs with respect to time answering the question raised at the beginning of the subsection. However, is this grow accounting only for objects dwelling on space after new launches per year, or are there events occurring within the existing population of RSO contributing to the increasing numbers as well? This question was already addressed by the scientific community and the results can be found in [3]. Since the beginning of the Space Age, on-orbit fragmentation events occurred contributing to 33 % of the total number of RSO as of 4 January, 2018. From the on-orbit fragmentation events, six events correspond to accidental explosions of rocket bodies, the intentional fragmentation of Fengyun 1C by an anti-satellite weapon besides the well-known collision between the satellites Iridium 33 and Cosmos 2251 in 2009. Up-to-date statistics extracted from ESA's 2021 space environment report, point into a total number of 566 fragmentation events, from which the largest proportion was associated to propulsion breakup events. More recent breakups

³<https://orbitaldebris.jsc.nasa.gov/quarterly-news/pdfs/odqnv25i3.pdf>

⁴<http://astria.tacc.utexas.edu/AstriaGraph/>

⁵<https://www.nasa.gov/directorates/somd/reports/2007/index.html>

events were observed on March, 2021, corresponding to the satellites NOAA 17, with International Designator number 2002-032A and Catalog number 27453, and YunHai 1-02 with International Designator number 2019-063A and Catalog number 44547. From each event a total number of 102 and 43 fragments, respectively have been parented with the main objects.

Conclusion

Despite the legal framework provided by the Outer Space Treaty available in [76], the current use of the outer space is unsustainable. If the current situation is left unaccounted for, the evidence points into an exacerbated situation with full potential to develop the well-known Kessler's syndrome. It is therefore clear that any contribution towards a sustainable use of the outer space is not only significant from the point of view of the novel scientific or technical developments, but also has an immediate impact in the preservation and long-term utilization of the outer space by current and future generations.

1.1.1 Mitigation Guidelines and International Recommendations

Previously it was shown that the current use of the outer space is not sustainable. The conclusion points into an urgent need of scientific and technical contributions paving the way towards a sustainable use of the outer space. The question that we will address here is: what are the current measures that are, or have been, implemented to guarantee a transition into a sustainable use of the outer space? To answer this question, we introduce the Committee on the Peaceful Uses of Outer Space (COPUOS) and the Inter-Agency Space Debris Coordination Committee (IADC). The COPUOS was set up by the United Nations General Assembly in 1959 to govern the exploration and use of space for the benefit of all humanity: for peace, security and development⁶. The IADC is an international forum of space agencies, authorized governmental or inter-governmental entities for the coordination of activities related to the issues of human-made and natural debris in space [38]; it uses, among others, all prior contribution provided by COPUOS and other organizations to provide up-to-date mitigation guidelines for the secure long-term use of the outer space. Both organisms define together the set of defunct RSOs as: *“all man-made objects including fragments and elements thereof, in Earth orbit or re-entering the atmosphere, that are non-functional.”* Bear in mind that the previously defined set of defunct RSOs is contained within the set of RSOs.

Within the latest revision of the space debris mitigation guidelines in [38], there are four distinguishable blocks namely: Limitation of Debris Released during Normal Operations, Minimization of the Potential for On-Orbit Breakups, Post-Mission Disposal and Prevention of On-Orbit Collisions. Technical standards to enable the implementation of the mitigation guidelines are conducted, e.g., through the International Organization for Standardization (ISO) with identifier 24113 : 2021. The previous top-level ISO standard contains many other low-level standards further developing each proposed mitigation

⁶<http://www.unoosa.org/oosa/en/ourwork/copuos/index.html>

guideline initially proposed by the IADC. As an example, all standards related to space systems, and the avoidance of collisions with RSOs, are presented in the ISO and Technical Report 16158 : 2021.

The contribution of this dissertation supports the COPUOS space debris mitigation guidelines. Specifically, we aim at the improvement of observational techniques, which will report an improvement in the updating of state vectors of existing RSOs, comprising position, velocity and attitude motion. Furthermore, by the implementation of laser ranging to space debris targets, the uncertainty of the estimates has the potential to be shrunk, thus aiding on the planning and execution of efficient avoidance maneuvers when a close conjunction is foreseeable.

1.1.2 Space Debris Removal and In-Orbit Servicing

Within the block of Post-Mission Disposal and Prevention of On-Orbit Collisions, further activities that benefit from low uncertainty updated state vectors of RSOs, including information about their attitude motion, are the ones related to active, or passive, space debris removal or in-orbit servicing. By direct removal of space debris, high risk objects are brought out of high risk-orbital regions reducing the probability of collisions. In this context, the risk might be defined proportional to the object's mass times the probability of collision at a given time. Likewise, for the definition of high risk-orbital regions, we use the definitions provided by the IADC particularized for the LEO and GEO orbital regimes. In addition, the implementation of in-orbit servicing will extend the lifetime of satellites preventing new launches for the replacement of defunct missions. In this subsection, we will address studies conducted on the aforementioned activities.

To reduce the number of defunct RSOs in the outer space, there are removal (both active and passive) strategies and in-orbiting services available. Passive removal may encompass natural decay due to external forces, mainly non-conservative forces such as solar radiation pressure or atmospheric drag, acting on the RSO, or the implementation of a post-disposal strategy, already implemented in the RSO, to be executed within the next 25 years after its lifecycle is completed. Note that the previous IADC guideline was changed in 2019 to the next 25 years once the future RSO is put into orbit. On the other hand, active removal will involve the design of a mission, which will exert an action upon the RSO to be removed. Note that the difference between the latter and in-orbit servicing initiatives is that in-orbit servicing, in principle, does not attempt to remove the RSO, but rather to extend its lifecycle. The study conducted in [46], particularized for LEO RSOs, projects the current RSO population and related space-based activities within the next 200 years. In particular, the population of RSOs is modeled simulating current number of launches, removal via post-disposal mechanisms and removal through active missions. The study analyses the following scenarios: case 1) a 90 % success rate for only post-disposal actions; case 2) post-disposal actions at 90 % success rate plus active debris removal, starting from 2020, with a success rate of 2 RSOs removed within one year, and case 3) post-disposal actions at 90 % success rate plus active debris removal, starting from 2020, with a success rate of 5 RSOs removed within one year. The conclusion from the study is that the only case that keeps the growth of RSOs constant

as hitherto is the case number 3 if, and only if, post-disposal actions have a success rate of 90 % and at least 5 RSOs are removed each year, which is unrealistic if compared to the current situation. In addition, the synergy between post-disposal actions and removal highlights the imminent impact on the growth management of RSOs. In the following, we will provide a summary of two missions, which were designed as a proof-of-concept demonstration of those mitigation plans.

KIKU-VII

The KIKU-VII, also known as Engineering Test Satellite No. 7 (ETS-VII), launched on November 28, 1997, with a foreseeable life expectancy of 1.5 years for a satellite with an altitude of 550 km and an inclination of 35 °, was the first attempt to demonstrate in-orbit operations between a chaser and a target using a robotic arm. Despite not being the first attempt in the field of teleoperations, the experiment was novel in the field of in-orbit servicing. The experiment was comprised by a chaser and a target both working under relative oriented mass-spring-damper models. In general terms, the mission was a demonstration for rendezvous docking operations including the manipulation of specific target components such as a slide handler. Furthermore, critical operational aspects involving telemetry and operator skills, among others, were tested for assessing the impact of those factors in the complete mission design and expected mission performance [37]. The demonstration conducted during the development of the mission design prior to launch comprised the following tasks:

- **Pushing tasks.** Within this task the interaction between the robotic arm of the chaser and the so-called task board was tested. For this test, the actions of the arm were specified as normal to the testing board, where a tracing slide was placed to be pushed by the tip of the robotic arm. Within the push phase, three different set-ups were tested: for the first one the operator received force feedback from the master control besides visual aid depicting the telemetry force data. For the second case, the operator received only force feedback without visual aid. During the third test, only visual aid was used as feedback for the test. The relevance of the different scenarios deems critical for potential failures that might occur withing the operational phase of the mission.
- **Slope tracing tasks.** Within the tracing tasks the goal was to prove the navigation of the tip of the robotic arm within a bumped mechanical device mounted on the task board. For this test, the correct position of the tip of the robotic arm with respect to unknown reference points, to the tip of the robotic arm, was tested. The set up for this test used constant force depicting different trajectories within the slope tracing device mounted on the track board, and comparing the position of the tip with respect to the reference points. Finally, the combination using visual aid, as described in the former experiment, with and without force feedback, i.e. bilateral and unilateral operating modes, was tested.
- **Peg-in-hole tasks.** Together with the other two phases, this one achieved the docking by the insertion of specific pegs into specified locations within the task

board. This experiment also tested the redundancy of data provided by the force feedback and visual aid. Furthermore, the feedback provided by the operator was included as an indicator of the smoothness of the operation from a humanistic sensorial perspective.

- **Slide handle task.** This test involved the clear task of handling a specific hardware component: the slid handler. One of the interesting features of this experiment was the intentional rotation of the orientation of the task-board X-Y plane, where the translational movements of the arm would be mapped into horizontal motions applied on the task board. This task points into the interaction of the arm with specific system components aiming at e.g. fixing or upgrading specific hardware components, refilling of propellant, etc.
- **Skill level and other factors.** Within the different factors affecting the resulting behavior of the robotic arm, the impact of the operator is deemed critical. Note that all actions performed by the robot were intended to be carried out either automatically by on-board software, or by a ground station via telemetry commands. The impact of using telemetry commands, in particular the time lag between emission and reception of the signal carrying the command, was further analyzed [37]. Furthermore, the previous study presents the conclusions drawn after using different operators arranged according to different degree of skillfulness regarding the remote operation of a robotic arm via telemetry commands.

For completeness, the global orientation of the spacecrafts for the ETS-VII successful mission was achieved by employing Global Positioning System (GPS) receivers, while for the rendezvous docking operations, the use of passive-optical systems was employed for resolving the relative orientation between target and chaser. For more information and details, the reader is directed to [37].

ELSA-D

The mission End-of-Life Services Demonstration (ELSA-d) is currently an operative mission, since March 2021, designed and operated by Astroscale. In general terms, it is a mission that serves as a testing interface for the preparation of future in-orbit servicing and active debris removal missions targeting LEO RSOs⁷. The payload consists of a servicer and a client performing a series of in-orbit demonstrations. Those demonstrations comprise the launching into a specific orbit at an altitude of roughly 550 km and inclination of 97.5 °, besides the commissioning of the payload (phase 1 and 2). The phase 3a of the mission proved the release and capture of the client (without tumbling) by the servicer at distances of not more than 10 m. The capturing mechanism is of the magnetic type with a ferromagnetic plate placed onto the client; the decision for the capturing mechanism was supported by the relaxation on the tolerances needed by the on-board measurement sensors in the servicer. The phase 3b proved the release of

⁷<https://directory.eoportal.org/web/eoportal/satellite-missions/content/-/article/elsa-d>

the client, besides proximity operations including docking with a tumbling and a non-tumbling client. The phase 4 is intended to demonstrate inertial navigation systems for approaching the tumbling client that will be diagnosed as the servicer senses the client with different sensors. The phase 5 consists of loosing the target from the detection of the sensors on-board of the servicer, and solving the absolute orientation of the servicer using a GPS receiver besides ground tracking. Once the absolute positioning of the servicer is found, a new capturing trajectory is computed with the final aim of seizing a non-tumbling client. The final phases 6 and 7 will include the reduction of orbit height and passivization of the payload with the final aim of a burn-up stage in re-entry.

Summary

Within this subsection, we presented in-orbit servicing and the potential of defunct RSO removal as concepts further contributing to the sustainable use of the outer space. We provided two examples of missions developed within this context. The examples were chosen according to their novelty, at the time of the development, besides the implementation of the mission in real life. There are several on-going research activities and future missions within this domain, but an in-depth study is deemed out of the scope of the current work. Nevertheless, three studies are briefly summarized.

The first one comprises the direct removal of a defunct RSO, in particular the Vega Secondary Payload Adapter (VESPA) currently scheduled to be removed in 2025 by the Swiss company ClearSpace. If compared to the ELSA-d mission, the removal of VESPA will consist of the phases 4 to 6. The main difference with respect to the ELSA-d mission stems from the fact that the RSO to be removed is completely uncooperative, i.e. the dynamic operating mode is unilateral with the docking rendezvous conducted by a robotic arm, which increases the difficulty of the task significantly. The target itself was chosen by the ESA due to its relative simple geometrical shape⁸.

The next study was presented as a doctoral dissertation exploring the use of nets for seizing defunct RSOs [64]. Specifically, Chapter 5 studies the impact of seizing a tumbling RSO when using different types of capturing mechanisms. In addition, it particularizes the impact of tumbling motion when using nets as capturing devices highlighting the limitations of the method in this regard.

Last but not least, there are several studies analyzing the so-called just-in-time collision avoidance measures. These type of collision avoidance measures render critical when a close conjunction is foreseen and the involved RSOs in the collision are non-maneuverable. We consider these types of events special cases, and as such, we further explore them in a separate subsection.

1.1.3 Just-in-Time Collision Avoidance

Until now, we have focused exclusively on the long term usage of the space. Activities and initiatives for reducing the human foot-print in terms of defunct RSOs in space were shortly revised to ensure its sustainable exploitation. The question we address in

⁸<https://spacenews.com/swiss-startup-clearspace-wins-esa-contract-to-deorbit-vega-rocket-debris/>

this subsection is: what are the up-to-date possibilities available for high risk encounters between RSOs happening with short notice? In particular, we assume non-maneuverable RSOs in need of a instantaneous change of velocity ΔV , hence lowering the probability of collision by changing the trajectory of at least one RSO.

Geometrical Considerations

The first parameter that deems crucial for a Just-in-Time Collision Avoidance (JCA) maneuver is the geometry between active segment, e.g. the responsible of executing the needed ΔV , and the passive RSO. The topology is defined as an active segment consisting of one or more systems able to interact with one or more RSOs, not necessarily simultaneously, after receiving a collision warning. To define the actionable window, i.e. the time span comprising the action by the system until reaching the needed ΔV , the actionable mechanism must be defined. If the mechanism consists of a highly dense particle cloud aiming at passively changing the velocity of the RSO by a force opposite to the flight direction, i.e. drag, the dynamics of such a cloud must be well-known to ensure that, by the time the object crosses it, the ΔV on the target occurs avoiding the collision. This possibility may add complications, since one has to answer the following questions: what is the readiness, i.e. the response time of the system to place the cloud in orbit so that when the object crosses it, its volume and density will ensure the needed ΔV ? How many clouds will be needed to reduce the ΔV cost effectively for critical encounters? How will these clouds evolve in time? Will these clouds be a threat to other RSOs? If the mechanism consists of a direct momentum transfer through electromagnetic radiation, we will be concerned about the availability of the system, the visibility between the RSOs and ground- or space-stations, besides the technical specifications of the system defined by the required ΔV to avoid a potential collision. Note that if we are using radiation within the visible spectral region and ground-based systems, the weather plays a critical role. Due to the domain encompassed by this dissertation, we will focus on ground-based momentum transfer techniques using laser systems.

Ground-based observing systems are by definition in the non-inertial topocentric Earth-fixed reference frame. Keplerian orbits, on the other hand, are defined in an inertial frame with the Earth in one of the foci of an ellipse. To relate both frames a series of transformations are needed. If we are interested in the relative geometry of the orbit with respect to the ground station, we start by transforming the orbital frame into the Earth-Centered-Inertial frame using as arguments for the transformation: the right ascension of the ascending node, the inclination and the argument of the perigee. Note that the Z component in the orbit reference frame is set to zero to be consistent with the involved three-dimensional rotations. Next, to transform from the Earth-Centered-Inertial to Earth-Centered-Earth-Fixed reference frame, we consider the precession, nutation, Earth and polar wobble rotations with arguments defined according to the selected convention (see for example the definitions provided by the International Earth Rotation Service⁹). Finally, to transform a given three-dimensional vector from

⁹<https://www.iers.org/IERS/EN/Publications/TechnicalNotes/tn36.html>

the Earth-Centered-Earth-Fixed reference frame to the topocentric, we need the geodetic and the cartesian coordinates of the ground station for the involved rotations and the translation, respectively. Note that the topocentric frame is left-handed while all the others are right-handed. Next, we divide the geometry into orbital shape and orientation of the orbital plane, with respect to the active segment, to determine its impact on the usage of momentum transfer by ground-based stations using laser systems.

- **Impact of the orientation of the orbital plane.** By consideration of the previous transformations, one deduces that the visibility of some portion of the orbit by a ground-based station will be limited by the inclination of the orbital plane with respect to the Equator. This constraint must be taken into account if a close conjunction is occurring between objects with orbital inclinations smaller than the minimum latitude of any given station from the active segment. In addition, unless we consider only circular orbits, the right ascension of the ascending node together with the argument of perigee will restrict the momentum transfer at the perigee to specific ground locations. Note that in-orbit maneuvers are more efficient either at apogee or perigee and that we are considering only imminent close conjunctions.
- **Impact of the orbital shape.** The orbital shape is defined unambiguously by the semimajor axis and the eccentricity, besides the perigee passing time to locate the target within the orbit. The total energy of a point mass particle is given by the sum of the kinetic and potential energy. Using the definition of the so-called *vis-viva* equation, the total energy E reads:

$$E = -\frac{\mu}{2a}, \quad (1.1)$$

where μ is the gravitational parameter of the Earth and a the semimajor axis. This expression highlights the fact that only the semimajor axis defines the energy of a particle of unit mass attracted by a central force. Assuming that one pass of an orbit, of one of the RSOs involved in the short notice warning, is visible from one ground station, an instantaneous change of the velocity $\Delta\mathbf{V}$ occurs as a result of irradiating the RSO with a laser beam. To understand the implications that $\Delta\mathbf{V}$ has on the trajectory of the RSO, we make use of Figure 1.1, where we show an instantaneous snapshot geometry of the active segment consisting of a ground-based laser system transferring an impulse, at an elevation angle ε from the local horizon, onto a RSO whose flying direction is represented by \mathbf{F}_T and its normal vector \mathbf{F}_N pointing inwards the described trajectory. The horizontal RSO reference frame (dashed line) is perpendicular to the geocentric radius vector of the RSO and relates to the body-fixed frame by the flight path angle γ . The geocentric angle φ subtends the angular distance between the RSO and the local zenith at the station for a spherical Earth. The vector basis in the body-fixed frame allows us to project the exerted momentum in such a frame, which is convenient to analyze the changes in the orbital elements, using for example the Gaussian Perturbation Equations. The resulting vector \mathbf{V}_R shows a deceleration of the RSO changing

its initial trajectory by considering only the tangential velocity. The impact of the magnitude of the pulse can be investigated by differentiating both sides of the *vis-viva* equation and considering that an instantaneous change in the total energy will change only the semimajor axis (see Equation 1.1) yielding:

$$da \propto v dv a^2, \quad (1.2)$$

where d should not be taken as infinitesimal, since its magnitude is not of that order of magnitude compared to the actual velocity of the RSO. In Equation 1.2, it is confirmed that to decrease a the particle must be decelerated, i.e. a change of velocity opposite to the flight direction. Other changes in the orbital shape, e.g. in the eccentricity and line of apsides, may be derived from the so-called Perturbation Equations e.g. in the Tangential, Normal and Out-of-Plane reference frame [9].

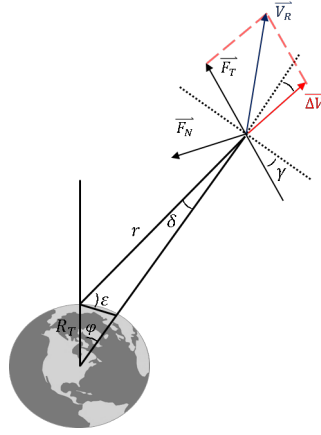


Figure 1.1: Instantaneous snapshot geometry of the active segment consisting of a ground-based laser system transferring a $\Delta\mathbf{V}$, at an elevation angle ε from the local horizon, onto a RSO whose flying direction is represented by \mathbf{F}_T and its normal vector \mathbf{F}_N pointing inwards the described trajectory. The horizontal RSO reference frame (dashed line) is perpendicular to the geocentric radius vector of the target and relates to the body-fixed frame by the flight path angle γ . The geocentric angle φ subtends the angular distance between the RSO and the local zenith at the station for a spherical Earth. The resulting vector \mathbf{V}_R shows a deceleration of the RSO to change its initial trajectory.

Finally, by considering the intersecting orbital planes for the RSOs involved in the short notice warning, we can derive the needed ΔV , using the magnitude of their respective velocities, the angle between them and the law of cosines.

System Considerations

Here, we will focus only on system components for specific momentum transfer through ground-based laser systems. Furthermore, we will split the subsection into the main subsystems involved in the usage of the aforementioned technique.

- **Effective Thrust.** The momentum transfer involves the transformation of irradiating electromagnetic energy into mechanical energy. To understand the different dependencies involved in the process, we use the following equation:

$$\Delta V = E_{las} C_m \tau^{-1} \sigma_{rso} L_{ss}, \quad (1.3)$$

were E_{las} is the nominal pulse energy of the operating system, C_m is the momentum coupling coefficient, τ the pulse duration, σ_{rso} the area to mass ratio of the RSO, and L_{ss} all losses involved due to target shape, optical properties, and attitude motion, among others. In Equation 1.3, we assumed implicitly a pulsed laser system, where short pulses will be translated into higher intensity and therefore larger ΔV , since instantaneous velocity changes should correspond to maximum peak power, i.e. $E_{las}\tau^{-1}$. Nevertheless, the use of a continuous wave laser system might be interesting to keep the output power constant, thus always maximizing C_m . Bear in mind that the latter, up-to-date has more commercial accessibility in terms of high output power (> 100 W) than pulsed systems. The behavior of C_m , depends on the characteristics of the irradiating system besides the chemical composition of the targeted RSO. Without loss of generality, the C_m shows three phases as a function of the laser fluence acting on a unit area of a defined material. First, the irradiating source transfer energy to the target heating it; after a certain threshold, the process turns into ablation evaporating, or sublimating, the solid material. For this two phases the C_m behaves linearly until reaching a global maxima, from where C_m drops quickly after continually increasing the intensity of the radiating source. That is an interesting outcome highlighting that after a certain intensity *more is not better*. The nominal intensity of the irradiating source must be selected according to the predominant material of the specific targeted subset of RSOs. Note that all studies related to spectroscopy, besides the estimation of the area-to-mass ratio, of RSOs may provide a suitable source for grouping RSOs, and propose a more general usage of the system enhancing its cost effectiveness. Finally, once we have a nominal figure of merit for the output power of the laser system, the number of needed pulses to avoid a potential catastrophic collision will be defined by the relative geometry of the observable pass.

- **Beam Collimation.** Another factor deemed crucial when employing this technique is the spot size of the laser beam onto the object. Considering a Gaussian beam, the angular beam size as a function of the distance z in the direction of propagation reads:

$$w(z) = \sqrt{\left(\frac{M^2 \lambda z}{\pi w_0 \sqrt{str}}\right)^2 + \left[w_0 + \left(1 - \frac{z}{f}\right)\right]^2}, \quad (1.4)$$

were M^2 is the beam quality factor, λ the wavelength of the operating system, w_0 the nominal beam waist at $\frac{1}{e^2}$, str is the Strehl ratio and f the focal length corresponding to the focused beam reaching w_0 . The first term inside the square root in Equation 1.4 corresponds to the behavior of a diffraction limited beam. From it, it becomes clear that to project the laser beam into a small spot on the object, the original beam waist must increase. The last requirement translates into telescope primary mirrors in the order of 13 m diameter to reach spot sizes of less than 30 cm diameter, for RSOs with altitudes of 1000 km, using the fundamental wavelength 1,064 nm, a hypergaussian beam parameter of 2, besides an effective aperture of 90 % of the total available. The latter is arguably one of the most expensive and delicate sub-components, requiring a tailored manufacturing process, i.e. there are not available commercially off-the-shelf. The second term inside the square root in Equation 1.4 corresponds to the change in the wave front curvature of the beam form as a function of the targeted altitude and focal length of the system. Note that the impact of an inaccurate pointing, tracking jitter and atmospheric turbulence were not included in Equation 1.4. Finally, notice the fact that the use of shorter wavelengths may reduce the needed size of the primary mirror, but the optical specifications for the mirror are stringer if compared to the near-infrared, and the atmospheric turbulence less forgiving.

- **Adaptive Optics.** Turbulence affects images acquired with a telescope and the transmitted laser beam by reducing the coherence and scattering the light with short correlation scale. The correlation scale, in this context, refers to the physical dimension of the vortexes involved in the interaction with the electromagnetic radiation according to Kolmogorov's law. By measuring the distortion of a reference wavefront traversing the atmospheric path, between telescope and reference, we may model the observed distortion correcting the incoming light for it before its projection into the focal plane of the imaging system. Within this vast topic, we will consider only the number of segments needed in the deformable mirror, which is responsible for the conjugated wavefront distortion, the impact of the so-called Fried parameter and the isoplanatic angle.

The Fried parameter r_0 might be computed using an estimate of the atmospheric seeing S_{atm} ([41]) as a function of the wavelength λ :

$$r_0 \approx \frac{\lambda}{S_{atm}}, \quad (1.5)$$

a seeing of 2 arcsec yields a Fried parameter of 6 cm at 532 nm, and of 11 cm at 1,064 nm. The broadening of the resulting point spread function in an imaging system due to atmospheric turbulence is proportional to the telescope's aperture and inversely proportional to r_0 . Therefore, it is convenient to account for this effect when selecting the nominal size of the primary mirror to minimize aberrations in the wavefront. With a fixed primary mirror, we derive the needed number of segments in the deformable mirror using the so-called fitting error, which is used to provide a figure of merit expressed as an error for the spatial frequencies for

which the deformable mirror cannot compensate, and reads:

$$\sigma_{fitt}^2 = k \left(\frac{D}{r_0} \right)^{5/3} Num^{-5/6}, \quad (1.6)$$

were Num is the number of segments used in the deformable mirror, and k a factor depending on the influence function of the deformable mirror. For a number of segments in the order of the thousand, we reduce σ_{fitt} by an order of magnitude of 10^{-3} , being competitive from the economical point of view, since the price of the deformable mirror grows quickly as Num increases.

When using adaptive optics to mitigate the impact of the atmosphere and yield diffraction-limited performance of the imaging system, the source for computing the distortion of the wavefront must be chosen. Using the emitted laser beam as the source for correcting the wavefront is discarded since the isoplanatic angle, i.e. the angular distance from which two stars can be separated yet their incoming light pass through the same volume of the atmosphere, is shorter by almost a factor of 5 than the lead-ahead angle for a LEO RSOs flying with a velocity of 7 km/s, yields a lead-ahead angle of about 10 arcseconds compared to an average seeing of 2 arcseconds:

$$\frac{r_0}{h} < \frac{2V}{c}, \quad (1.7)$$

were r_0 is the Fried parameter, h the altitude at which we are evaluating the isoplanatic angle, V the velocity of the RSO and c the speed of light. To overcome the previous restriction, the use of a laser guide star becomes imperative. In this regard, there are at least two common possibilities: the use of a Rayleigh beacon which scatters incoming electromagnetic radiation at altitudes of about 20 km, or the use of a sodium beacon exciting sodium particles at altitudes of about 90 km. The latter might be preferred, since the light passes through a larger portion of the atmosphere and is less affected by the so-called cone effect [79].

1.2 Sensing Resident Space Objects

The remote sensing of RSOs from ground- or space-based systems has the ultimate goal of retrieving information otherwise inaccessible. The retrievable information permits to derive not only an extended state comprising e.g. tri-dimensional position, velocity and attitude motion, but physical quantities such as optical, or radar, properties or even the so-called area-to-mass ratio. Likewise, the continuous surveillance of the outer space, thus the seamless measurement acquisition of RSOs, allows to construct catalogs of RSOs enabling the study and monitoring of the observed RSOs from a macro-scale perspective, and even derive dynamical models of an ensemble of RSOs. An example of such dynamical models have been used to confirm the so-called Kessler syndrome, but more daily uses of it might include: the parenting of objects e.g. after a break-up event, or the prediction of close conjunctions between RSOs.

To be able to sense and derive information of RSOs, we make use of the electromagnetic

radiation, its interaction with the targeted RSO, and the physical systems involved from the measurement acquisition process, until the extraction of information of interest. The electromagnetic radiation may be either generated and received by a specific system, i.e. an active system, or only received after being reflected from a RSO – radiated by an external source to the system, e.g. the Sun – defining a passive system. In addition, the spectral regime of the electromagnetic radiation of the observing system distinguishes, in general, between optical and radio regimes.

Specific subdivisions of the electromagnetic spectrum, within either the radio or optical domains, are dependent on the standard utilized; one widely used for the radio domain is provided by the International Telecommunication Union (ITU), but others include e.g. the discretization of radio bands according to the United States Institute of Electrical and Electronics Engineers, or even the one defined by the North Atlantic Treaty Organization. Using the ITU nomenclature, we find e.g. that the Haystack Ultrawideband Satellite Imaging Radar operating with a wavelength of 3 cm falls into the Super High Frequency band together with the Haystack Auxiliary Radar, which operates with a wavelength of 1.8 cm. Similarly, the German Space Tracking and Imaging Radar is able to switch between a wavelength of 23 cm to a wavelength of 1.80 cm, i.e. from Ultra High Frequency to Super High Frequency according to the ITU standards. Within the optical domain, its bandwidth has been associated with the spectral sensitivity curve of the human eye corresponding to 400 - 700 nm. Nevertheless, the impact of the atmosphere has played a role decreasing the previously defined lower bound to 300 nm, where radiation with lower wavelengths will be absorbed by ozone molecules, and the upper limit increased to 800 nm due to a better atmospheric transparency on that optical region. In addition, the use of spectral filters may subdivide the optical domain according to their spectral response. Examples of the aforementioned divisions are defined as photometric systems such as the Johnson-Cousins UBVRI, or the one defined by the Hypparcos-Tycho $H_P B_T V_T$.

Active optical observations usually operate under the principle of light amplification by stimulated emission of radiation, where the output wavelength is a function of the pumping source used to stimulate a specified material enclosed in a chamber. The aforementioned material after being excited by the pumping source reaches the so-called inversion state. While there is absence of radiation, the material gets back to its normal state releasing photons in the process. Those photons preserve the monochromaticity and phase derived from the pumping source and molecular, or atomic, constitution of the lasing material.

Depending on the needed information the type of observable varies. For orbit determination and improvement we use: ranges, range-rates and angular measurements – either in the horizontal or equatorial frames. For studying the attitude motion of a RSO, we might use range residuals, i.e. the observed range minus the computed using available ephemerides, changes in brightness, or even color photometry. To derive cross-sections and other optical properties we may use calibrated magnitudes and observed brightness including calibrated color indexes associated to a specific photometric system. Finally, the use of spectroscopy permits the correlation of RSOs with certain known materials used in the manufacturing process of satellites such as insulation layers. All this in-

formation will allow us to gain more insight into the behavior of defunct RSOs serving as the basis for future remediation activities to ensure the sustainable use of the outer space.

1.2.1 Passive and Active Electro-Optical Systems

The first developments of the different observation techniques, within the domain of space surveillance and tracking, had a military motivation. After the launch of Sputnik-I in 1957 by the Soviet Union, the United States of America created several programs devoted to the development of technology helping to keep track of the progress done by the Soviet Union in terms of missiles and satellite technology. Prior to the launch of Sputnik-I, the so-called Operation Moonwatch, comprising volunteer and amateurs astronomers distributed over the entire Earth, provided the prior information needed by the stations for pointing the new photographic Baker-Nunn observing system towards the RSOs of interest. The development of such a system was the aim of the Smithsonian Precision Optical Tracking program, based on prior optical work conducted in 1940 for the Harvard Meteor Project. The fact that only skilled observers were able to track continuously and reliably, motivated the director of the Vanguard project, Milton Rosen, to inquire for a fully electronic-based detection and tracking system. The analogous project to the optical initiative was denominated as Moonbeam operating radio wavelengths for extracting information through interferometry. The fact that the Moonbeam project was tailored for American radio signals did not permit the acquisition of the signals broadcast by Sputnik-I, thus the first information of Sputnik-I was acquired by the network of Baker-Nunn systems. In parallel, the Massachusetts Institute of Technology was developing the first prototype for the detection and tracking of missiles under the Ballistic Missile Early Warning System. The latter was the first active radio system detecting Sputnik-I.

The developments of active electro-optical systems were influenced by military applications as well and emerged after the invention of the laser in 1958. However, the idea of using short pulses of light to measure distances was initiated in 1933 by Lebedev investigating at the Vavilov Optics State Institute located in Saint Petersburg, Russia. The first prototypes of operable laser radar systems became available from 1960 to 1970 for military applications such as rangefinders, proximity fuses and weapon guidance. The use of rangefinders was extrapolated for extraterrestrial uses with the first reported successful reception of echoes in 1962 [69], which were coming from the Moon's surface. The Massachusetts Institute of Technology was pioneering the lunar laser ranging technique by using 50 J pulses of 0.5 msec length.

Over time, the technology has improved substantially. Within the next subsections we will focus on the type of information retrievable by each system, enhancements and further developments contextualized by the work encompassed within this dissertation.

Passive Electro-Optical Systems

Within this category we analyze systems that do not have a radiating source, but collect the reflected solar radiation by the targeted RSO or even several of them. In the following, we will analyze the system particularizing for those aspects that have a direct impact on the final quality of the observable.

- **Angular Measurements.** Observations of passive systems are defined in the camera reference frame. To retrieve angular measurements the transformation between the camera reference frame and the frame of interest, e.g. the International Celestial Reference Frame, must take place. To relate both frames we use the gnomonic projection, which grants radial symmetry with respect to a central axis ideally passing through the center of the image plane and the tangent point of an imaginary plane in the celestial sphere. Once the telescope is pointing in a given direction, we can derive relative coordinates of known stars from a catalog available within the frame besides getting their respective coordinates on the camera reference frame. Solving for an affine transformation with unknown parameters being: the scale relating pixels to angular distances, the translation in both axis matching the origin for both frames, the shearing in both axis due to inherent deformations and the rotation needed to match the axis of both frames, we can map any given coordinate on the camera reference frame into the frame of interest. Note that the previous operation needs of at least 3 reference stars properly separated within the frame and might be time consuming. For challenging scenarios where the previous transformation may fail, a direct transformation might be preferred where the arguments for the direct transformation are provided by the pointing direction. The latter will be further developed in Chapter 3.

Finally, the angular measurements must be time tagged. Considering the mean motion of the Environmental Satellite (ENVISAT) being of $0.1^\circ/\text{sec}$, 1 millisecond error introduces an error of 0.3 arcseconds. The previous argument supports the decision of using e.g. a PC-card synchronized to a GPS unit, providing an accuracy of 100 nsec to UTC. Alternatively, low-costs systems may use the network time protocol, with preferable a local private network setup, for synchronizing the machine time to UTC (accuracy of tens of milliseconds). Furthermore, the fact that we are integrating the reflected energy from the target RSO, poses a challenge for selecting the associated event trigger, e.g. opening or closing of the mechanical shutter of the camera to time tag the measurements. To mitigate this effect, one might store the shutter opening and closing times, and estimate the arithmetic mean of both. Note that this is critical when using long exposures or particularly when using mechanical instead of electrical shutters, which may add a delay. Finally, a good practice is to estimate the impact of potential delay variations that might be corrupting the time tag, or even the measurements themselves, by including a set of target RSOs with precise available ephemerides during an observation session and comparing the observations to those targets with the interpolated ephemerides at the epoch of each acquired measurement.

- **Brightness.** The apparent magnitude of a RSO is given by the reflected sunlight irradiance by any surface of the RSO with a given orientation with respect to the observing station. After the passive electro-optical device is exposed, the reflected irradiance is mapped into the position of the object in the frame that covers the field of view defined by the specifications of the system. Once the photoelectric effect takes place, the irradiance is transformed into a charge and later into Analog-to-Digital units (ADU), after an Analog-to-Digital conversion, where the digital number is represented according to the radiometric resolution of the sensor. Note that we are using diffraction-limited devices, and assuming no correction for the impact of the turbulent layers in the atmosphere, the corresponding point-source from which the solar energy is reflected will be mapped thus as the so-called point spread function. To derive the corresponding flux, we may integrate the signal from the source over the area covered by the point spread function. By doing so, we may compute apparent magnitudes in a given spectral filter, e.g. V using:

$$m_V = -2.5 \log_{10} \left(\frac{F_V}{F_{ref}} \right), \quad (1.8)$$

where F_V is the flux extracted from the digital frame and F_{ref} is the reference flux determining the zero-point for the filter V . When observing without a specific filter, we will not have a reference flux, hence we will refer to instrumental apparent magnitudes. After the successful tracking of RSOs, we will have available a series of frames that will be used to extract a time series of the brightness values of the target. The latter is used to derive information related to the attitude and attitude motion of the targeted RSO.

- **Target Identification.** Both angular measurements and brightness require to successfully identify the targeted RSO on the digital frames by digital processing techniques. From a statistical perspective, the event of receiving the reflected photons rates by the target RSO while the sensor is exposed, assumes that the photon rate must be constant – neglecting variations on the rates due to the external physical systems –, besides the fact that the exposures are independent from each other, i.e. the event of exposing once a frame is independent of exposing any other. With the previous premises we can represent the counting of photons via a Poisson distribution. The first and second moments of the Poisson distribution match with the constant mean rate of the physical event under consideration, in our case photon rates. Having defined the statistical model, we can compute the ratio between the first moment and the root square of the second moment yielding the so-called signal-to-noise ratio [36]:

$$\frac{S}{N} = \frac{N_*}{\sqrt{N_* + n_{pix}(N_{bck} + N_{drk} + N_{rdt}^2)}}, \quad (1.9)$$

where N_* is the total number of photons collected from the object of interest, n_{pix} the total number of pixels used for the estimation of each error source, N_{bck}

the total number of photons collected from the sky background per pixel, N_{drk} the total number of dark counts per pixel and N_{rdt} the total number of counts per pixel due to read noise. Lower signal-to-noise values are translated into less precise measurements, i.e. larger uncertainties, meaning that those measurements contain less information of pixels for extracting physical parameters of interest.

Assuming the presence of two distinguishable classes within one single image, e.g. foreground and background, we can compare the physical magnitude of both classes, e.g. provided by their ADU hereafter referred as intensity, to infer a figure of merit for the detection of one of them: the target RSO. We may use:

- the Weber's contrast, which is given by the following expression:

$$C_w = \frac{I_{for} - I_{bac}}{I_{bac}}, \quad (1.10)$$

where I_{for} and I_{bac} corresponds to the intensity of the foreground and background, respectively. Note the correspondence with the signal-to-noise equation after rearranging it.

- the colorimetric purity discrimination ratio, which is given by:

$$C_p = \frac{I_{for}}{I_{bac} + I_{for}}. \quad (1.11)$$

C_p gives the minimum amount of source intensity, given by the foreground class, that allows a mixture of foreground and background signal, yet being able to distinguish the foreground class.

Note that both expressions are equivalent providing how many times the magnitude of the foreground contains the magnitude of either only the magnitude of the background or the total of the available signal, i.e. foreground plus background.

Example

In Figure 1.2 we show two examples of stars observed during daylight. In the following, we use the aperture photometry method for estimating the centroid and radii for estimating the source and background sampling areas. For the left image in Figure 1.2 acquired with a 16-bit radiometric resolution sensor and using an exposure time of 0.05 seconds, the estimated radius for the source is 38 pixels, the total net counts of the source within the aperture, after subtracting the background, is 8012137 ADU with an estimated error yielding 11479 ADU. The ratio of the previous two quantities give us the signal-to-noise ratio, which equals 699. Diving the total net counts, after subtracting the background, by the area occupied by the aperture of the source, we get the numerator of the Weber's contrast equation. The estimated intensity of the background per pixel is 21041 ADU, which after being plugged into Weber's

contrast equation gives a contrast of 8 %. Likewise, the amount of incoming light from the source out of the total available is of 7.74 %.

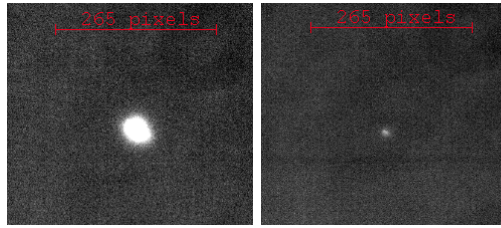


Figure 1.2: Left: Observation of a star during daylight using a sensor with a radiometric resolution of 16-bit and an exposure time of 0.05 seconds. Right: Acquired frame corresponding to a star observed during daylight using a sensor with a radiometric resolution of 16-bit and an exposure time of 0.1 seconds. The scale on the top of both images is provided for comparison of the different properties of the observed stars under nearly same observation conditions.

The right image in Figure 1.2 was acquired with the same radiometric resolution as before, but with an exposure time of 0.1 seconds. The estimated radius for the aperture of the source is 19 pixels. The total net counts of the source within the aperture, after subtracting the background, is 273297 ADU with an estimated error yielding 7532 ADU; the signal-to-noise ratio is 36. The contrast in this case yields a value of 0.6 %, and the total of incoming light from the source out of the total available is 0.6 %.

Active Electro-Optical Systems

Within the category of active electro-optical systems we will focus on pulsed laser systems. The working principle starts with the retrieval of ephemerides of interest, from which the telescope derive where it has to point and when. A standard form of those ephemerides is the so-called Consolidated Prediction Format (CPF), which gives tri-dimensional coordinates in the Earth-Centered-Earth-Fixed reference frame (the last available release in the form of the International Terrestrial Reference Frame). The ephemerides available through the ILRS are estimated using a set of globally distributed ground-based laser ranging stations providing observations as continuously as weather and technical constraints allow. The quality of the observations – in the order of the cm root-mean-square for normal points [52] –, together with their network configuration permit the retrieval of ephemerides with high precision – orders of magnitudes ranging from cm to m – and accuracy. Nevertheless, the RSO catalog available for tracking, utilized within activities of the ILRS, comprises selected mission with RSOs that have at least one nadir-pointing retroreflector on-board, i.e. the so-called cooperative target. In spite of the high quality of the predictions, provided by CPFs, there is no standardised dynamical model used by the different prediction providers. In the space debris domain, the CPFs may come from the predictions derived from Two-Line-Element sets

(TLEs), which must be propagated according to a standardised dynamical model, e.g. the Simplified General Perturbation Theory 4. The latter uses the latest available orbital and dynamical state after an orbit improvement, or determination using observations available from the ground-based network operated by the United States Air Force Space Command. One current challenge is given by the specifications of the systems, in particular radar systems with rather low precision if compared to the standard laser ranging. Having said so, we may expect ephemerides with accuracies ranging from hundreds of meters up to tens of kilometers.

Once the pointing of the telescope is set for the tracking of a given object, the laser system is ready to start irradiating it. Within the laser ranging system, the laser source is the main subsystem orchestrating all subsequent operations with the final aim of retrieving ranges. At a general description level, the laser may be characterized by its repetition rate, output energy, locking mode, pumping source, lasing material, operation wavelength, pulse length, beam profile, besides the specific optical assembly needed for shaping and aligning the outgoing laser beam. Once a laser pulse triggers an event on the start diode, an event timer does the timekeeping of the round trip after the emission, reflection by the RSO retroreflector, on-ground reception and detection. The observed range is calculated multiplying the measured round trip time with the speed of light times a factor of 0.5 due to the round trip. In addition, the pulse length will define the precision of the system and nowadays it is even used as a distinctive feature for categorizing different classes of laser systems. It is common to associate defunct RSO laser systems to *nanosecond laser systems*. Alternatively, laser systems dedicated to geodetic activities are often referred as *picosecond laser systems*.

Within the receiving optical chain, the detector releases negative charges upon the impact of a photon through the photoelectric effect. Those negative charges, after being multiplied using different mechanisms, are collected and transformed into an electric signal that triggers the stop event of the round-trip pulse travel time for an emitted pulse. Available detectors employed within the laser ranging community are: Photomultiplier Tubes, Multi-Channel Plates or Single Photoavalanche Diodes. To understand the relevance of a given detector, we study the signal-to-noise ratio from the hardware perspective [80]. The internal current i_{sig} within a photodiode undertakes changes due to the presence of signal:

$$i_{sig}^2 = 2qP_{sn}\rho_iBG^2, \quad (1.12)$$

where q is the electron charge, P_{sn} signal power, ρ_i is the current responsivity, B is the electronic bandwidth, and G is the gain of the device. The existence of surrounding background radiation being quantified by:

$$i_{bk}^2 = 2qP_{bk}\rho_iB, \quad (1.13)$$

where P_{bk} is the background power. The detector dark current:

$$i_{dk}^2 = 2qI_{dk}B, \quad (1.14)$$

where I_{dk} is the inherent dark current triggering an event on the diode. The thermal noise current:

$$i_{th}^2 = \frac{4kTBNF}{R_l}, \quad (1.15)$$

where k is the Boltzmann constant, T is the temperature of the device, NF is the detector noise factor and R_l is the detector load resistance. Combining the previous factors one may obtain the signal-to-noise equation at the hardware level yielding:

$$SNR = \frac{\eta_d P_{sn}^2}{hf[2B(P_{sn} + P_{bk})] + KP_{dk} + Ki_{th}^2} \quad (1.16)$$

where h is the Planck's constant, f is the transmission frequency, $K = \frac{\eta_d}{\rho_i^2}$, $P_{dk} = \frac{A_d B}{D_*^2}$ the equivalent dark current power, A_d the chip area, η_d the quantum efficiency, and D_* the specific detectivity. An optimization process involves either the minimization of the denominator in Equation 1.16, or the direct maximization of the numerator. We immediately see that the first term in the denominator (ignoring for the moment the background radiation) is a function of the signal power, which also depends on the gain of the detector. So, even though detectors with high intrinsic gain will have a higher signal, the noise will also be amplified. We also see the dependence of the dark counts as a function of chip size and operation bandwidth. In order to reduce noise, detectors should be ideally gated, i.e. a temporal window should be set up at the expected return epoch for an emitted pulse, and the chip area should be kept to a minimum. For photon counting applications where the signal can be focused on the small active area of the detector, together with a controlled photon flux in the order of less than 10^6 photons/sec, SPAD devices offer an improvement in detectability of a factor of 100 compared to PMT [80]. For SPAD detectors the avalanche effect happens in such an exponential manner that the response time decreases compared to the one of the photomultiplier tube. Due to the superior performance of the SPAD against the PMT, we will further develop the working principles of this type of detector. A single photon avalanche diode photodetector works under the principle of photoconduction, i.e. excited carriers after impact of an incident photon with enough energy are accelerated by an electric field to generate photocurrent (photoionization). The generation of the electric field is achieved by a p-n junction design. The difference between the p-type (excess holes), and n-type (excess electrons) is due to the dopant. A doped semiconductor, as opposed to an intrinsic semiconductor, is one that has specific impurity atoms introduced into it to shrink the band gap, i.e. to break free the bond state of an electron with less energy. An n-type is a pentavalent element, i.e. 5 valence electrons, where an additional electron, e.g. to the already existing 4 in the outer shell for the silicon atom, shrinks the band gap by expanding the conduction band. A p-type is a trivalent element; it donates holes to the structure and shrinks the band gap by expanding the valence band. When both are put together they reach an equilibrium state where the negative charged ions fill in the holes. To break the equilibrium, and therefore generate current, a voltage is induced. Depending on the arrangement of the current supply, the induced voltage can be either forward or reverse. If negative terminal of the input supply is connected to the anode (p-side) and the positive terminal of the input supply is connected to the cathode (n-side)

then the diode is said to be reverse biased. In this condition, an amount equal to reverse biasing voltage increases the height of the potential barrier at the junction facilitating the movement of electrons on the n-side to move onto the p-side, and vice-versa, hence increasing the depleted region at both sides of the junction. At this bias, the electric field is so high that a single charge carrier injected into the depletion layer can trigger a self-sustaining avalanche. The current rises swiftly, in the order of sub-nanosecond rise-time, to a macroscopic steady level in the milliampere range. If the primary carrier is photo-generated, the leading edge of the avalanche pulse marks, with about picosecond time jitter, the arrival time of the detected photon. The current continues until the avalanche is quenched by lowering the bias voltage down to or below the breakdown voltage. While the avalanche recovery circuit is quenching the avalanche and restoring bias, the SPAD cannot detect photons. As the number of photons increases such that the time interval between photons gets within a factor of ten out of the avalanche recovery time, missing counts become statistically significant and the count rate begins to depart from a linear relationship with detected light level. At this point the SPAD begins to saturate. If the light level was to further increase, ultimately to the point where the SPAD immediately avalanches the moment the avalanche recovery circuit restores bias, the count rate reaches a maximum defined purely by the avalanche recovery time in the case of active quenching, which is about hundred million counts per second or more. This can be harmful to the SPAD as it will be experiencing avalanche current nearly continuously.

Example

Here we will compare two devices: a SPAD with identification code C11202-100, and a PMT with identification code H7421-40 both working in photon counting mode and being manufactured by Hamamatsu ¹⁰. The active area of the SPAD is of 0.003 mm², while the PMT has one of 20 mm². The photon detection efficiency of the SPAD at 532 nm yields 61 % compared to the quantum efficiency of the PMT of 33 %. The dark counts are of 100 counts/second and 300 counts/second for the SPAD and PMT, respectively. Finally the output width of the pulses is of 17 nsec and 30 nsec for both the SPAD and the PMT, respectively. The estimated signal-to-noise ratio figures as a function of incident flux at a wavelength of 532 nm are shown in Figure 1.3.

¹⁰<https://www.hamamatsu.com/us/en/product/optical-sensors/mppc/photon-counting-module/>

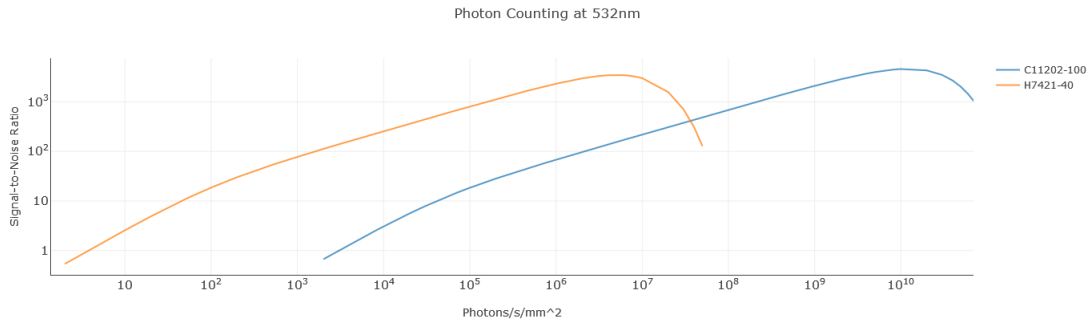


Figure 1.3: Comparison of the SPAD C11202-100 against the PMT H7421-40, both working in photon detection mode.

In Figure 1.3 we see two main features: the better performance of the PMT under rather low fluxes compared to the SPAD, but also its sooner saturation, which will prevent the detection of new incoming photons. The absolute magnitudes of the signal-to-noise ratios maxima are similar, which might be justified by equivalent gain factors on both devices. Despite not being shown in Figure 1.3, the SPAD has faster rise and fall times, with minimum dead time. It should also be noted that the enhanced performance, as described in [80], of the SPAD compared to the PMT, for this set up, is achieved at higher fluxes, i.e. 10^7 and 10^8 .

1.2.2 New Developments and Current Challenges

Within this subsection, we present the most relevant technical progress in terms of passive and active electro-optical observing sensors. Due to the main topics covered by this dissertation special emphasis is placed into active electro-optical observing systems using lasers. In addition, all possible optimization measures at the hardware and software level will be explored for the utilization of such systems for ranging defunct RSOs. Finally, the technological advancements are contextualized within the research activities of other groups, where we highlight possible novelties related to the presented work.

Geodetic vs. Space Debris Lasers Systems

At the beginning of this subsection, we introduced the role of the lasers and event timers for deriving the time-of-flight per emitted pulse. At this stage, we will provide an example of different results achievable when combining laser systems with different pulse length and different event timers. To do so, we collected raw calibration measurements from the Real Instituto y Observatorio de la Armada, known also as the San Fernando laser ranging station, located in Cádiz, Spain, during a research visit conducted in 2021. Both laser systems used at this station, Ekspla-NL317 and Ekspla-PL2250, match with respect to lasing material (neodymium-doped yttrium aluminum garnet), operating wavelength of 532 nm after frequency doubling, laser head dimensions of 1200 mm(L) X 500 mm(W)

X 300 mm(H), vertical polarization and repetition rate (10 Hz). The main differences are provided by the pulse length of 5 nanosecond and 30 picosecond, the beam diameter of 18 mm and 12 mm, and energies of 2500 mJ and 50 mJ, both for Ekspla-NL317 and Ekspla-PL2250 respectively. To see the impact of the pulse length in the single-shot root-mean-square of a set of measurements, we present in Figure 1.4 measurements acquired using both laser sources and an interval counter (the Stanford counter SR620) together with the Riga event timer A032. Basic statistical descriptors of the data shown in Figure 1.4 are provided in Table 1.1 and Table 1.2.

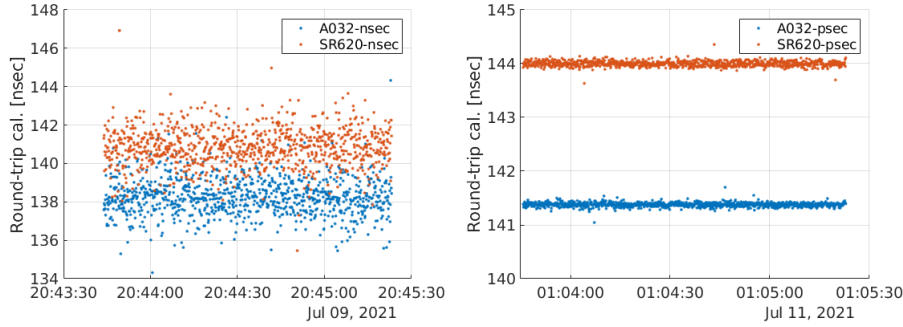


Figure 1.4: Comparison of calibration measurements acquired using the laser source Ekspla-NL317 (left) and Ekspla-PL2250 (right), corresponding to laser sources with pulse lengths of 5 nanoseconds and 30 nanoseconds, respectively. In addition, the round-trip time travel to the calibration target was recorded using two different timers: the Stanford counter SR620 and the Riga event timer A032. The statistical descriptors of the presented data are provided in Table 1.1 and Table 1.2.

As we can see, there are no surprising results, i.e. the nanosecond pulse length provides worse single-shot root-mean-square than the picosecond one, however, when using the nanosecond laser system we can yield an average emission power of 25 W, which allows to range RSOs that do not carry any highly reflective element on-board, i.e. a non-cooperative target. On the contrary, the average emission low power of 0.5 W achieved by the picosecond laser system, benefits from the optical cross-section of retroreflectors on-board of the RSO of interest, while minimizing the single-shot root-mean-square. Note that such a precision is needed for geodynamical investigations demanding a sub-centimeter precision.

Regarding the interval counter and event timer, we provide the specifications for both the Stanford counter SR620 and the Riga event timer A032. The resolution is of 4 picoseconds against 1 picosecond, the jitter yields 25 picoseconds against 8 picoseconds, the linearity yields 50 picoseconds against 1 picosecond, and the maximum repetition rate is of 100 Hz against 10 kHz, both for the Stanford counter SR620 and the Riga event timer A032, respectively. Comparing the time-of-flight recorded per each device and the two laser pulse length regimes, we see that there are offsets between all possible

comparisons between laser source and timer device. Those offsets must be controlled and calibrated on a regular basis to ensure that they remain as constant as possible in time, therefore allowing to estimate and remove them. The direct removal in each single measurement acquired at the station is performed by determining a calibration constant through measuring the range of the so-called calibration target, from which a geometric distance has been retrieved through classical surveying.

Table 1.1: Statistical descriptors corresponding to the data presented on the left plot in Figure 1.4.

Statistical Descriptor	A032	SR620
Maximum [nsec]	144.3	146.9
Minimum [nsec]	134.3	135.5
Mean [nsec]	138.2	140.8
Median [nsec]	138.2	140.8
Standard deviation [nsec]	0.96	1.00

Table 1.2: Statistical descriptors corresponding to the data presented on the right plot in Figure 1.4.

Statistical Descriptor	A032	SR60
Maximum [nsec]	141.7	144.4
Minimum [nsec]	141.0	143.6
Mean [nsec]	141.4	144.0
Median [nsec]	141.4	144.0
Standard deviation [psec]	40.2	50.3

Dual Wavelength Systems

One of the most significant losses within a laser ranging system occurs at the frequency doubling of the fundamental wavelength. In the following, unless specified otherwise, we consider the fundamental wavelength to be of 1064 nm and its second harmonic to be of 532 nm. Historically, the fact that within detector packages sensors had the highest quantum efficiency within the short and medium wavelength in the visible spectral regime, mostly even with the peak within the green spectral band, motivated its use in spite of the losses involved in the wavelength conversion. In addition, the alignment sessions of the optical beam when using the near-infrared was significantly at higher risk overall because the human eye is not sensitive at that particular wavelength. With the development of more sophisticated detector packages, the historical limitation of the quantum efficiency has been overcome, and by that, the use of the fundamental wavelength becomes an interesting choice for laser ranging stations operating the second harmonic avoiding the

purchase of a new laser system. The total gain provided by the fundamental wavelength has been already employed to perform lunar laser ranging [19]. In the same study, it is reported that the conversion has a shrinking effect on the length of the pulse length after the wavelength conversion, enhancing the single-shot root-mean-square for those measurements acquired with the second harmonic wavelength. For geodetic purposes, the usage of dual-wavelength systems allows to estimate the impact of the dispersive atmosphere in the round-trip propagation of the emitted pulse, but one has to consider that firstly wavelength dependent range biases must be estimated and monitored over time. At the SwissOGS, the previous laser system, which was able to operate either in 423 nm or 846 nm, was able to operate in either wavelength or simultaneously in both with the capability of selecting the energy per wavelength out of the total available. For more information about its implementation at that time the reader is referred to [30].

Observing Networks and Study Groups

In the following, we present a non-exhaustive list of observing networks or specific study groups addressing issues related to the observation of RSOs:

- **The United States Space Surveillance Network (SSN)** is a combination of passive electro-optical optical and radar sensors used to support the Joint Space Operations Centers (JSpOC) to detect, track, identify, and catalog all detectable RSOs orbiting the Earth [65]. The highlight from this observing network is the provision of TLEs used extensively within the space debris community. The fact that the TLE format was designed with a 5 digit field for the catalog identification number, the detectable RSO population is expected to surpass that limit – encouraged by the deployment of the Space Fence on Kwajalein Atoll –, the technical improvements in ground- and space-based observing platforms, a significant increase of uncorrelated tracklets due to a lack of accuracy provided by the dynamical models associated to the TLEs, provide enough arguments for requesting an improvement not only on the dynamical models, but also in the formatting of the ephemerides within their existing catalog. The Aerospace Corporation together with the United States Space Force, and the Consultative Committee for Space Data Systems are tackling this issue with the development of a new available propagator, the so-called SGP4-XP, and e.g. the Orbit Mean-Elements Message that is part of the so-called Orbit Data Messages standard ¹¹.
- **The European Union Space Surveillance and Tracking (EU SST)** is a network of ground-based and space-based sensors capable of surveying and tracking space objects, together with processing capabilities, provision of updated ephemerides, collision warning, re-entry monitoring, etc. aiming to provide data, information and services on space objects that orbit around the Earth [53]. Furthermore, it aims at having full coverage of the GEO and Medium Earth Orbit (MEO) regions for objects larger than 35 cm by 2023. For the LEO region, EU

¹¹<https://celestrak.com/NORAD/documentation/gp-data-formats.php>

SST aims at covering almost 100 % of objects larger than 50 cm and approximately 20 % of the objects larger than 7 cm. The research efforts foresee an improvement in the Sensor Function Activities, e.g. through the use of telescopes, active and passive, together with radars to catalog objects in the High LEO, and the application of Artificial Intelligence and Deep Learning techniques for an improved detection and characterization of RSOs. Further enhancements are addressed to the improvement of functional services within the processing of data within the EU SST, as well as the creation of new services such as support for active debris removal and in-orbit proximity operations.

- **The Australian Space Environment Research Center (SERC)** was established in 2014 to develop technologies to reduce the threat to space-based infrastructure from defunct RSOs. The project had four different research areas with a clear timeline defined within the years 2014 to 2021. The four research programs included: 1. The development of space debris-tracking hardware and adaptive optics-based solutions for reliable and accurate tracking of space objects. 2. Developing tools to improve the accuracy and reliability of orbit predictions for LEO RSOs. 3. Creating algorithms, databases and techniques to improve conjunction, prediction and prevent collisions in space, and 4. Apply the knowledge gained and technologies developed to maneuver space objects using ground-based lasers. A report informing about the fulfillment of goals defined within each research program is provided in ¹².
- **The IADC** was introduced at the beginning of this chapter. Here, we present the structure, consisting of a Steering Group and four specific working groups, covering measurements (WG1), environment and database (WG2), protection (WG3), and mitigation (WG4). Within the WG1 emphasis is put in the standardization of attitude observations through passive and active observing systems. Existing databases¹³ developed and maintained by single organizations, or institutes, have their own format posing a difficulty for the comparison, interoperability and merging of the data coming from different sources.
- **The International Laser Ranging Service (ILRS)** collects data observed by globally distributed ground-based laser ranging stations to RSOs equipped with retroreflectors within their active tracking catalog, following their specific standardized formats developed over time. As a historical note, the service started with a joint campaign with 30 stations within the so-called research program Monitor the Earth Rotation and Intercompare the Techniques (MERIT). Moreover, it combines the data to offer products comprising predictions, the already introduced CPF, raw or post-processed data from any station, besides the contribution of the measurements for estimating e.g. geodetic products. For more information, the

¹²https://irp.cdn-website.com/4b30def0/files/uploaded/SERCAAnnualReport_FINAL2021.pdf

¹³<http://www.satobs.org/ppas/ppas8.html>, <https://www.sdlcd.space-debris.sk/>, <http://mmt9.ru/satellites/>

reader is directed to the ILRS website¹⁴. Within the ILRS, we find a dedicated group covering all new aspects related to the target acquisition, tracking, ranging and monitoring of defunct RSOs: the Space Debris Study Group (SDSG). The SDSG was established at the ILRS Governing Board meeting held on October 26, 2014 in conjunction with the 19th International Workshop on Laser Ranging. The latest results were presented in January 2022 within an ILRS Network and Engineering Standing Committee meeting with the following highlights:

- **Daylight measurements of defunct RSO** using a dedicated space debris laser system by the Space Research Institute of the Austrian Academy of Sciences.
- **Simultaneous light curves and ranging of defunct RSO** by the Space Research Institute of the Austrian Academy of Sciences.
- **Multistatic campaigns** organized by the Space Research Institute of the Austrian Academy of Sciences.
- **Tumbling motion of defunct ILRS RSOs** by Daniel Kucharski.
- **Attitude determination methods** by Daniel Kucharski.

A final remark regarding the use of the laser ranging technique to targets out of the ILRS RSO catalog is the lack of stations with dedicated powerful space debris laser systems, but the emerging new application of the technique can take advantage of all the heritage provided by the geodetic use to support and further promote its utilization for the space debris domain.

- **The International Scientific Optical Network (ISON)** is an open non-governmental scientific project having as goals: the provision of reliable scientific output on space debris, asteroids and the so-called Gamma Ray Burst afterglows, using passive electro-optical observations; offering support to the astronomical observatories of the Former Soviet Union (FSU) countries besides involving amateur astronomers in scientific activities; and improving the international collaboration between FSU observatories and scientific organizations in other countries. This cooperation already consists of 23 observation facilities of various affiliations and is coordinated by the Keldysh Institute of Applied Mathematics of the Russian Academy of Sciences (KIAM). Recent highlights of the research activity of the ISON network comprise the study, observation and follow-up of fragmentation events. In 2018 two major fragmentation events in GEO and HEO were observed corresponding to a Titan 3C Transtage, with international designation id 1969-013B, and the fragmentation of the Atlas Centaur upper stage with international designation id 2014-055B. The network is specialized and well suited for the tracking of RSOs in Highly Elliptical Orbit (HEO), GEO, Geostationary Transfer Orbit (GTO), and beyond, and includes the study, observation and characterization of not only man-made RSOs, but asteroids and other celestial bodies or phenomena.

¹⁴<https://ilrs.gsfc.nasa.gov/>

Compact Laser Ranging Systems

The fact that the sensors of observing networks are unevenly distributed over the Earth (see e.g. the current ILRS network ¹⁵), that only selected ground stations are fully automated, that the standard infrastructure needed to host a laser ranging system involving the integration of the laser system within a building providing a stable geological ground support for the rather heavy mounts and optical benches, the installation of rather complex optical benches together with coudé paths for the transmission of the laser beam from the laser head to the telescope, both presumably located in different parts of the hosting building, among others, may provide the motivation for developing new concepts to ease the installation and operation of such systems. Compact systems have the potential to be cheaper, simpler to be operated and more cost efficient to be maintained. Assuming that enough candidates decide for acquiring and installing new laser ranging systems, it might be possible to reach better geographical distribution of the observing network, and presumably more data rate and system availability, which is deemed crucial for any space surveillance and tracking application, or any new emerging use of the technique such as optical communications.

First, we analyze the installation of the laser head on top of the fork of the telescope, i.e. the piggy-back concept, to avoid the installation of a coudé path, yet permitting the use of relatively heavy mounts, which may be needed to support relatively large primary mirrors (> 60 cm). The advantages given by this type of installation are provided by avoiding a transmit-receive switch, e.g. a rotating shutter, for installations sharing receiving and transmitting optical paths, i.e. monostatic configurations, the potential to use a dual-wavelength system avoiding complex adjustments of a second wavelength with respect to a reference one, or even the use of systems using different repetition rates. A disadvantage of this configuration, however, may be provided by the added weight on the mount causing structural stress, which could cause pointing issues. The cooling and controlling of environmental conditions may add complications in the design since the desired design should be compact with minimum weight.

Second, the development of the fiber optics permits the avoidance of complex coudé paths for directing the beam in the transmit, or receiving, optical chains, and, on the other hand, may be an excellent substitute for calibrating the system and defining local ties with submillimeter precision. There are nevertheless three aspects to be considered: the cost, operating wavelength and longevity of the fiber optic. The cost is a function of the wavelength and the longevity of the fiber optic. Furthermore, the power used by the optical beam will set a specific range of possibilities within the commercially available fiber optics; usually a good trade-off may include a variable neutral density filter, attenuating high power systems (> 1 W), thus reducing the costs, coupled to a collimation lens set on the front-end, and an optical amplifier on the back-end of the fiber before the detector. The operating wavelength will define the type of material within the core of the fiber optic, which could be made of plastic, for shorter wavelengths, or glass for longer wavelengths. Within the operating wavelength it is also important to consider the internal losses due to the selected wavelength, which is higher for shorter than for

¹⁵<https://ilrs.gsfc.nasa.gov/network/stations/index.html>

longer wavelengths.

Finally, there are research groups that have been able to create physical prototypes of the so-called MiniSLR systems with commercially-off-the-shelf components [31]. We will not provide more details since we encourage the reader to peruse the mentioned publication and relate it to the concepts developed within this chapter.

Controlling of Laser Ranging Systems

A laser ranging system is by definition a distributed system, i.e. a system with multiple components, or modules that communicate and coordinate actions to appear as a single coordinated system to the end-user. Within the controlling of a laser ranging system, we distinguish the following components or subsystems:

- **Frequency Standard.** This subsystem is the *heartbeat* of a laser ranging system. The frequency of the station will define the pulse per second (PPS) signal that will be used to synchronize all other processes available within the laser ranging system including its synchronization to a standard time scale, e.g. UTC. In addition, it may be used to define a specific frequency at which one or more intelligent units can perform a specific action. For example, at the SwissOGS the frequency input is derived from a Hydrogen maser outputting frequencies of 1 MHz, 5 MHz or 10 MHz using a digital frequency synthesizer. The output frequency is then divided to 40 kHz to feed the Programmable-Multi-Axis-Controller, which commands the telescope by translating ephemerides into analog signals ensuring the movement of the mount in a given direction. The software controlling this subsystem must be independent of the real-time operating mode of the laser ranging system, but may permit output operations providing specific flags regarding the status of the subsystem to the main control unit.
- **Laser.** This subsystem is not only responsible for releasing monochromatic light pulses after surpassing a certain energy threshold, but also how often they are released, i.e. the repetition rate of the station. The laser synchronizes to the station PPS and from it adjusts its own frequency. The software controlling this subsystem must interface with one, or more, I/O units of the laser system, e.g. the air-traffic system may output a *stop firing signal* to avoid firing in a direction, which must be read by the main control unit and translated into a stop command understandable by the laser software. If one considers the potential of a system to use any laser available in the market, ideally the software controlling this subsystem should be designed as a plug-in interfacing with the main control unit e.g. via the TCP/IP communication protocol, thus if one wants to change the laser only, it will only be needed to configure the plug-in for that new laser while the remaining part of the system, in principle, will not be affected by the change.
- **Event Timer.** The event timer synchronizes itself internally with the PPS from the station. Once synchronized, it is ready to receive input signals either from the start diode of the laser, or from the stop detector, only in case of being triggered

by a detection event, for deriving the time-of-flight of an emitted pulse. Note that any signal coming after the detection of optical electromagnetic radiation comes in the form of a specific voltage, NIM or TTL. The event timer must establish communication with the main central unit for sending the records comprising the time tag associated to the start event, and the time tag associated to the stop detection, if any. The subtraction of both timestamps yields the time-of-flight of an emitted pulse. Note that in the previous description, we are assuming event timers contrary to counters. The communication between the event timer and the main control unit should preferably use communication protocols such as TCP/IP, or the Universal Serial Bus instead of the deprecated parallel port standard.

- **Main Central Unit and Range Gate Generators.** Depending on the type of architecture, we can distinguish at least two main variants. The first one includes the Range Gate Generator mounted on a computer, which controls and collects the data needed for the laser ranging system. At the SwissOGS, the range gate generator consists of a field-programmable gate array (FPGA). It is synchronized to the 10 MHz and 1 PPS of the station, and may trigger:
 - Control pulses at the repetition rate of the laser to ensure its expected working mode.
 - Rectangular pulses of length equal to a configured time-window, i.e. a range gate, used for the expected return of the emitted pulse.
 - A frequency of operation for the rotating shutter, which is needed since we share the transmitting and receiving optical path.
 - Pre-pulses firing signals for the safety monitoring of the rotating shutter.

The interacting mode with the main central unit is through Fortran commands accessing I/O registers within the control unit. It becomes clear that, in this case, the main control unit consists of a closed loop running on the Central Processor Unit (CPU) of the hosting computer, coupled to the range gate generator. The second variant corresponds to an autonomous range gate generator with an embedded CPU and I/O peripherals, being function of the brand and model, which is synchronized to the frequency and PPS of the standard frequency of the station. Internally, this type of FPGA synchronizes its real-time internal clock to the input signal once the provided signal passes an internal quality and stability check. At this point, the internal signal generated by the FPGA might be compared to the reference either internally within the FPGA, or using an auxiliary device such as Stanford counter. The temporal offset between the two signals must be kept within defined limits and provide a quality check of the correct synchronization of the FPGA to the frequency of the station. Once the PPS and time of the FPGA has been set with respect to a reference, the output frequency of the FPGA may be used for synchronizing the firing signals of the laser, besides the signal needed for gating the receiver and any other. Note that even if the two variants may seem equivalent at this time, one distinctive difference comes next: the FPGA works independently from the main controlling software of the laser ranging system, i.e.

the main control unit is the FPGA itself and the controlling software is now a subsystem. The main consequence of the previous statement is that the controlling software does not need to run in real time, which may be a significant challenge to overcome in kHz repetition rates laser ranging systems with the architecture described by the first variant.

Example for the second variant

The controlling software wants to track a given satellite from which it has previously downloaded the latest ephemeris. It communicates via TCP/IP with the FPGA before the beginning of the pass, sending the ephemeris besides the instructions and configuration parameters needed by the FPGA. After acknowledging the reception of the message, the embedded Central Processor Unit in the FPGA, processes the received message, interpolates the ephemeris at the firing times and sets the range gates for the detector; the FPGA synchronizes the first firing epoch with its internal real-time clock, and by being already synchronized to the station frequency, it can set the firing signals for the laser, the range gate for the detector and e.g. any other external frequency. The event timer time tags the firing signals and waits for an event on the detector. If a detection on the detector occurs, the event timer time tags the detection event, sending back the information to the controlling software where afterwards both emission and reception events must be correlated. Simultaneously, the controlling software may be requesting meteorological or air-traffic information, or any status update of a specific subsystem.

- **Controlling Software.** As seen before, depending on the architecture of the system, one programming paradigm may be better than other for the development and implementation of the controlling software. Nevertheless, we may define the controlling software as an upper layer containing subsystem software modules responsible of data management, post-processing, laser ranging subsystems interaction, and others. There are other factors that play a crucial role when deciding the design and implementation of such a software system, e.g. the portability, maintainability, legacy, time frame, licenses, end-user, previous experience, just to name a few. On the other hand, there are common rules that apply to any programming paradigm such as adaptability, modularity, simplicity, unit testing, regression checks and version control. The previous concepts are recommended for a good programming practice regardless of the paradigm in which a software project will be developed.

1.3 Outline

In this chapter, a general overview of the context for this dissertation was given. Particular effort was put in actual applications employing active electro-optical systems using lasers specifically for its application within the space debris domain. From all possible

enhancements, we will focus specifically on optimizing the acquisition and observation of targets with ephemerides of compromised accuracy, on extending observation windows, mostly restricted to dawn or dusk observation session, as well as on analyzing and implementing changes needed for an existing geodetic laser ranging system, to enable laser ranging to space debris. To do so, the current dissertation will have the following structure:

- **Chapter 2.** In this chapter the laser ranging system will be introduced at the instrumental level. From this chapter, the reader might expect to find all technical information needed in the following chapters were one or more hardware, or software, components were either changed or adapted for the successful fulfillment of the goals aimed at by this work.
- **Chapter 3.** In this chapter, we focus on the so-called stare and chase observation strategy, which is a target acquisition and tracking approach using both active and passive electro-optical systems. The final aim is to correct the pointing of the telescope so that the target will be within the field of view of the laser beam, thus enabling the acquisition of laser ranges. By doing so, objects with poor ephemerides, available e.g. from Two Line Elements (TLE), will not pose a problem anymore for the rather small field of view of the laser beam. The system gathers both angular and range measurements, which can be used for an immediate orbit determination, or improvement, that will enhance the accuracy of the predictions helping other stations to acquire the target faster and permitting the station to more easily reacquire the object in future passes.
- **Chapter 4.** In this chapter, we will study the system, available at the SwissOGS, dividing it in different components that will permit to optimize the observations in terms of maximizing the detection of photoelectrons triggered by the backscattered photons from the target object. In particular, we address the signal-to-noise ratio for those objects that do not carry any highly reflective element on board. Special emphasis is put in the modeling of the return rates based on the technical specification of the station, together with its comparison with data retrieved from our archive. In addition, the operational implementation of the 1,064 nm wavelength will be described and first preliminary results will be shown.
- **Chapter 5.** In this chapter, we analyze the impact of optical daylight observations, within the domain of space debris, with respect to the currently restricted nighttime observation windows, relative geometry between the Sun, the RSO and the ground station, besides the type of observable acquired by the observing station. We highlight the role of key hardware components deemed critical for current optical ground stations to enable daylight measurement acquisition. Once we have inspected all factors deemed crucial for daylight observations, particularized for our system, we present successful daylight observations, from which we derived angular observables, ranges and apparent brightness and provide an example where the combination of measurements acquired by the different systems, operating in

the optical regime only, contributed to a partial disambiguation of the tumbling motion of a selected rocket body.

- **Chapter 6.** In this chapter we summarize the main achievements of this work and provide recommendations for the continuation of the research activity.

Employed Systems and Instrumentation

2.1 Telescope

THE Zimmerwald Laser and Astrometry Telescope (ZIMLAT), shown in Figure 2.1, is a 1 m class Ritchey-Chrétien telescope, with an alt-azimuth mount, used to acquire both active and passive observations.



Figure 2.1: The Zimmerwald Laser and Astrometry Telescope.

It has a coudé path for the laser beam and a Nasmyth platform hosting 4 possible focusing stations with focal lengths of 1.2 m, 2 x 4 m, and 8 m. Three of them are currently equipped with the Neo scientific CMOS tracking camera, the Spectral Instruments 1100 with a CCD sensor and a single photon counter. The telescope's effective aperture area is 0.78 m^2 and besides the primary and secondary mirrors on the main fork, we use a tertiary and a dichroic mirror permitting the simultaneous acquisition of active, from the laser system, and passive observations of sensors located on the Nasmyth platform. A schematic of the telescope including the transmitting and receiving optical paths is shown in Figure 2.2.

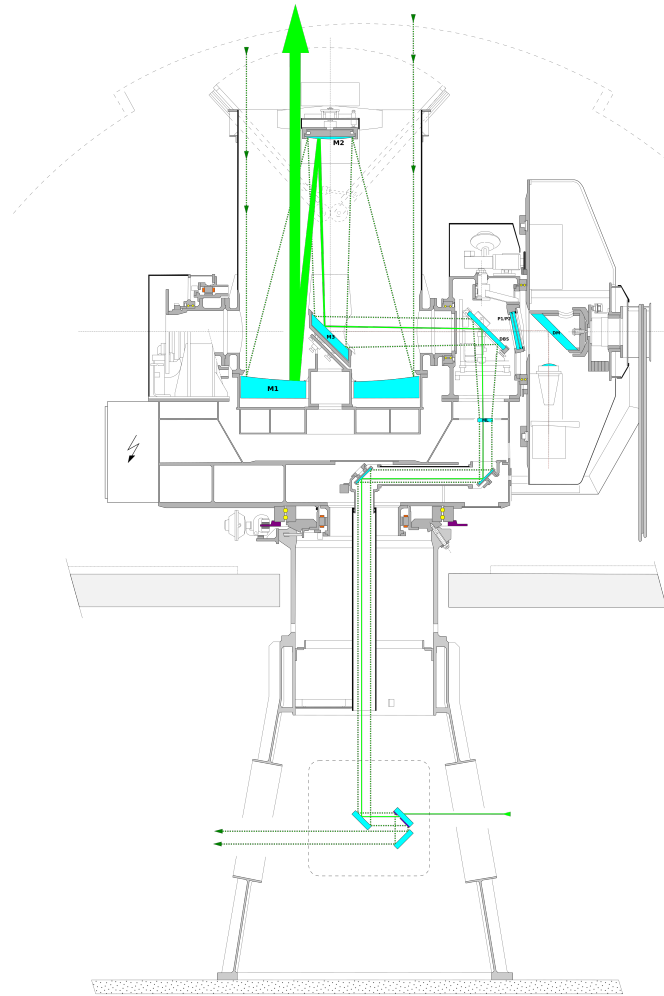


Figure 2.2: Technical drawing of ZIMLAT depicting active and passive optical paths. At the right-hand side, the Nasmyth platform depicts the position for using the tracking camera as passive electro-optical sensor with its respective focal reducer.

After measuring the system transmittance on the receiving passive optical path, the wavelength dependent efficiency of ZIMLAT increases from 10 % at 400 nm, to 60 % at 500 nm, yielding a steady value of 80 % from 600 nm until 800 nm. For the remaining part of the presented work, we will use the band [400, 800] nm for all remaining calculations for comparing measured against calculated figures, specifically, such comparisons will take place in Chapter 4. Finally, the pointing of the telescope is modeled through the so-called mount model that is estimated after observations to reference stars, specific

RSOs from the active catalog of the ILRS, or by doing active tracking using a CMOS sensor. The corresponding model that is currently in use was presented in [56] within the context of calibration tasks at the SwissOGS.

2.2 Telescope Control

The controlling of the telescope may comprise the following steps: firstly, the command to point in a given direction, which in this case is executed by a central processor in the form of a Programmable-Multi-Axis-Controller (PMAC) that takes the pointing information from a shared memory slot; secondly, the controlling software must ensure that the switch limits are within the predefined tolerances; thirdly, the correctness of the pointing is evaluated by a close-feedback loop, where the commanded position is compared against the actual position read out by the angular encoders in the telescope. A schematic of the working logic of the servo-control system of ZIMLAT is provided in Figure 2.3.

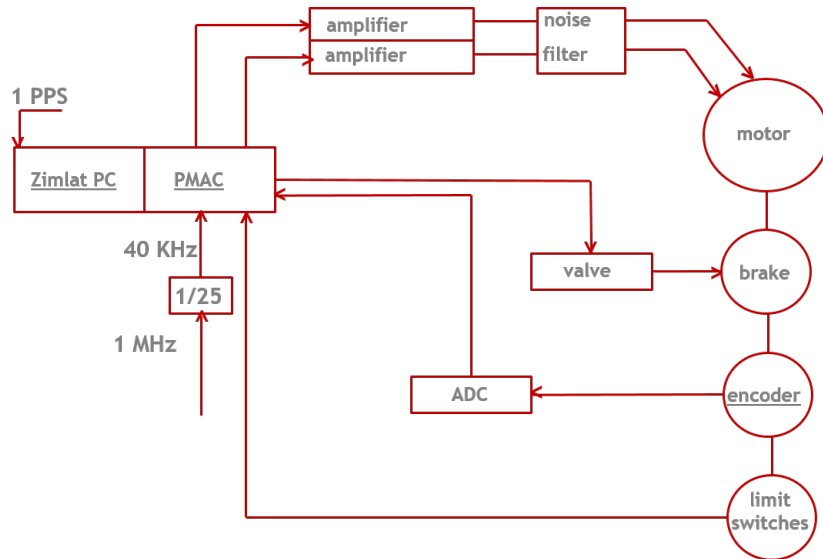


Figure 2.3: Control architecture for azimuth and elevation axis for ZIMLAT.

The actual pointing of the telescope may be given by the following equations, which correspond to the apparent local horizontal coordinates azimuth and elevation:

$$Az = Az_{pred} + \Delta Az_{MM} + \Delta Az_{\delta Corr} \quad (2.1)$$

$$El = El_{pred} + Refra + \Delta El_{MM} + \Delta El_{\delta Corr} \quad (2.2)$$

where Az_{pred} and El_{pred} correspond to the predicted angular values provided by the ephemerides, ΔAz_{MM} and ΔEl_{MM} correspond to the corrections retrieved after evaluating the estimated mount model in the pointing direction, $Refra$ corresponds to the

refraction correction to be applied only in the elevation component, and $\Delta Az_{\delta Corr}$ and $\Delta El_{\delta Corr}$ correspond to the so-called manual corrections used specifically to correct the pointing of the laser beam attempting to maximize the return rate; it may be computed using a spiral search, or given by an external device as might be a passive electro-optical target acquisition system. The measurement timestamp is requested at the read out epoch of the angular encoders in the telescope from the available PC-card IRIG-B signal.

2.3 Passive Electro-Optical System

Within the passive electro-optical system, we utilize the Andor 5.5 Neo Scientific-CMOS¹, which main characteristics are one electron read noise, a cooling temperature of $-40\text{ }^{\circ}\text{C}$, a 5.5 Mpix sensor ($6.5\text{ }\mu\text{m}/\text{pixel}$), an electronic shutter with two possible modes, global or rolling, at different frequencies, easily adjustable through the Software Development Kit. It is mounted using the 8 m focal length position in the Nasmyth platform, which gives an approximate field of view of 7 arcmin x 6 arcmin for a chip size of $2.38 \cdot 10^{-4}\text{ m}^2$. The pixel scale of the tracking camera is 0.173 arcseconds/pixel. The latter, as the correct orientation matrix of the camera reference system, with respect to the horizon reference system, was derived by plate-solving a series of images containing star fields at different azimuth and elevation positions. The system lens is equipped with filters that block incoming radiation below 500 nm and at $532 \pm 5.3\text{ nm}$. Those filters are used to mitigate the effect of sky background and stray light coming from the backscattered photons from our laser. The timestamp is acquired from a PC-card with IRIG-B signal derived from a GPS receiver at the time of request of the angular encoder values.

2.3.1 Novelties and Contribution

Our passive electro-optical sensor was available prior to the developments presented in this thesis, thus an optimization prior to the acquisition of the different system components was not possible. Nevertheless, the new developments include the optimization of the following components:

- The focal length. Several tests were carried out both during nighttime and daylight to choose the best focal length within the different available focal stations in the Nasmyth platform.
- A narrowband blocking filter centered at the wavelength of the nominal laser source to mitigate the impact of straylight coming from the laser system.
- A broadband blocking filter between 400 and 500 nm to reduce the impact of the daylight sky diffuse radiance.

¹<https://andor.oxinst.com/assets/uploads/products/andor/documents/andor-neo-scmos-specifications.pdf>

- An improvement in the epoch acquisition. Before, the timestamps were requested from ZIMLAT-PC, instead of the PMAC. That was found to be critical for the quality of the acquired angular observables, which were intended to be used for orbit determination and improvement.

2.4 Active Electro-Optical System

Within the active electro-optical system, we can distinguish a laser with nominal power of 1 W operating at the 532 nm wavelength after frequency doubling of the fundamental wavelength, i.e. 1,064 nm, with a repetition rate of 100 Hz. The receiving sensor is a time walk Compensated Single Avalanche Photodiode Unit 0420 (C-SPAD); with a 200 μm diameter; two-stage Peltier cooling system; operating above a breakdown voltage of 5 V; with a maximum detection efficiency of 10 % at 532 nm, and < 160 kHz dark counts. The field of view on the optical chain is regulated through an iris of adjustable aperture currently set up at 10 arcseconds. The receiving optical path is equipped with an air spaced etalon with a spectral width of 1 nm centred at 532 nm. The efficiency of the receiving optical path was measured using the available measurements from the mirrors on the telescope multiplied by the efficiency measured in the coudé path using the internal calibration target yielding a value of 50 %. The receiving optical path for both available wavelengths is different after the separation of each by the beam splitter. Technical details about the 1,064 nm detector will be provided on request, since we are still testing some of the nominal features. The timing unit used for measuring the time-of-flight of emitted laser pulses is the so-called Riga event timer A032². The time stamps are provided after the synchronization of the PPS from the station with a GPS receiver unit currently with an accuracy of 15 nanoseconds to UTC.

2.4.1 Novelties and Contribution

The existing laser ranging system at the SwissOGS is a dedicated system that provides data seamlessly to the ILRS. To enable laser ranging to space debris, we adapted several subsystem components. Specifically, we needed to develop a target acquisition system using a passive electro-optical system, enable daylight optical tracking, and analyze the current performance power-wise of the system. Those changes involved:

- The implementation of a new software module that creates the observation planning of space debris targets including the generation and uploading of ephemerides into the system. To be compliant with the existing architecture and working logic, we needed to create a new group of targets and parameterize it accordingly to the existing parameters required by the system. Many of these parameters have a direct impact on the tracking strategy implemented at the SwissOGS. Those parameters were refined after simulation and an extensive experimental phase.

²http://www.eventechsite.com/files/13_e6b62b59.pdf

- Enabling a TCP/IP communication protocol to send $\Delta Az_{\delta Corr}$ and $\Delta El_{\delta Corr}$ retrieved from the passive electro-optical target acquisition system to be applied to the current pointing position of the telescope as described before.
- A fine adjustment of the Fabry-Pérot filter for reducing the background diffuse contribution, while maximizing the signal strength of backscattered photons from the target. Therefore, once the laser beam is collimated on the object, we may focus on the range gate and on finding the trace of the object for its subsequent optimization.
- Testing of the iris in the receiving optical path, from which the variable aperture permits to reduce the field of view up to 10 arcseconds, thus minimizing the contribution of the diffuse sky photons.
- Operational implementation of the 1,064 nm wavelength including: the installation of the new CSPAD receiver, performance test for new receiver using the Stanford counter, test on event timer, coarse alignment of optical beam, readjustment of the mount of the receiver, as well as the fine alignment of the optical beam.

Target Acquisition and Tracking

3.1 Introduction: the State of the Art

CURRENT observing systems within the framework of Space Situational Awareness (SSA) include the use of radars, passive-optical telescopes and active-optical, i.e. lasers, for tracking, cataloguing and characterization of space debris. If compared against radar or passive-optical systems, lasers have the advantage that their observable, the range, is extremely precise (centimetre level for normal points as shown in the last global International Laser Ranging Service (ILRS) report card [52]). On the other hand, there are important limitations such as the dependency on weather conditions, energy of emitted pulses (particularly important for the so-called non-cooperative targets, i.e. targets without retroreflectors) and of utmost importance: the rather small field of view. The last one prevents the tracking of objects with poor ephemerides, which is a problem rarely found when ranging active targets from the ILRS catalog [52]. To overcome such limitation, we designed and implemented the stare and chase observation strategy particularized for the Zimmerwald Laser and Astrometry Telescope (ZIMLAT). The applicability of the implemented observation mode is critical when a close conjunction is foreseen and its uncertainty needs to be reduced. Furthermore, the main difference from the traditional observation strategies, employed in traditional laser ranging observation strategies, comes either from the retrieval of angular measurements without classical astrometric reduction or from the improved quality of angular measurements, which are usually provided by the coarse position of the pointing of the telescope.

The name of the stare and chase was coined after the merge of two well-known observation strategies used in passive electro-optical systems namely survey and follow-up. Since the novel technique emerged from only passive observation techniques, its evolution up to now will be developed and contextualized by the use of active electro-optical systems for the observation of space debris.

The first manual implementation of the stare and chase procedure, within the space debris community, dates back to the 4th of September 1992 [26]. The operator was screening acquired frames for glints of objects and then chased the object employing an

acceleration joystick. Once the target was close to the boresight, the remaining tracking was done via a video tracker. In one of the successful cases, after five minutes of metric data acquisition, all data was processed and an initial orbit determination (IOD) was performed. About 100 minutes later, the object was reacquired with 46 seconds of time bias [26].

The first successful laser ranging experiments to space debris were conducted within 2001/2002 led by Electro Optic System (EOS), which operates an observatory located in Mount Stromlo, Australia [28]. The RazorView project was a dedicated program to demonstrate an operational capability for tracking small space debris objects using laser ranging techniques [67]. The experiments demonstrated capabilities for tracking 15 cm objects at altitudes between 1100 and 1250 km. The stare and chase procedure corresponds to their denominated Target Acquisition System (TAS) and Beam Locking System (BLS). The TAS consists of an $f/0.75$ wide-field telescope equipped with a Charged-Couple Device (CCD) sensor. Its task is to detect the target and to centre it within the BLS field of view. The BLS is a CCD sensor located at the end of the Coud path of a 1.8 m telescope. Upon initial acquisition, the TAS has control of the telescope tracking servo system, until the target appears in the BLS field of view. Afterwards, the TAS hands-off to the BLS for fine guiding and beam locking [67].

The next attempt to implement and validate a stare and chase observation mode, this time using only passive-optical systems, was done during an observation campaign in the year 2005 [1]. The collaboration between the University of Michigan and the National Aeronautics and Space Administration (NASA) developed a method in which resident space objects orbiting the geostationary ring could be observed and followed for future passes. The discovery of the object was done using the 0.6/0.9 m Michigan Orbital Debris Survey Telescope (MODEST). For the survey and detection, the telescope is initialized and tracks stars moving at fixed lengths in right ascension and declination close to the anti-solar point and avoiding the Earth's shadow. Using a Time Delay Integration strategy, while the object is within the field of view, images are stored. A minimum number of four detections are needed to go to the next step: orbit computation. The correlation of the object per image is done manually by visual inspection and astrometric reduction takes place while the images are acquired. If a minimum number of 4 detections are successful, a circular orbit is estimated and ephemerides are sent directly to the NASA Orbital Debris Program Office at Johnson Space Center in Houston, Texas, where a chaser telescope uses the recently computed ephemeris to reacquire the target [1].

The next study conducted in October 2016 was reported in [32]. Their study focuses on a comparison during the staring mode of the stare and chase observation strategy between two optical-passive sensors: a scientific Complementary Metal-Oxide-Semiconductor (CMOS) and a CCD [32]. Compared to the initial algorithm proposed in [1] the stare, or survey mode, commands the staring camera to point into the near zenith direction with an exposure time of about 0.5 seconds allowing fast-moving objects to leave a trail and therefore to be discriminated from a point-like star field. For those objects which leave a trail, two subsequent images are subtracted and a threshold algorithm filters the background from the source. For objects observed with shorter exposure time, at least three

frames are needed in order to minimize potential false positives. Once the object has been detected, the astrometric reduction takes place by an external commercial software. From the detected positions on the image, a straight line is fitted and extrapolated to a given ahead time which will be used by the telescope to reacquire the target. After their study, it becomes clear that the use of different chip technology according to a different observation task must be highlighted and recommended, e.g. the use of CCD sensors for the detection of fainter objects despite the longer readout times if compared against CMOS. The proposed methodology was developed as a test-bed for its near future use with laser ranging.

In early 2017 the first successful European stare and chase observation strategy, using a laser ranging system, was reported by the space research institute from the Austrian Academy of Science in Graz, Austria [72]. The hardware corresponds to an analog video camera with an objective with a focal length of 50 mm and f/1.4 piggyback mounted on the 0.5 m Satellite Laser Ranging (SLR) telescope. While the system is in staring mode, the initial pointing of the telescope in azimuth and elevation is transformed into right ascension and declination. By doing that, the search space is reduced when performing astrometric reduction. Moreover, the number of stars accounted for during plate solving is of the 50 brightest. The plate-solving algorithm takes about 0.2 to 0.5 seconds and is performed every two seconds; the remaining 1.5 seconds are used for all object identification tasks. Once a target is detected a number of four frames are acquired to ensure object identification. In order to remove the stars from the background, a relative movement of one pixel between subsequent images is set as a threshold for the removal of the stars. At the same time, the effect of noisy pixels is mitigated by setting a lower bound to the relative movement between successive frames of 15 pixels. The target of interest should move in the range of 1 to 15 pixels between subsequent frames. Once the detection is performed, the retrieved angular data is used to estimate an initial orbit, which is propagated and transformed into the Earth-Centered-Earth-Fixed reference frame, establishing a set of coordinates that will be used by the SLR system to fire laser pulses to the object of interest.

Besides an initial orbit determination, there is the option of active tracking, i.e. a correction of the pointing of the telescope using all measurements available during the object recognition phase. One implementation of such approach was presented in [47]. In the publication, the stare and chase procedure is modularized into three fully parallelized main segments. The first one is the image acquisition; the Georgia-Tech Space Object Research Telescope (0.5 m f/8) points towards the ephemerides given by an initial orbit calculated from a Two-Line Element (TLE) set with a finder scope aiding the telescope in the localization of the target. The second segment is the image processing, which uses an enhanced thresholding method. The subsequent data reduction was done via the external tool Astrometry.net [47]. The last segment performs controlling and commanding tasks; the tracking takes as input all differential corrections derived from the object recognition and performs active tracking utilizing a Kalman filter updating the differential corrections with respect to the original orbit given by the TLE. The three modules work together within a closed-feedback loop which proved to work successfully for the case study of the low-Earth orbit (LEO) flying target Iridium 914 [47]. Despite

the use of a specific tracking module, the committed error is in the order of arcminutes, which proved enough for their application (only-passive) but it is not if the object is planned to be ranged with a laser system.

The previous analysis of the state-of-the-art was needed in order to define the context of the current work, thus highlighting the scientific novelties presented by our research. Specifically, we will present a comparison of methods for the real-time object recognition. We will investigate the advantages and disadvantages of using active tracking instead of an initial orbit determination, and we will guide the reader through the implementation of the selected methods in our operational environment at the Swiss Optical Ground Station and Geodynamics Observatory Zimmerwald (SwissOGS). The latter includes a validation of the measurements acquired by our tracking camera. All the previous work was needed to achieve the final aim of correcting the pointing of the telescope so that the target will be within the field of view of the laser beam, thus enabling the acquisition of laser ranges.

3.2 Validation of Measurements

Besides the use of angular measurements derived from the tracking camera to correct the pointing of the telescope, all angular observations may be utilized for orbit determination or improvement. An earlier study [17] showed the usability of the measurements collected by the tracking camera for orbit determination. To better understand the outcome from the orbit determination, a comparison against precise ephemerides was conducted. The comparison of the observations collected by the tracking camera, against their interpolated values from precise ephemerides, displayed an error between 15-20 arcseconds [17]. Since the magnitude of the error was 3 times higher than the root-mean-square of the estimated mount model error for ZIMLAT, we decided to inspect the acquisition chain in order to improve the accuracy. We were able to pinpoint issues in the timestamp of the measurements and on the estimation of the laser beam position in the camera reference system.

The timestamp issue was solved by taking the time when requesting the encoder value from the Programmable Multi-Axis Controller (PMAC). Before, the timestamp was derived from the control PC clock which has a time offset of few milliseconds with respect to the actual readout of the angular encoder of the telescope.

In order to solve the second issue, the orientation of the camera reference system was studied. In contrast to the popular plate solving approach, the orientation of our camera reference system is given directly by the pointing of the telescope [17]. In order to find the pointing of the telescope in the camera reference system, a night-calibration session is conducted where only images are stored if there were successful returns from targets ranged by our laser system. For this particular setup, we chose regular targets with accurate predictions from the active catalogue of the International Laser Ranging Service (ILRS) [52]. While we were successfully ranging the target, images were acquired and a pointing position was derived per image in the camera reference system X_i, Y_i . We define the reference point X_{ref}, Y_{ref} as the average of all previously derived pointing

positions within the calibration session [17]. In order to transform from the camera into the horizontal reference system, we use the following transformation:

$$\begin{bmatrix} \Delta Az_{app} \\ \Delta El_{app} \end{bmatrix} = \begin{bmatrix} \sin\beta & -\cos\beta \\ \cos\beta & \sin\beta \end{bmatrix} \begin{bmatrix} (X_i - X_{ref}) * PixScale \\ (Y_i - Y_{ref}) * Pixscale \end{bmatrix} \quad (3.1)$$

Note that $PixScale$ is the pixel scale of our sensor (0.173 arcseconds/pixel). The rotation matrix that relates both sets of coordinate systems depends on β which is defined as:

$$\beta = Elevation - DerotatorPos, \quad (3.2)$$

where $Elevation$ is the elevation of target and $DerotatorPos$ is the position of the derotator, with respect to the elevation axis, both at acquisition time.

The left plots in Figure 3.1 show the differences of each pointing position with respect to the reference point in the horizontal coordinate system. An enhancement of the estimation of the reference point includes the modelling of the computed differences. The horizontal and vertical components of the computed differences are each periodic functions ($f(\cdot)$) of azimuth (Az) and elevation (El), as such, admit representation via the two-dimensional Fourier series expansion which can be written as [14]:

$$f(Az, El) = \sum_{i=0}^{\infty} \sum_{j=0}^{\infty} (a_{i,j} \sin(jAz) \sin(iEl) + b_{i,j} \cos(jAz) \sin(iEl) + c_{i,j} \sin(jAz) \cos(iEl) + d_{i,j} \cos(jAz) \cos(iEl)). \quad (3.3)$$

Particularizing Equation 3.3 with a given degree and order, the coefficients $a_{i,j}$, $b_{i,j}$, $c_{i,j}$ and $d_{i,j}$, are estimated via a regular linear least-squares adjustment. Once the coefficients are estimated, the model is computed for the hemispherical domain in azimuth $[0^\circ, 360^\circ]$ and elevation $[20^\circ, 90^\circ)$. Note that we consider an elevation mask of 20° and account for avoiding the pointing in the zenith direction. The representation of the estimated model using a degree and order equal to 3 is shown in the right plots in Figure 3.1.

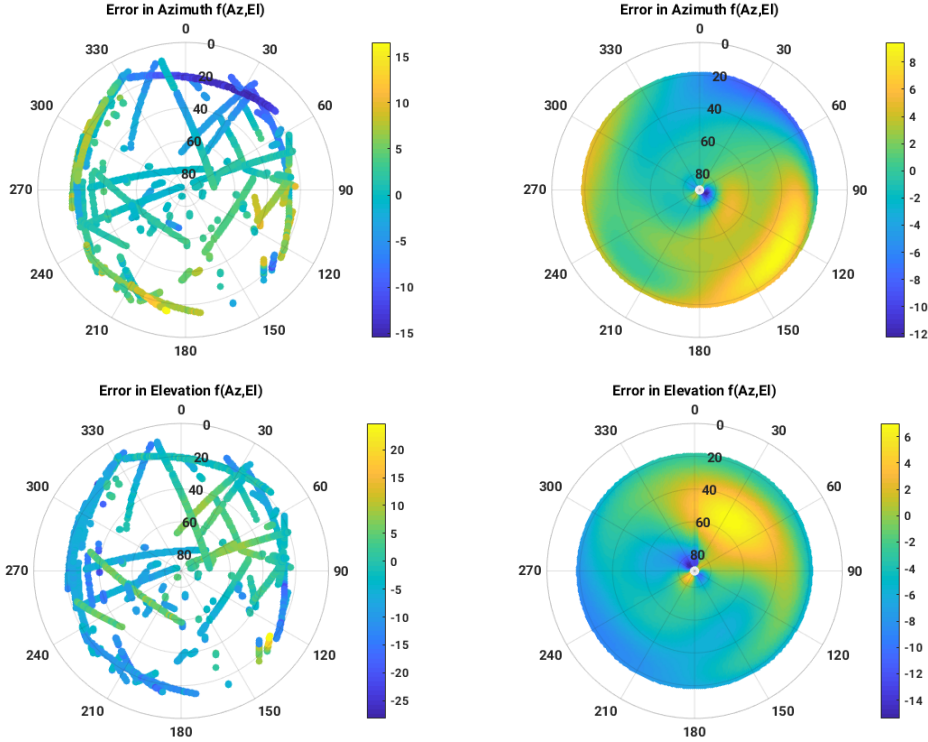


Figure 3.1: Left plots: differences of the estimated pointing position per image with respect to the reference point in azimuth (top) and elevation (bottom) as a function of observed azimuth and elevation. Right plots: modelled error of the reference point in azimuth (top) and elevation (bottom) as a function of observed azimuth and elevation. Units of colorbars: arcseconds.

The root-mean-square of the estimated coefficients is of 3 arcseconds – both in azimuth and elevation. From the estimated models we can also see that certain patterns suggest a lack of isotropic theoretical behaviour. A potential reason may be the fact that the estimation of the mount model used for regular SLR observations considers the coudé path, while the tracking camera is mounted on the Nasmyth platform. The conclusion for this section is that we were able to improve the estimation of the reference point using the two-dimensional Fourier series expansion. That correction proved to be crucial for the improvement of the accuracy of our angular measurements.

For the validation of the tracking camera measurements, we chose the Laser Geodynamics Satellite (LAGEOS) -1 which is a regular geodetic target of the ILRS [51]. The observation session on July 11, 2019, lasted 35 minutes including a gap used by the laser system for avoiding the zenith direction. The apparent angular measurements, collected by the tracking camera, are reduced into topocentric azimuth and elevation and transformed into topocentric right ascension (α) and declination (δ) (J2000 [74]). The approach used for the current validation is a routine orbit improvement with five days of normal points collected from all ILRS network stations. The a priori orbit was taken

from the last TLE available through the Space-Track website¹. By adding the angular measurements to the ranges from the ILRS in the orbit improvement, it is possible to provide residuals of our angular measurements with respect to the improved orbit estimated using a single batch weighted-least-squares adjustment. The contribution of our angular measurements is that of 35 minutes of observations with one observation every 3 seconds (exposure time), with respect to 5 days of range measurements every 120 seconds (bin size for normal point formation). The weighting of the observation was that of 50 cm root-mean-square for distances and one arcminute root-mean-square for angular observations. Note that the angular observations were down-weighted to assess their goodness-of-fit to an only ranges solution. The weighting for the distances was computed as twice the average of the full-width-at-half-maximum of the pulses emitted by the used stations. The results from the adjustment are shown in Table 3.1 in the radial, along and cross-track satellite-fixed reference frame for the last epoch of observation.

Table 3.1: Results for the orbit determination of LAGEOS-1 using five days of normal points gathered from the ILRS network plus 35 minutes of angular observations acquired by the tracking camera. Results are shown in the satellite-fixed reference frame. σ stands for the standard deviation of the estimated component at a 68% of confidence for a normally distributed data set.

Component	Magnitude
σ_{Radial} [m]	0.012
σ_{Along} [m]	0.107
σ_{Cross} [m]	0.045
$\sigma_{V_{Radial}}$ [m/s]	0.001
$\sigma_{V_{Along}}$ [m/s]	0.00001
$\sigma_{V_{Cross}}$ [m/s]	0.0001

The high precision is in agreement with the expected one due to the precision of the used measurements (centimetre level for normal points as shown in the last global ILRS report card [52]), the observed arc (≈ 5 days), and the different portions of the orbit observed by the different tracking stations of the ILRS network. Figure 3.2 shows the residuals for the collected angular observations after the orbit improvement.

The root-mean-square for both right ascension and declination is of one arcsecond. The gap in the middle of Figure 3.2 is due to the telescope avoiding the zenith direction. The fact that the residuals are not evenly distributed along a zero mean might be due to a time bias, a systematic error in the measurements or due to an orbit modelling deficiency, e.g. we did not estimate scaling factors for the solar radiation pressure. Only the six classical Keplerian elements were estimated, to avoid the absorption of any systematics by the inclusion of dynamical orbital parameters. The symmetry of the trend may be explained by the geometry in the horizon coordinate system: if the pointing is behind the true position of the target before the zenith, the difference between observed minus

¹<https://www.space-track.org>

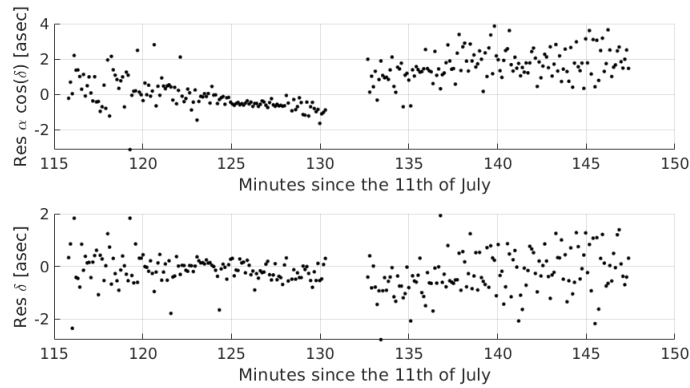


Figure 3.2: Angular residuals in arcseconds after orbit determination.

computed will be negative while after crossing the zenith, the difference will be positive. A potential explanation for this systematic error could be addressed to the mapping of station-dependent biases from any of the stations used for the estimation of our improved orbit since, in our solution, we did not estimate range biases per station. The inclusion of additional parameters, besides the six classical Keplerian elements in the orbit improvement, could improve the results, however we preferred a minimum parametrization of the problem since we could test for systematic errors directly as we compared directly the collected measurements to precise ephemerides in the form of Consolidated Predicted Format (CPF) [52]. An example of the comparison is shown for a LAGEOS-1 pass on July 5, 2019. The differences between reduced raw observations and interpolated angular values from the CPF ephemeris are shown in Figure 3.3. The root-mean-square for both azimuth and elevation is of one arcsecond, and the subtle trend may be explained by the tracking of the controller of the telescope. Furthermore, this cross-validation was also conducted with Cryosat-2, Jason-3 and Lares, all Low Earth Orbit (LEO) satellites. Finally, after the assessment of the order of magnitude of the errors coming from an orbit determination, and a comparison with accurate ephemerides, we conclude that the measurement accuracy has been significantly improved with respect to the first results shown in [17]. In addition to the validation of the measurements, the implemented pipeline is ready to exploit the benefits of including angular measurements, coming from the tracking camera, in the orbit improvement of space debris.

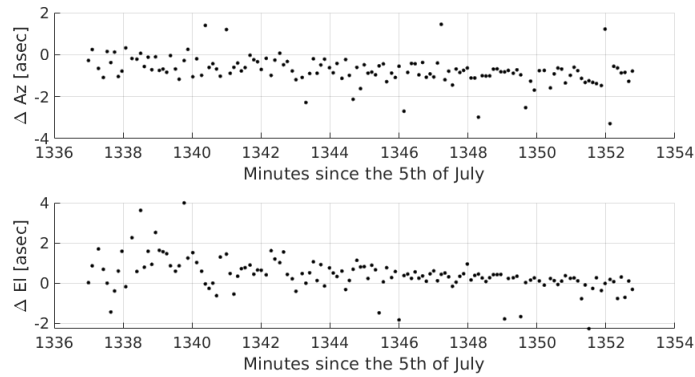


Figure 3.3: Differences in azimuth (top) and elevation (bottom) between angular measurements acquired by the tracking camera and interpolated CPF predictions at the observation epoch. Units of differences: arcseconds.

3.2.1 Methodology

In this subsection we will analyze the main modules of the stare and chase observation strategy. To do so, in Figure 3.4 we show a general schematic of the complete observation strategy.

The first step, in the stare and chase observation strategy, is to observe in a given direction either fixing an absolute pointing as done e.g. in [32] and [72], or by using an a priori orbit as done in [47]. We opt for the latter since we have specialized telescopes for discovering new objects [15]; therefore, in our case, existing ephemerides are used for initializing the staring mode. Once the object is within the field of view of our staring device, we acquire a series of images. The series of images are processed in real time with the final aim of detecting the object. Object detection is done mainly by thresholding [32, 72]. Even though in [47] several algorithms were tested, there is no in-depth quantitative study of the different methods for an accurate real-time application. The stringent tolerance is given by the rather small field of view of the laser beam, which is between 20-30 arcseconds. In general, it seems that a robust algorithm is needed in order to minimize the false detection provided by thresholding algorithms. In Section 3.3 we will analyse 3 different object recognition methods highlighting performance and computational time. Additionally, almost all cases reviewed in the state-of-the-art part use an external engine to do plate solving in order to derive astrometric positions from the acquired images. Plate solving is a relatively computational expensive step for a real-time tracking system. In Section 3.2 we proved that we are able to obtain angular errors in the order of one arcsecond (root-mean-square) by using only the pointing of the telescope, thus proving the capabilities for acquiring angular measurements without astrometric reduction.

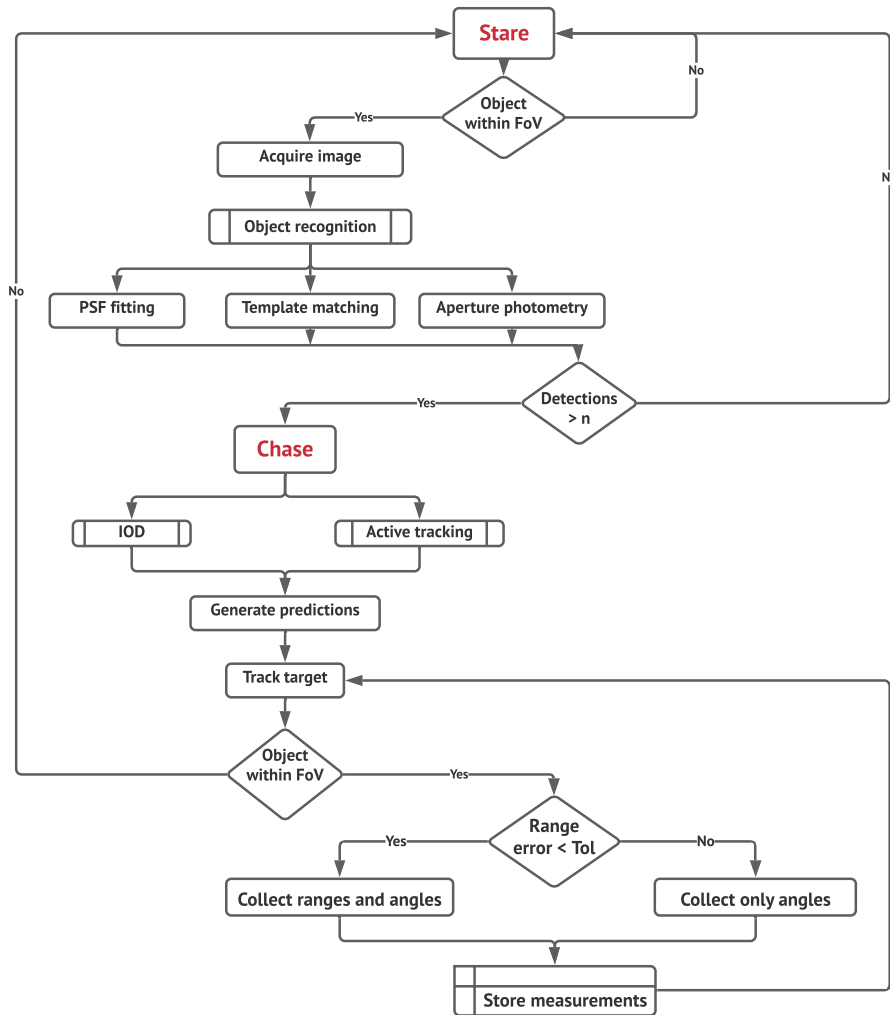


Figure 3.4: Flowchart of the stare and chase observation strategy. PSF: point spread function. IOD: initial orbit determination. FoV: field of view.

Depending on the tracking strategy, a threshold for a minimum number of detections (n) becomes imperative, e.g. in [1] a minimum number of 4 detections is needed to compute an initial circular orbit. Systems observing in a fixed direction are limited to collect enough observations while the object crosses the field of view of the staring device; this dependency might be critical for staring devices with a small field of view aiming at fast-moving targets. After n successful detections, the chasing phase of the strategy begins. There are two possibilities regarding the tracking, either the use of new ephemerides after an initial orbit determination [1, 72], or active tracking [32, 47]. In Section 3.4 we will compare the two of them selecting the most appropriate one for our system.

Once the tracking starts, we continuously check that the target is within the field of view of the staring device. When the target is within the field of view of the laser beam and the committed radial error is smaller than the 1 km tolerance of our system (Tol), we can collect ranges and angular measurements. The tolerance in the radial error is used for defining the maximum width of the range gate when using laser ranging measurements. Relaxed tolerances will potentially prevent the identification of returns coming from the target since those could be embedded in photoelectron noise. In case we do not comply with the defined tolerance, we can collect only angular measurements. After the setting of the object, all collected measurements will be used for an orbit improvement. The estimated orbital elements will be propagated and possibly disseminated through standard prediction files, e.g. CPF, to other observatories as done in [1, 26].

After the selection of suitable algorithms for object detection and tracking, we will analyse their performance in a real-time system. In Section 3.5 we show how the selected choices can be optimized to achieve high computational performance while complying with the demanding tolerance posed by the small field of view of the laser beam. Finally, in Section 3.6 we evince one of our successful case studies for the decommissioned Environmental satellite (ENVISAT) when we were able to acquire simultaneously: the apparent changes in brightness, angular and range measurements. Note that the apparent changes in brightness is a by-product of the selected algorithm for object recognition.

3.3 Object Recognition

The automatic detection of sources in astronomical images can be formulated under different approaches. Two widely used are threshold methods based on simple hypothesis binary tests [32, 72], and template matching, which correlates a known template against newly acquired images [47]. To further characterize the source, the detected signal is used to derive information about the location of the object on the image, the so-called centroid, as well as the shape, intensity, orientation and other information of the object image. Available methods for centroiding include the weighted average of the coordinates of pixels belonging to the source using their intensity as weight [35], the fitting of a defined point spread function [7] and locating the coordinates of the pixel with maximum cross-correlation between acquired image and template [20]. Note that the fitting of a point spread function could be used as a detection method if prior information about its characteristics is available. In this section, we will focus on the selection of an optimal algorithm that will allow us to perform a real-time object recognition operation minimizing the computational time. Previous studies for source detection in astronomical images, for non-real-time applications, can be found in [24, 48, 75]. Our study compares three different approaches highlighting disadvantages and benefits.

3.3.1 Fitting of a Point Spread Function

The point spread function (PSF), assuming a perfect imaging system, is the diffraction pattern, in three dimensions, of light emitted from an infinitely small astronomical object and transmitted to the image plane through an aperture objective. A fraction of the light

emitted by the source object is collected by the objective focusing it at a corresponding point in the image plane. When the incoming waveform converge and interfere at the focal point, it yields a diffraction pattern of concentric rings of light surrounding a central, bright disk, when viewed in the image plane. The radius of the disk, so-called Airy disk, might be determined by the aperture of the telescope [7]. The image of the diffraction pattern can be modelled by a certain distribution of intensity, e.g. Gaussian, Lorentz or Moffat [7]. In addition to the Airy-disk, the effect of the light transmitted through the atmosphere is quantified by the on-site seeing, which also affects the focusing of the object in the image plane. We model the distribution of intensity of our object image as the following point spread function:

$$I(X, Y) = Zo + A \exp(-a(X - Xc)^2 + 2b(X - Xc)(Y - Yc) + c(Y - Yc)^2), \quad (3.4)$$

where $a = \frac{\cos^2\theta}{2\sigma_x^2} + \frac{\sin^2\theta}{2\sigma_y^2}$, $b = -\frac{\sin 2\theta}{4\sigma_x^2} + \frac{\sin 2\theta}{4\sigma_y^2}$, $c = \frac{\sin^2\theta}{2\sigma_x^2} + \frac{\cos^2\theta}{2\sigma_y^2}$, θ is the orientation of the object image in the image plane, Zo is the averaged background level, A is the amplitude of distribution, X, Y are the coordinates in pixels in the image reference system, Xc, Yc are the coordinates of the centroid of the distribution in pixels and σ_x, σ_y are the standard deviation of the X and Y components of the distribution in pixels.

The observables y of our model correspond to the intensity value (I) for a given position X, Y in the image plane. The cost function to be minimized reads:

$$C(\mathbf{x}) = \|y - A\mathbf{x}\|_2^2, \quad (3.5)$$

where $\mathbf{x} = [\delta\theta, \delta Zo, \delta A, \delta Xc, \delta Yc, \delta\sigma_x, \delta\sigma_y]^t$ and $A = \frac{\partial I}{\partial P_i}$, $P_i = \{\theta, Zo, A, Xc, Yc, \sigma_x, \sigma_y\}$. Note that the problem is non-linear, therefore Equation 3.4 is linearised and differential corrections are estimated per each iteration until reaching convergence. The Levenberg-Marquadt optimization algorithm [49] was implemented in order to avoid convergence towards local minimum. Figure 3.5 depicts an example of a space debris object image and its estimated point spread function.

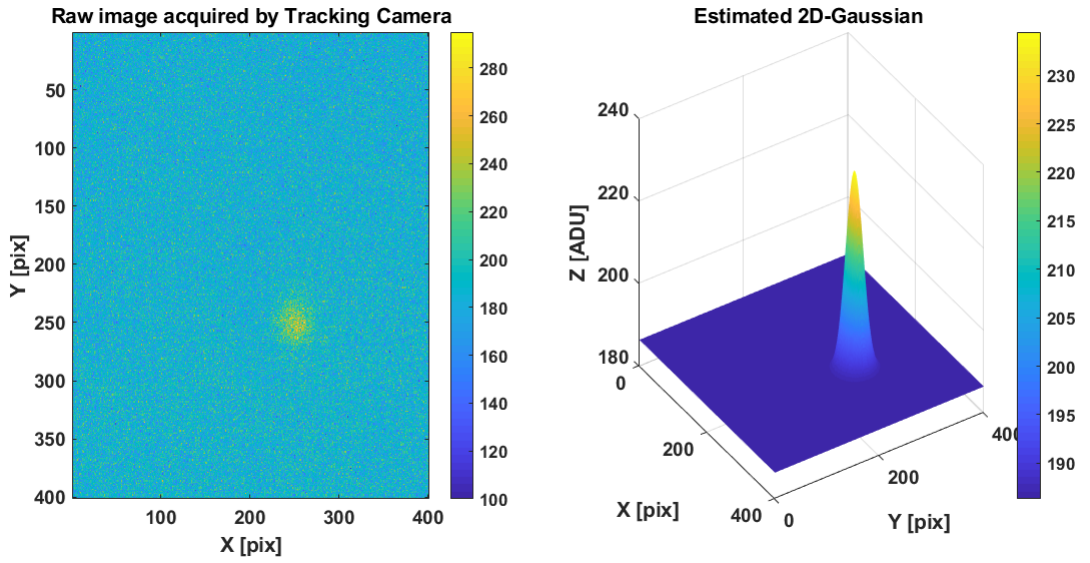


Figure 3.5: Case study of fitting a Gaussian point spread function given a raw image acquired by the tracking camera. Units of colorbars: Analog-To-Digital unit (ADU).

The estimated parameters and precision are shown in Table 3.2. Note that for those parameters describing the shape of the PSF in pixels, their correspondent angular unit can be computed by multiplying the value with the pixel scale (0.173 arcseconds/pixel).

Table 3.2: Estimated Gaussian point spread function parameters. Units of estimated values and their corresponding precision are given by the unit of the parameter (first column).

Parameter	Estimated Value	Precision (1σ)
θ [deg]	163	± 0.83
Z_o [ADU]	186	± 0.007
A [ADU]	48	± 1.8
X_c [Pix]	251	± 0.51
Y_c [Pix]	250	± 0.53
σ_x [Pix]	19.5	± 0.72
σ_y [Pix]	20.1	± 0.75

One advantage of using this method is that it relies on the physical representation of the imaging process on the image plane. The fact that all parameters describing the point spread function can be estimated all at once is desirable since the use of a different

method for computing e.g. the background can influence the other sets of parameters. Contrary to the benefits, the algorithm took up to five seconds in order to converge until a rather conservative tolerance of e^{-16} . The explanation for the tolerance is given by the seek of the true computational minimum within the function which is minimized. If the tolerance is relaxed, it is possible that the estimated solution does not satisfy the strict minimization of Equation 3.5. Additionally, due to the non-linear nature of the distribution of intensity, the algorithm needs a first guess so that the estimated differential corrections are close enough to the linear term of the Taylor series expansion. An increase in the magnitude of the background due to clouds, trails of stars, etc. might prevent the convergence of the least-squares solution.

3.3.2 Template Matching

The principle of this method is the two-dimensional cross-correlation, which for a discretized spatial domain reads:

$$Corr(x, y) = \sum_{u=-h}^h \sum_{v=-h}^h I(x+u, y+v)T(u, v), \quad (3.6)$$

where the resulting pixel in $Corr(x, y)$ is the result of taking the pixel $I(x, y)$ from the image, multiplying it by every single pixel of the template $T(u, v)$, and adding all – in the spatial domain. We define the template $T(u_{0...(2*h)-1}, v_{0...(2*h)-1})$ as a square sub-image, or kernel, of radius h . Afterwards, the pixel coordinates with maximum correlation, with respect to the template, are the ones estimated for the centroid. Its use for a real-time application was reported in [47], but discarded due to the long processing time. In our case, we were able to code the algorithm with a computational time in the order of 0.01 seconds per image which is translated into about two arcseconds for a low Earth orbiter object with an apparent angular velocity of 3.11 arcminutes/sec. After an in-depth study of the method, we found that there are three ways in which the computational time of the algorithm can be decreased, e.g. by using the convolution theorem and performing all operations in the frequency domain [68], by using the definition of the separable kernel for the template [68] – possible if we model our template as a 2D-Gaussian kernel – or by transforming the two-dimensional problem into a one-dimensional. Furthermore, the use of a multicore machine will allow us to split the incoming image into the number of cores, perform the algorithm core-wise, and reconstruct the final solution. Further details about its implementation are provided on request since this procedure failed with newly acquired images containing trails of stars or noisy background with random saturated pixels.

3.3.3 Aperture Photometry

This method is widely used for the determination of light curves [35]. The method consists of placing inner and outer concentric circles on the target, for the estimation of the source and background respectively. The estimation of the brightness of the target

takes place by summing all pixel counts within the source aperture after the subtraction of the background estimated from the outer ring [35]. If compared against the fitting of a point spread function, we only estimate the parameter A for all pixels inside the inner aperture, i.e. the amplitude of the point spread function. In order to estimate the shape of the distribution defined by σ_x , σ_y , we assume $\sigma_x = \sigma_y$ and that its value is given by the site seeing conditions, which is obtained by taking the full width at half maximum (FWHM) provided by its PSF [10]. We approximate its PSF by computing a profile plot of normalized integrated intensities around concentric circles as a function of the distance from the centroid of the object image. Once we are able to obtain the FWHM, the radius for source and background are obtained by multiplying the distance at FWHM by 1.7 to get the source radius, 1.9 to get the inner-radius of the background ring and 2.55 to get the outer-radius of the background ring [13]. Figure 3.6 shows an example of the estimation of radius both for source and background.

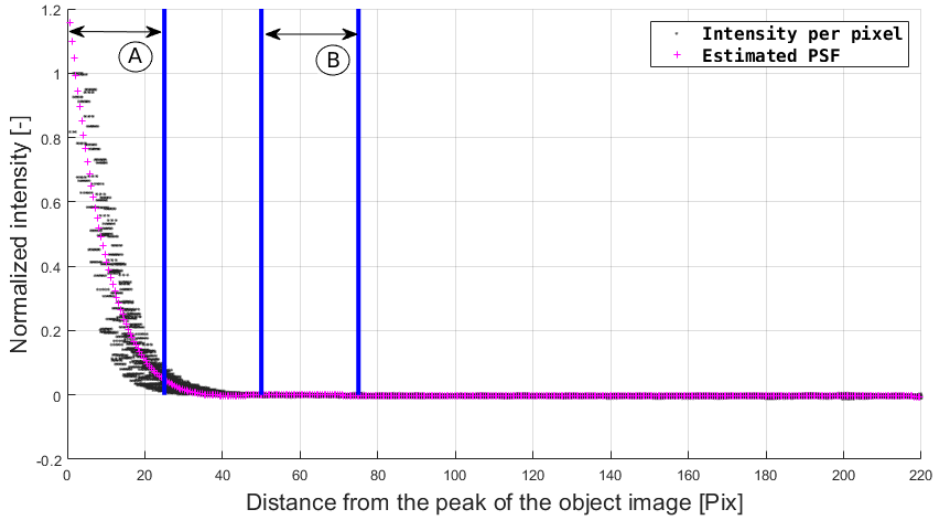


Figure 3.6: Radial PSF profile showing normalized intensity values against distance from the peak of the object image. A: radius of the inner aperture. B: radius of the outer aperture.

In order to find the centroid coordinates X , Y of the object image, a sequence of processing steps is needed. Those steps are implemented in Algorithm 1. Despite the sequence of steps needed in this method, an efficient implementation yields a computational time of 0.005 seconds per image. It also proved to be more resilient for images containing star trails, clouds and bright background. In Section 3.5, we will provide more details regarding the optimization of parameters for the presented approach.

Algorithm 1: Estimation of the centroid coordinates of the object image.

```
Procedure SubFrame // Crop image around the object image into a
subframe.
Procedure MedFilt2 // Convolve the subframe against a median
filter.
Procedure SubBack // Subtract the estimated background from the
convolved image.
Procedure GetCentroid // Estimate the coordinates of the centre of
the object image by a weighted average of the non-negative
pixels using the intensity of each of them as weight.
```

It is important to notice that besides detecting the object, we are also able to retrieve evidence of the attitude and attitude motion of the target. The outstanding by-product is a real-time light curve depicting apparent changes in brightness of the object. The new observable provides another measurement to the original set of azimuth, elevation and range. In addition to the information about the attitude and its evolution with respect to time, the estimated changes in brightness might correspond to specific epochs when the target, despite of being centred in the field of view of the laser beam, was not reflecting back enough photons to distinguish them from the photoelectron noise. Furthermore, the fusion of light curves obtained by ranges and apparent brightness might complement and refine the target attitude information.

3.3.4 Centroiding and Light Curve Validation

In Subsection 3.3.3 we showed that the outcome of the object recognition comprises the coordinates of the object image and its apparent brightness. To validate the results after the full implementation of the procedure in the processing chain, and to set a lower and upper bound to the committed error, we do a comparison against the solution obtained by a non-real-time software: AstroImageJ (AIJ) [13]. The validation compares the real-time estimated centroid and light curve using our implementation against the post-processed centroid and light curve extracted from AIJ. The target used for the current validation is the decommissioned satellite ENVISAT observed on the 17th of October 2019 during daylight.

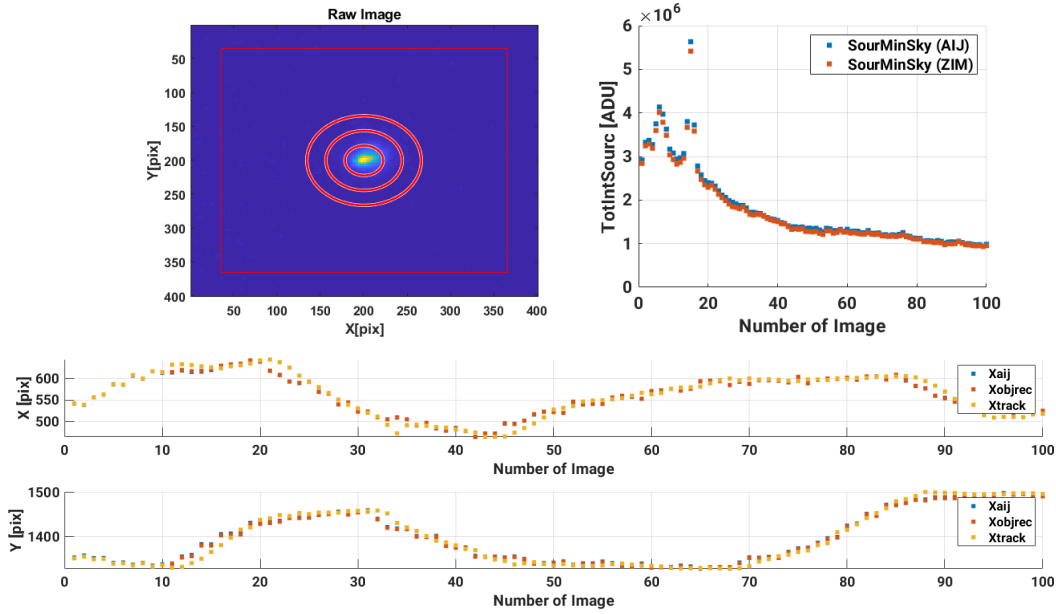


Figure 3.7: Validation of the algorithm for centroiding and light curve determination. Top-left: raw image with estimated inner and outer rings. Top-right: comparison of source-minus-background between AIJ and our solution (ZIM). Bottom: comparison between centroid estimates using AIJ (\mathbf{X}_{aij}), object recognition (\mathbf{X}_{objrec}) and predicted values (\mathbf{X}_{track}).

In Figure 3.7 top-left plot, we can see that the object image does not have a homogeneous point-like shape but has a rather spread feature in a nonsymmetrical fashion. Main reasons for this shape might be attributed to a combination of the site seeing with strong turbulence, the astigmatism of the telescope optical assembly and the active tracking. The estimation of the inner and outer rings (top-left plot in Figure 3.7) corresponds to the method explained in Subsection 3.3.3. The comparison, between our light curve and the one retrieved by AIJ (top-right plot in Figure 3.7), shows that both solutions are in agreement. The differences can be explained by the slightly different values in the estimated centroid (bottom plot in Figure 3.7), which will not place the annular rings in the exact same location affecting also the estimation of the new apertures and subsequent parameters derived thereof. The comparison of the estimated centroids shows that the solution provided by the object recognition and prediction are the same for the first eight frames due to the construction of the sliding window. The remaining part depicts a rather smooth trajectory with no outliers. The maximum difference is less than 20 pixels which correspond to 4 arcseconds. Given that the tolerance demanded by the SLR system is of about 20 arcseconds, we conclude that the method complies with the system constraints delivering also an extracted real-time light curve.

3.4 Tracking

In the review of the stare and chase observation strategy, we saw that the chasing step of the procedure involves either the use of an initial orbit determination, or active tracking. The use of an initial orbit determination might not be optimal for highly automated systems, since the inclusion of the newly generated ephemerides might not be done within an existing session. Furthermore, one unanswered question addresses the usability of the IOD solution. Specifically, it is not a trivial matter to give a bounded solution to the question: how good is the estimated initial orbit and therefore until when will the target be within the field of view of my chasing device? The number of observations used in an initial orbit determination corresponds to the number which the sensor can collect while the object crosses the field of view of the staring device. Consequently, the number of observations is a function of the apparent velocity of the target, the field of view of the system and the exposure time. In cases with reduced field of view aiming at fast-moving targets, a real-time correction for the pointing of the telescope is preferred, i.e. active tracking. A disadvantage of the active tracking approach, when it relies only on an object-recognition step, is that wrong estimates of the corrections will involve wrong slew movements of the telescope. To prevent an undesired slewing motion, a close-feedback loop is developed guaranteeing a smooth trajectory of the object, which makes use of a sliding window containing the historical record of the coordinates of the target previously determined in the object recognition step. In this section we will study the advantages and disadvantages of using either IOD or active tracking.

3.4.1 Initial Orbit Determination

After the computation of an initial orbit using only angular measurements with the method described in [6], its propagation and inclusion within the observation scheduler must be analysed. Ideally, the solution provided by the initial orbit determination should be updated as soon as the target is close to exiting the field of view of the chasing device. Nevertheless, it might be a more convenient strategy to correct the pointing of the telescope in real time, i.e. active tracking, so that the observed arc is longer and the orbit improvement will be significantly better. In order to support the previous statement, a case study for the Experimental Geodetic Payload (AJISAI) is presented. The target was chosen since there is accurate ephemeris available [51], which will be used to compute formal errors with respect to each of our solutions. Note that for the application of the Stare and Chase observation strategy, i.e. the space debris domain, the ephemerides available through the the different analysis centres are considered to be accurate [51]. We took such ephemerides as reference since we were able to track the targets, e.g. AJISAI, using its latest available ephemerides with our laser system, meaning that the ephemerides were good enough to enable the gathering of laser ranges, which is the main aim of the observation strategy. Real observations collected by ZIMLAT and the tracking camera on the 8th September 2018, corresponding to a high culmination pass, are used for simulating a stare and chase observation scenario. An exposure time

of 0.1 seconds was used through the entire pass. Range measurements in full rate form are available from our laser system using a repetition rate of 100 Hz. Table 3.3 shows the type, angular (Ang) or ranges (Rg), and the number of observations used in the orbit determination procedure. The target acquisition fields correspond to: the possibility to follow the target until setting (Vis Pass), ranging the target within the same pass (Rg pass), reacquiring the target using the staring device for the subsequent pass (Vis Next) and ranging the target within the subsequent pass (Rg Next). We define the acquisition of the target (Vis) if the total angular error is smaller than the field of view (≈ 9 arcminutes) of our tracking camera. Likewise, we consider acquisition of ranges (Rg) for radial errors smaller than 1 km. The latter is given by the maximum admissible width of the range gate of the laser system.

Table 3.3: Orbit solutions using a different set of observations within different parts of the observed arc. Case study for AJISAI observed the 8th of September by ZIMLAT and tracking camera.

<i>Orbit Solutions AJISAI</i>						
	Type Obs.		Target Acquisition			
Case	Ang	Rg	Vis Pass	Rg Pass	Vis Next	Rg Next
IOD	22	0	No	No	No	No
OI*	82	0	No	No	No	No
OI**	262	0	Yes	Yes	No	No
Ang Mid	292	0	Yes	Yes	No	No
Mer Mid	292	30	Yes	Yes	No	No
Ang Mid-End	322	0	Yes	Yes	No	No
Ang Mid- Mer End	322	30	Yes	Yes	No	No
Mer Mid-End	322	60	Yes	Yes	Yes	Yes

The first orbit solution (IOD) is estimated using only angular measurements collected while the object was crossing the field of view of the staring device. In addition, the eccentricity and perigee passing time were constrained to zero under a circular orbit assumption. The case IOD in Table 3.3 shows that with the minimum number of angular observations collected by the tracking camera, while the object with an apparent angular velocity of ≈ 3.11 arcminutes/sec crosses the field of view of the staring device, is not enough for chasing the target. Two more orbit improvements are needed in order to chase the object until it sets. The orbit improvements (OI* and OI**) are performed also assuming a circular orbit. The second orbit improvement is needed since the first one does not allow to follow the target until the end of the pass, making use of the measurements collected until the tolerance is exceeded. Note that after the second orbit improvement (OI**), the improved orbit enables the use of ranges, since the error

committed in the range is within the tolerance of the range gate. To reacquire the target, orbits with the classical six Keplerian orbital elements are estimated considering perturbations due to the gravitational potential of the Earth, third body perturbations and the solar radiation pressure acting on the known cross-section of the target. Five different situations are simulated: using only a few angular observations in the middle of the arc (Ang Mid), few angular and ranges in the middle of the arc (Mer Mid), only angular observations in the middle and end of the arc (Ang Mid-End), angular observations in the middle of the arc and merged at the end (Ang Mid - Mer End) and using merged observations in the middle and end of the arc (Mer Mid-End). The latter is the only combination that allows the reacquisition of the object for the next pass. In order to see the evolution of the error with respect to each solution and time, we did a comparison against precise ephemerides in the form of CPF. The total angular error (top plots), besides the range error (bottom plots), are shown in Figure 3.8 for the same and subsequent pass. The comparison starts with the solution obtained from the IOD using the measurements available while in staring mode. As soon as the total angular error is greater than the fixed tolerance, we compute an improved orbit using all measurements collected until then (blue dots in Solution for Same Pass plots of Figure 3.8). After the first orbit improvement (OI*), we see in the red dots a drastic immediate reduction of the angular error, but soon the angular tolerance is reached and again all observations collected until then are used for another orbit improvement (OI**). The latter solution enables the tracking of the target, and therefore acquisition of angular observations and ranges, until the object sets. Finally after adding different measurements in different portions of the observed arc, the only combination that allows the reacquisition of the target is the one that uses merged observations at the middle and at the end of the arc (green dots Solution for Subsequent Pass plots of Figure 3.8).

The main conclusion is clear: the observation of a longer arc spanning the complete pass of the target over the station, besides the possibility to fuse angular observations and laser ranges, will generate an orbit that will allow the reacquisition of the target for subsequent passes. The decision on what for a tracking approach to use relies mostly on the system which runs the SLR observation software. If the inclusion of updated ephemerides can be done within an existing observation session, then the use of an initial orbit determination should be implemented. On the other hand, for highly automated systems running a session, which will need to abort the current session in order to update the predictions, another approach must be used. A disadvantage of the latter is the need to use an a priori orbit of the object to generate differential corrections to rectify the pointing of the telescope in real time. Nonetheless, such orbit can be retrieved from public catalogues, TLE predictions, or even generated by other telescopes, possibility that we have at the SwissOGS thanks to the variety of telescopes and sensors. Note that if the chasing device is passive-optical and has a wide field of view, the angular tolerances are relaxed and therefore the usability of the solutions depicted in Figure 3.8 could be used for a longer time. However, the timing issue related to the uploading of recomputed ephemerides remains critical for fast-moving objects.

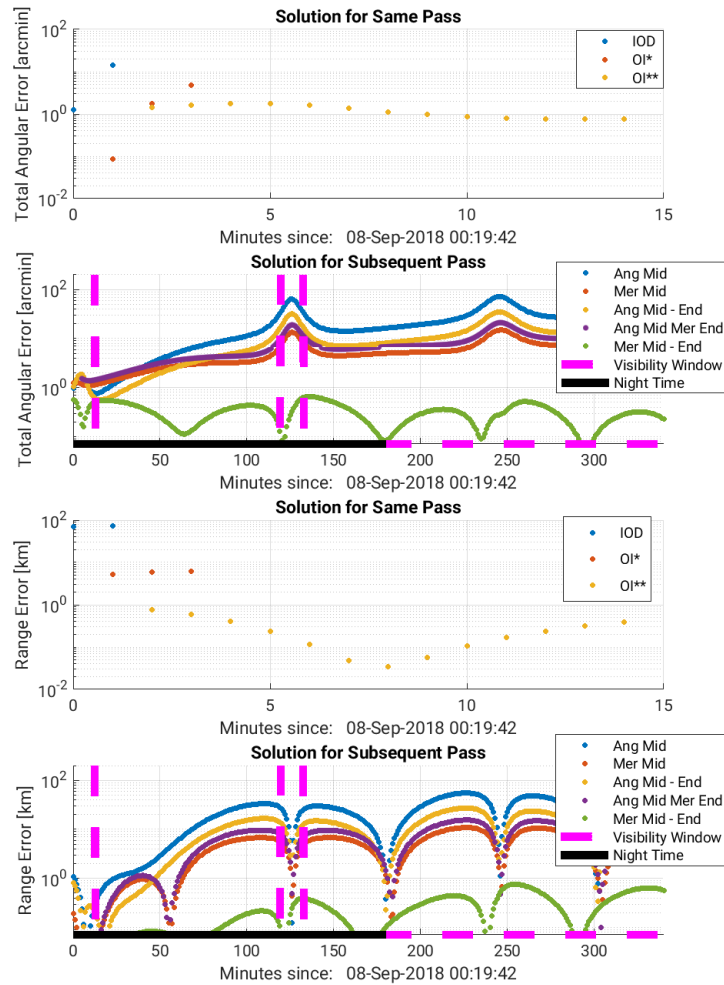


Figure 3.8: Comparison of orbit solutions using a different set of observations within different parts of the observed arc against precise ephemerides in form of CPF. The solutions available for the same pass are an initial orbit determination under a circular orbit assumption (IOD), and two subsequent circular orbit improvements (OI* and OI**). The solutions available for the subsequent pass show a full orbit improvement (six Keplerian elements) adding only angular observations in the middle of the arc (Ang Mid), adding merged observations in the middle of the arc (Mer Mid), adding only angular observations at the middle and end of the arc (Ang Mid-End), adding only angular in the middle and merged observations at the end of the arc (Ang Mid Mer End) and finally merged observations in the middle and at the end of the arc (Mer Mid-End).

3.4.2 Active Tracking

Contrary to an initial orbit determination, an active tracking approach makes use of an existing orbit and improves it using the offsets in azimuth and elevation derived from the object recognition step. In case of wrong detections by the object recognition, the tracking may fail. To prevent such situations a closed-feedback loop is developed. For the design of the closed-feedback loop, we study how these corrections may look like. To achieve this, we simulate a TLE vs. CPF scenario for AJISAI, which shows the type of corrections that we will most likely encounter in a real-time situation. The TLE acts as the ephemerides that we will have available while the CPF represents the real position of the object in the sky. Figure 3.9 shows the differences in the horizon coordinate system (left) and the satellite-station geometry (right).

In Figure 3.9 we see that we have two smooth functions that depend on time and orbit (TLE and CPF). The maximum error in azimuth occurs as soon as the target gets closer to the zenith direction. The symmetry of the error in elevation corresponds to the explanation provided in Section 3.2 and is minimum at the time of closest approach with respect to the observing station. We approximate the trajectory by a polynomial of degree n justified by the approximation Stone-Weierstrass theorem [29]. Additionally, the observation equation reads:

$$\begin{aligned} X_{obs} &= X_{true} + \eta_x, \\ Y_{obs} &= Y_{true} + \eta_y, \end{aligned} \quad (3.7)$$

meaning that the observed position of the object is our measurement for the estimation of the trajectory. The term $\eta_{x,y}$ refers to the noise of the measurements whose probability density function is unknown. Note that the estimation of the probability density function of the noise is not trivial since our observation conditions are different every time that we observe, thus influencing the noise differently. The latter implies that the samples are not independent, identically distributed and ergodic [8]. Despite the fact that the distribution of the measurement noise is unknown, the estimation of the trajectory can be done via a regular least-squares adjustment [42].

Having formulated the dynamical model, i.e. trajectory, and the observation equations, we derive our tracking algorithm as a sequential sliding window method. The algorithm consists of a prediction window based on an autoregressive approach, i.e. estimation of the future state vector based on its past values. The mathematical model reads:

$$X_t = \sum_{i=0}^{Degree} \phi_i (t - t_0)^i + \varepsilon_{t-1}, \quad (3.8)$$

where X_T is the coordinate component at time t , ϕ_i are the coefficients to be estimated for predicting the state at time t and ε_{t-1} is the committed error in the estimation of X_T . The estimation of the coefficients is done via a regular linear least-squares using the available $t - 1$ observations within the sliding window. Simultaneously to the previous window, we construct an error window based on an autoregressive moving

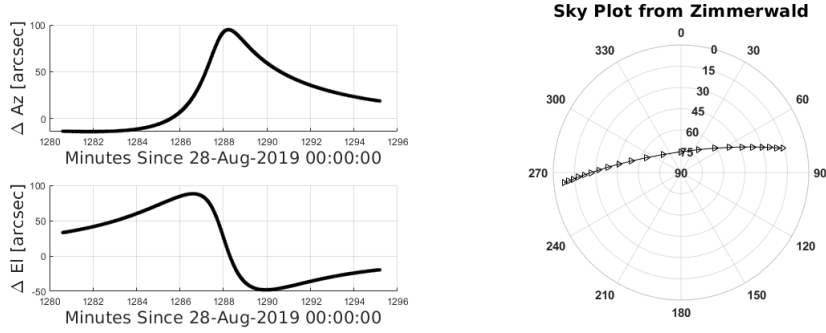


Figure 3.9: Differences in the horizon reference system of ephemerides generated by TLE and CPF for AJISAI (left) for a high culmination pass over Zimmerwald (right).

median approach. From a historical records of observations and predictions, we calculate the observed-minus-computed (OmC) term and estimate the median for all entries within the window. The mathematical model reads:

$$\tau_t = MED(\tau_{t-1}), \quad (3.9)$$

where MED is the median estimator over the window containing OmC values. In order to exclude outliers in the estimation of the updated state of the target, a scoring window marks an observation as a potential outlier if the following condition holds true:

$$SC_t = \begin{cases} 1, & |OmC|_t > \tau_t + 6MAD, \\ 0, & otherwise, \end{cases} \quad (3.10)$$

where MAD is the median absolute deviation. The factor of six is used as a reference [61]; it comes from the relationship between the MAD and the standard deviation, at 99.998% confidence, for normally distributed data sets. All the previous steps are gathered in a set of procedures described in Algorithm 2. It is assumed that there are a minimum number of detections within the sliding window which will initialize all procedures described in Algorithm 2. The inversion of the normal equation system, needed for the estimation of the coefficients of the polynomial of degree n , was performed using the Cholesky factorization algorithm [62].

Algorithm 2: Active tracking based on an autoregressive approach.

Procedure PWLSQ // Predict state of the target using unmarked observations.

Procedure GetNewMeas // Subtract the new observation from the prediction.

Procedure UpdErrorWin // Update the error window and estimate its median.

Procedure MarkObs // Mark observations which exceed the threshold.

Procedure UpMeasWin // Remove marked observations from observation window.

From the implementation of the algorithm, we were able to pinpoint the following dependencies: number of points within the sliding window, degree of the polynomial and the handling of data gaps within the observation session. Figure 3.10 shows the tracking solution of the trajectory (shown in Figure 3.9) using different data points, within the sliding window, and different polynomial degree. A higher degree than two was found to yield an over-parametrized solution, which led to the modelling of outliers as part of the trajectory in worst-case scenarios.

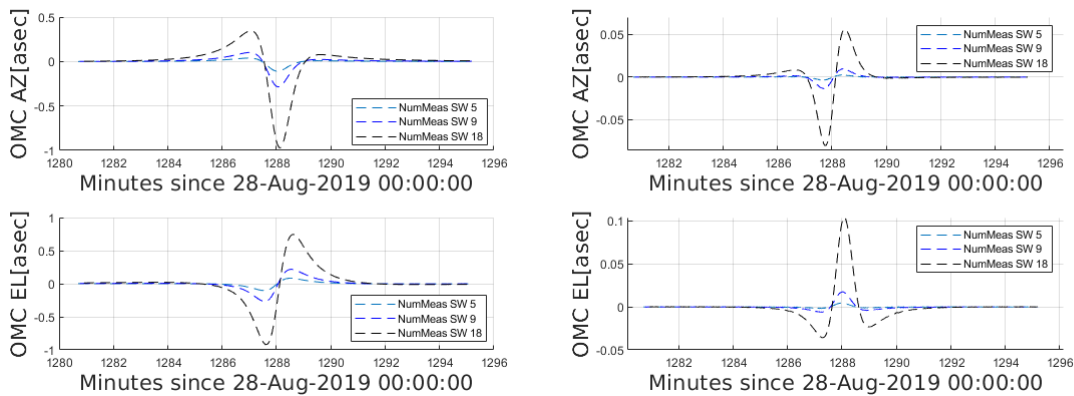


Figure 3.10: OmC terms in arcseconds for azimuth (top) and elevation (bottom), using a linear (left) and a quadratic (right) polynomial for the prediction of the coordinates of the target. Each solution depicts the number of measurements within the sliding window (NumMeas SW) that were used for the tracking.

The number of points available in the sliding window is a function of the exposure time which affects the frame rate, thus critical for long exposures. Assuming a frame acquisition every second, we found that a number of nine data points was enough to keep a fast execution time while keeping the target within the field of view of the laser beam. Further test involving a frame acquisition every 5 seconds demonstrated to keep the target within the tolerance of 20 arcseconds. Regarding the degree of the polynomial,

both linear and quadratic proved to keep the target within the specified tolerance, but as it can be seen in Figure 3.10 the quadratic solution yields better accuracy. The critical points of the functions in Figure 3.9, after differentiating using a finite-difference scheme, match with those local extrema of the OmC displayed in Figure 3.10. It is expected since the difference between the function itself (Figure 3.9) and the function used to approximate its future value (a polynomial of degree n), when taken for a such a short interval of time yield the n th derivative. That explains why a higher polynomial degree yields better accuracies, i.e. it adapts better to the function to be approximated reducing the difference with respect to it. The same reasoning explains why a higher number of points in the sliding window yields larger errors. Finally, the data gaps can occur because the telescope might be scheduled to observe other targets (interleaved with the current pass) or it needs to avoid certain pointing directions, e.g. at the zenith, consequently, the algorithm was designed to handle those gaps and reinitialize by itself when the event is detected.

3.5 Implementation in a Real-Time System

All algorithms shown in Section 3.3 and in Section 3.4 were implemented in a Matrix Laboratory (MATLAB) software suite avoiding the use of built-in functions to ensure portability. Only selected ones were migrated into Delphi and coded using the Delphi XE2 / C++Builder XE2 compiler. The migration into Delphi was driven by the already existing baseline of the software interfacing with the Software Development Kit of the tracking camera. The implementation of the selected algorithms in a real-time system posed several challenges. It had to be flexible, thus regular operators can make use of it without changing parameters within the source code, the execution time must be short and the algorithm for object detection must be accurate in order to lock the target within the field of view of the laser beam. In the previous subsection, we saw that the procedure is accurate when compared to an ultra-precise photometric software suite [13]. Nonetheless, in this section we explore in detail several customizations of the method in order to decrease even more the computational time.

3.5.1 Optimization of the Object Recognition Procedure

In Subsection 3.3.3 we showed that to find the radii for source and background we make use of the cross-section of the object image, in the X and Y axes, and use their respective profiles as an approximation of the PSF, computing finally the different radii for source and background using the FWHM.

The object of interest on the image plane takes only a portion of the full-frame; since the computational load depends on the size of the image, a subframe of the image will yield a faster execution. We decided to specify a subframe of 400x400 pixels, which will give a diagonal of approximately 1.6 arcminutes. It will take about half a second, for an object with an apparent angular velocity of 3.11 arcmin/sec, to cross that diagonal. The algorithm proved to run at the millisecond level, thus being able to correct the pointing

of the telescope with enough margin.

The next procedure that was optimized was the selection of a suitable kernel and step size for the convolution of the subframe against the median filter. The criteria used for the selection of the kernel and step size of the median filter are the minimization of wrong pixels classified as signal, which will affect the computation of the centroid, and the execution time. Figure 3.11 depicts the sequence of steps performed in the estimation of the centroid with the optimal selection of parameters.

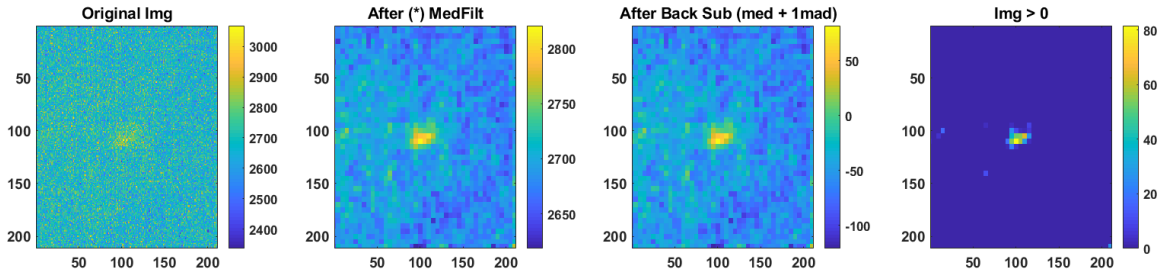


Figure 3.11: Sequence of steps performed for the estimation of the centroid. The first image to the left shows a portion of the original frame. The second shows the result after convolving the subframe against a median filter using a kernel of 9x9 pixels and a step size of 5 pixels. The third shows the result after subtracting the estimated background. Finally, the last image shows all non-positive values masked to zero. Units colorbars: ADU. The X and Y axes correspond to the pixel position on the subframe.

From Figure 3.11 we can see that the target, TOPEX/Poseidon, was deeply embedded in background noise. After the convolution with a median filter, the shape of the target was enhanced enabling a clear identification. After the background subtraction and masking of all non-positive pixels, it can be seen that the background was effectively removed and that the centre of mass will indeed be estimated for the target.

3.5.2 Statistical and Geometrical Considerations

In general, from a statistical point of view, we search a single value, or estimate, representative of a sample from the population of a given measurable physical quantity. Example: an image is a finite set of pixels, i.e. a sample of the infinite population of pixels. If e.g. we want to derive an estimate for the sky background, using the intensity of the pixel as the measurable physical quantity, then we are interested in deriving a function which gives us a single value out of all possible values within the sample space. Note that by single value we do not mean a unique estimator, i.e. we might want to derive an estimator to characterize the central tendency of the samples, or to measure the dispersion of the samples with respect to a central quantity, or in general: any information given by a n th statistical moment.

The immediate following question might be: how to derive such a function? Without

loss of generality, one can study the distribution of the measured quantity, compare to an existing analytical one and run a statistical test to see if the initial hypothesis holds true at a given confidence level. Note that by doing so, we are deriving estimators for describing the needed statistical moments that parameterize the distribution. Following our previous example, we could plot the histogram of the intensity of the image, assume that it is distributed according to a normal $N(\mu, \sigma)$, where μ is the arithmetic mean and σ its standard deviation, and run e.g. the Kolmogorov-Smirnov statistical test to see if our assumption is correct. If we succeed in the test, then we can argue that the background is distributed according to a $N(\mu, \sigma)$ at a given confidence level.

From our previous example, let's assume that the samples of the sky background intensity were actually drawn from a normal distribution, meaning that the quantities μ and σ are representative estimators of the total pixel-wise measured sky-background intensity. The next question is: if within the sample space we have a set of saturated pixels due to a malfunction of the sensor, how would it affect my estimates μ and σ ? The obvious answer will be a question addressing the sample size and the magnitude of the intensity for those saturated pixels compared to the estimates of the background. Nevertheless, the actual point is that those saturated pixels belong to a different distribution than the one of the background. We did not test how representative were μ and σ for the resulting distribution given by the background and the saturated pixels. We can see how the estimates μ and σ degrade gracefully as soon as the assumption of their theoretical distribution fails, i.e. as soon as the number of pixels and magnitude of intensity for the saturated ones depart from the ones of the background.

The breakdown point BD of an estimator quantifies the admissible number of wrong observations before the estimator breaks not holding the initial assumption of being a representative measure of a set of samples. For example, given a sample space of size S , the breakdown point of the sample mean is 1 while for the sample median is $S/2$. According to the previous definition we can say that the sample median estimator is more robust than the sample mean.

Another way of quantifying the robustness of an estimator is by studying the cost function $C(x)$ to be minimized and its first derivative $\Psi(x)$: the influence function. The definition of error is given by $\epsilon = y - E\{y\}$, where $E\{\cdot\}$ is the expectation operator and y is the measurable physical quantity. For the sample mean μ_s the cost and influence functions are given by:

$$C(x) = \|y - Ax\|_2^2, \quad (3.11)$$

$$\Psi(x) = \|x\|_1. \quad (3.12)$$

Note that Equation (3.11) is just the sum of squared differences between observations and estimated parameter, i.e. *the squared error*. For the sample median MED_s both cost and influence functions read:

$$C(x) = \|y - Ax\|_1, \quad (3.13)$$

$$\Psi(x) = \|x\|_1. \quad (3.14)$$

Equation (3.13) corresponds to the sum of absolute differences between observations and estimated parameter, i.e. *the absolute error*. Note that although the derivatives of the

cost function for the sample mean and median yield a L-1 norm, the slope of the straight line for the sample mean is different from zero. In Figure 3.12 we can see the sensitivity of the sample mean quickly growing, in an absolute sense, as soon as departing from the ideal residual of zero. On the other hand, the sample median shows a bounded influence function, meaning that we know exactly that the estimator will break as soon as the breakdown point is reached. It is also important to notice that the cost function for the sample median, despite being continuous, is not differentiable at zero.

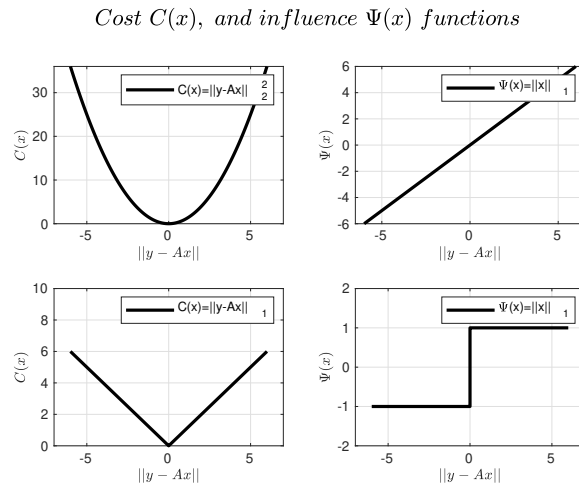


Figure 3.12: Cost (top-left) and influence function (top-right) of the the sample mean. Cost (bottom-left) and influence function (bottom-right) of the sample median.

Next, we will focus on defining what is an efficient estimator. In general, the definition of an efficient estimator may be associated with an optimal criterion such as minimum variance estimator or the maximum likelihood of samples drawn from a specific distribution. If we estimate the variance of the sample mean and median using samples drawn from a normally distributed data set, we can see that the variance for the sample median is larger than for the sample mean, i.e. the sample median estimator is less efficient. Note that the efficiency in this case is a function of the number of samples and that the asymptotic efficiency can be derived analytically [81]. Nevertheless, the sample median proved to be more robust so, in general, the application will dictate which estimator fits best.

The next list enumerate situations where the selection of a suitable estimator is of paramount relevance:

- To mitigate the impact of different error sources in the estimation of source and background in the passive system. Potential error sources could be due to hot and dead pixels in the imaging sensor, stray light from the laser beam, if used in

combination with an active system, presence of clouds or star trails within the field of view of the sensor.

- During the object recognition phase during daylight, the terminator or nighttime if close to a celestial or artificial bright object. The brightness of the background might be close to the one of the source challenging the localization of the object image in the frame.
- During the active tracking, for deriving best estimates of the pointing of the telescope in real time. Note that inaccurate and unreliable estimates coming only from the object recognition module could lead in worse-case scenarios to hardware failures, e.g. wrong slew movements of the telescope.

For the fulfillment of the previous points, a combination of robust and efficient estimators is selected as the preferred choice for estimating the properties of the object image, i.e. the centroid and brightness, as well as its future position in the camera reference frame using the historical records available from successful detections, which is needed for the active tracking.

From the geometrical point of view, the implementation of apertures, i.e. circles, is more computationally expensive than using the circumscribed square of the circle. In the following, we compare the estimation of the background using the subframe against placing circular apertures. In the same comparison, we include the solutions using the median, with its respective median absolute deviation, and the mean, with its respective standard deviation (Top plot in Figure 3.13). We can see how the mean is affected by the inhomogeneous background, larger standard deviation, when using the entire subframe for the estimation of the background. The use of the subframe or apertures with the median estimator does not show significant variations, as expected, due to the aforementioned properties of the estimator. The middle and bottom plots in Figure 3.13 show the estimation of the background varying the geometry of the aperture from a circle to the circumscribed square of the circle, and the computational time, respectively. The gain in execution time using squares is noticeable while preserving the value of the estimated background, therefore we decided to implement it in the real-time system.

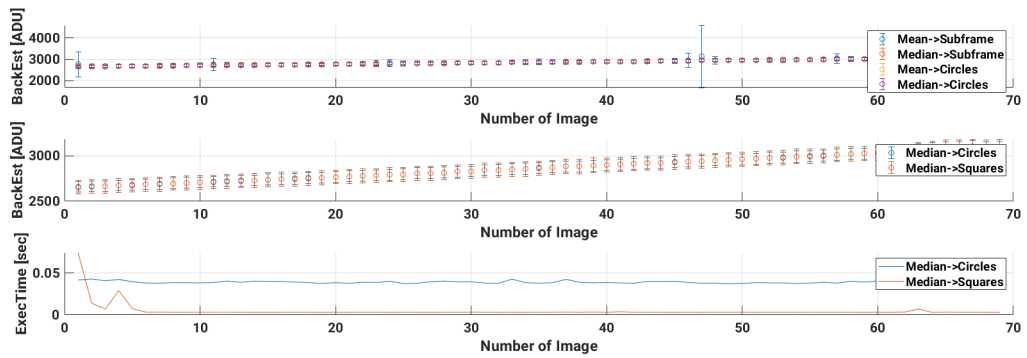


Figure 3.13: Top: estimation of the background using the entire subframe vs. circular apertures using the mean, with its standard deviation, and the median with its median absolute deviation. Middle: estimation of the background with the median and its associated median absolute deviation using circles and squares. Bottom: execution time for the estimation of the background using circles and squares.

For further clarification of the digital image processing pipeline shown in Figure 3.11, we will inspect the steps regarding the estimation of the background, its removal, as the procedure for estimating the centroid. In Figure 3.14, we show the subframe of the image, and the area that will be used to extract the samples for the estimation of the background using circular and square apertures. The raw image has a radiometric resolution of 16 bit and, as it can be seen in the raw subframe, the used dynamic range is that of 18% of its total capacity. The example shows a nighttime frame acquired for Topex-Poseidon using an exposure time of 0.05 seconds. Additionally, from visual inspection, we see that the extracted background using squares is more heterogeneous than the one using circles, in particular the lower right and left corners. It is clear that the geometrical pattern is not the cause, but rather the fact that the square apertures reach a brighter region of the background that is more heterogeneous.

In Table 3.4 we compare the estimation of the background for each case evinced in Figure 3.14. Our ground truth is defined by the values estimated using the circular apertures. The reason is that we computed the normality Kolmogorov-Smirnov statistical test, and it succeeded at a confidence level of 95% using the samples contained in the background ring. Despite the fact that the background is more heterogeneous when using squares, the estimates for the background using the sample mean and median are close to the ones provided by our ground truth. The difference can be neglected if one considers the dynamical range of the image. The estimated background using the complete subframe, including the source, show the expected increase in the magnitude for the background estimated using the sample mean, but the impact of the source is significantly attenuated when using the sample median. Note that despite including the source within the estimation of the background, due to the large number of samples, the impact of

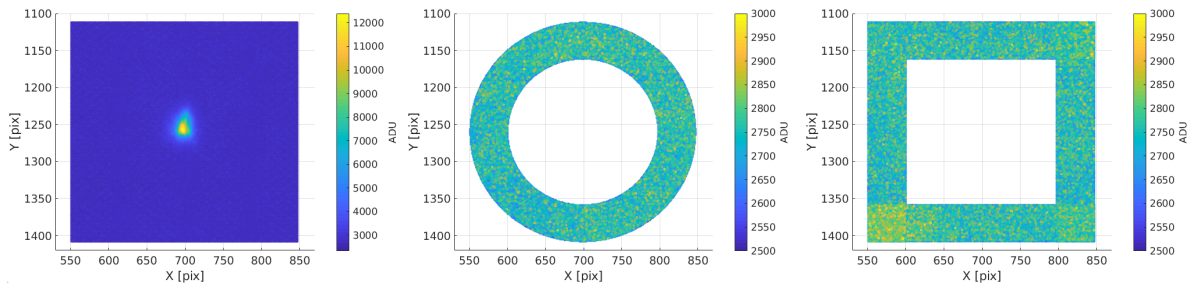


Figure 3.14: Subframe of original image centered on the object image (left). Area of the subframe defined by the difference between outer and inner background radii (middle). Area of the subframe taking the circumscribed square of the difference between outer and inner background radii (right). Unit colobars: Analog-To-Digital (ADU) units.

the source is further attenuated. Regarding the estimators measuring the dispersion, we see no difference between the estimation of the variance with respect to the mean or median due to the large number of samples for each of the 3 cases. The latter result is commonly found in actual symmetric distributions. The estimated standard deviation with respect to the sample mean and sample median reflects the heterogeneity of the background containing the source when estimating the background using the subframe. Finally, when taking the median absolute deviation, a robust estimator to measure the dispersion of a set of samples, we see that it is able to isolate those pixels that do not belong to the homogeneous distribution of the background, i.e. the source.

We conclude that the use of robust estimators for the reckoning of the background, as well as for its dispersion, mitigates the impact of error sources not coming from its expected distribution. We proved the previous statement computing the background including the source itself, which may be considered an extreme case. We implemented the described approach in our real-time system using the square apertures besides the median and median absolute deviation as estimators for the background.

Once we have representative estimates for the background, the next step is its removal. To see the impact of removing the estimated $MED(back) + kMAD(back)$, where k is a constant and $back$ is the set of background samples, we extract two cross-sections from two different frames acquired from the Topex-Poseidon pass, where the object was deeply embedded in background noise. For the statistical interpretation of k the reader is referred to [61]. In Figure 3.15 we show two profiles of the object image fixing the row. After the subtraction of only $MED(back)$, it becomes clear that a suitable threshold for masking the pixels which do not belong to the source is zero. Nevertheless, the zero threshold will not maximize the removal of the background, i.e. there will be scattered pixels which not belonging to the source will impact the determination of the centroid. The threshold $MED(back) + MAD(back)$ was found to yield a good compromise between high and low contrast images. Larger values for k will work for brighter targets

Table 3.4: Estimation of the background varying the geometrical pattern from where samples of the background are extracted. Std: standard deviation. Mad: median absolute deviation. We highlight in gray the combination of estimators that minimize the impact of the source in the estimation of the background.

	Circle	Square	Subframe
Num. Samples	38300	59400	88209
Sample Mean [ADU]	2661	2664	2715
Sample Median [ADU]	2661	2663	2672
Std. Mean [ADU]	86	89	422
Std. Median [ADU]	86	89	424
Mad. Mean [ADU]	58	58	70
Mad. Median [ADU]	58	58	58

but may remove the weak signal of the source for images with low signal-to-noise ratio (see bottom plot in Figure 3.15).

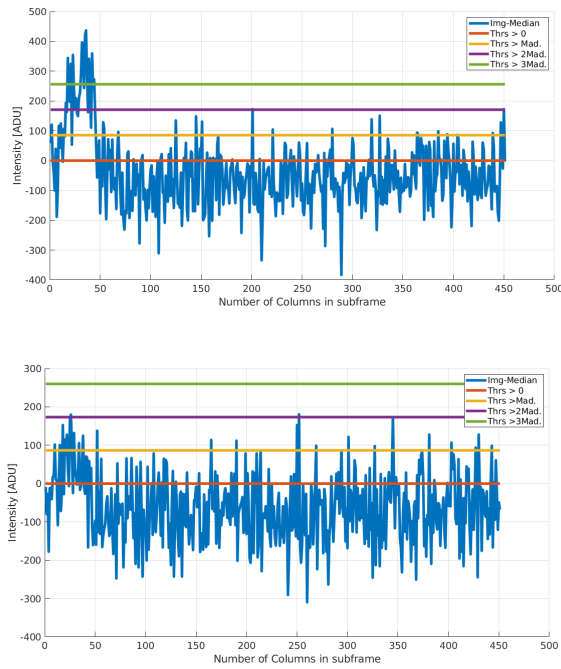


Figure 3.15: Profiles of two frames acquired during the observation of a Topex-Poseidon pass using the tracking camera. The top plot shows that there is enough contrast to distinguish the object image compared to the bottom one. The figure highlights the impact of choosing a specific threshold for the removal of the background.

Once we are able to remove the background, we proceed with the estimation of the centroid. The estimation of the centroid is given by the weighted average of the coordinates of the source pixels defining as weighting factor the intensity at the location of the different N pixels within its distribution. The formula reads [36]:

$$X_{CoG} = \frac{\sum_{i=0}^{N-1} I_{x,y} X}{\sum_{i=0}^{N-1} I_{x,y}}, \quad (3.15)$$

where X_{CoG} is the coordinate component for the center of gravity of the object image with an intensity $I_{x,y}$ at a given coordinate component X . Note that the estimator used for finding the centroid minimizes *the weighted mean square error*. At this stage, after the pre-processing steps, the estimation and removal of the background, we minimize the contribution of background pixels in the estimation of the centroid for the source.

3.6 Results: Algorithm Implementation

The current study focused on the conceptual basis of algorithms to implement the stare and chase observation strategy. In the previous section, we explored different possibilities for the object recognition and tracking phases highlighting the benefits of the selected choices. At this stage, we will review the steps that we have conducted in order to reach the implementation of the stare and chase observation strategy. After the study of the different methods available for object recognition, it was demonstrated that the aperture photometry was more resilient to the variabilities presented by the sky background and system constraints. Once angular observations are available, the chasing phase begins. The use of an immediate initial orbit determination showed that it does not always follow the object until it sets, within the same pass, if it is only estimated with the first few angular observations available from the staring mode. Furthermore, the inclusion of the updated ephemerides in highly automated systems may require the restart of a session which can lead to potential loose of a fast-moving target with a low culmination pass. As a consequence of the feasibility study, we decided to develop a closed-feedback loop combining object detection and tracking. Finally, we tested different tuning configurations to achieve the best performance in terms of computational running time. Next, we will analyze the implementation in a real case when the tracking camera is working in parallel to the SLR system. Figure 3.16 depicts an all-sky image and the observed south-north pass over Zimmerwald for the decommissioned satellite ENVISAT observed on the 11th of March 2020 at 17:24 Coordinated Universal Time (UTC).

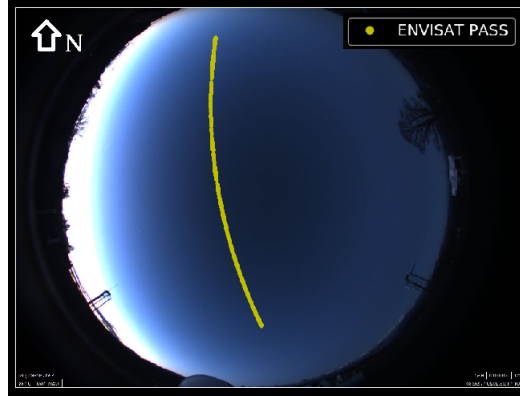


Figure 3.16: ENVISAT pass over Zimmerwald on the 11th of March 2020 at 17:24 UTC.

The selected pass had a high culmination (70°) near the terminator. In particular, the low elevation regions are still bright since the Sun was only a few degrees below the horizon. That situation presents a challenge to the stare and chase observation strategy, in particular for the object recognition phase, besides being a usual scenario for the observation of space debris.

Figure 3.17 shows that from 17.42 to 17.44 hr the estimation of the centroid from the object recognition and the prediction by the filter are in good agreement (differences smaller than ten pixels). Before 17.45 hr we see a sudden change in the trajectory of the target, neglected by the filter at the beginning, since at deviating from the median of the error window the measurements were marked as outliers. Once the filter desaturated, it was able to continue the tracking. In the right plots shown in Figure 3.17, we can see how resilient the filter is in terms of neglecting wrong measurements coming from the object detection. The reason for those wrong measurements is that the contrast of the brightness between source and background is rather low. That means that after we subtract the background, there are scattered pixels through the subframe which do not belong to the target thus affecting the estimation of the centroid.

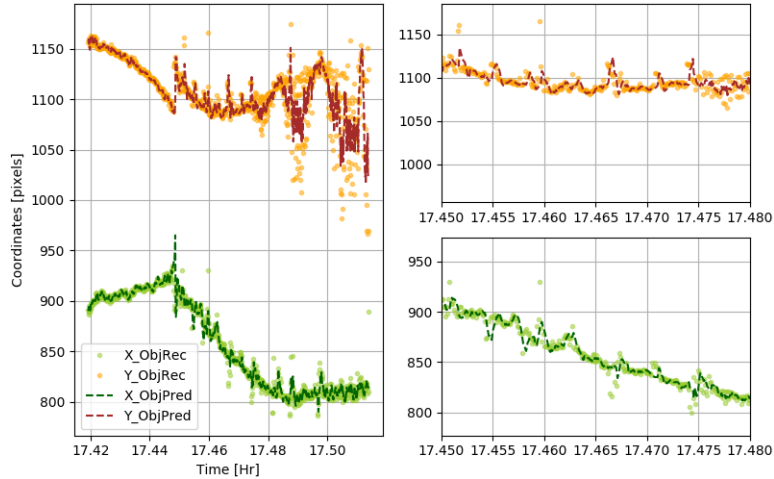


Figure 3.17: Time series of the object image centroid after its estimation with the object recognition procedure and predicted values by active tracking for the decommissioned satellite ENVISAT on the 11th of March 2020. Left: complete pass. Right: detail in the Y (Top) and X (bottom) components. The results were acquired in real time.

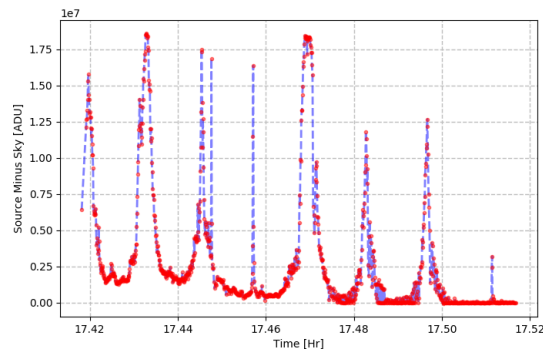


Figure 3.18: Apparent brightness changes acquired in real time by the tracking camera for the decommissioned satellite ENVISAT on the 11th of March 2020.

The filter is able to smooth enough the trajectory so that we can retrieve the real-time light curve of the target showing noticeable periodicities as depicted in Figure 3.18.

Besides being able to track the target and generate real-time information about its attitude, the main goal was to keep the target within the field of view of the laser beam for maximizing chances of retrieving ranges. In Figure 3.19, we can see the detections by our SLR real-time filter. From the observed pass, we were able to retrieve 2708 hits for an 8 minutes pass using a repetition rate of 100 Hz (black dots in Figure 3.19), a number which can be improved in a post-processing step as many returns were not detected by

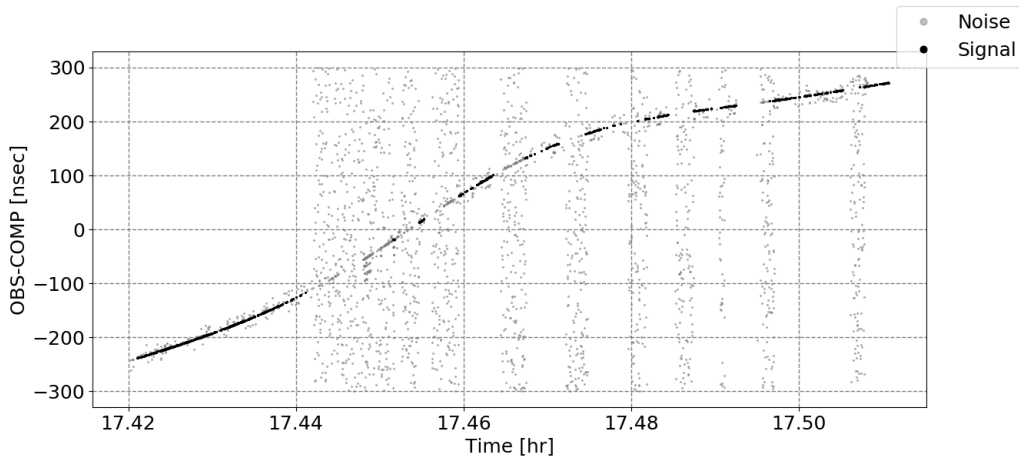


Figure 3.19: Real time detections by our SLR system for the decommissioned satellite ENVISAT on the 11th of March 2020.

the SLR real-time filter (string of grey dots). The along-track error for this case was estimated to be -0.007 seconds. The range gate was initially set to 600 nanoseconds, shrinking to 40 nanoseconds as soon as the SLR real-time filter detected hits.

Since March 2020 until today, we have been using the automated mode of the tracking camera regularly. The only drawback of the current implementation is that the corrections sent by the tracking camera must be integrated into the Proportional-Integral-Derivative (PID) control algorithm running within our telescope controller. At a frequency higher than 0.5 Hz, the corrections are buffered leading to an undesired drifting effect. Nevertheless, the current implementation has proved to keep the target within the subframe even in the worst-case scenario.

3.7 Summary and Outlook

The stare and chase is the resulting observation strategy after the merge of two well-known observation strategies namely survey and follow-up. The main aim was to use a passive-optical system to correct the pointing of the telescope locking the target within the field of view of the laser beam. The use of laser ranges will improve drastically the orbit determination of the target facilitating its future reacquisition. In particular, through the presented research we were able to:

- **Validate the measurements acquired by the tracking camera mounted on ZIMLAT.** The validation included an improvement in the measurement accuracy. The improvement of the accuracy was done by requesting the timestamp from the telescope PMAC. In addition, the modelling of the laser beam position in the camera reference system, through a 2D Fourier expansion, proved to contribute significantly to the improvements in accuracy. The validation of the measurements

was done via an orbit determination scheme and by using precise ephemerides in form of CPF. Hence, proving that the pointing of the telescope can be used to define the orientation of the camera reference system without reference stars. The latter would not be feasible in case of fast moving SLR targets or in case of daylight observations, as not enough reference stars would be recorded by the camera.

- **Compare and implement three object recognition algorithms for the staring phase.** Those methods are the fitting of a defined PSF, the template matching and the aperture photometry. The fitting of a PSF takes on average 5 seconds which is above the limit for a real-time application; it also needs of a priori knowledge of the object image and its characteristics, and it is sensitive to trails of stars. The same sensitivity, with respect to the background, applies to the template matching approach. The aperture photometry method proved to be more resilient after proper selection of tuning parameters such as the kernel and step size used by the median filter.
- **Compare and implement two possibilities for the chasing phase.** Those are the use of an initial orbit determination and active tracking. The use of an initial orbit determination approach might not be optimal for highly automated systems, since the inclusion of the newly generated ephemerides may not be done within an existing session. In such cases, a real-time correction for the pointing of the telescope is preferred. In combination with the object recognition algorithm, we implemented a filter used for predicting the coordinates of the target using a sliding window approach. The trajectory of the target is modeled as a polynomial preferably with a degree lower than three. The number of data points within the sliding window may vary depending on the exposure time, but a number of nine historical records demonstrated to be enough to keep the target centered within the field of view of the laser beam. Additional windows for error control and outlier detection run in parallel to the one used for the trajectory to ensure robustness.
- **Optimize the selected algorithms for its implementation in a real-time system.** We studied suitable parametrizations that will allow for a reduction in the computational time while complying with the stringent requirements of our system namely: the field of view of the laser beam. The most expensive computational operations are within the object recognition phase, specifically the convolution of the subframe against the median filter, and the estimation of the background. However, the time taken for the estimation of the background was reduced by changing the geometrical pattern to squares from circles.
- **Increase the set of observables to azimuth, elevation, range and apparent brightness.** The outstanding by-product of the object recognition phase is a real-time light curve depicting apparent changes in brightness of the object with respect to time, which can be used for orbit improvement and attitude determination of RSO. All the gathered information within our 4-dimensional measurement set was validated and is ready for conducting more case studies than the one provided in

Section 3.6. Finally, we showed that the observations of a longer arc, besides the fusion of observables of a different type, will allow the reacquisition of the object for subsequent passes.

Soon, we are planning to implement the estimation of the coordinates of the laser beam on the camera reference system automatically. By doing so, each single observation night can be used to collect the information needed to estimate the laser beam on the camera reference system (see Section 3.2), without a special session storing and post-processing images, increasing the amount of data and data distribution over the sky. Moreover, the corrections to the predicted trajectory should be computed as along-track/cross-track components. The latter showed a smoother behaviour over time when compared with corrections in azimuth and elevation as in Figure 3.9. Finally, for complete automation of the tracking camera, we are planning to implement an autofocus function. Currently, the focus must be iteratively adjusted by the operator.

Analysis of a Dual-Wavelength Laser Ranging System

IN Chapter 1 it was pointed out that one current limitation of the laser ranging technique for the observation of non-functional RSOs is the power of the emitted radiation, which depends on the repetition rate of the station and the nominal energy of the laser pulse. Most of all available current satellite laser ranging systems, use nominally low power (<1 W) with short pulse width (tens of picoseconds). In this chapter, we will study the system, available at the SwissOGS, dividing it in different components that will permit to optimize the observations in terms of maximizing the detection of photoelectrons triggered by the backscattered photons from the target object. In particular, we address the signal-to-noise ratio for those objects that do not carry any highly reflective element on board.

4.1 Optical Link Equation

A convenient first approach to study a laser ranging system may be through the optical link equation. The optical link, which is also known as photon budget, describes the expected incoming power measured on-ground given an emitted power by a system characterized through technical specifications. Factors that contribute significantly to the on-ground measured incoming signal are, e.g., the free-space loss, the gain achievable by the system, the impact of the atmosphere (particularly relevant to optical measurements), the type of target, its position in space with respect to the observing station, among others. A classical expression used extensively in the literature for the calculation of the optical link is given in [21] and reads:

$$E_{rx} = E_{tx} G_{tx} \frac{\sigma_{sat} A_{rec}}{(4\pi R_{sl}^2)^2} \eta_{tx} \eta_{rx} \eta_{qe} T_{atm}^2, \quad (4.1)$$

where E_{rx} is the expected power measured at the receiver in watts, E_{tx} is the emitted power in watts, G_{tx} is the unitless transmission gain, σ_{sat} is the cross-section of the target in m^2 , A_{rec} is the receiver aperture effective area in m^2 , R_{sl} is the slant range station-satellite in m, η_{tx} is the efficiency of the transmission in the transmit optical chain with a

value between $[0,1]$, η_{rx} is the efficiency of the receiving optical chain with a value between $[0,1]$, η_{qe} is the quantum efficiency of the detector with a value between $[0,1]$, and T_{atm} is the one-way atmospheric transmission with a value between $[0,1]$. Note that Equation 4.1 may be transformed into the sum of all the previous factors if transformed into decibels, which is a format often used by the radar community. In addition, Equation 4.1 assumes that the distance between target and an observing station, besides the atmospheric conditions, did not change significantly within the round trip of the signal, and holds for antennas, or telescopes, working in a monostatic configuration, i.e. same telescope for transmitting and receiving the signal. For bistatic or multistatic configurations those assumptions must be revised.

4.1.1 Free-Space Loss, Gain, Transmitting and Receiving Efficiencies

The factor $1/4\pi R_{sl}^2$ reflects the fact that an isotropic antenna emits radiation of same power density per unit area. If totally isotropic, the propagation waveform will be spherical and therefore the area equals that of the sphere. Note that it is not the case for the emitted laser beam since it has a directivity and the spreading factor is given by $4/\pi(\phi R_{sl})^2$, where ϕ is the field of view of the laser beam in radians. Equation 5.6 might be written in that way since the directivity factor may be accounted for in the gain. Note that the smaller ϕ , the higher the gain will be. The previously defined directivity, which is the capability of concentrating energy in a given solid angle, will define the gaining factor from the ideal spherical isotropic radiating distribution. The maximum gain achievable by a perfect beam with monochromatic (λ) intensity distributed according to a Gaussian transverse pattern radiating mode, i.e. TEM00, reads [21]:

$$G_{tx} = \frac{4\pi A_{tx}}{\lambda^2}, \quad (4.2)$$

where A_{tx} is the effective aperture area of the telescope in m^2 and λ is the specific operating wavelength of the system in m. Note that the maximum gain might be damped if the configuration of the telescope contains an obscuration element, e.g. a secondary mirror, or if there is any off-axis misalignment. An obscurator element may create a diffraction effect on the transmitted beam that will affect the intensity of the radiating source. For a Gaussian distributed radiating source transmitted using a circular aperture, we find that the far field pattern is given by [33]:

$$I_{ff} = \frac{2}{\pi R^2 \Theta_{div}^2} e^{-2 \frac{\Theta_{poi}^2}{\Theta_{div}^2}}, \quad (4.3)$$

where R is the distance to the target in meters, Θ_{div} is the divergence angle in radians, and Θ_{poi} is the pointing accuracy angle in radians. If the intensity of the far field is divided by the intensity's spreading of a perfect isotropic spherical radiator, i.e. $1/4\pi R^2$, the transmission gain yields:

$$G_{tx} = \frac{8}{\Theta_{div}^2} e^{-2 \frac{\Theta_{poi}^2}{\Theta_{div}^2}}, \quad (4.4)$$

which is the expression given in [21]. A further attenuation factor might be given by the tracking jitter:

$$\frac{1}{1 + \left(\frac{\Delta\Theta_{jit}}{\Theta_{div}}\right)^2}, \quad (4.5)$$

where Θ_{jit} is the tracking jitter in radians.

The next terms to account for are the optical efficiencies in the transmitting and receiving optical paths. In general, we can express those as:

$$\eta_{tx,rx} = \prod_{n=0}^{numEle-1} Eff_n(\lambda, R, Coa, i, FFDP, NFDP), \quad (4.6)$$

where the efficiency of each mirror or lens, i.e. Eff_n , either in the transmitting or receiving path, is a function of the operating wavelength of the system (λ), the radius (R), the coating (Coa), the incidence angle of the incident radiation (i) and the near and far diffraction patterns ($FFDP$ and $NFDP$). The total optical efficiency in either transmitting or receiving paths, $\eta_{tx,rx}$, is given by the product of the efficiency of each element. In some existing systems, such as the one available at the SwissOGS, the inclusion of a spectral filter in the receiving path centered at the operational wavelength of the station will be an additional element in Equation 4.6. At the SwissOGS, this filter consists of an air-spaced etalon, known also as a Fabry-Pérot in combination with a narrow band of 0.1 nm centered at the 532 nm wavelength.

4.1.2 Atmospheric Transmittance

The study of the Earth's atmosphere is a substantial part of all available literature involved in the transfer of radiation, see e.g. [33], [4] or [39]. In this section we will explore the general impact, in terms of signal degradation through its propagation along the atmosphere utilizing the LOWTRAN software ([44], [45]). In addition, we will explore the degradation of the beam profile as a function of factors such as the scintillation index and the refractive index structure parameter.

Beam Profile Degradation

The degradation of the beam profile refers to the physical changes on the intensity distribution of the laser beam profile due to changes in the propagation media. Those changes include scintillation, which are changes in the intensity of the received signal, beam profile broadening, beam profile wandering, which is the displacement of the maximum of intensity with respect to the optical axis, and the phase degradation of the wavefront. All the previous changes could be modeled by the Helmholtz equation for a monochromatic wave in a random media, which implies the solution of a stochastic differential equation, characterized by a random refractive index [33]. Rather than presenting the mathematical formalism that treats this phenomenon in-depth, we describe qualitatively the most important factors. The first factor is the atmospheric turbulence, which is defined as local changes in the refraction index of the atmosphere as a function

of the date, time, geographical location, altitude, air density, pressure, temperature and other atmospheric dynamic processes such as the local wind and the stream. After the discretization of the atmosphere into smaller units, the so-called atmospheric cells, the heterogeneous cells will trigger changes in the propagated pulse shape at the boundaries between them; considering a local air column, one possible way to model those random changes may be through the refractive index structure parameter C_n^2 in $\text{m}^{-\frac{2}{3}}$, which is given in [33] through different parameterizations. The second factor is the atmospheric scintillation σ_I . This factor is a consequence of the air turbulence as well and one possible way to measure it is through the dispersion, i.e. variation with respect to a central tendency measure, of an averaged registered signal.

Modeled Transmission

The LOWTRAN software suite calculates atmospheric transmittance, irradiance and radiance averaged over 20 cm^{-1} intervals in steps of 5 cm^{-1} . The implementation uses a single-parameter band model for molecular absorption, and includes the effects of continuum absorption, molecular scattering and aerosol extinction. Refraction and Earth curvature are included in the calculation of an atmospheric slant path, which is deemed critical for the evaluation of the propagation of radiation at low elevations. The transmittance along a path through the atmosphere depends upon the total amount and the distribution of the absorbing or scattering species. The total integrated amount is the so-called air mass. The calculation of air mass for realistic atmospheric paths requires the inclusion of the Earth's curvature and changes in the refractive index. The general configuration assumes a spherical symmetrical discretized atmosphere. Between boundaries within the model, the temperature profile is assumed to be linear, while the pressure and concentration of particles is assumed to follow an exponential profile. The retrieval of the aforementioned profiles involves the use of observations from space, air and ground. Figure 4.1 shows the temperature profile for two different macroscopic models: midlatitude winter and summer, which were chosen due to the geographical location of the SwissOGS. Figure 4.2 shows the different molecules or element species used for the computation of the atmospheric transmission along the atmosphere for the used macro models. Further parameters that are deemed crucial for the retrieval of the atmospheric transmission as a function of the wavelength are the rural aerosol model, a visibility of 23 km and the height of the station that is 950 m. The final outcome after the retrieval of the one-way atmospheric transmission using LOWTRAN is shown in Figure 4.3.

From the experience gathered during the experimentation with LOWTRAN it becomes clear that the parameterization is critical for the modeling of the transmittance. Likewise, the retrieved transmittance will impact the optical link (see Equation 5.6). Nevertheless, from Figure 4.3 we can distinguish several features.

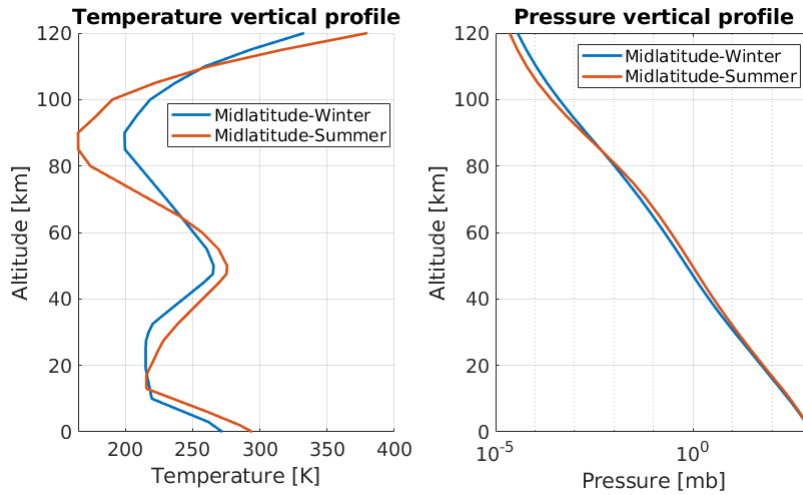


Figure 4.1: Examples of temperature and pressure vertical profiles used in the computation of the atmospheric transmission by LOWTRAN at the SwissOGS.

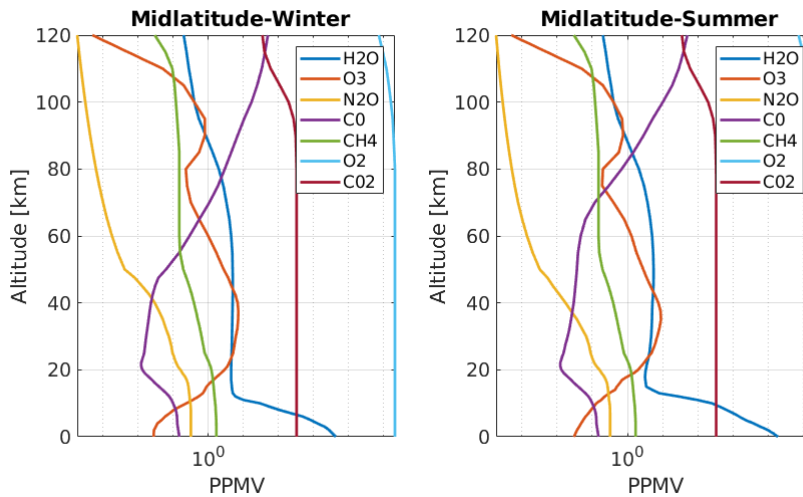


Figure 4.2: Examples of season dependent vertical profiles depicting the concentration of molecules used in the computation of the atmospheric transmission by LOWTRAN at the SwissOGS.

First, the transmission in the spectral region of the blue is attenuated due to scattering attributed mainly to the presence of aerosols. Laser ranging observations will be significantly affected if the operational wavelength is that of 532 nm if compared to longer wavelengths. After the relatively monotone increase of the transmission, the next sharp relative minima are produced due the absorption of radiation by the H₂O and CO₂ molecules. The next important drop, and affecting a wider spectral region is given at 950 nm and may be attributed chiefly to H₂O. Next at about 1,100 nm, we see a

significant attenuated spectral region caused again by the H₂O molecule. Note that the transmission at the fundamental wavelength of 1,064 nm on average is higher than that found at 532 nm by almost 20 %. The latter is an improvement to be considered when both, the transmitted and received signal need to be maximized. The resolution provided by Figure 4.3 could be further exploited for designing and exploring laser ranging systems with new wavelengths.

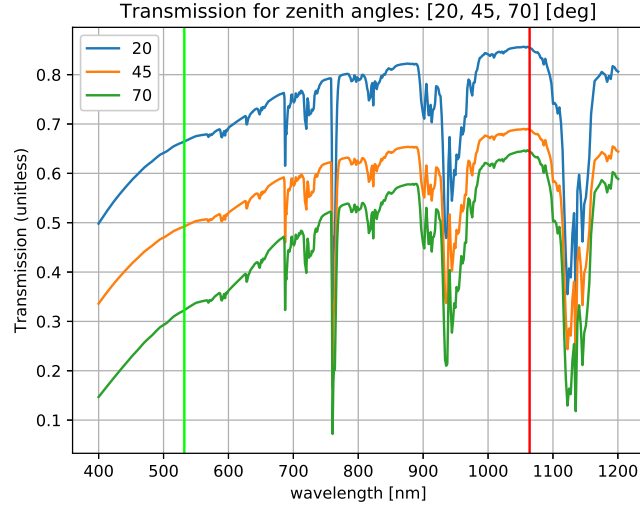


Figure 4.3: One-way transmission curve as a function of the wavelength retrieved using LOWTRAN at different zenith angles. The green and red vertical lines depict the wavelengths available at the SwissOGS, i.e. 1,064 and 532 nm after frequency doubling. The models used include the midlatitude winter profiles, a rural aerosol model, a ground elevation of 950 m and a visibility of 23 km.

Simplified Model

Previously, an atmospheric transmittance model was derived with a relative extensive parameterization. Here, we present an alternative for the estimation of the transmittance accounting only for the visibility, the wavelength of interest and the elevation of the pointing direction. The visibility V , expressed usually in km, is defined as the distance to an object where the image contrast drops to 2 % of its original value. The simplified mathematical model proposed in [27] reads:

$$\gamma_0(\lambda) = 10 \log(e) \frac{3.912}{Vis} \left(\frac{\lambda}{0.55} \right)^{q(V)}, \quad (4.7)$$

$$q(V) = \begin{cases} 1.6, & Vis > 50, \\ 1.3, & 6 < Vis < 50, \\ 0.585 Vis^{1/3}, & Vis < 6, \end{cases} \quad (4.8)$$

$$\gamma(H) = \gamma_0 e^{-1}, \quad (4.9)$$

$$\tau(\theta) = -\gamma_0 H \csc(\theta), \quad (4.10)$$

where e is the Euler constant, H is the unitless characteristic height, γ_0 is the specific attenuation, Vis is the visibility in km, λ is the wavelength in km, $g(V)$ is the specific atmospheric attenuation visibility coefficient and θ is the elevation angle in radians. Next, we show the two-way atmospheric transmission dependency as a function of wavelength for an elevation angle of 45° varying between different visibility conditions.

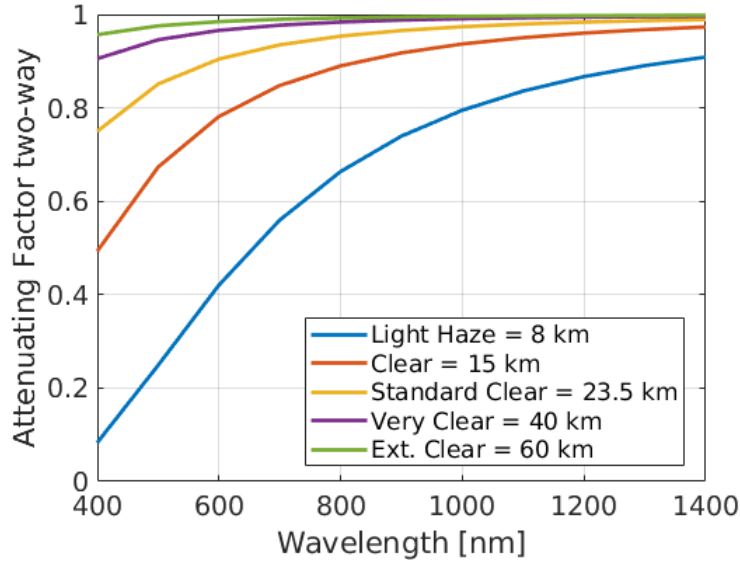


Figure 4.4: Atmospheric transmittance using the simplified model proposed by [27] for an elevation angle of 45° and different visibility conditions.

Comparing the numerical values obtained from Figure 4.4 against Figure 4.3, we may infer that the best approximation is given by the visibility light haze condition of 8 km. It is also shown that Figure 4.4, keeps the monotone increasing feature that was also depicted by the solution shown in Figure 4.3. Nevertheless, the attenuating factors are overall optimistic for values of visibility larger than 10 km.

4.1.3 Target Cross-Section

In Equation 5.6 the term σ_{sat} was defined as the cross-section of the target object. There are different ways in which a cross-section can be defined. First, there is the geometrical cross-section: this type of cross-section may be obtained through the intersection of two bodies with known geometrical shapes. An example of this type of cross-section is given by the intersection of a conical shape and a plane rendering the well-known hyperbola, parabola and ellipse conic sections. In the case of laser ranging, the effective area is given by the resulting intersection of the laser beam with the target object's surface; a few

examples are shown in Figure 4.5. Second, besides the geometrical component, we have the ratio between reflected and incident power, which is proportional to the geometrical cross-section and reflective properties of the target object.

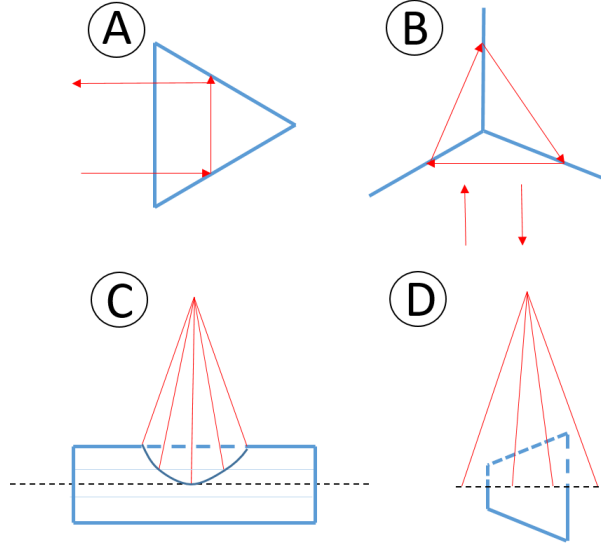


Figure 4.5: Schematic examples of cross-sections. A: dihedral reflector. B: trihedral reflector, also known as corner-cube reflector. D: Intersection between a beam and a cylinder. C: Intersection between a beam and a truncated cone.

Assuming that the irradiated area is larger than the wavelength of the radiation, we can approximate σ_{sat} as the product of the gain of the irradiated area G_σ times the actual effective area A_σ yielding:

$$\sigma_{sat} = \frac{4\pi A_\sigma^2}{\lambda^2} \quad (4.11)$$

if instead of a planar irradiated area, we might be irradiating a trihedral corner cube retroreflector, the effective area might be expressed as a function of the distance a from the intersection of the three faces of the irradiated cube. Note that in both cases we are assuming a specular reflection with ideal reflectivity (see A and B plots in Figure 4.5). From it, it is shown ¹ that the effective area yields $A_\sigma = \frac{a^2}{\sqrt{3}}$. By substituting the effective area in Equation 4.11, we end up with the cross-section of a trihedral corner cube retroreflector, which reads:

$$\sigma_{sat} = \frac{4\pi A_\sigma^4}{3\lambda^2}. \quad (4.12)$$

Equation 4.11 and Equation 4.12 show how the regime of the electromagnetic radiation, e.g. optical vs radio waves, will have a different quantitative behavior of several orders of magnitudes. While in the optical domain, e.g. $\lambda = 1 \mu\text{m}$ a trihedral reflector with

¹<https://www.radartutorial.eu/17.bauteile/bt47.en.html>

circular aperture size in the order of the 2.2 cm will produce a cross-section of about 10^6 m^2 , its counterpart, the radio waves e.g. $\lambda = 1 \text{ cm}$, will need a reflector with a size of about 2.2 m, to reach the same cross-section. Note that we have not included the reflective properties of the target object's in the previous example.

When departing from the assumptions set in the previous examples, we have to define a reflective model, e.g. the bi-directional reflectance distribution function, the irradiated area, which for the sake of generalization might be set initially to an infinitesimal area ds , and the reflective optical properties of the target being represented by ρ_0 . Using a contracted form of the optical link communication, the cross-section reads:

$$\sigma_{sat} = 4\pi R^2 \frac{E_{ref}}{E_{tx}}, \quad (4.13)$$

where E_{ref} is the power in watts reflected by the surface of the target object being radiated. The latter yields the following expression [40]:

$$E_{ref} = \rho_0 E_{tx} \cos_i(\theta) \cos_r(\theta) ds, \quad (4.14)$$

where $\cos_i(\theta)$ comes from the chosen diffuse lambertian reflection proportional to the incidence angle of the incoming radiation, which is further attenuated by $\cos_r(\theta)$ representing the fraction of radiance reflected back in a hemisphere with respect to the normal vector of ds . By plugging in Equation 4.14 into Equation 4.13 and taking the limit of Equation 4.13 when R tends to infinity, we yield:

$$\sigma_{sat} = 4\pi\rho_0\cos^2(\theta) ds. \quad (4.15)$$

The following steps will involve the study of the differential surface element with respect to the direction of the incoming radiation.

Example

An infinitesimal spherical surface element might be written in spherical coordinates as:

$$ds = r^2 \sin(\theta) d\phi d\theta, \quad (4.16)$$

where r is the radius of the sphere, $d\phi$ is an infinitesimal angular element of a circular plane perpendicular to the incident radiation and $d\theta$ is an infinitesimal angular element on the direction of the incoming radiation. To compute the cross-section, we use the differential form of Equation 4.15.

$$d\sigma_{sat} = 4\pi\rho_0\cos^2(\theta) ds. \quad (4.17)$$

Particularizing for a spherical infinitesimal element we have:

$$\sigma_{sat} = 4\pi\rho_0 r^2 \int_0^{2\pi} d\phi \int_0^{\pi/2} \cos^2(\theta) \sin(\theta) d\theta = \frac{8\pi^2 r^2 \rho_0}{3}. \quad (4.18)$$

From this example, it is possible to draw the following conclusion: if the surface element depends on θ then the term $\cos^2(\theta)$ cannot be assumed constant, thus is not being taken

out of the integral.

Now, the infinitesimal surface element is defined by a tumbling disc. From the previous example, the factor $\cos^2(\theta)$ is independent from the geometry of the disc assuming a constant θ with respect to the normal direction of the disc at every moment of the irradiation of the disc; the latter yields the trivial solution for the irradiated area of the disc. If the ideal geometry is that of the disk being perpendicular to the beam, the ideal area of the disc will be reduced by the cosine of the angle α given by the tilted and perpendicular position of the disc with respect to the beam. Furthermore, the incident and reflected angle θ will be affected by the change in orientation of the disc. We might in this case express the cross-section as:

$$d\sigma_{sat} = 4\pi A_{disc}\rho_0\cos^2(\theta + \alpha) \cos(\alpha)d\alpha, \quad (4.19)$$

where A_{disc} is the total area of the disc. A solution for the previous expression as an integral function depending only of the tilted angle α with respect to the normal position of the disc with respect to the incident radiation reads:

$$\begin{aligned} \sigma_{sat} = 4\pi \rho_0 A_{disc} \cdot & (\cos^2(\theta) \int \cos^3(\alpha)d\alpha + \\ & + \sin^2(\theta) \int \sin^2(\alpha)\cos(\alpha)d\alpha - 2\cos(\theta)\sin(\theta) \int \cos^2(\alpha)\sin(\alpha)d\alpha), \end{aligned} \quad (4.20)$$

where the limits of the integrals were not set since those depend on the case study of interest.

4.1.4 Proposed Taxonomy According to Optical Cross-Section

For targets observed using laser ranging systems, we consider a new taxonomy of objects including those which carry highly reflective elements onboard, e.g. retroreflectors, which in some cases were optimized optically at the most common wavelength used by the network of tracking stations of the ILRS, i.e. 532 nm. We distinguish between:

- **Cooperative:** targets that carry retroreflectors on-board and have a controllable or stable attitude. This group is comprised mainly of active missions. The order of magnitude of the optical cross section is of 10^6 m^2 estimated within ILRS activities [52].
- **Pseudo-Cooperative:** targets that carry a retroreflector, or a highly reflective element on board, but have an unstable or unknown attitude. Those targets are mainly decommissioned satellites. Presumably, the optical cross section is in the order of 10^6 m^2 , but aging effects, unstable attitude, unknown geometry between line of sight and reflective elements, may vary the expected optical cross section.
- **Non-Cooperative:** targets that do not carry a retroreflector on board, have presumably unknown optical physical properties and attitude. The order of magnitude for the optical cross section is 10^0 m^2 . Note that often the radar cross section is used for approximating the optical cross section in spite of the different interaction between the physical properties of the target and each radiation regime.

The previous classification clearly shows another contributing factor complicating the signal strength on active systems for space debris, specifically for the pseudo-cooperative and non-cooperative categories, thus stressing the need for the optimization of the system to improve the received power on-site.

4.2 Theoretical vs. Estimated Return Rates

In this section we will examine the optical link equation derived using the technical specifications of the laser system available at the SwissOGS. Furthermore, a specific target namely the LAGEOS -1 will be chosen to perform a validation of the estimates provided by the theoretical link.

Theoretical Link at 532 nm

In Figure 4.6 we show the output for the calculation of the two-way monostatic theoretical optical link for the current operational laser system at the SwissOGS. The explicit parameters highlighted in green, or red, are the numerical values extracted from the technical specifications of the station and target object specifications representing either gains or losses respectively for the calculation of the optical link budget. Bear in mind that there are parameters that are not explicitly used for the calculation of the optical link, but are needed to model the performance of subsystems such as the dark current counts being a function of the cooling temperature of the detector.

```

-----Intrinsic System Parameters-----
Wavelength:          5.32e-07 [m]
Energy:              0.8 [watts]
Repetition rate     100 [Hz]
Number of photons per pulse:  2.14e+16 [photons]      163 [DB]
Efficiency Tx optical chain:  0.9                      -0.458 [DB]
Efficiency Rx optical chain:  0.5                      -3.01 [DB]
Quantum efficiency of detector: 0.2                      -6.99 [DB]
Dark current count:  4e+05 [Hz]
Cooling temperature: -60 [C]
Divergence half-angle: 4.85e-05 [rad]
Pointing error:      7.27e-05 [rad]
Maximum gain:       3.4e+09                      95.3 [DB]
Actual gain:       3.78e+07                      75.8 [DB]
Aperture diam. of receiver  1 [m]
Area of receiver aperture:  0.785 [m2]
Obscuration factor:  0.3
Effective Aperture area  0.715 [m2]                      -1.46 [DB]
-----Target Parameters-----
Target Optical Cross-Section: 15e+06 [m2]                      60 [DB]
Elevation of target:  45 [deg]
Altitud Target:      5.9e+06 [m]
Altitud Station:    950 [m]
Slant Range:        6.91e+06 [m]
Free-space loss:    2.78e-30 [m]                      -296 [DB]
-----Atmospheric Parameters-----
Two-way atmospheric loss:  0.25                      -6.02 [DB]
-----Optical Budget-----
Gain = NumPhot + Gain + TarCroSec 299 [DB]
Loss = EffTx + EffRx + Qe + Aeff + FreSpaLos + 2AtmLos -311 [DB]
Diff = Gain + Losses; 0.071 [photele/pulse] -11.5 [DB]
----- Theoretical Return Rate [photele/sec]-----
Return Rate: 7.1 [photoelectrons/sec]

```

Figure 4.6: Output optical link considering the technical specifications of the laser system at the SwissOGS and LAGEOS -1. In red it is highlighted all losses while in green all gains.

For this particular output, we selected the initialization file for LAGEOS like objects, which means that the emitted energy was selected to be maximum (8 mJ), and the divergence was selected to be minimum (10 arcseconds). The pointing error was conveniently chosen to be 3 times the root-mean-square of the estimated mount model, using only nighttime observations, which conveniently matches with the largest angular sensitivity (15 arcseconds) within all the mechanical-driven lenses and mirrors arranged within the laser transmitting and receiving optical chains. Note that during daylight the pointing of the telescope worsen as a result of thermal stress, due to the telescope being irradiated directly by the Sun. Regarding the target cross-section, we chose the minimum value estimated within the ILRS. We particularized the specific location of the target at an elevation of 45° for retrieving the two-way atmospheric loss and the slant range of the target object assuming a circular orbit with an altitude of 5900 km. Assuming a circular orbit the slant range is derived using the altitude of station and satellite, the elevation

angle and a nominal radius for the Earth by simple trigonometry:

$$R_{sl} = \sqrt{H_{sat}^2 + H_{sta}^2 - 2H_{sat}H_{sta}\cos(\gamma)}, \quad (4.21)$$

$$\gamma = 180 - (elev + 90) - \beta, \quad (4.22)$$

$$\sin(\beta) = \frac{H_{sta}\sin(elev + 90)}{H_{sat}}, \quad (4.23)$$

where H_{sat} is the semimajor axis of circular orbit in m, H_{sta} is the altitude of the station station plus the radius of the Earth in m and $elev$ in degrees is the angular elevation of the target object over the local horizon. Note that the previous derivation allows us to compute the slant range as a function of the elevation of the target. By doing that, all losses depending on the position of the object in the sky may be expressed as a function of the elevation. To further exploit the previous advantage, we take cross-sections of representative target objects from specific orbital regimes and depict the return rates assuming that all targets were culminating at the zenith.

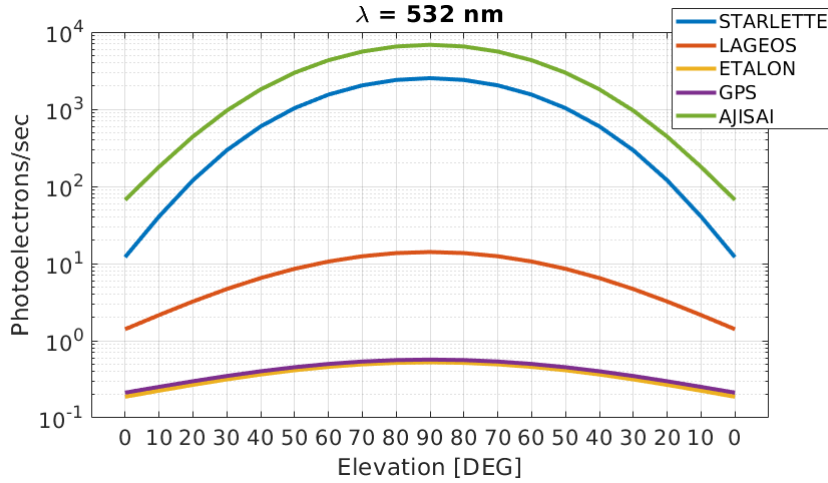


Figure 4.7: Examples of theoretical return rates for target objects at different orbital regimes using as cross-sections parameters the values provided by the ILRS.

In Figure 4.7 we show different return rates for target objects at different orbital regimes using the system and atmosphere parameters derived from Figure 4.6 and the cross-sections of the targets calculated by the ILRS. Figure 4.7 depict several interesting features: For the observation of LEO target objects the return rates are significantly higher than for the other regimes; despite that being a clear conclusion only if considering the free-space loss, it also highlights the need for a variable neutral density filter in the receiving chain. At the SwissOGS it is implemented and currently set up to attenuate return rates higher than 10 %. As shown in Chapter 1, high return rates may saturate

the device, or even increase the jitter at the back end of the detector, due to changing rise times. The previous fact, is one of the reasons why LAGEOS -1 was selected for the comparison between estimated and theoretical return rates, because the expected incoming signal is already below the 10 %. For return rates higher than 10 %, the variable neutral density filter on the receiving path, will ensure that the return rates will not exceed the 10 %. Another conclusion from the figure is the low return rates of targets at altitudes higher than 6000 km, i.e. Global Navigation Satellite System (GNSS) and the Etalon satellites. The schedulers within the observing system should consider this when deciding the ranging time-slots within one observation session and a set of target objects above the horizon.

Observed and Estimated Return Rates

The fact that since 1984 the SwissOGS has performed satellite laser ranging observations, allows for the collection of a significant amount of data, besides all the technological and scientific developments achieved through time. In this subsection, we will retrieve one year of observations of a selected target. We chose the timespan of one year since, from the analysis of the link equation, there was evidence of a seasonal influence on the quality of the transmission in the atmosphere. By taking data from one year and dividing it by months and analysing passes with presumably nearly same observation conditions within each month, we attempt to compensate for this effect. From the theoretical return rates, we saw that in order to see the dependency with respect to the elevation, we need to select targets that have an altitude of more than 6000 km, for target objects with cross-sections in the order of 10^6 m^2 to avoid the cut-off that will occur as the return rate increase to more than 10 %. The ideal target is LAGEOS -1 since it complies with the previous requirements and there are good predictions available from different analysis centres. The availability of accurate predictions is deemed crucial for setting short range gate windows that will enhance the signal-to-noise ratio derived from the observations; this is particularly important to avoid a dependency during daylight and nighttime observations.

The observable, obtained through satellite laser ranging, corresponds to time-tagged single time-of-flight data entries after the emission of one single pulse. From one single pulse it is needed to have a photoelectron triggered at the receiver either from a backscattered photon from the target, dark current or from the sky background, to derive the time-of-flight. Note that it is possible that even if a pulse was emitted no photoelectron was triggered on the receiver, and therefore there will not be an event on the detector to be associated to the emitted pulse. The previous statement is specific for the laser system at the SwissOGSs; there are other stations which also store as entries emitted pulses without returns on the receiver, but obviously no time-of-flight can be computed. Assuming that per each pulse we have a triggered event on the receiver, the number of entries per second will correspond to the repetition rate of the station. The direct use of the measurements exploit the high precision of the measurement provided by the pulse-length that is in the order of 50 picoseconds. Furthermore, the timing system used to measure the time-of-flight, i.e. the event timer, and the timestamp of the measurement,

i.e. the synchronization of the station time with respect to a universal timing scale, e.g. UTC, yield an accuracy of picoseconds for the time-of-flight and of about 15 nanoseconds with respect to UTC root-mean-square. Simultaneously, we may record the readout of the angular encoders at the emission of the laser pulse and bin the data according to either a temporal or angular criterion. The binning of a quasi-continuous data set may be defined as the discretization of the variable representing the feature of interest. For the next steps, we select time as our binning criterion and split the feature space into signal (actual backscattered photons from the target) and noise (all other sources that triggered an event onto the detector). To select a suitable binning size we considered as upper limit the bin size used for the formation of normal points (120 seconds), according to the recommendations provided by the ILRS, and to find a good compromise between spatial coverage and information content we tried different binning options as shown in Figure 4.8.

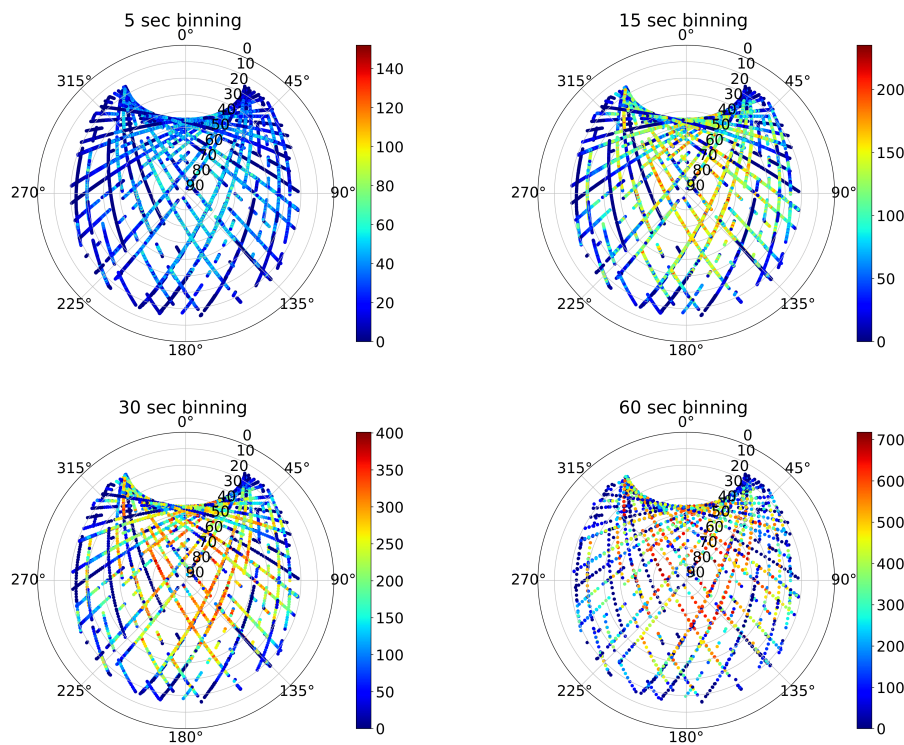


Figure 4.8: Comparison of different binning sizes for the retrieval of estimated return rates for LAGEOS-1 observed on March 2020 at the SwissOGS with its laser ranging system. Units of colorbars: photoelectrons/bin.

For each case shown in Figure 4.8 the averaged return rates, for mid and high culmination passes, are estimated to be 14, 8.3, 6.6, 5.8 photoelectrons/second for binning sizes of 5, 15, 30 and 60 seconds respectively. Using a binning size of 5 seconds was found to be too sensitive to small changes in return rates, which prevented to see directly trends

on the data. In addition, using a binning size of 60 seconds affected the spatial coverage and was smoothing out the information content. Between binning sizes of 15 and 30, we yield a good compromise setting up the fixed value of 30 for the yearly comparison. Note that the gap in the horizontal coverage occurs as a consequence of the target object's orbital inclination.

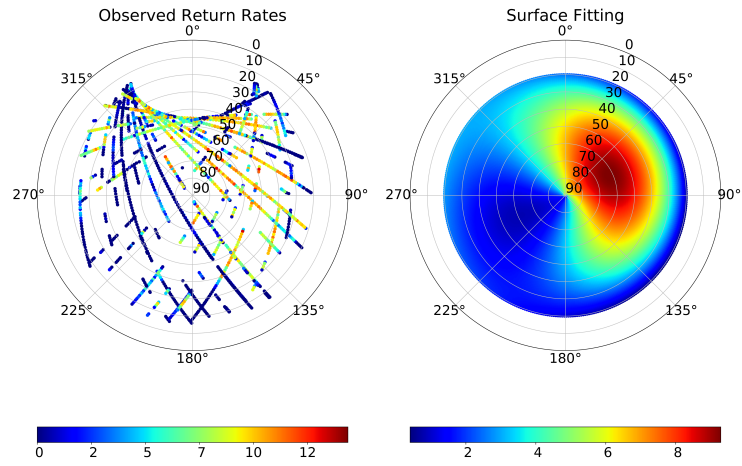
Once we have a discretized spatial distribution of the observed data, we can fit a surface to the retrieved data to further compensate for local variabilities. Due to the nature of the problem, i.e. data fitting onto a spherical geometry, the best approach was to fit the discrete data into a 2D Fourier series expansion of degree and order 2. It may be argued that according to the theoretical study a 2D quadratic function could be used. The issue with this approach was found to be the preservation of the properties of the spherical geometry, i.e. the polar coordinates are transformed into cartesian and those are used for the fitting showing that the estimated 2D quadratic function showed slightly different values at the boundaries. This issue could be fixed by setting proper constraints at the equation level to force same values at the boundaries and a unique one at the zenith direction. Despite the analytical equivalent form between the 2D quadratic function and the Fourier series expansion, there is one effect that is neglected by the quadratic approximation: no correlation with respect to the azimuth direction. As we will see next, the azimuth component also plays a crucial role and should not be considered isotropic for this exercise.

In Figure 4.9 we show the discretized bins containing the return rates in photoelectrons/second over the local horizon of the SwissOGS for 14 months of observations to the target object LAGEOS-1 presented on a monthly basis. From the represented data, we can see that there is a significant heterogeneous spatial data coverage per each month. Potential reasons for that may be mainly the weather, technical issues and system availability. Keep in mind that the laser system at the SwissOGS is interleaved with astrometric observations, besides the fact that within the year the system may participate in campaigns that will restrict the observation windows for LAGEOS-1. The clear impact of lack of passes becomes evident in the estimated model, which can be seen in the months of May and November 2019. To avoid misrepresenting the observed data, we chose to compute the best fitting surface with an order and degree not higher than 2. From the point of view of the discretized-only data, for the majority of the months, the impact of the elevation does not become evident at a first glance. Nevertheless, the feature is well captured after the surface fitting. In addition, one can see that for several passes the return rate is rather low in spite of tracking high culmination passes; possibly that effect could be addressed to the transparency of the atmosphere, technical issues or even due to the quality of the predictions, which is theoretically possible but rarely occurs for this type of target for which there are daily precise ephemerides available. Through observational experience, it became evident that due to a rather low transparency of the atmosphere, besides the thermal stress induced during daylight observations affecting the estimated mount model, the system was not finding the targeted objects easily with the implemented spiral-search mode. Even though the spiral-search mode maximizes the chances to hit the target given an initial trajectory, if the pointing is beyond a certain quality due to e.g. a poor mount model, or if the object is eclipsed

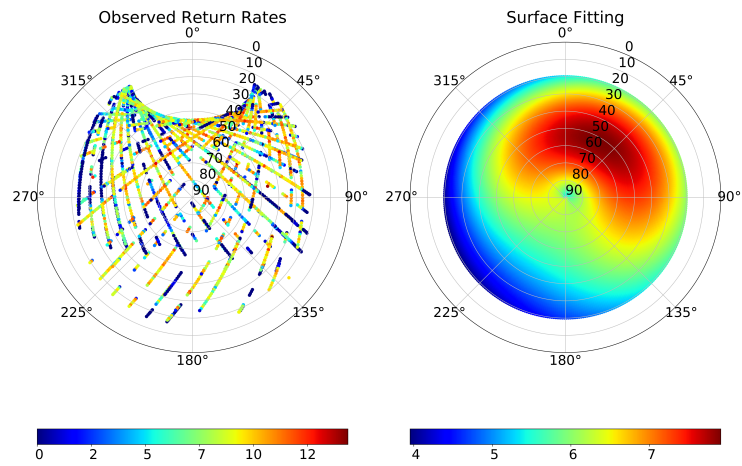
by clouds, there will be data gaps during observed passes.

The impact of those passes with low return rates strengthen the azimuth dependencies on the estimated surface. The correlation between all involved parameters, involved in the acquisition chain, poses a difficulty to evaluate uniquely the azimuthal dependency on the observed return rate, but the impact of the observed arc for the target in an orbit determination, or improvement, could be further analyzed. The previous statement is supported through the quality of the generated normal points for the orbit improvement, whose standard deviation is implicitly a function of the return rate, and the fact that the highest return rates are observed in specific regions of the orbit. On the other hand, if one considers the amount of data provided by the available stations of the network, this effect might be further smoothed, thus not playing a significant role in the parameters derived thereof.

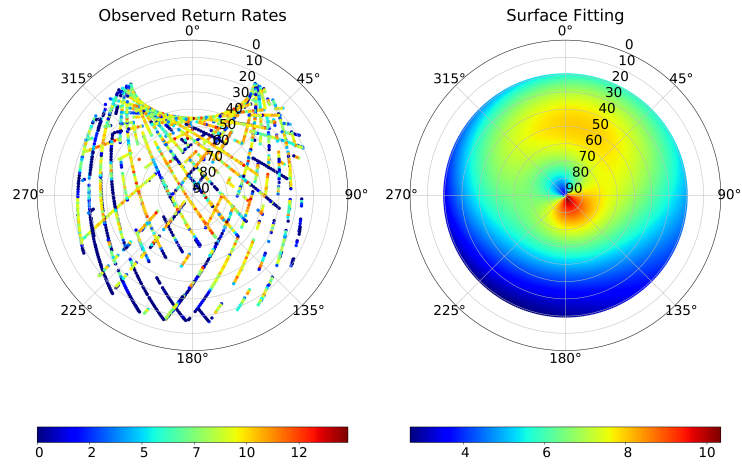
Considering the presented evidence in Figure 4.9, the elevation mask, which is currently set up at 20° at the SwissOGS, should be increased at least to 30° for the observation of LAGEOS-1, first to increase the signal to noise ratio, and second because that specific time could be used to observe other target objects with better observability. Nevertheless, if we consider orbit improvement solutions using observations from one single station only, the use of a higher elevation mask will reduce the length of the observed arc.



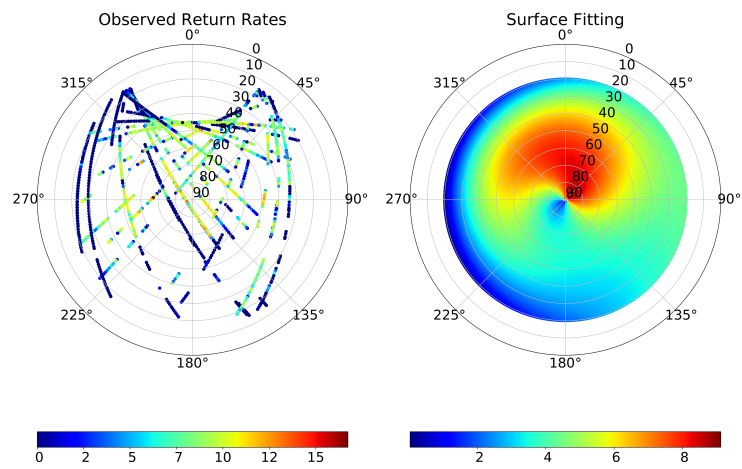
(a) Observed return rates on January 2019. A total number of 43 passes was observed.



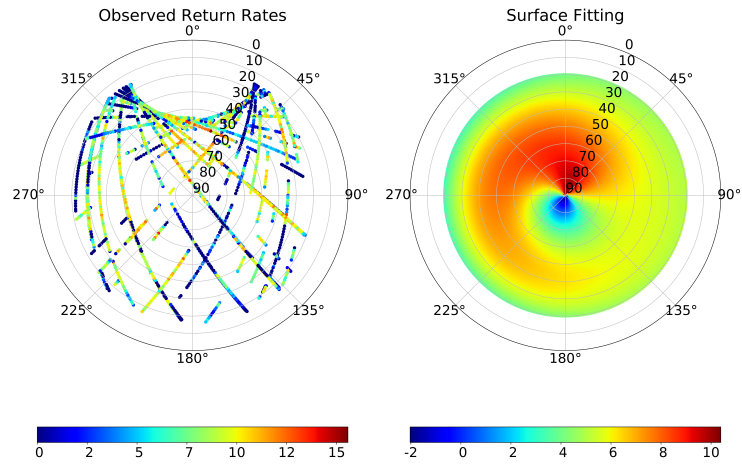
(b) Observed return rates on February 2019. A total number of 89 passes was observed



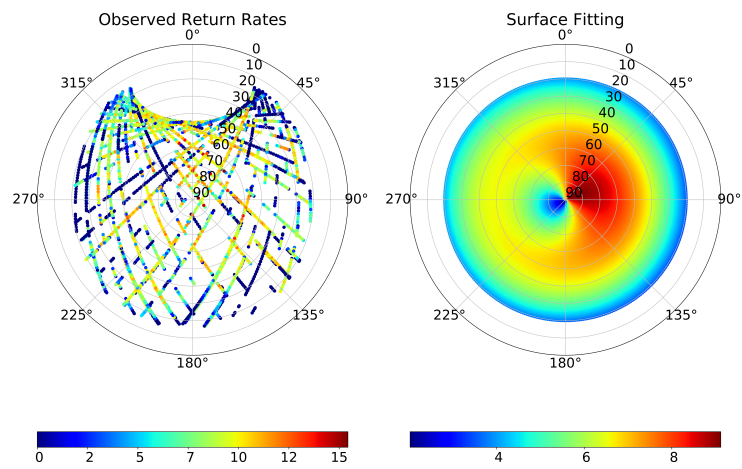
(c) Observed return rates on March 2019. A total number of 82 passes was observed



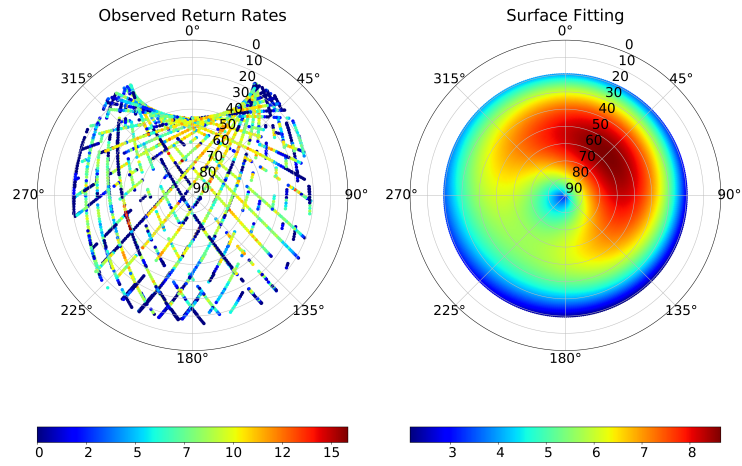
(d) Observed return rates on April 2019. A total number of 34 passes was observed



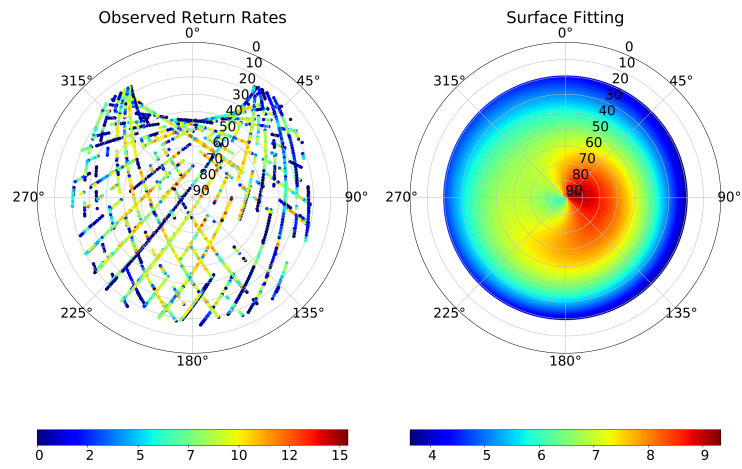
(e) Observed return rates on May 2019. A total number of 57 passes was observed



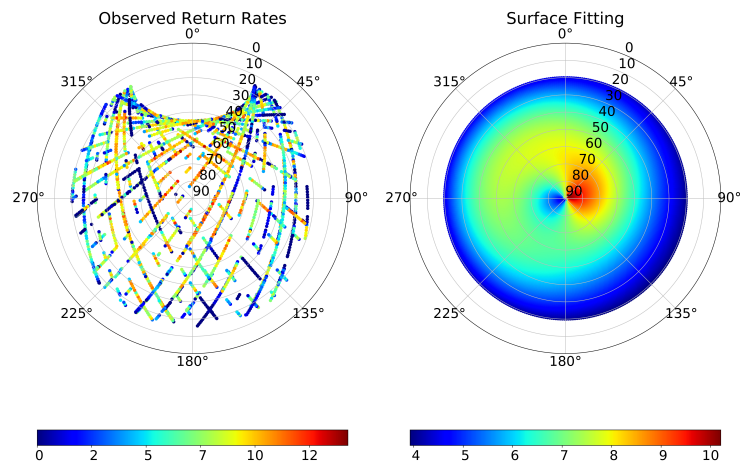
(f) Observed return rates on June 2019. A total number of 75 passes was observed



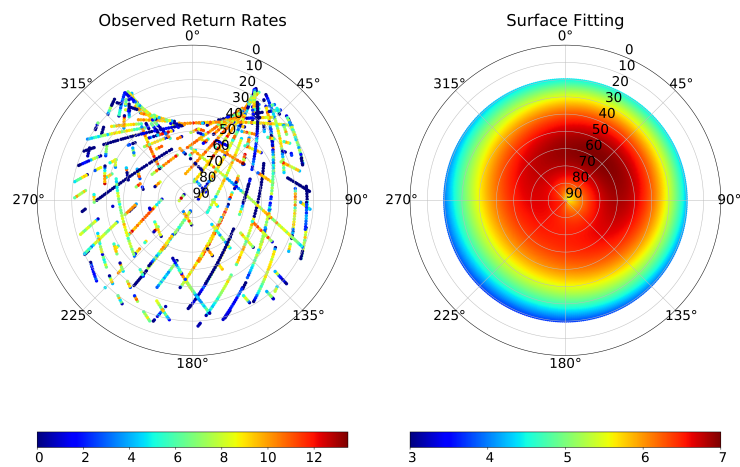
(g) Observed return rates on July 2019. A total number of 85 passes was observed



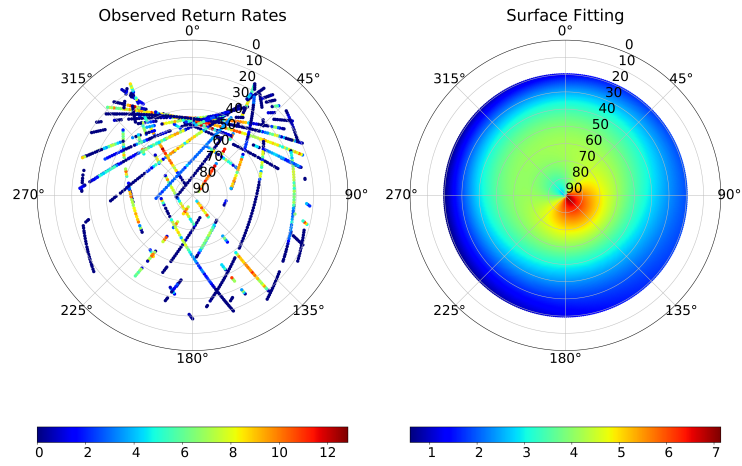
(h) Observed return rates on August 2019. A total number of 88 passes was observed



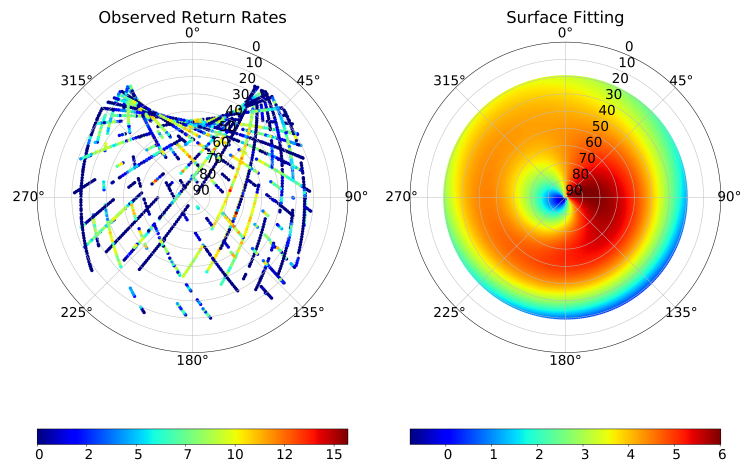
(i) Observed return rates on September 2019. A total number of 87 passes was observed



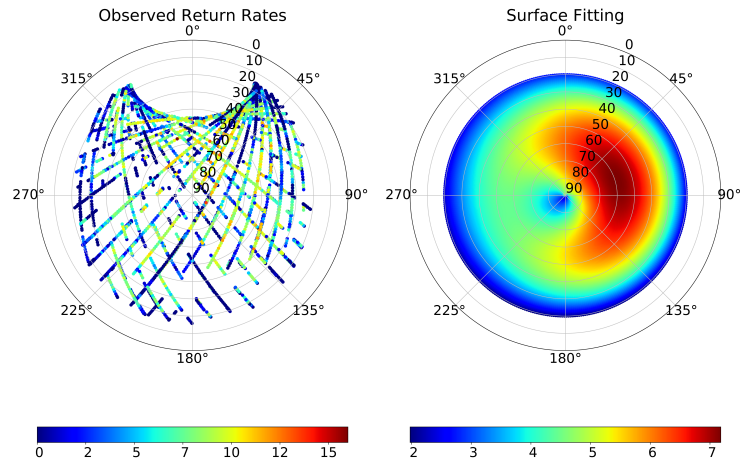
(j) Observed return rates on October 2019. A total number of 52 passes was observed



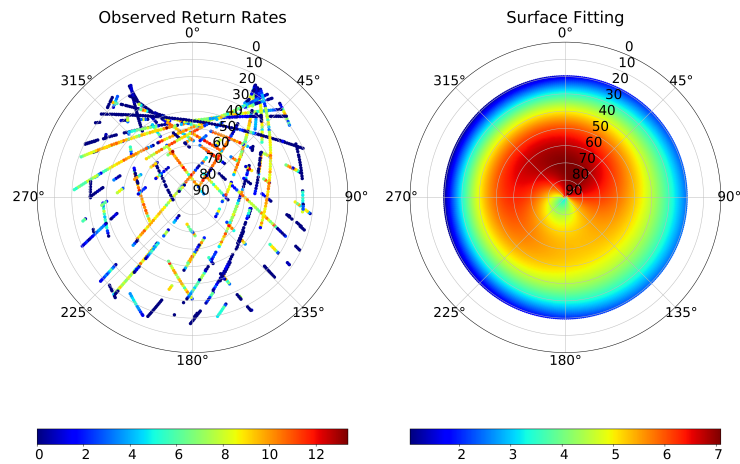
(k) Observed return rates on November 2019. A total number of 41 passes was observed



(l) Observed return rates on December 2019. A total number of 59 passes was observed



(m) Observed return rates on January 2020. A total number of 99 passes was observed



(n) Observed return rates on February 2020. A total number of 39 passes was observed

Figure 4.9: Observed and fitted return rates for LAGEOS-1 during the years 2019 and 2020. Units of colorbars in photoelectrons/second.

4.2.1 Analysis of the Current Performance at 532 nm

In the previous subsections, we analyzed the expected theoretical return rates using the technical specifications from the laser system at the SwissOGS. In addition, raw data from 14 months was post-processed to estimate return rates from the observed passes. Next, we will use the observed return rates to derive a statistical figure of merit per each month, and compare it against the theoretical values. To do so, we decided to use the so-called box plot showing per month, from bottom to top, the minimum, the first quartile, the median, the third quartile and the maximum return rates per each month using as observable set the 30 seconds binned observations. The results are shown in the next figure.

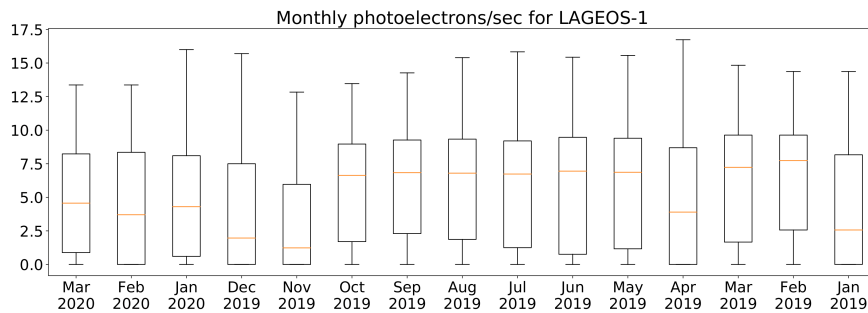


Figure 4.10: Box plot depicting monthly estimated return rates for LAGEOS-1 observed on 2019 and 2020 at the SwissOGS with its laser ranging system.

From Figure 4.10, it is shown that the central tendency for the return rates is found at 7.5 photoelectrons/second. In particular there are four months that show presumably an out-of-trend behavior namely January, April, November and December 2019. From the analysis in Figure 4.9, we can see that for those months the number of passes with low to non return rates is significantly higher than for the rest. Those empty bins affect the statistics when inferring the performance of the station. To remove the influence of the empty bins in the final computations, we filtered the data according to two criteria: first, the real time filter flag must be true indicating the closeness of the measurements in the observed-minus-computed domain, and second the flag indicating a successful 3σ screening procedure, after an orbit improvement, should also be set to a true value. Those two logical conditions guarantee that the used data has a minimum quality, hence might be used for retrieving reliable information about the performance of the station. Note that the previous two steps are station dependent and we use the post-processing scheme available at the SwissOGS for that purpose. In Figure 4.11 we show the results after the filtering of the raw data.

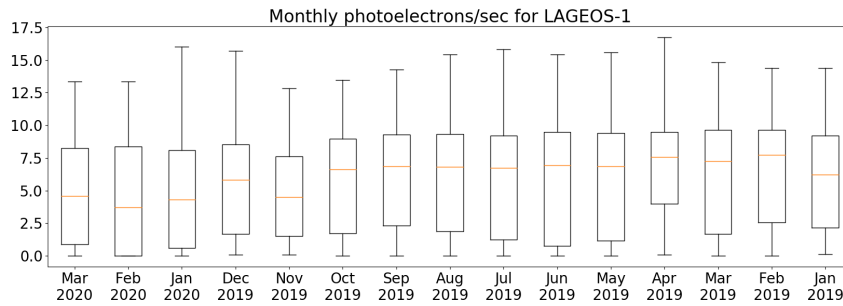


Figure 4.11: Box plot depicting monthly estimated return rates for LAGEOS-1 observed on 2019 and 2020 at the SwissOGS with its laser ranging system after filtering the raw data using the real-time and screening flags.

The filtered results show a better consistency with the general trend. There is still a sudden change in the return rates for observations acquired by the end of 2019. After inspecting the data again, there were not indications of artifacts implicit in the data acquisition or processing. The decrease in the return rates might be indicating that there is a loss of emitted power assuming that all other factors involved in the optical link remained constant in time. In case that the previous assumption would be true, a decrease in the output signal after the frequency doubling of the laser pulse should be measurable. The employed instrument to conduct this test is a thermal sensitive power meter, which operates under the principle of the variation in temperature of a black coated absorber structure after the incidence of quasi-monochromatic light at a given rate. The history of measurements taken by this device indicates that at the beginning of 2019 the average pulse energy was 7.8 mJ, by the end of summer 2019 the measurements showed energy values of 6.7 mJ and at the beginning of 2020 the measured energy reached a minimum of 5.3 mJ, thus we find a good correlation between the decrease in output power measured with the power meter and the data depicted in Figure 4.11. Note that we stress the fact that we considered all other involved elements in the optical link constant, therefore we cannot completely address the decrease of return rates depicted in Figure 4.11 to only the emitted power. On the other hand, the analysis of the data triggers a warning in the system, which might be helpful for conducting further inspections within the system.

Finally, through the estimated return rates we can see that there is good correspondence between the theoretical and the observed values. In Figure 4.7, we saw that the minimum return rate was of 0 at low elevations and of 12.5 photoelectrons/second at the zenith. Those values correlate with the observed ones shown in Figure 4.11. However, one has to consider that the theoretical link is quite sensitive to small variations in parameters that may change within time such as the pointing accuracy, target cross-section – being vulnerable to modifications as a result of variations in the incidence angle of the beam, thermal variations of the optical elements, aging and others –, efficiencies in transmitting and receiving optical chains, emitted power or most importantly atmospheric conditions. Bearing that in mind, once the system setup is ready and measurements are acquired,

the best way to characterize the performance of the station with respect to a given target might be by using historical data sets to target objects from which we have specifications available, as we did with LAGEOS-1, and derive this new information relatively to the one extracted using the long series of observations available from the historical archive. We will provide an example of this in the next chapters.

4.2.2 Operational Implementation of the 1,064 nm Wavelength

The laser system at the SwissOGS has been intentionally designed to operate at two wavelengths since its original design back in 1997. All optical elements within the transmitting and receiving optical chains have nominal efficiencies of about 99 % for both wavelengths. The atmospheric refraction error is wavelength dependent, thus ranges acquired with two different wavelengths will be affected by the refraction differently. However, since the wavelengths of the system are known, a linear combination could be derived using both simultaneously acquired ranges, and their respective atmospheric corrections, which are also function of the on-site meteorological parameters – using e.g. the Marini-Murray refraction model. Currently, the operational system operates only at 532 nm after frequency doubling of the fundamental 1,064 nm. The doubling process involves losses of about 40 %, which in terms of energy translates into a decrease from ≈ 18 mJ to ≈ 7.2 mJ. This reduction in energy may not be critical for targets with retroreflectors as demonstrated in previous subsections, but is crucial for ranging to non-cooperative targets. To exploit the gain in emitted power, the current system must be modified to support operations at 1,064 nm.

The changes needed into the current operational system comprised the alignment of the optical beam at 1,064 to the one at 532 nm, besides the installation of the SPAD receiver sensitive in the spectral region of 1,064 nm, which requires a mechanical adapter to be properly integrated within the receiver box. Specifically, the steps needed for the setup of the fundamental wavelength are:

- Optomechanical alignment: this step consists of the visual alignment of the 1,064 nm beam in the transmitting and receiving optical chains besides the manual tuning of the Fabry-Pérot to project the beam onto the detector. A sensitive to 1,064 nm laser viewing card was use at this step. This was the first iteration for the alignment of the 1,064 nm beam. Once we were able to project the laser beam onto the receiver, we did a fine adjustment of the 1,064 nm laser beam to the 532 nm. To do so, we projected each beam onto the station workshop wall and by the aid of a webcam we matched maximum intensity values on both wavelengths. Note that only the mechanical screws involved in the transmission and reception of the near-infrared were modified to match the beam direction in green. Furthermore, the relationship between small turns in the mechanical screws of the mounts of the lenses and mirrors, and the alignment of the two beams, was controlled through an ancillary alignment target place between the projection of the beam on the wall and the last reflection from an external mirror placed in the control room. Once both projections coincided a fine tuning of the Fabry-Pérot spectral filter took place.

- Electrical: once we ensured the match of both beams in the near field, we used a Stanford counter to verify the correct gating of the detector within the receiving chain. To do so, we connected both the FPGA and the detector to the Stanford counter. Afterwards, we compared the signals generated by the FPGA, i.e. the gates, with the triggered signal in the detector directly commanded by the FPGA. The test was passed successfully. Furthermore the SPAD was connected to the oscilloscope and adjusted manually to maximize the signal detection. It must be noticed that every time that the detector was moved, we verified that the optomechanical alignment was still in place.
- Software: at the software level the changes had to be introduced without disrupting the regular observations to ILRS target objects at the operation wavelength of 532 nm. Changes at the software level included the definition of the new counter, i.e. the event timer, the newly defined wavelength (1,064 nm), operation mode, which could be only 532 nm, only 1,064 nm or both, and calibration constants which are wavelength dependent. Since, we are still in the testing phase, we wanted to prevent corrupting the normal operation mode of the station by separating all observations in the near-infrared from the ones performed at green.

Once the optomechanical and electrical tests were carried out, we started taking measurements using the different calibration targets available at the station, i.e. C1, C2 and C3. Both C1, and C2 are inside the observation building, while C3 is the external calibration located at 672.3 m from the station. The C1 calibration target is located within the transmit/receive optical table at a distance of 8.769 m. The C2 calibration is located in the dome at a distance of 21.450 m. Note that for calibration purposes the emitted energy was attenuated by about 99 % for safety reasons. The attenuation of the emitted energy is done via polarizers on the transmitting path and through variable neutral density filters on the receiving path. A last note about the operational implementation of the 1,064 nm was that at the beginning we were not convinced that we would see the near-infrared beam on the webcam used for the fine alignment. It turned out that even at an attenuation of 99 %, the beam profile was significantly brighter and broader than for the green; as a matter of fact, one unexpected result after ranging to the calibration targets was the presence of a second trace in the range measurements acquisition chain. More insight regarding this issue will be provided in the next sections.

4.3 Comparison Between System Performance at 532 and 1,064 nm

We first analyze the current operational system. To do so, we split the link equation in different components and match the corresponding theoretical optical link equation with the estimates provided by one year of observations to LAGEOS-1. The analysis of the laser ranging system aims at finding critical elements that affect the performance of the station being candidates for optimization without drastic changes in the system. To enable ranging capabilities to pseudo- and non-cooperative target objects, the use

of the fundamental wavelength of 1,064 nm was an interesting choice, since after frequency doubling we have a loss of the nominal power of the laser source of about 40 %. Furthermore, we expect the same performance on both wavelengths at the transmitting and receiving optical paths since all elements within those chains were selected to match performance at both wavelengths. There are, however, certain elements on the link that needed to be readjusted: the half-angle divergence is expected to be larger in the near-infrared than in green; so far, we have not tested for this effect and therefore, we use the divergence provided by the current setup for both green and near-infrared. We have not tested the width of the pulse at 1,064 nm since even if it would be worse by a factor of 10, it will be still acceptable for defunct RSO applications. At the detector level we expect a quantum efficiency of 10 % and the number of dark counts is pending to be tested. Besides the system dependencies, the impact of the atmosphere and the target cross-sections differ from 532 to 1,064 nm. The two-way atmospheric attenuation at an elevation of 45 ° is of 45 % using the 1,064 nm wavelength, which is a factor of two better than the one obtained at 532 nm under the same conditions. Regarding the values available for the optical cross-sections of certain target objects provided by the ILRS, those values are given only for the 532 nm wavelength. In the following, we will use those values for the sake of comparison of the other factors that differ, but we bear in mind that the performance of the reflectors on-board of the satellite for the near-infrared might be different from the ones in green.

4.3.1 Theoretical Link at 1,064 nm

We now compute the return rates for different targets using for cross-sections the values provided for the 532 nm wavelength; the latter might be a wrong assumption, but useful to compare the return rates obtained at 532 nm varying the other parameters sensitive to the new wavelength of interest. The equivalent plot depicted in Figure 4.7 particularized for the fundamental wavelength is shown in Figure 4.12. For the case of LAGEOS like target objects, we have at 532 nm a maximum return rate of 14 photoelectrons per second; likewise, for the 1,064 wavelength we have a maximum of 69 photoelectrons per second, meaning that we have strengthened the link by a factor of 5 provided that all assumptions made are valid. The relevance of the target cross-section comes from the fact that not all satellites have spectral responsive retroreflectors at 1,064 nm. As an example, the target objects Etalon (-1 and -2) have from the total of 2146 retroreflectors per each sphere, only 6 that are germanium corner-cube reflectors optimized for near-infrared ranging. Also LAGEOS satellites have only 4 germanium out of 426 corner cube retroreflectors distributed over the total sphere. Note that this distribution may be exploited for attitude determination analysis. The previous information was retrieved from the ILRS website in the section of current missions in the tab of reflector information per mission of interest.

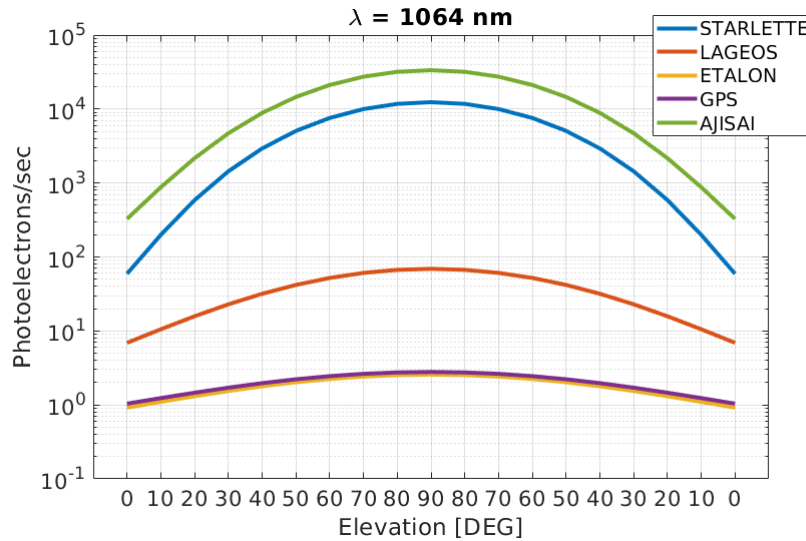


Figure 4.12: Examples of theoretical return rates for target objects at different orbital regimes using as cross-sections parameters the values provided by the ILRS using the 1,064 nm wavelength.

4.3.2 Single-Shot Root-Mean-Square to Calibration Target 3

The fact that we have not measured the pulse width at 1,064 nm does not prevent us from deriving a figure of merit for the single-shot root-mean-square at that wavelength. The purpose of this subsection is to derive such figure of merit at both wavelengths using calibration measurements to an external single cornercube retroreflector located at a distance of 672.30 m from the reference point of the laser measurement system.

The measurements acquired at 1,064 nm to the external calibration target provide evidence that the optomechanical alignment between green and near-infrared was sufficiently good to retrieve measurements using the 1,064 nm wavelength. With system recognized hits, the pointing was further optimized by introducing incremental steps in the order of the arcsecond for maximizing signal returns.

An analysis of the quality of the measurements was done by using the so-called calibration measurements to the external calibration target C3. Those measurements were compared against the submillimeter precision distance retrieved by classical surveying. Furthermore, the fact that C3 is a static target leads to range measurements were there should be no trend assuming that all electro-optical and electrical components are behaving nominally. In Figure 4.13, we show the estimated calibration values for measurements acquired during one minute at different time epochs within the day, using the 532 nm wavelength with its associated precision (1σ) observed on November 25, 2020. In addition, to check the stability of the estimates, the difference between estimates at epoch i and $i + 1$, is shown (dashed blue line in Figure 4.13). From the total of the measurements, the estimated two-way time-of-flight is 4514.683 nsec \pm 0.037 nsec. In terms of the stability between measurements at different epochs within the day, the largest

difference was found to be 10 psec.

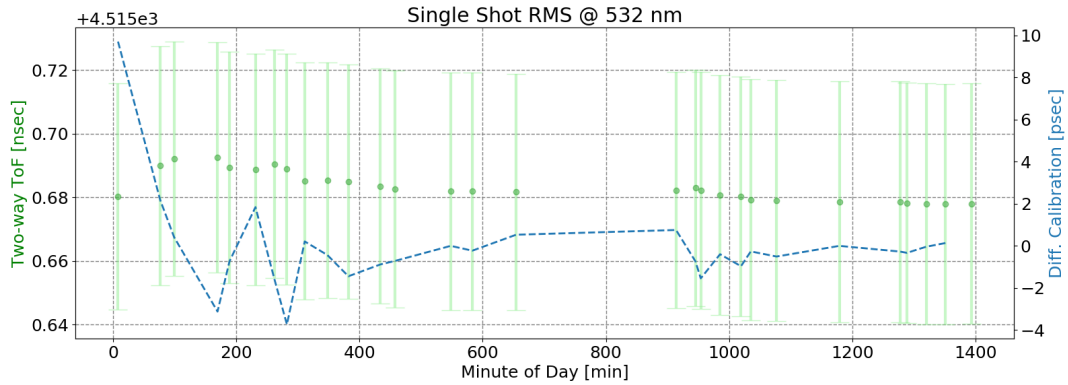


Figure 4.13: Calibration measurement estimates and precision ($\pm 1\sigma$) using observations at 532 nm collected in one minute through the 25th of November 2020. The dashed blue line represents the difference in estimates between the i th and i th + 1 estimated calibration value.

The same analysis was conducted using the 1,064 nm wavelength and the results are shown in Figure 4.14.

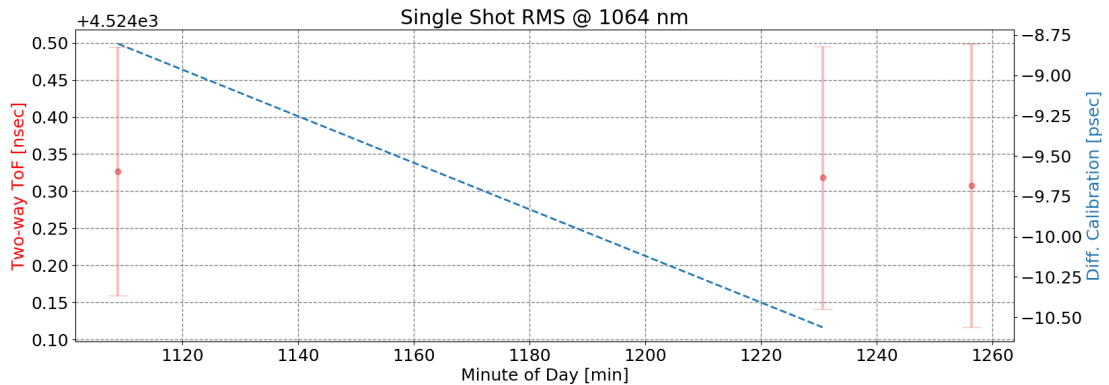


Figure 4.14: Calibration measurement estimates and precision ($\pm 1\sigma$) using observations at 1,064 nm collected in one minute through the 25th of November 2020. The dashed blue line represents the difference in estimates between the i th and i th + 1 estimated calibration value.

The first feature to be noticed is that, only for experimental purposes, we took three calibration observations sets at 1,064 nm during November 25, 2020, contrary to the 33 calibration observations sets at 532 nm collected during regular operations. In addition,

the calibration constant at 1,064 nm differs from the operational one since it has its own electronic set-up being different for each wavelength. Finally, from the total of the measurements, the estimated two-way time-of-flight using the 1,064 nm is $4524.318 \text{ nsec} \pm 0.167 \text{ nsec}$. In terms of the stability between measurements at different epochs within the day, the largest difference absolute value was found to be 10.5 psec.

In order to provide further insight into the calibration measurements, we analyzed each first set of the measurements for both wavelengths. The results are shown in Figure 4.15.

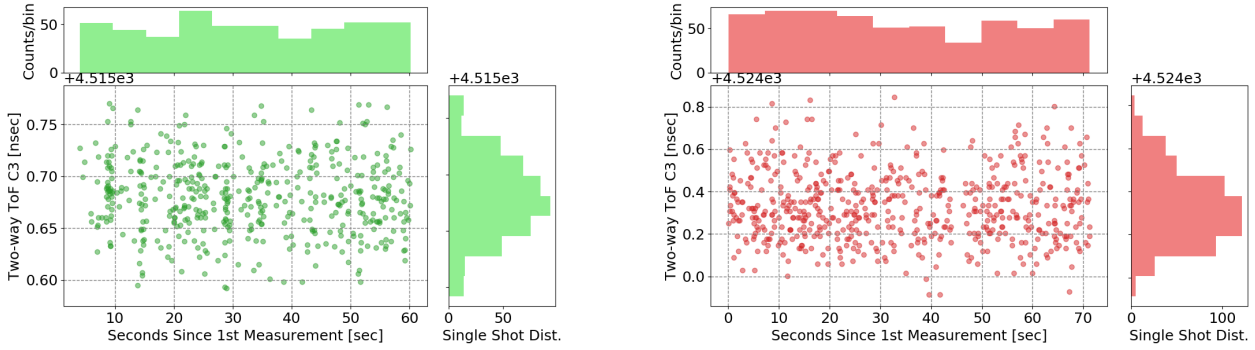


Figure 4.15: Detail of the first measurement set at 532 (left) and 1,064 nm (right) to the external calibration target. Both top histogram depict the counts/bin with a bin size of 6.5 seconds. The right vertical histogram depict the empirical distribution of the calibration measurements. Note the different spacing y-ticks magnitude values for both measurement sets.

The distribution for the measurements acquired at 532 nm is more asymmetrical than the one at 1,064 nm, which shows a larger right tail. Notice that for the signal characterization in terms of counts per bin, a bin size of 6.5 seconds was chosen. On average the return rates were estimated to be of 8.5 photoelectrons/second at both wavelengths. The previous value indicates that the attenuation system response is currently keeping the return rates to values lower than 10 %. From Figure 4.15, we can conclude that the single-shot precision in near-infrared is worse than in green by a factor of 4.5. Note that the presented infrared measurements are initial experimental results and that further tuning of the involved hardware components is required. Nevertheless, the results show its potential for space debris applications since the precision requirement is less stringent than the required within the geodetic domain mainly due to the target depth, i.e the geometrical relationship between the portion of the object which is reflecting the incoming photons with respect to the center of mass of the irradiated RSO. Together with the target depth, the attitude motion of unstable RSOs plays a role since the target depth becomes time dependent; likewise, depending on the mass and geometry of the targeted RSO, the non-conservative forces affecting the flight dynamics might be more complex to be modeled affecting the estimation of orbits with relatively long arcs.

4.3.3 Experimental Observations to ILRS Targets

After the verification of the expected quality of the measurements obtained with the operational implementation of the 1,064 nm wavelength, we prepared dedicated campaigns for the observation of target objects from the catalog of the ILRS. By doing that, we tried to address the following issues: verification of the beam alignment in the far-field, target cross-section response at 1,064 nm for selected targets and potential issues not identified before. From the different observation sessions employing the 1,064 nm wavelength, we present observed passes with their equivalent observed ones, in terms of relative geometry, at 532 nm as close in time as possible, assuming that the transparency of the atmosphere was nearly similar. The results are presented in Figure 4.17 and depict recorded measurements that may be further classified by the real-time filter as noise or signal. To classify measurements as signal, a comparison between measurements within a defined temporal sliding window is conducted. If at least half of the total number of measurements lie within the temporal window, and a predefined target depth, i.e. a two-dimensional binning in the x- and y-axis, then those entries satisfying both logical conditions are classified as signal; if any of the previous conditions is not satisfied, then those entries are classified as noise. Furthermore, once an entry is classified as signal, the system automatically reduces the width of the range gate to increase the signal to noise ratio, facilitating the detection process. The set of objects that we were able to observe at 1,064 nm include Ajisai, CryoSat-2, LARETS, Terrasar-X, Tandem-X and Geo-IK-2. Next we describe our conclusions based on the evidence collected through the measurement campaign.

Beam alignment

A number of 7 passes was observed within the 10th and 11th of August, 2021, from which Ajisai has the maximum altitude, among the observed target objects, with an altitude of about 1,500 km. From those 7 passes, the SLR real-time system was able to automatically classify successful returns from 4 of them. From the other 3, we recognized the signal by visual inspection. Few attempts were carried out to LAGEOS -1 and -2 satellites without success hitherto. Future steps include the observation of more passes with the final aim of estimating a mount model with those observations for comparing it with the one we estimated using observations acquired with the 532 nm wavelength. By doing so, and trying to observe more passes from LAGEOS targets, we can provide a quantitative figure of merit for the alignment of the beam in the near-infrared and in green.

Target Cross-Section Response at 1,064 nm

In Table 4.1, we present a summary containing the date of observations, the observation epoch, the length of the pass, the employed wavelength, the bearing of the pass as well as its culmination, the maximum return rate measured along the pass and the number of hits recognized by the SLR real-time system as triggered events from actual photons reflected by the target. Prior to the 2021 campaign, we successfully observed Ajisai on

June 22, 2020 (see plot *a*) in Figure 4.17). So far it has been the target from which we have observed the highest return rate with the 1,064 nm wavelength. The highest return rate observed for Ajisai, with the 1,064 nm wavelength, was, however, lower than the theoretical predicted value, i.e. we were expecting at least three times the return rate obtainable with the 532 nm wavelength. Nevertheless, the neutral variable density filter will attenuate the incoming flux keeping it to a maximum of 10 %. To discard an issue with the alignment of the near-infrared beam, we used manual incremental steps in a spiral mode, to see if by adding certain angular offsets to the pointing, the return rate would increase. For this test, we used observations to Ajisai and LARETS, i.e. cannon-ball geodetic satellites, for which there were medium culmination passes, and our findings show that the highest return rate was when using zero offsets, hence the alignment of the beam might not be the main responsible for the rather low return rates when using the 1,064 nm wavelength for some of the observed targets within this campaign. In addition, the low return rates observed for all other targets may indicate a lower reflectivity of the retroreflector array on-board of the satellite for the 1,064 nm wavelength.

Other Features of Interest

One interesting feature depicted by the 1,064 nm measurements may be seen in the subplots *a*) and *d*) in Figure 4.17. The effect corresponds to multiple traces within the observed-minus-computed data. The presence of multiple traces may be explained due to the release of pre- or after-pulses, with respect to the main pulse, having enough energy for triggering a detection event in the constant fraction discriminator. In our system the pre-pulses have the energy of about 5 % the total energy of the main pulse. The latter is translated into a rather poor pulse contrast, which can lead to multiple trace effects separated one another by a constant multiple of the laser cavity length. To further investigate the effect of the multiple traces, we acquired measurements to the external calibration target. A sample of the acquired measurements is shown in Figure 4.16.

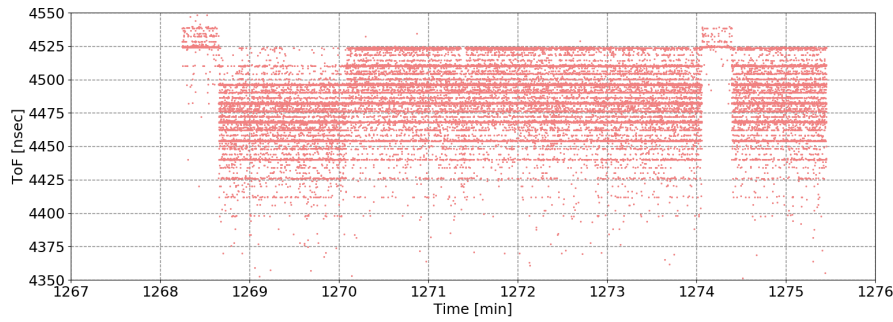
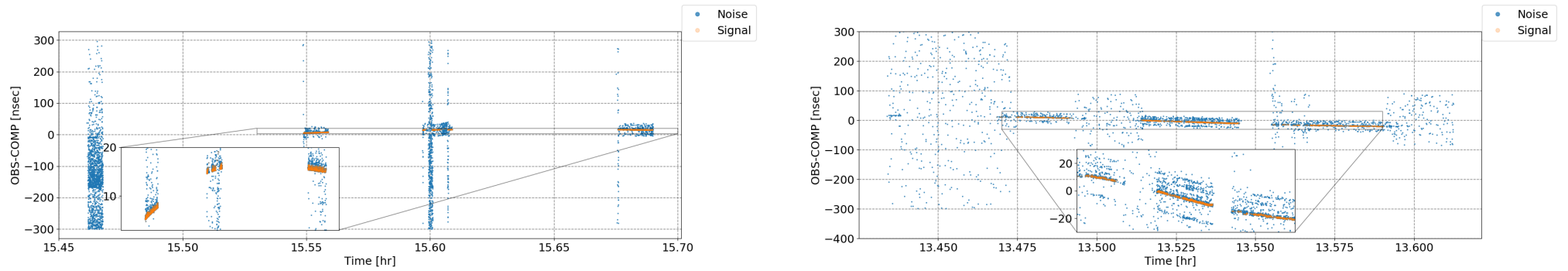


Figure 4.16: Observations to the external calibration target employing the 1,064 nm wavelength. The different discontinuities depicted in the plot correspond to changes in the emitted power, which was adjusted manually. The discontinuities at 1268.5 and 1274 min correspond to an attenuation of 99 % of the total energy, while for the rest only 60 % attenuation was used. After 1268.5 the attenuation was performed gradually, while for the other cases it was set up instantaneously.

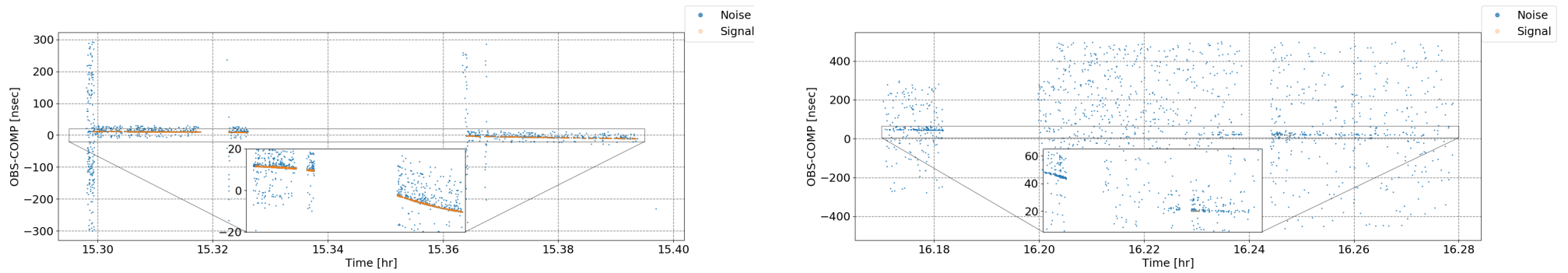
From the measurement set acquired when ranging to the external calibration, several conclusions were drawn. The system delay constant changes as a function of the selected wavelength, since for each wavelength there is a specific electronic assembly. Note that the system delay is computed after the subtraction of the geometrical distance, from the reference point of the laser system to the external calibration, from the measured distance using the laser ranging system. Likewise, even when using the same wavelength, changes in the output power were producing different calibration measurements.

In Figure 4.16, the measurements acquired attenuating 99 % of the total output energy, shown at minute 1268.5 and 1274, depict multiple traces at a constant factor multiple of 4 with respect to the measurements corresponding to the main pulse; after utilizing the oscilloscope, we verified that those traces corresponded to after-pulses. The measurements acquired when attenuating 60 % of the total output energy show sharp traces multiple of 14 nanoseconds, which correspond to the length of the cavity length, thus corresponding to pre-pulses; there are also weaker traces spanned every 4 seconds and even traces separated 1 nanosecond from the main trace. The latter might be related to issues in the detector, since a higher flux on the detector may worsen the high event timing performance needed for precise laser ranging. Nevertheless, the presented conclusions may be taken as preliminary since further investigation is deemed crucial. Additionally, there are another two features that we noticed during the observation campaign summarized in Table 4.1. First, considering that all passes were observed during daylight, thus neglecting the dark counts, the background noise is significantly lower at 1,064 than at 532 nm. At a first glance, the effect can be observed in plot *a*) and *e*) in Figure 4.17. In the following chapters, the issue will be further explored. Second, in spite of having a lower background noise, the signal detection algorithm fails to detect photons that display a likely object trace. The latter points into the improvement and revision of the

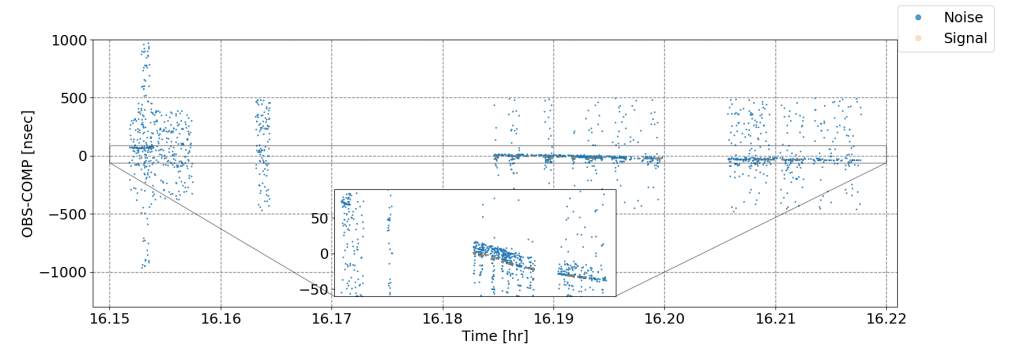
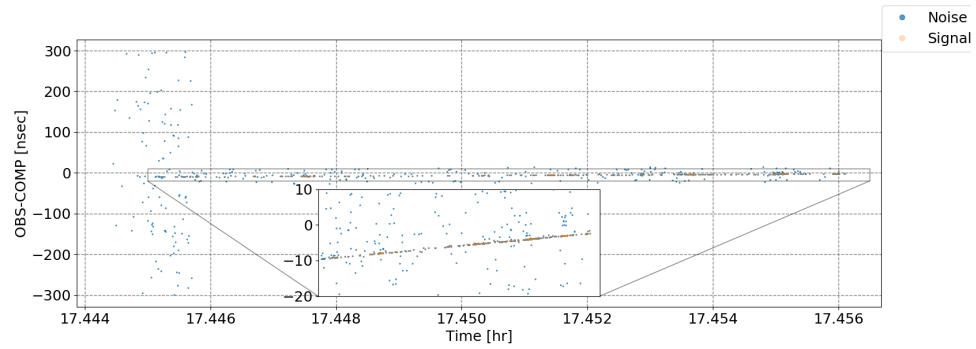
real-time laser ranging filter. However, a more representative sample of observations is required before proposing, designing and implementing new changes into the system.



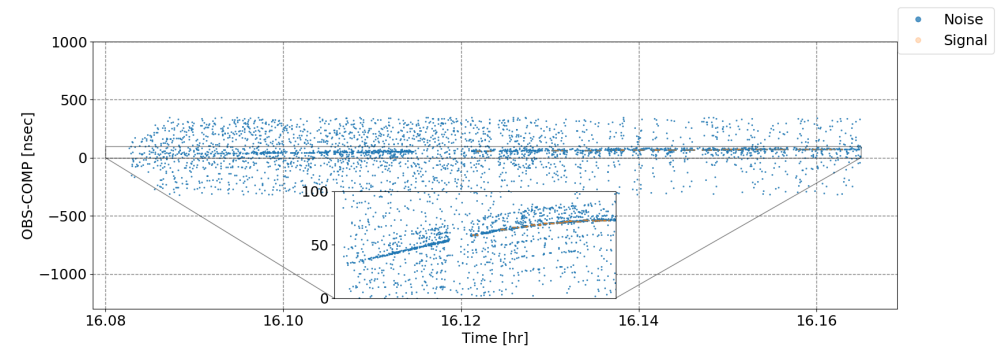
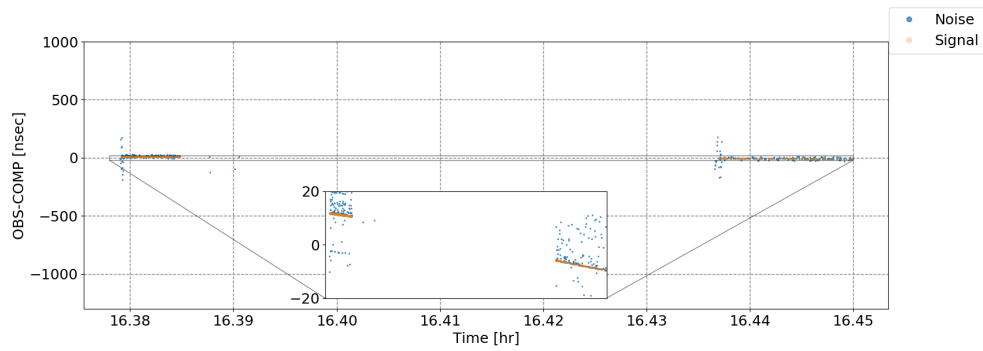
(a) Observations to Ajisai using the 532 nm doubled frequency (left) and the 1,064 nm fundamental wavelength (right) on the 22nd of June, 2020.



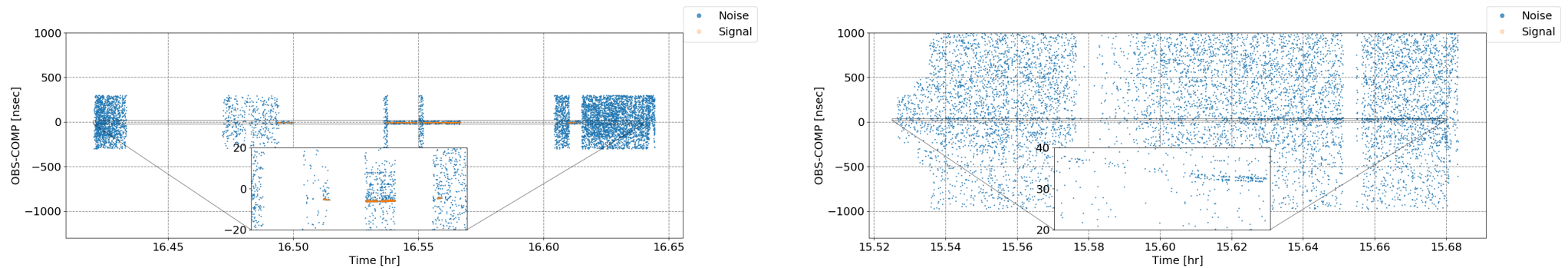
(b) Observations to CryoSat-2 using the 532 nm doubled frequency (left) and the 1,064 nm fundamental wavelength (right) on the 12th and 11th of August, 2021, respectively.



(c) Observations to Tandem-X using the 532 nm doubled frequency (left) and the 1,064 nm fundamental wavelength (right) on the 11th and 10th of August, 2021, respectively.



(d) Observations to Geo-IK-2 using the 532 nm doubled frequency (left) and the 1,064 nm fundamental wavelength (right) on the 12th of August, 2021.



(e) Observations to LARETS using the 532 nm doubled frequency (left) and the 1,064 nm fundamental wavelength (right) on the 12th and 11th of August, 2021, respectively.

Figure 4.17: Experimental observations to ILRS targets using the 532 (left plots from *a* to *e*) and 1,064 (right plots from *a* to *e*) nm wavelengths available at the SwissOGS. The gaps within the displayed measurements occur as a consequence of local air-traffic safety measures. Likewise in orange it is shown the detected photoelectrons being triggered presumably by reflected photons from the target, while in blue photoelectrons classified as noise.

Table 4.1: Summary of observations presented in Figure 4.17 per each target object observed employing either the 532 or 1,064 nm wavelength. The attributes correspond to the pass identifier, the observation date, the beginning of the pass (T0) in UTC, the end of the pass (TE) in UTC, the wavelength (λ) in nm, the bearing of the pass, the culmination of the pass in degrees, the maximum photoelectron rate in photoelectrons/second (Max Re. Ra.) and the maximum of photoelectrons identified as signal by the real-time filter of the laser ranging system at the SwissOGS (Num. Hits).

PassID	Date	T0	TE	λ	Bearing	Culmi.	Max Re.Ra.	Num. Hits
AJ22JN20P (a)	2020-06-22	15:27	15:41	532	NW-SE	76	13	1603
AJ22JN20N (a)	2020-06-22	13:26	13:36	1064	W-E	73	9	1552
CR12AU21P (b)	2021-08-12	15:17	15:23	532	SE-N	44	12	1650
CR11AU21Q (b)	2021-08-11	16:10	16:16	1064	SW-NW	65	0.3	10
TD11AU21R (c)	2021-08-11	17:26	17:27	532	SW-NW	41	2	260
TD10AU21Q (c)	2021-08-10	16:09	16:13	1064	E-N	39	1	92
G212AU21Q (d)	2021-08-12	16:22	16:26	532	NE-N	39	9	565
G211AU21Q (d)	2021-08-11	16:04	16:09	1064	E-NE	31	2	169
LA12AU21Q (e)	2021-08-12	16:25	16:38	532	NW-NE	52	6	697
LA11AU21P (e)	2021-08-11	15:31	15:40	1064	NW-NE	30	0	0

4.4 Summary and Outlook

Through this chapter we have shown:

- **Theoretical estimation of return rates at both wavelengths.** Using the technical specifications of the station and targets, we were able to estimate return rates for target objects in different orbital regimes. The optical cross-sections were available only at 532 nm, thus when using it for the links at 1,064 nm one should expect a lower gain if compared to an identical spectral response at 532 nm. Furthermore, a theoretical revision of the cross-sections was carried out including different reflection models and geometrical considerations. The impact of the different factors affecting the measured power in the receiver was studied separately and, in the case of the atmosphere, transmission curves were derived using LOWTRAN.
- **Observation and estimation of return rates.** The target LAGEOS-1 was chosen to exploit the full theoretical behavior of the return rates unaffected from devices attenuating the incoming return rates higher than 10 %. A total of 14 months was selected since from the analysis of the atmospheric impact, there was evidence supporting seasonal variations. Finally, all the observed data was discretized in 30 seconds bins yielding a balance between spatial coverage and information gain. The observed data was used as input for the estimation of a return rate surface, as a function of azimuth and elevation, using a two-dimensional Fourier series expansion of degree and order not higher than 2. In addition, the monthly observations were analyzed to derive a figure of merit for the return rates by using boxplots. The observations needed to be screened according to the real-time filter and screening flags. Finally, as a cross-check for any potential issue in the system, the emitted power was measured regularly employing a thermal sensitive power meter correlating its output with the behavior extracted from the data.
- **Agreement between theoretical and observed return rates.** The results show a good agreement between the observed and theoretical return rates. Nevertheless, from the analysis of the optical link, it can be seen how sensitive the budget is with respect to slight changes in specific components of the system. Additionally, the monthly observations depict a dependency on azimuth that might have an influence in the different geodetic products derived thereof. This hypothesis is to be further investigated and analyzed. The comparison also unveiled different actions that could be implemented to improve the system performance, e.g. avoid ranging at low elevation for targets orbiting at altitudes higher than 5000 km, the use of variable neutral density filters for cooperative LEO targets, besides the analysis of observed data to infer indirectly the system performance or optical cross-sections of other targets relative to the ones from which we have data sets available.
- **Implementation of the operational 1,064 nm wavelength.** An alternative optimization of the on-site return rates was demonstrated to be given by the use of

the fundamental wavelength. In general, the 1,064 nm wavelength is less affected by the atmosphere, has at least 40 % more energy than the operational 532 nm, and potentially improve the signal detection for observations conducted during daylight. The operational implementation of the near-infrared wavelength included the optomechanical beam alignment, with a finer electronic adjustment, besides changes at the software level to avoid interrupting the regular operational mode.

- **Single-Shot Precision Using Both Wavelengths.** Once the alignment of the near-infrared beam was done, a series of observations to the external calibration target was conducted. We compared the root-mean-square for the observations at both wavelengths showing that the observations at 532 nm are more precise by a factor of 4.5 with respect to those measured at 1,064 nm. In addition, the stability of successive measurement was found to be at the picosecond level for both wavelengths. Despite the larger root-mean-square at 1,064, the quality of the measurements is well-suited for space debris applications.
- **First observations using the 1,064 nm wavelength.** After the alignment of the near-infrared beam, the next logical step was to range target objects from the ILRS active object catalog. After dedicated campaigns, we were able to retrieve a target trace from Ajisai, CryoSat-2, LARETS, Terrasar-X, Tandem-X and Geo-IK-2. Nevertheless, the success rate for all of them was significantly lower except for Ajisai. Further investigations need to be done to draw reliable conclusions, however, the campaigns provided evidence for the alignment of the beam at 1,064 nm besides showing the lower background photon contribution at the same wavelength during daylight.

Regarding future activities, the most relevant might be the continuous acquisition of passes with the 1,064 nm wavelength. More passes are required to provide a quantitative figure of merit for the beam alignment as a function of the pointing direction. Furthermore, we were not able to get measurements from the target objects LAGEOS-1 and -2. In parallel with continuous near-infrared observations, a fine tuning of the system hardware must take place. Specifically, the polarizers and the variable neutral density filters must be tested and the proper analog-to-digital conversion factors derived. From the point of view of the data analysis, the presented time series retrieved for LAGEOS-1 could be used for other GNSS or Etalon target objects. Finally, the impact of the return rates and the distribution of observations along the arc might be further analyzed in the context of derived geodetic products.

Daylight Optical Observations

5.1 Introduction: the State of the Art

HISTORICALLY, the first successful experiments to conduct daylight observations using a passive electro-optical system was reported in [60]. The Ground-Based Electro-Optical Deep Space Surveillance (GEODSS) Experimental Test System (ETS) consisted of a 0.78 m aperture f/5 telescope using a silicon vidicon television camera together with a video processing system that was able to discern RSOs with an apparent magnitude of up to 8.3. In one single day, they were able to reduce the data acquired from 20 passes, from which 13 were finally sent out to the North American Aerospace Defence Command Space Defence Center for its fusion with radar data for orbit improvement. The main problems encountered by the Group 94 of the Massachusetts Institute of Technology were: first, the tracking angular rates, which was solved by the modification of the servo loop parameters, however, gaps were present in passes crossing the north pole since the equatorial mount of the telescope could not keep up with the angular rates of those RSOs passing through that particular location. Second, to estimate the sensitivity of detection, the group calculated the visual magnitude of a sunlit Low Earth Orbit (LEO) RSO using the knowledge they acquired from observing, reducing and calibrating observations to geosynchronous RSOs considering the impact of the phase angle, i.e. the angle between the Sun, RSO and ground station. Their conclusion was that the sensitivity limit needed to be dimmer than an apparent magnitude of 8 to be able to observe RSOs at about 1000 km altitude, pointing into needed modifications at the hardware and software level in the nighttime system used until then. As part of the sensitivity study, the group measured directly the diffuse background contribution, which appeared to vary from 3.8 to 5.4 apparent magnitudes per square arcsecond at locations of the sky away from the Sun. Finally, by observing calibrated stars during daylight, they were able to confirm the sensitivity computed for their system to be 10 apparent magnitudes after several iterations modifying specific components at the hardware and the software. For hardware specifications, including details about the implemented spectral filters, and a comparison between the silicon vidicon and ebsicon (main sensors available at that

time), the reader is referred to [60].

The study presented in [60] served as a baseline for the next incremental technological improvements, i.e. the advent of the Charged-Couple Device (CCD) or the Complementary Metal-Oxide-Semiconductor (CMOS) imaging detectors, and the exploration of new non-silicon-based semi-conductor material in the sensors substrate, exploiting a higher quantum efficiency at the sensor level in the near- and short-wave infrared spectral regions. Studies conducted exploring this options are provided in [23, 63] and focus exclusively on the observation of geosynchronous and geostationary (GEO) RSOs. Note that while the presented work in [23] focuses more on observation strategies to maximize the signal to noise ratio, by analysing the phase and aspect angles, besides the impact of the atmosphere, the work in [63] analyses a complete, commercially available, passive system solution demonstrating an optimized system transmission in the short-wave infrared region besides the improvement in the detector characteristics with a customized cooling system.

Besides the unprecedented technical achievements presented in [60], there are other two factors that are critical and have been further expanded in recent studies: the signal processing system and the astrometric reduction of the acquired images. Successful daylight imaging systems are characterized by a small field of view, relatively large aperture telescopes, short exposure times and high frame acquisition rates. Short integration times become mandatory to avoid saturating the detector. Furthermore, the short integration time combined with a high frame rate allows using techniques such as lucky imaging, which might increase the angular resolution of the image helping in the discrimination and detection of the RSO. Further information concerning lucky imaging and variations thereof used in the domain of defunct RSOs are available e.g. in [5]. Finally, the second factor concerns the astrometric reduction of the data, which consists of the determination of the coordinates in the image with respect to a given reference frame, e.g. the International Celestial Reference Frame. Currently there are two possibilities: either to determine them on-the-fly if there are enough reference stars at the acquisition time, or to use the pointing information derived from the angular encoders in the telescope. Due to the narrow field of view available in current successful systems, the fact that we are targeting LEO RSOs, and that stars dimmer than an 8 apparent magnitude will not be easily discernible, the second option seems to be more attractive. The use of such a technique has been reported in [58, 63].

Laser beams of active electro-optical systems have fields of view of tens of arcseconds requiring extremely accurate ephemerides that are currently not available for most of RSOs. To compensate for this, one approach might be to use a passive aiding optical target acquisition system that will correct the pointing of the telescope to lock the RSO within the field of view of the laser beam. Once we ensure that we are collimating the laser beam on the RSO, the next challenge concerns discriminating the photons backscattered from the RSO, from the ones coming from the background, plus the ones produced by thermal current in the detector. At the system level, analysis of daylight active electro-optical systems can be found e.g. in [22, 82]. Note that the first reference alludes to RSOs carrying a highly reflective element on-board such a retroreflector; those RSOs are also known as cooperative RSOs, whilst the absence of highly reflective elements

on-board of the RSOs corresponds to the so-called non-cooperative RSOs. Successful retrieval of signal reflected by non-cooperative RSOs during daylight was presented in [71].

In this work, we study the impact of daylight observations at the level of information gain for the domain of defunct RSOs, and at the technical level particularized for the Swiss Optical Ground Station and Geodynamics Observatory Zimmerwald (SwissOGS), for which the capabilities have been extended to enable measurement acquisition during daylight with a passive and active electro-optical system. Specifically, we start with an in-depth analysis focused on the current geographic distribution of optical systems and their current available nighttime observation windows through one year. We then analyse the impact of observations for the defunct Environmental Satellite (ENVISAT), for which there is currently a substantial optical data gap for European ground-based observatories during the summer season. The impact of the data gap is addressed from the point of view of a full state vector comprising not only the orbital elements but the attitude state and its motion. At the technical level, we study the contribution of the diffuse daylight sky background in our optical systems. For both active and passive electro-optical systems, we quantify the signal to noise ratio, which permits to identify critical components, both in software and hardware, and allows us to identify RSOs in current existing catalogues for which we expect a high detection probability. Finally, we present raw measurements acquired by our systems stressing factors not directly accounted for during the analytical study of the signal to noise ratio, but rather from the knowledge acquired during an extensive experimental phase. In addition, we present a case study where the simultaneous observation of the RSO with an active and passive electro-optical system allowed us to partially disambiguate its tumbling motion after being tracked at the SwissOGS.

5.2 Impact of Daylight Observations in the Monitoring of defunct RSOs

In this section we present the potential benefits, achievable by current observing space surveillance and tracking networks, if enabling the acquisition of daylight observations. Within the scope of this study, we define surveillance and tracking as the capability of a sensor to retrieve observables of different nature to create, complete or refine RSOs orbits and attitude catalogues. Those catalogues will establish the basis for computing collision probabilities and the monitoring of RSO-specific attitude states. The number and type of observations, provided by the sensors, will play a crucial role for the estimation of the attitude of the targeted RSO, its evolution in time besides the estimation of realistic collision probabilities derived from updated state vectors using precise and accurate measurements; the latter being critical to e.g. perform efficient avoidance manoeuvres between RSOs. In the next subsections, we present three arguments that highlight the relevance of daylight observations in the framework of space surveillance and tracking.

5.2.1 Length of Day

In general, the observation of defunct RSOs with altitudes between 400 and 2000 km by a passive electro-optical system is restricted to the twilight zones, i.e. dusk and dawn. During these zones, the RSO is expected to be sunlit with a sufficient signal to noise ratio, thus enabling the discrimination of the RSO from the sky background. When using an active system such as laser ranging, the sunlit condition is not mandatory, but the rather small field of view of the laser beam demands high accuracy predictions, which are not usually available in the domain of defunct RSO. Hence, the system needs of a passive optical system for correcting the pointing of the telescope. Note that we exclude the possibility of blind tracking, i.e. the systematic search of the RSO according to a defined pattern, since, in principle, it will be dominated by luck. In the following, we study the relationship between the geographical distribution of current observing sites and the length of day in the pursuit of an extension of the current observing twilight time windows.

Most of the current dedicated ground-based optical ground stations are concentrated in the mid latitudes of the northern hemisphere. Examples of the distribution of such networks are given by the International Scientific Optical Network (ISON), for the passive electro-optical case, and by the International Laser Ranging Service (ILRS) for the active electro-optical; note that from the ILRS only selected stations are able to observe either cooperative RSOs during daylight, or non-cooperative RSOs with high power dedicated defunct RSOs lasers. Even though there are recent developments of tracking networks with a better geographical distribution, as the Small Aperture Robotic Telescope Network (SMARTnet), the productivity of such observing network is restricted mainly to night observation sessions. To better understand the impact of daylight observations, we show in Figure 5.1 the length of day in hours as a function of the day of the year starting from the winter solstice. The main problem becomes evident: the summer season for mid latitudes, both in the northern and southern hemispheres, is critical due to the long daylight hours. Enabling the daylight measurement acquisition capability will result in a significant production gain. Nevertheless, the relationship between available observing hours and actual useful observations is not straight forward for optical sensors. Critical factors involving the local weather, the configuration Sun-RSO-station and its evolution with respect to time, or even air-traffic (only for active electro-optical), could prevent the observation during certain timeslots within the available observing hours. To overcome the latter, planning algorithms must be developed to account for the aforementioned factors selecting within all possible available passes those yielding the highest probability of detection of the RSO.

5.2.2 Attitude Determination

Within the surveillance of the outer space, the information about the attitude state of RSOs, and its change in time, is critical for on-orbit servicing and active defunct RSOs removal initiatives. Those initiatives address the direct disposal of defunct RSOs via direct momentum transfer using either a space- or ground-based lasers [54], drag augmenta-

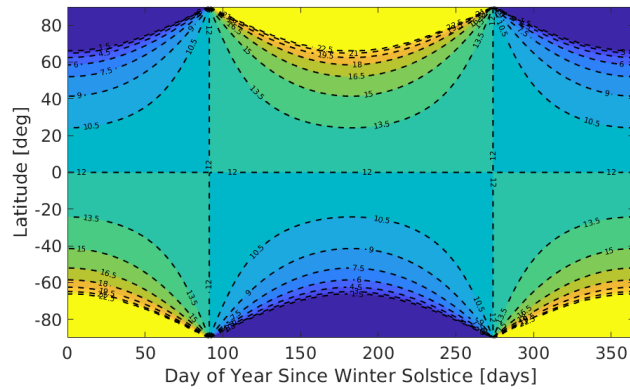


Figure 5.1: Length of day as a function of latitude and day of the year starting from winter solstice. The contour lines indicate the length of day, i.e. the elapsed time between the rise and set of the Sun.

tion devices in the form of foam or sales [2], or by using catching devices e.g. grapplers [50]. Other type of initiatives propose the on-orbit repairing, refuelling, stabilizing or even helping in the deployment of specific components that became unresponsive, such as antennas or solar panels [50]. Using either active or passive observing systems, we can retrieve evidence of the attitude state at each observation epoch, which is deemed critical prior information to any mentioned on-orbit servicing activities. Examples of attitude determination using passive optical systems can be found in [66]. Likewise, a comprehensive attitude study using only an active electro-optical system was reported in [55].

Successful observations conducted during daylight could provide additional information about the RSO's state, i.e. orbital elements and attitude motion. For all attitude-related analysis, this additional information may come either from the different illumination conditions, or from the observation at different aspect angles. In the following, we present one example that highlights the usefulness of daylight observations in the context of attitude determination.

The RSO ENVISAT has a specific orbit: a sun-synchronous polar orbit¹. The main characteristics of this orbital type are first that the orientation of the orbital plane with respect to the Sun remains constant in time and second, by being a polar orbit, it assures coverage of the entire globe. The two aforementioned features are attractive for Earth observation missions having equal on-ground illumination conditions per revisiting ground tracks of the satellite over same locations. Specifically, the orbital and body dynamics of ENVISAT are of interest due to its size and mass, but the development of potential contingency plans requires an updated state, i.e. orbital and attitude related up-to-date information. The retrieval of regular updates of its state is a missing gap during summer season for midlatitude northern nighttime optical observatories for

¹<https://earth.esa.int/eogateway/missions/envisat/description>

ENVISAT. There might be gaps of months impeding the determination of an updated state. To demonstrate the contribution of daylight observations, we show two passes of the decommissioned satellite ENVISAT that were successfully observed during daylight at the SwissOGS. The average frame rate of the passive electro-optical observations for both passes was of 5 frames/second. The exposure time used for both passes was of 0.01 seconds. Figure 5.2 shows the raw light curve of ENVISAT acquired on April 15, 2021, at 5:02 Coordinated Universal Time (UTC). From the upper plot in Figure 5.2 we can see periodicities that might correlate with the synodic period of the RSO; on the bottom plot we can see that the pass had a high culmination; in addition, the Sun was rising with an elevation of only 2.4° . Figure 5.3 shows the raw light curve of ENVISAT acquired on April 24, 2021, at 15:46 UTC. It is interesting to see how at the end of the light curve in Figure 5.3 the instrumental magnitudes depict more scattering, which may be explained by a lower signal to noise ratio due to an increase of the sky background. By comparing Figure 5.2 and Figure 5.3, we can see presumably different attitude states, or aspect angles, in each pass, further verified after detrending the raw measurements from the phase angle, station-RSO geometry and air mass effect as a function of the elevation. Furthermore, the illumination conditions are different since the observation geometry with respect to the illuminating source was different per each day. We estimated the synodic spin period using the detrended magnitudes using two methods: the Lomb-Scargle [78] and the Phase Dispersion Minimization (PDM) [73], using two different methods as cross-validation of our estimations. The spin periods estimated by both methods are shown in Table 5.1.

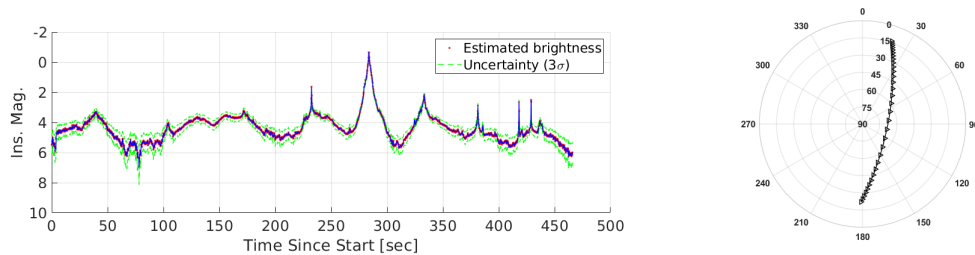


Figure 5.2: Light curve of ENVISAT observed on April 15, 2021, during daylight. The elevation of the Sun was 2.4° at the beginning of the observation time, i.e. at 5:02 UTC. The left plot shows the brightness variations of the RSO while crossing the SwissOGS. The geometry of the pass with respect to the observing station is shown in the right plot as azimuth and elevation in the horizon system centred at the SwissOGS.

Despite the results showed in Table 5.1, further observations are recommended to be carried out since the estimated synodic spin period corresponds nearly to half the total duration of the observed complete pass. To further disambiguate the tumbling motion of ENVISAT, neighbouring stations to the SwissOGS could track the RSO before, or after, observable passes, which will extend the total duration of each pass, i.e. a coverage of a longer arc, allowing to estimate the synodic spin period more reliably.

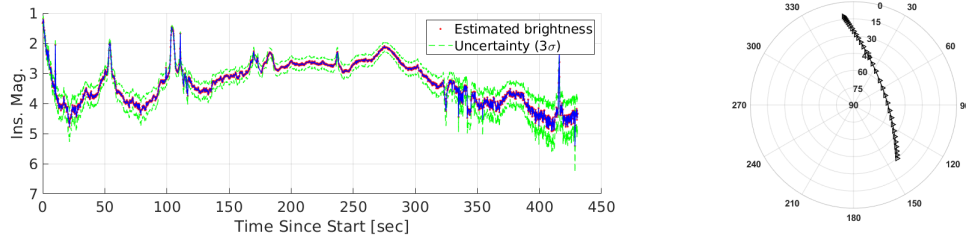


Figure 5.3: Light curve of ENVISAT observed on April 24, 2021, during daylight. The elevation of the Sun was 26.9° at the beginning of the observation time, i.e. at 15:46 UTC. The left plot shows the brightness variations of the RSO while crossing the SwissOGS. The geometry of the pass with respect to the observing station is shown in the right plot as azimuth and elevation in the horizon system centred at the SwissOGS.

Table 5.1: Estimated synodic spin periods of ENVISAT during daylight passes after detrending the light curves depicted in Figure 5.2 and Figure 5.3.

Pass	Lomb-Scargle	PDM
2021/04/15	230.5 ± 1 [s]	230.1 ± 0.1 [s]
2021/04/24	202.6 ± 1 [s]	226.7 ± 0.5 [s]

5.2.3 Observation Geometry and Orbital Arc

The impact of the observed orbital arc and the measurement type on orbit determination and improvement of defunct RSOs has been shown in [18]. Furthermore, studies focused on single-pass solutions varying the number and distribution of the observations within passes over the station at different culminations can be found in [57]. Note that we describe the length of the arc with respect to the revolution period. The results from the aforementioned studies highlight and recommend the observation of longer arcs, i.e. as long as possible, and data fusion between observables of different nature, i.e. angles and ranges, for an improvement in orbital accuracy of orders of magnitudes.

In this section, we focus on the observable arc from one single station, the SwissOGS, to perform a visibility study of the decommissioned satellite ENVISAT. We start by analysing the ground track of the satellite. The orbital parameters were extracted from the latest Two Line Element set available in². The orbital elements were propagated for 36 hours storing the state vector every 10 seconds. The resulting state vectors were transformed into the Earth-Centred-Earth-Fixed reference frame being represented as ground tracks in Figure 5.4. Likewise, we represent in magenta the tracks that are visible from the SwissOGS, which correspond to passes with a minimum elevation of 20 ° over the station. For the 36 hours of propagation there are 5 passes over the SwissOGS for a satellite with a revolution period of about 100.2 minutes. From all passes 4 out of 5 are ascending passes (south-north direction) and one is a descending pass; the latter is the longest observable pass from all. Figure 5.4 highlights the importance of a global tracking network since most of the revolutions are left untracked using only one station. For the monitoring of ENVISAT, the non-updated state vectors, due to lack of observations between revolutions, will change significantly in time due to gravitational and non-gravitational perturbations acting on a RSO flying at an altitude of about 770 km. Note that the non-gravitational perturbations, such as solar radiation pressure and air drag, will act on an average cross-section of 74 m². The poor predictions derived from the non-updated state vectors will challenge observatories to do follow-up observation strategies with limited field of view sensors, such as laser ranging systems.

Next, we check the observability conditions of those passes from the SwissOGS assuming a cloudless sky and dedicated passive and active electro-optical systems.

Figure 5.5 shows a sky plot corresponding to the 5 passes of ENVISAT that are visible from the SwissOGS. The beginning and end of the passes are marked with a cross and a dot respectively to indicate the flight direction. The five passes might be further classified into 3 high culmination passes (light and dark blue, dark red), and 2 low culmination (purple and yellow). The time of each pass is displayed in the box in Figure 5.5, from where we can immediately see that all available passes occur during daylight. Note that the low culmination passes will be significantly affected by extinction effects due to a larger air mass besides the attenuation due to larger distances of the RSO with respect to the station. To ensure the observability of any pass, we computed the position of the Sun over the SwissOGS at the starting epoch of each pass. Comparing the entries in Table 5.2 with Figure 5.5, we see that the observation conditions for the first pass

²<https://www.space-track.org>

are excellent, reaching a phase angle of about 0° at the culmination of the RSO. The observation of the second pass will be challenging since there is an inferior conjunction between the Sun, the RSO and the observer, i.e. a phase angle of nearly 180° shortly after the culmination of the RSO. For the third pass the alignment between the three bodies is in inferior conjunction, but the culmination of the pass by the RSO is nearly at the zenith, which gives an angular distance from the position of the Sun reducing the amount of sky background. The fourth pass has a similar configuration as described for the first pass. Finally for the fifth pass, there will an azimuthal encounter between the telescope and Sun, but a difference in elevation of about 30° . From all passes, it is reasonable to expect that during nearly inferior conjunctions, there will be a gap of observations due to the sky background contribution and large phase angles, which compromise the amount of signal to noise ratio on the observation site.

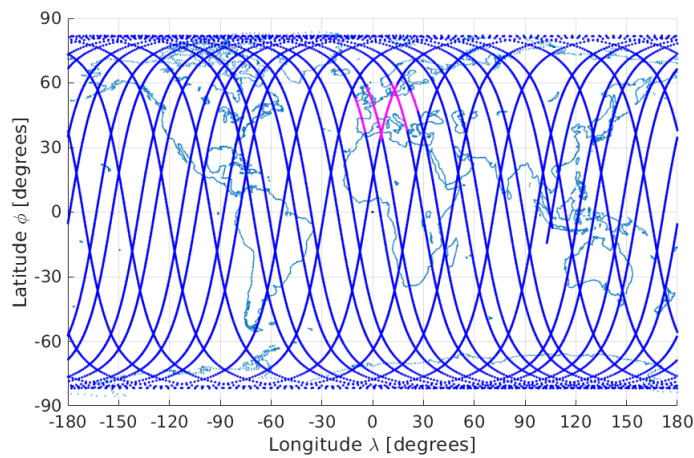


Figure 5.4: Ground track of ENVISAT starting on July 28, 2021, at 10:00 UTC until July 29, 2021, at 22:00 UTC. The orbital elements were extracted from the latest TLE available from space-track at starting date. The segments of the track represented in magenta represent the portion of the orbit observed from the SwissOGS using an elevation mask of 20° .

From this analysis we can conclude that for daylight observations, the observation geometry plays a critical role. The impact of the atmosphere, distance between satellite and station and phase angle, both from the illumination and sky background contribution, will determine the observability of the pass. Nevertheless, the observation during daylight using passive and active optical systems will allow to monitor arcs of the orbit of ENVISAT, which otherwise would not be accessible.

Table 5.2: Horizontal coordinates of the Sun at the starting epoch of visible passes for ENVISAT over the SwissOGS.

Start pass UTC	Azimuth [deg]	Elevation [deg]
2021-07-28T15:13:20	256.529	37.901
2021-07-28T16:53:20	275.565	20.912
2021-07-29T04:57:40	70.200	7.140
2021-07-29T14:38:40	248.465	43.376
2021-07-29T16:15:10	268.520	27.260

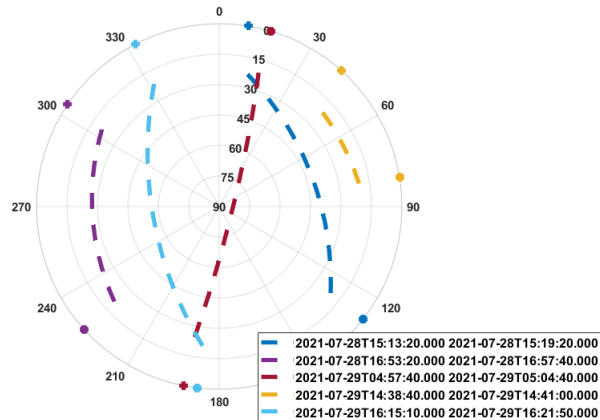


Figure 5.5: Sky plot centred at the SwissOGS for ENVISAT starting on July 28, 2021, at 10:00 UTC until July 29, 2021, at 22:00 UTC. The hours of each pass are shown at the bottom-right of the plot in UTC. The beginning and end of the pass are marked with a cross and a dot respectively to indicate the flight direction.

The last part of this subsection focuses on the length of the observed arc and its distribution along the orbit of ENVISAT. Figure 5.6 represents each potential observable pass at the SwissOGS (Figure 5.5) in the orbit reference frame. The highest culmination passes shown in Figure 5.5 cover not only the largest portion of the orbit in Figure 5.6, but also have a better distribution over the orbit. On the other hand, all except the longest arc, fall into nearly the same portion of the orbit. The consequence of using only passes over the same portion of the orbit is that the predictions for stations observing that portion will most likely be better than for the ones observing in the opposite portion of the orbit.

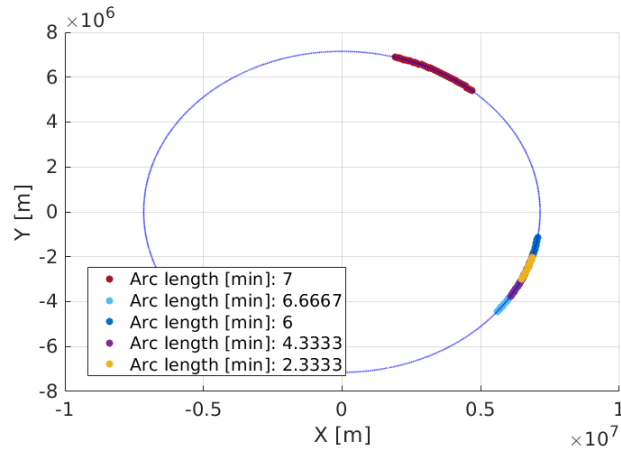


Figure 5.6: Observed orbital arc in Figure 5.5 represented in the orbit reference frame. Colours match with the passes displayed in Figure 5.5.

It becomes clear, by the analysis of the observation geometry, the arc length and the distribution of observations along the orbital arc that a tailored observation session can be optimized to maximize the productivity yet achieving high quality observations. The latter are crucial for an orbit determination or improvement, which will permit the re-acquisition of the RSO by the same or other observing stations. For the case of observations from ENVISAT from one single station, two passes corresponding to ascending and descending observable passes cover the largest portion of the orbit with the best distribution of observations. However, the other passes could be useful for attitude state analysis since the illumination conditions and aspect angles are different.

5.3 Background Noise

In the previous section we showed the benefits of conducting daylight observations for the monitoring of defunct RSOs in the context of space situational awareness. In this section, we will analyse the impact of daylight observations, at the receiving sensor level, for passive and active electro-optical systems. After a generic analytical description of the daylight radiation for each system, we describe newly implemented system components, or modification on previous ones, at the SwissOGS to mitigate its impact. Finally, we provide recommendations and insights based on the experience gained during an experimental phase.

5.3.1 Solar Photon Budget

The number of photons that we receive on the Earth is the resulting superposition of the radiation reflected or emitted from all extraterrestrial bodies, being the latter a function of their own temperature. The distribution of the spectral flux density, while in thermal equilibrium and assuming an ideal black body radiator, is given by Planck's law. The

closest radiating source to the Earth is the Sun, which is at about 5,772 K³. Studying how the generated radiation will propagate interacting along its path with a defined medium, we can derive estimates of the number of photons that we will receive on ground for a given integration time. The body of knowledge studying the aforementioned radiation, its interaction and propagation within a medium is the radiative transfer theory. In the following, we will use the so-called direct-diffuse splitting of the radiance field. The mathematical formalism from which we will support the following work can be found in [83].

Fixing physical boundaries from ground up to the top of the atmosphere, physical processes of emission, absorption and scattering occur along the atmosphere. In order to know the amount of photons that will arrive at the receiver site, we solve the radiative transfer equation (RTE). The solution of the radiative transfer equation is not trivial and depends heavily on the parametrization of the type of molecules or atoms present in the atmosphere, their distribution and concentration, besides the temperature and pressure profiles as a function of the altitude. In particular, we consider only extinction processes, i.e. scattering and absorption, in the propagation of the solar radiation. Current available models that represent atmospheric radiation propagation solve the RTE numerically using a parallel spherical multilayer approach. The numerical library used for the retrieval of the solar radiation at observation site is the LOW-resolution-atmospheric-TRANsmision software package based on the code provided in [44] further enhanced with the new modules provided in [45].

In Figure 5.7 we show the theoretical distribution of the spectral flux density according to a black body in thermal equilibrium at a temperature of 5,772 K, the resulting distribution of the solar irradiance on the top of the atmosphere (100 km altitude) and the distribution of the solar irradiance on ground.

³<https://nssdc.gsfc.nasa.gov/planetary/factsheet/sunfact.html>

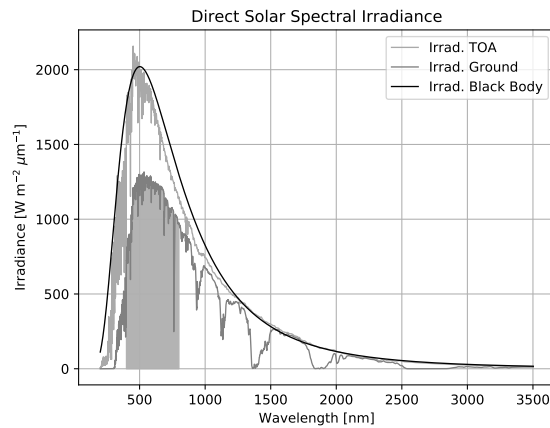


Figure 5.7: Distribution of the direct solar spectral flux density according to a blackbody radiator, on top of the atmosphere (TOA) and on ground. The last two curves were extracted using the LOWTRAN7 software package [45]. The filled area under the curve represents the total amount of direct solar intensity in the visible domain [400 nm, 800 nm] yielding a total integrated value of 366 W/m^2 .

The parametrization of the medium through which the solar radiation propagates considers: a macro atmospheric mid latitude winter model, molecular constituents such as water vapour, ozone, methane, nitrous oxide and carbon dioxide, among others using updated profile distribution with respect to the altitude, winter temperature and pressure altitude profiles and a local rural extinction model with a visibility of 23 km (selected after being the nominal visibility at the SwissOGS during cloudless days). One of the main interesting features in Figure 5.7 is the actual fluctuating solar flux on top of the atmosphere in the ultraviolet region of the solar spectrum. This behaviour may be explained by the modelled extinction physical processes occurring as a function of size, content and distribution of the defined molecules and the wavelength of the interacting radiation, in that specific region, for a variable layer length of 1 m. Once in the visible domain, the irregularities progressively diminish as a function of longer wavelengths. The spectral lines of emission and absorption due to the interaction of the incident radiation with specific molecular constituents are explained in detail e.g. in [83].

For the validation of the retrieved spectral flux density on top of the atmosphere, we compare our solution against the current value for the so-called *solar constant* of 1360 W/m^2 [12]. To do so, we integrate our retrieved distribution from 250 nm until 3500 nm, the solar spectrum, using the Simpson's numerical integration scheme. Our result yields 1327 W/m^2 , showing an error of 2% compared to the standard reference. That difference might come from the spatial resolution of the models described before and the resolution used by Lowtran (5 cm^{-1}), which also have an impact on the integration error. Nonetheless, for our application the committed error is tolerable. The validation of the spectral flux density on ground was done by comparing the transmission curves obtained

for specific testing cases using the calibrated models provided in [44, 45]. Finally, after the integration of the solar irradiance on ground, the total direct solar flux on ground yields a value of 366 W/m^2 . Note that the direct solar flux accounts only for the attenuation, i.e. deems only absorption processes of the direct solar beam incident upon the atmosphere of the Earth. The diffuse radiation component depends on the angular distance θ with respect to the normal of an infinitesimal irradiated area, obeying the well-known Lambertian model. In Figure 5.8 we show the calculated diffuse radiation component for an angular distance θ of 45° . Here we assume an elastic multiscattering model, i.e. we do not consider the variations on wavelength due to Doppler broadening and we consider that the scattering occurs more than once within one single layer. The larger scattering occurs in the blue region of the solar spectrum confirming the known Rayleigh scattering, which explains why the sky looks blue during daylight. This regime considers that the particle has a size significantly smaller (λ^{-4}) than the wavelength of the incident wave [10]. Note that when the size of the particle is comparable to the wavelength of the incident wave, the physical phenomenon is described by Mie scattering [83]. In addition, optical sensors observing in the near-infrared spectral regime will have a lower sky background contribution. After the integration of the distribution of the diffuse solar spectral radiance on ground, we get a total of $40 \text{ W/m}^2\text{sr}$. From here onward, we will consider only the diffuse solar radiance distribution on ground, since the direct observation of the Sun is certainly avoided in our routinely RSO observations.

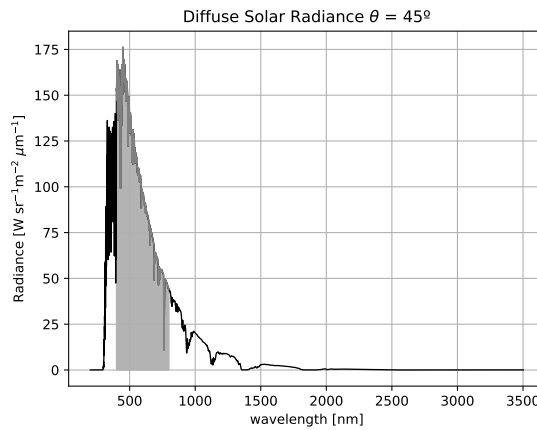


Figure 5.8: Distribution of the diffuse solar spectral flux density on ground at an angular distance of 45° . The filled area under the curve represents the total amount of diffuse solar intensity in the visible domain [400 nm, 800 nm] yielding a value of $40 \text{ W/m}^2\text{sr}$ after numerical integration.

5.3.2 Mitigation of Background Noise in Passive Electro-Optical Systems

Once we have a model that quantifies the spectral diffuse solar radiance, we can derive the observed number of solar photons per unit time at a given direction for a passive

electro-optical system using the following equation:

$$B_p = \int_{400}^{800} Q(\lambda)_{eff} \eta_{rx} \Omega_{rec} \cos(\theta) A_{rec} B(\lambda)_{diff} d\lambda, \quad (5.1)$$

where B_p in watts is the diffuse solar radiance measured on the passive optical receiver, $Q(\lambda)_{eff}$ is the quantum efficiency of the sensor as a function of the wavelength, η_{rx} is the efficiency of the imaging system, i.e. the receiving optical chain, $\Omega_{rec} \cos(\theta)$ in sr is the field of view of the sensor; the factor $\cos(\theta)$ is included since the power received at an angle to the normal is proportional to Ω_{rec} in a unit sphere, and therefore to the cosine of that angle θ , as per Lambert's cosine law. A_{rec} in m^2 is the effective aperture area of the telescope, and $B(\lambda)_{diff}$ in $\text{W}/\text{sr m}^2 \mu\text{m}$ is the on ground spectral solar radiance. In order to estimate the expected photoelectrons triggered by the diffuse solar spectral radiance on the receiver, we solve Equation 5.1 numerically using the same scheme explained at the beginning of the section to validate the solar constant. All system specifications were described previously. Finally, for the estimation of the number of counts in terms of photoelectrons per wavelength, we transformed from watts to photons/sec and consider an integration time of 0.01 seconds. The retrieved counts per wavelength are shown in Figure 5.9. After the integration, we estimated a total theoretical number of counts of 31,547 and 16,043 per imaging pixel, without and with the use of a broadband rectangular filter between 400 and 500 nm, respectively. To validate the previous theoretical estimates, we conducted daylight observations to stars with angular distances of nearly 45° with respect to the Sun for consistency with the values used for the theoretical modelling. From the measurements acquired to different stars, the estimated background level in terms of counts per pixel was measured to be 34,248 and 38,420 after conversion between analog-to-digital units to photons using the gain of the device. Note that the measurements to stars were taken without the broadband rectangular filter. From this first validation, we conclude that the modelling of the sky radiance is in good agreement showing an average error of 13 % with respect to our measured value, which was cross-validated using two different stars. In a second step, we estimated fluxes via aperture photometry for both stars, and by using the standard value of the surface brightness per each reference star, we derived the relative magnitude per square arcsecond between the reference star and background yielding $\Delta_{star_1}^{bck} = -0.8$ for the reference star of 2 magnitudes per square arcsecond and $\Delta_{star_2}^{bck} = 3.5$ for the reference star of 6.5 magnitudes per square arcsecond. The average background surface brightness was estimated to be of 2.9 magnitudes per square arcsecond, which is in agreement with the values found in the literature [11].

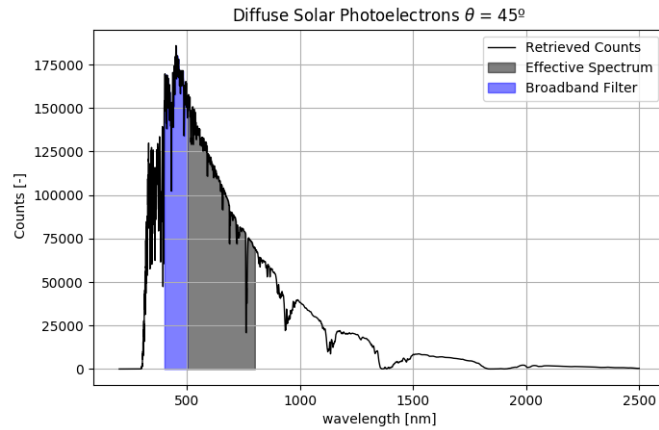


Figure 5.9: Count of triggered photoelectrons after incident solar diffuse spectral radiance on the receiver using an integration time of 0.01 seconds. The plot shows the area removed by using a spectral broadband rectangular filter from 400 nm to 500 nm, and the remaining portion of the visible spectrum. The diffuse solar radiation direction is that of 45° away from the direct incidence.

It is foreseen that a thorough campaign will be conducted to account for more stars distributed along the horizon, tests with and without filter, and for different positions of the Sun over the local horizon.

To find the limiting observable magnitude, we use the calculated magnitude of the daylight sky background and we computed the percentage of incoming starlight varying the magnitude of stars as done in [70]. In our computations, we allow for variations in the surface brightness of the background from 2 up to 8 magnitudes per square arcsecond. Furthermore, using the atmospheric seeing [10] as a first-order approximation of the resulting point spread function of the star in the image plane, we can derive the limiting surface brightness for daylight observations as shown in Figure 5.10. Note that in Figure 5.10 an atmospheric seeing value of 2 arcsec was chosen, since it is the average seeing at the SwissOGS. Worse seeing conditions, which are expected during daytime, will set the limiting observing magnitude to brighter values.

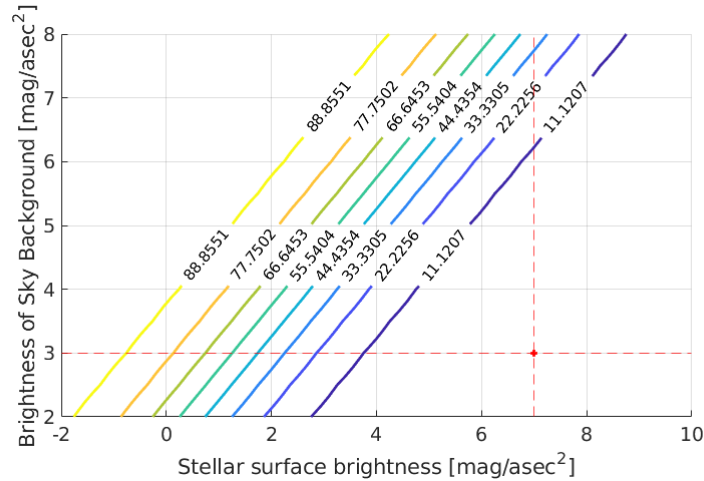


Figure 5.10: Percentage of incoming starlight as a function of the daylight sky background with surface brightness ranging from 2 to 8 magnitudes per square arcsecond and stars within a surface brightness range from -2 to 10 magnitudes per square arcsecond. The dashed red lines indicate the limiting surface brightness for a daylight sky background of 2.9 magnitudes per square arcsecond; it shows that up to stars with a magnitude per square arcsecond of 7 , the percentage of incoming starlight is larger than 1 %.

According to Figure 5.10, we are limited to detect RSOs fainter than a magnitude per square arcsecond of 7 for daylight observations with a sky background contribution of 2.9 magnitudes per square arcsecond, since the amount of incoming starlight is less than 1 %, a value found through empirical experimentation for recognizing the RSO on the image by the naked eye. First results after observing stars with varying magnitudes were presented at the ILRS Technical Workshop on October 2019 showing good agreement with the theoretical findings [16].

Finally, after inspection of Equation 5.1 combined with the experience gained by analysing real observations, we propose mitigation strategies for reducing the impact of the diffused solar photons on passive electro-optical observing systems. First, the use of a blocking filter from 400 nm up to 500 nm can reduce the impact of the resulting diffuse solar photons on the receiver by changing the lower limit of integration in Equation 5.1 from 400 to 500 nm. The implementation of this type of broadband filter attenuates the largest sky background contribution (see Figure 5.9) compared to the amount of sunlight reflected by the RSO assuming that the RSO does not have favourable optical properties between 400 and 500 nm (see spectral signature examples of different RSO in [77]). Second, in Equation 5.1 we see that the on-site sky background radiance is proportional to the field of view. Likewise, the field of view is inversely proportional to the focal length, therefore by using a larger focal length, we reduce the field of view, thus the contribution of the sky background on the detector. Finally, the observation of passes in inferior conjunction must be avoided to avoid the saturation of the sensor,

or the implementation of a manoeuvre while observing the remaining part of the pass should be executed. In our system that feature is implemented at the software level as the minimum angular distance between the pointing direction and the position of the Sun in the sky currently set up at a minimum value of 25 °.

5.3.3 Mitigation of Background Noise in Active Electro-Optical Systems

The fact that laser pulses are generated in a specific wavelength, i.e. monochromatic light, pointing directly to the RSO with a defined beam divergence, i.e. collimated beam, enables the design of a receiving optical chain centred on that specific wavelength. The estimation of triggered photoelectrons from the diffuse solar photons collected by the receiver particularized for a specific wavelength, in our case 532 nm after frequency doubling of the fundamental 1,064 nm, reads:

$$B_{A_{532}} = \int_{532-0.05}^{532+0.05} Q(\lambda_{532})_{eff} \eta_{rx} \Omega_{rec} \cos(\theta) A_{rec} B(\lambda_{532})_{diff} d\lambda, \quad (5.2)$$

where the only difference with respect to Equation 5.1 is that we take the diffuse solar radiance and quantum efficiency at that specific wavelength of 532 nm, and the limits of integration correspond to the spectral width of 1 angstrom from the used narrowband filter. In addition, the emitted laser pulses are shifted in wavelength due to the relative motion of the RSO with respect to the tracking station, natural broadening, Doppler broadening – in this case due to the thermal motion of the radiating source – and collision broadening, but fall into a second order change in the emitted wavelength if compared to the width of the employed narrow band filter.

In Table 5.3 we show the diffuse solar flux at 532 nm, varying the angular distance θ between the pointing of the telescope and the location of the Sun in the sky over the station. Taking $\theta=10^\circ$ as a worst-case scenario, we calculate by solving Equation 5.3

Table 5.3: On-receiver diffuse solar radiance at 532 nm.

	$B(\lambda_{532})_{diff}$
$\theta = 10^\circ$	219 W/sr m ² μm
$\theta = 45^\circ$	81 W/sr m ² μm
$\theta = 60^\circ$	68 W/sr m ² μm

a mean diffuse solar photoelectron flux rate of 21 MHz. The most favourable scenario, $\theta=60^\circ$, yields photoelectron rates of 3 MHz. Our findings were validated with the values provided in [22]. Note that during daylight, the dark counts (≈ 120 kHz) are negligible compared to the observed rate of photoelectrons triggered from the sky background.

The solar photoelectrons will affect the identification of the backscattered photons from the RSO, being more critical for RSO that do not carry retroreflectors on board, i.e. non-cooperative RSOs.

All recommendations given for passive-optical systems apply also for active ones. The only difference regarding blocking filters is that for active systems we use narrowband filters instead of the broadband blocking ones. The reduction of the field of view was implemented through an iris of variable aperture with an adjustable diameter between 10 and 40 arcseconds. In addition, it becomes clear, after inspection of Figure 3.11, that the use of the 1,064 nm wavelength has a significant lower diffuse solar radiation contribution. Finally, by using a gated receiver, we can further reduce the impact of solar photons by setting small range gates, i.e. temporal windows, at the expected return epoch of the emitted pulse, however, in order to fully exploit that capability accurate ephemerides are needed, which is usually not the case with defunct RSOs.

5.4 Signal

Having in mind that the ultimate goal of daylight observations is the detectability of the RSO, we focus fundamentally on the signal to noise ratio using its definition for both active and passive systems as provided in [36]. In the previous subsection, we assessed the impact of the background noise on the receiver, neglecting terms such as the dark counts, read out and digitization noise of the used receiving sensors due to their order of magnitude compared to the background noise. Likewise, factors that contribute to the amount of signal available are the type of RSO, e.g. spent upper stage or decommissioned satellite, its size, shape, optical properties, orbital regime, the phase angle, the observation geometry of the pass, aspect angle and the observation epoch. Note that in case of active systems, we can expand the previous factors with those accounting for the energy of emitted pulse, pointing accuracy and divergence of the laser beam.

5.4.1 Minimum Observable RSO

To derive the minimum observable RSO size, we divide the analysis into: geometrical cross-section, orbital regime, optical properties of the targeted RSO, in particular the albedo and the reflectance, and the detection capabilities by a passive and active electro-optical system. In the case of passive electro-optical systems, the reflected radiation by a RSO illuminated by the Sun is given by [25]:

$$E_{rso} = \frac{E_0 \pi \sigma_{rso} \phi(\Theta) \rho \alpha}{16\pi R_{sln}^2}, \quad (5.3)$$

where E_{rso} is the reflected radiation by the RSO in W/m^2 , E_0 is the incident direct radiation from the Sun in W/m^2 , σ_{obj} is the cross section of the RSO in m^2 , R_{sln} is the slant range of the RSO with respect to the observing station in m, $\phi(\Theta)$ is the phase function, with Θ as phase angle, in radians, ρ is the albedo of the RSO and α is the reflectivity. By using the apparent magnitude of a known star, in this case the Sun, we can derive the relative magnitude using the expression:

$$M_{rso} = M_{sun} - 2.5 \log\left(\frac{E_{rso}}{E_0}\right), \quad (5.4)$$

where M_{sun} is the the apparent magnitude of the Sun within the visible spectrum of -26.74 and M_{rso} is the apparent magnitude of the RSO of interest. By combing and rearranging Equation 5.3 and Equation 5.4, we can derive photon rates as a function of the RSO cross section and slant range yielding the following expression:

$$\sqrt{\sigma_{rso}} = R_{sln} 10^{\frac{M_{rso} - M_{sun} - 2.5 * \log(16.10^{-10} \phi(\theta) \rho \alpha)}{-4.5}}, \quad (5.5)$$

where σ is the radius corresponding to the geometrical cross section of the RSO in cm^2 (to keep the dimensional analysis consistent, the constant factor includes the transformation from square meters to square centimetres), R_{sln} is the slant range in km and M_{rso} the apparent brightness of the RSO. Taking an average albedo of 0.05 [34], a near zenith pointing and an elevation of 30° for the elevation of the Sun, which yields $\phi(70) = 0.11$ rad, the minimum observable defunct RSO with an apparent magnitude of 7 at 400 km is of 28 cm radius. At 2000 km the minimum observable RSO has a radius of 1.4 m.

For the estimation of the minimum observable RSO size using an active system, we make use of the so-called radar link equation [21]:

$$E_{rx} = \frac{E_{tx} G_{tx} \sigma_{rso} A_{rec} \eta_{tx} \eta_{rx} \eta_{qe} T_{atm}^2}{(4\pi R_{sl}^2)^2}, \quad (5.6)$$

where E_{rx} is the expected power measured at the receiver in watts, E_{tx} is the emitted power in watts, G_{tx} is the unitless transmission gain, σ_{rso} is the cross-section of the RSO in m^2 , A_{rec} is the receiver aperture effective area in m^2 , R_{sl} is the slant range station-RSO in m, η_{tx} is the efficiency of the transmission in the optical chain, η_{rx} is the efficiency of the receiving optical chain, η_{qe} is the quantum efficiency of the detector, and T_{atm} is the one-way atmospheric transmission. Note that Equation 5.6 may be transformed into the sum of all the previous factors if transformed into decibels, which is a format often used by the radar community. In addition, Equation 5.6 assumes that the distance between RSO and an observing station, besides the atmospheric conditions, did not change significantly within the round trip of the signal, either for antennas, or telescopes, working in a monostatic configuration, i.e. same telescope for transmitting and receiving the signal. For bistatic or multistatic configurations those assumptions must be revised.

The next question will be: how can one determine a photon budget for any RSO if there is presumably no knowledge of its cross section? To answer this question, we use a different approach: selecting a cooperative RSO with known optical cross section, sufficiently large sample of observations, e.g. one year, and the technical specifications of the station, we can calculate its expected return rate by solving Equation 5.6. Likewise, we set up the equation for the RSO. Having the two equations, we divide the budget equation particularized for the cooperative RSO into the budget equation for the non-cooperative one. We can then solve for the optical cross section of the RSO. The quotient of the two photon budget equations yields:

$$\frac{E_{rx}|_{lag}}{E_{rx}|_{rso}} = \frac{R_{rx}|_{lag}^4 \sigma_{lag}}{R_{rx}|_{rso}^4 \sigma_{rso}} \zeta, \quad (5.7)$$

where $E_{rx|lag}$ is the expected return rate in photoelectrons per second for the reference RSO, e.g. the Laser Geodynamics Satellite 1 (LAGEOS-1) and $E_{rx|rso}$ for the RSO, $R_{rx|lag}$ and $R_{rx|rso}$ correspond to the slant range to both LAGEOS-1 and the RSO in km, σ_{lag} , σ_{rso} are the cross-sections for LAGEOS-1 and the RSO in m^2 and ζ is the ratio between the gain as a function of configuration parameters, which may change per RSO, such as beam divergence, pointing accuracy, tracking jitter, etc. To solve for σ_{rso} in Equation 5.7, the parameters that have to be fixed are $E_{rx|rso}$ and $R_{rx|rso}$. Note that the value plugged in $E_{rx|rso}$ is defined mainly by the threshold used to discriminate the signal from the noise, which can be formulated using only the knowledge from the noise (see Equation 5.3). Fixing $E_{rx|rso}$ to 2 photoelectrons per second, and setting $E_{rx|lag} = 7$ photoelectrons per second from the estimated return rates for LAGEOS-1, we calculate the estimated cross-sections of RSOs with varying altitudes at different elevation angles as shown in Figure 5.11.

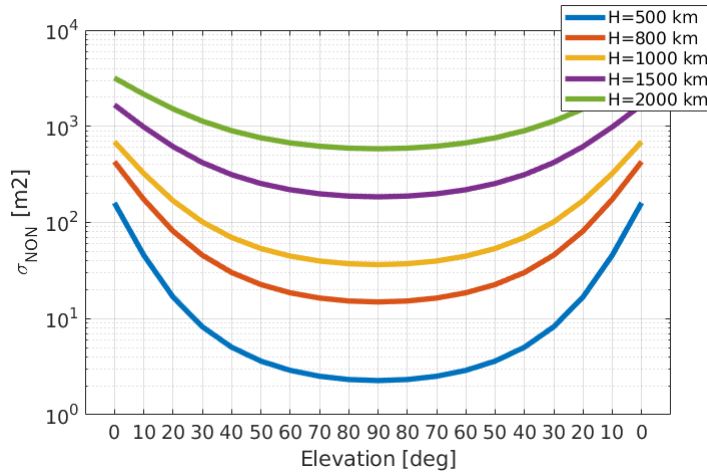


Figure 5.11: Minimum observable cross section as a function of altitude for a expected return rate of 2 photoelectrons/second derived relative to the measured return rates of 7 photoelectrons/second using one year of observations to the LAGEOS-1 satellite.

For the correct interpretation of Figure 5.11, several considerations must be deemed. First, in Equation 5.7 if $\zeta = 1$ the system configuration, i.e. beam divergence and output power is exactly the same for both reference (LAGEOS-1) and relative RSO. Nevertheless, the pointing to LAGEOS-1 is favoured due to the availability of accurate ephemerides besides the geometrical shape and dimensions of the RSO. For ranging to defunct RSOs, we enhanced the pointing of the telescope using a passive electro-optical system, which permits us to collimate the laser beam on the RSO using active tracking. Second, the reference RSO was chosen to be LAGEOS-1 since return rates higher than 10 % are further attenuated, via a variable neutral density filter on the receiving optical chain, which is the usual scenario when observing LEO RSOs with our system. The resulting effect will hide the elevation dependency, which has a clear impact on the

observed return rate. Third, the trend in the observed minus computed measurements coming from the use of inaccurate predictions is neglected. The latter will affect in finding the actual trace of photoelectrons coming from the RSO with respect to the ones triggered by the background diffuse solar photons. In addition, Figure 5.11 highlights that high culmination passes, i.e. passes with a culmination at an elevation higher than 50° , for orbital altitudes between 500 and 800 km will maximize the return rates for the observing station. Considering the population of RSOs, the previous information represents an optimal filter for non-dedicated observing stations.

5.4.2 Signal Strengthening

In passive electro-optical observing systems, the signal may be enhanced through the observation of larger RSOs or better illumination conditions; changes in the receiving system will contribute to enhancements on the sky background contribution as well. In the active case, we can analyse the laser output power to increase the backscattered signal reflected by the RSO. After inspecting Equation 5.6, given an emitted power E_{tx} , the received power E_{rx} , coming from a monochromatic, highly directed radiation beam, is proportional to the inverse of the solid angle subtended by the intersecting RSO with the beam. Considering the two-way radiation path, and assuming the same distance station-RSO, one derives the free-space loss, which is proportional to the inverse of the forth power of the distance station-RSO. The impact of the free-space loss for an orbiting satellite at an altitude of 1000 km is in the order of 10^{-24} . Furthermore, assuming ideal transmit-receiving optical chains, atmospheric transmission, an effective area of 1 m^2 , and an optical cross section of 1 m^2 , after the emission of 1 W , the received power is $8 \cdot 10^{-14} \text{ W}$. Subjected to the previous premises, we can strengthen the budget by including the transmitting gain G_{tx} , which may be computed rigorously to account for off-axis intensity distribution and obscured telescope apertures. Assuming that the laser source is operating in the lowest cavity mode, i.e. TEM00, and that the antenna gain patterns are measured in the far field, the transmitting gain can be expressed as [43]:

$$G_{tx} = \frac{2}{\pi R_{sl}^2 \theta_{div}^2} e^{-2 \frac{\theta_{div}^2}{\theta_{poi}^2}} \quad (5.8)$$

where θ_{div} is the beam divergence, θ_{poi} is the pointing error and R_{sl} is the slant range. To understand the impact of the pointing error and beam divergence, we compare the ratio between Equation 5.8 and a unit power spherical radiator:

$$\frac{1}{4\pi R_{sl}^2}. \quad (5.9)$$

The results are shown in Figure 5.12 varying the pointing accuracy and beam divergence.

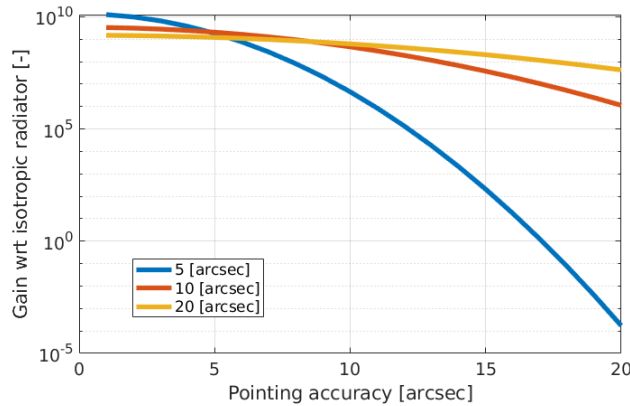


Figure 5.12: Antenna gain as a function of beam divergence and pointing accuracy with respect to a unit power isotropic radiator.

The conclusion is clear: the use of minimum beam divergence when the pointing of the telescope is inaccurate affects severely the transmitting gain and therefore the received power. Following the previous conclusion, potential recommendations to mitigate the laser pointing error are: first, in the near field verify the alignment between the peak of the laser beam profile and the optical axis of the passive acquisition telescope. Second, we model the alignment of the optical axis of the passive acquisition telescope with respect to the maximum laser system response in the far field by observing geodetic cannon-like satellites at distances larger than 3,000 km, from which the observing station has a history of high return rates of passes with varying relative geometry between RSO and station. Third, if the RSO is sunlit, the use of a tracking camera might help to collimate the laser beam on the RSO.

5.5 Observation: Signal-to-Noise Ratio

So far we have developed the conceptual hardware basis to optimize the observation of RSOs during daylight for both passive and active electro-optical systems including the impact of the observation conditions and the RSO's characteristics. In this section, we present examples of daylight observations to defunct RSOs acquired at the SwissOGS. Moreover, we will present one case study when we were able to acquire simultaneously angular measurements, ranges and brightness from a rocket body.

5.5.1 Passive Observations

In Figure 5.13 we show two raw frames acquired for three RSOs: TanDEM-X and TerraSAR-X (top plot in Figure 5.13) and the Zenit-2 second stage (Zenit-2M) (bottom plot in Figure 5.13), with Copsar identification numbers 2010-030A, 2007-026A and 2007-029B, respectively. The presented RSOs have radar cross sections of 2.5, 2.4 and 9 m², and altitudes of 515, 515 and 850 km as retrieved from space-track. Note that

in spite of TanDEM-X and TerraSAR-X being not decommissioned satellites, they show the potential capability for tracking close approaches between RSO that could occur as a result of relative formation flying for active defunct RSOs removal or in-orbit servicing initiatives. The measurements for the top plot in Figure 5.13 were acquired on August 28, 2019, at 16:52 UTC and for the bottom plot in Figure 5.13 were acquired on October 16, 2019, at 10:49 UTC. For both days the apparent position of the Sun was that of 244° , 33° , and 139° , 25° in azimuth and elevation respectively. The exposure time for the top plot in Figure 5.13 was set to 0.02 seconds, while for the bottom plot was set to 0.04 seconds.

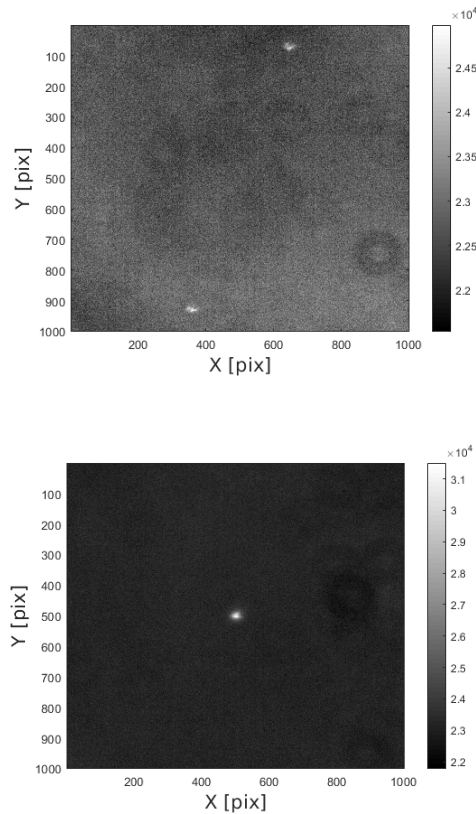


Figure 5.13: Examples of subframes acquired during daylight for TanDEM-X and TerraSAR-X (top plot) and the second stage Zenit-2 (bottom plot). The RSOs were observed on August 28, 2019, at 16:52 UTC (top) and on October 16, 2019, at 10:49 UTC (bottom). For both days the apparent position of the Sun was that of 244° , 33° , and 139° , 25° in azimuth and elevation respectively. Units of colorbars: Analog-Digital Units (ADU).

The extracted averaged number of counts per pixel for TanDEM-X (upper RSO in top plot in Figure 5.13) and TerraSAR-X (bottom RSO in top plot in Figure 5.13) was 488 and 421, respectively. On the other hand, the background in terms of counts per pixel for both RSO was found to be of 22,470 and 22,988, which clearly shows the

dominance of the brightness of the daylight sky background. Nevertheless, for the used exposure time for this frame only 38 % of the dynamic range was used, suggesting that we could further enhance the signal to noise ratio. To provide a better insight from the previous calculations, we show in Figure 5.14 and Figure 5.15 the estimated apertures for both source and background, with the normalized intensity profile as a function of the estimated centroid (further details could be found in [58]). From the point of view of the representation of the point-like source on the image plane, we see in both Figure 5.14 and Figure 5.15 speckles caused chiefly due the short exposure time and the fast changes in the refractive index of the atmosphere. Considering the intensity profiles, we can see how scattered the observed pixels are with respect to the retrieved point spread function. The explanation is given by the low signal to noise ratio.

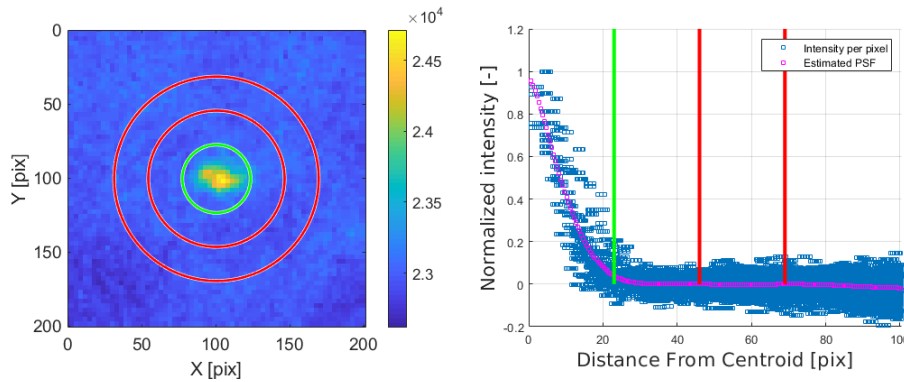


Figure 5.14: Left plot: RSO image and estimated apertures on the image plane; the green circle represents the aperture for the source TerraSAR-X, while the red annulus represents the area sampled to estimate the background. The unit of the colorbar is given in ADU. Right plot: normalized intensity profile as a function of the estimated centroid with the resulting estimated point spread function.

The extracted number of averaged counts per pixel for Zenit-2M is 1,514. Likewise, the counts per pixel from the sky background were estimated to be of 23,280, which still shows a dominant sky background per pixel, but with higher signal content for the source if compared to the previous case. The dynamic range in this case is of 47% of the total available, suggesting that we could have increased the exposure time to better exploit the different grey levels given by the 16 bit radiometric resolution of the sensor. In Figure 5.16, we show the results provided by aperture photometry with the corresponding radial profile intensity distribution. If compared with the ones in Figure 5.14 and Figure 5.15, the representation of the point-source on the image plane is rather symmetrical and homogeneous. The intensity profile shows less scatter than the previous examples, due to the signal to noise ratio further enhanced by a longer exposure.

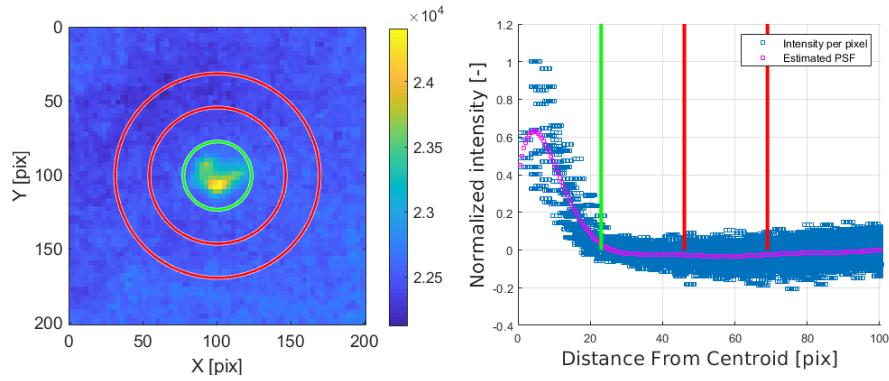


Figure 5.15: Left plot: RSO image and estimated apertures on the image plane; the green circle represents the aperture for the source TanDEM-X, while the red annulus represents the area sampled to estimate the background. The unit of the colorbar is given in ADU. Right plot: normalized intensity profile as a function of the estimated centroid with the resulting estimated point spread function.

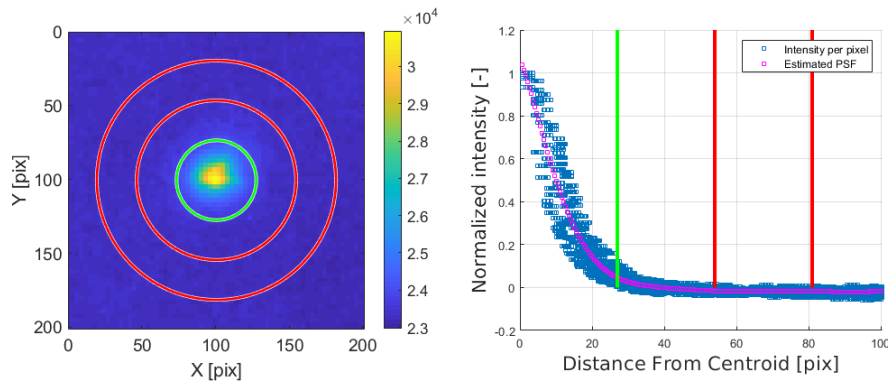


Figure 5.16: Left plot: RSO image and estimated apertures on the image plane; the green circle represents the aperture for the source Zenit-2M, while the red annulus represents the area sampled to estimate the background. The unit of the colorbar is given in ADU. Right plot: normalized intensity profile as a function of the estimated centroid with the resulting estimated point spread function.

The retrieved observables from the passive optical observations, are encoder angular measurements in the horizon reference system and temporal changes in brightness, i.e. the raw light curve of the RSO. Further information about the quality of the angular observables can be found in [58]. We highlight that for the case of multiple RSOs within the main frame, as shown in Figure 5.13, we are able to retrieve the angular measurements for both RSOs. Despite the available individual measurements, the relative angular po-

sition of one RSO with respect to the other may be introduced as an observable for computing the relative trajectory of the RSO with respect to e.g. the chaser after a suitable transformation into the chaser satellite-fixed reference system.

5.5.2 Active Observations

The geodetic satellite laser ranging system at the SwissOGS has been extended for the tracking of defunct RSOs. Changes regarding the system modifications at the hardware level were given in Subsection 5.3.3 and Subsection 5.4.2. Further changes at the software level were summarized and presented in [59].

In Figure 5.17, we show two examples that correspond to Topex/Poseidon (top plot in Figure 5.17) and L-55 (YF24) (Long March (CZ) 2C) (bottom plot in Figure 5.17) with Cospar identification numbers 1992-052A, 2004-046B, respectively. The RSOs have radar cross-sections of 8.7 and 10.6 m², and altitudes of 1342 and 812 km as retrieved from space-track. Note that Topex/Poseidon has a revised optical cross section of $33 \cdot 10^6$ m² [51], which is significantly higher than the estimated via radar measurements due to the presence of a retroreflector on-board of the spacecraft. From the taxonomy defined in the previous chapters, both RSOs belong to the pseudo-cooperative category; moreover, the two pseudo-cooperative RSOs are one decommissioned mission, i.e. Topex/Poseidon, while Long March is a rocket body. All passes had a high culmination and were observed on August 18, 2021, at 16:18 UTC and August 15, 2020, at 18:47 UTC. On both dates the azimuth and elevation of the Sun was 238 °, 41 ° and 270 °, 18 °, respectively. Before analysing Figure 5.17, we define our digital real-time filter and the criterion used to classify returns into signal. To find the backscattered signal from the RSO, we check for the distance between at least $N_p/2 + 1$ entries, where N_p is the total number of entries within a predefined sliding temporal window. The distance between entries is defined in two different spaces: the light travel observed-minus-computed time, and the time bias space. The time bias space is defined by the solution of the variational equation of the perigee passing time orbital element per each entry, i.e. the quantity that gives the rate of change of the state vector for the RSO due to a change in that particular orbital element (the mathematical derivation is available in [6]). The distances are then compared against RSO-specific prior root-mean-square values, to classify the entries as signal if the distances of at least $N_p/2 + 1$ entries is smaller than the a priori value. Note that once the procedure finds signal, the range gate, i.e. the temporal window when the returning pulse is expected to trigger an event in the receiver, is reduced and only the perigee passing time coming from the a priori orbit is corrected using a Kalman filter as soon as new detections are available.

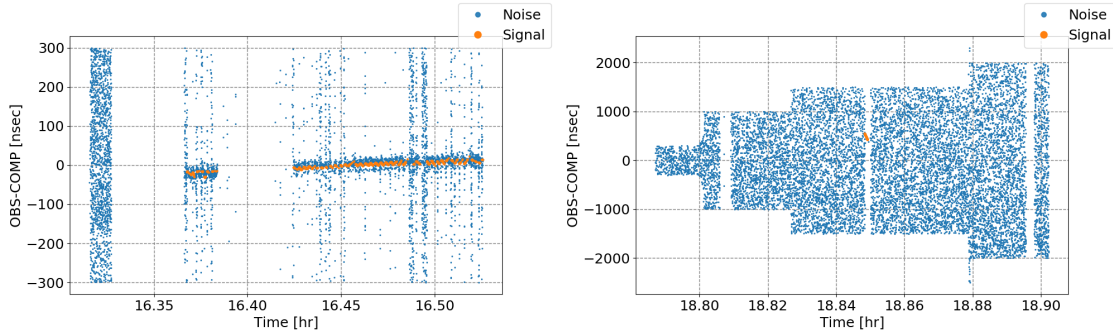


Figure 5.17: Examples of laser ranging measurements to two pseudo-cooperative RSOs being the left plot measurements to the decommissioned RSO Topex/Poseidon observed on August 18, 2021, at 16:18 UTC, and the right plot for the rocket body L-55 (YF24) (Long March (CZ) 2C) observed on August 15, 2020, at 18:47 UTC. Both passes were observed during daytime and show different widths for the range gate at observation epochs.

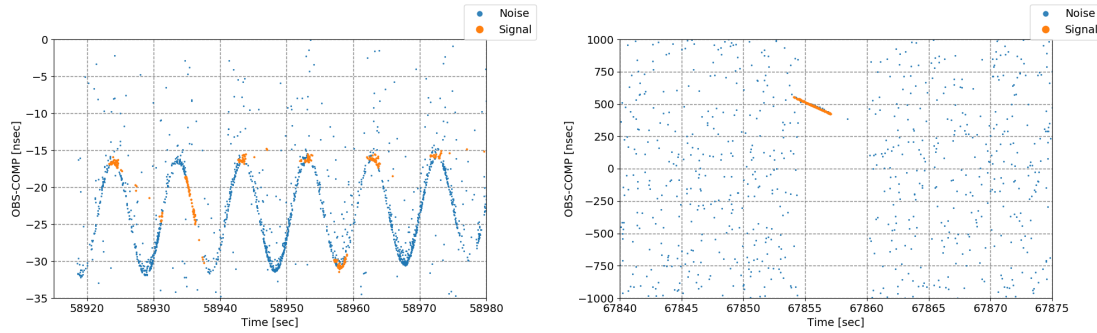


Figure 5.18: Left: detail of triggered photoelectrons on receiver showing the entries classified by noise (blue) and the entries classified as signal (orange) by the real-time filter to the decommissioned satellite Topex/Poseidon on the 18th of August at 16:18 UTC. The sinusoidal pattern reflects the rotation of the retroreflector with respect to the centre of mass of the RSO. This plot exemplifies how the tumbling motion of a RSO can pose a difficulty for the real-time laser ranging filter detector. Right: detail of classified photoelectrons in spite of a trace showing a significant slope, about $\Delta OBS - COM = 200$ nsec per 5 seconds, due to the quality of the used ephemerides for the rocket body L-55 (YF24) (Long March (CZ) 2C) observed on August 15, 2020, at 18:47 UTC.

The left plot in Figure 5.18 shows a portion of the observed passed depicted on the top plot in Figure 5.17. The clear trace depicted by the real returns allows to see the tumbling motion of Topex/Poseidon. Nevertheless, we see how the tumbling motion affects the detections by the real-time filter. For this particular case, due the large

optical cross section of the RSO, the signal can be easily extracted in a post-processing step. On the other hand, when the photon budget is rather low, we may lose the RSO of interest, which could be totally embedded in photoelectron noise. It is interesting to note that in this case, the laser ranging observations are providing evidence of the attitude and attitude motion of the retroreflector with respect to the centre of mass. The by-product might be used to cross-validate results obtained by different observation techniques using passive electro-optical systems.

Another crucial factor that we identified is given by the quality of the available ephemerides. In the right plot in Figure 5.18, the signal was found for a very short time, mainly due to the steepness of the trace produced by the RSO's returns. In Subsection 5.4.1 we derived theoretical minimum observable cross sections, but on that analysis it was not included the impact of the attitude state, and motion, in addition to the quality of the ephemerides. The last two contributors proved to be relevant for finding the photoelectron trace of the RSO's backscattered photons in the sea of background photoelectrons. The signal events could only be detected and confirmed after extensive analysis of the data. Despite the short trace detected by our system, shown as signal in the bottom plot in Figure 5.17, we were able to process the acquired measurements and perform an orbit improvement. In Figure 5.19 we present the residuals after a constraint-less orbit improvement for the Long March rocket body. The bottom trace might correspond to the backscattered signal of a highly reflective element on board of the rocket body, e.g. a retroreflector, which is a hypothesis supported by the relatively high observed return rate. The upper trace might correspond to reflections either from the remaining part of the irradiated body or by the diffuse reflections of another highly reflective element on board of the rocket body. At second 3,054.5 we see a trace of few measurements that does not correspond to the trend depicted by the two other traces; most likely, those entries correspond to outliers. The lack of information about the reflective elements on board of the rocket body poses an ambiguity for the interpretation of the results. But the fact that there are reflecting elements makes this RSO an ideal candidate to perform more regular observations to infer its attitude and attitude motion. Assuming that the upper trace in Figure 5.19 comes from the remaining irradiated part of the rocket body, this case highlights the importance of having good ephemerides for the tracking of defunct RSOs with geodetic laser systems; consider how challenging it will be to find the upper trace only if one considers the measurement space depicted in the bottom plot in Figure 5.17. Bear in mind that current geodetic laser systems are about an order of magnitude less powerful than dedicated defunct RSOs laser systems.

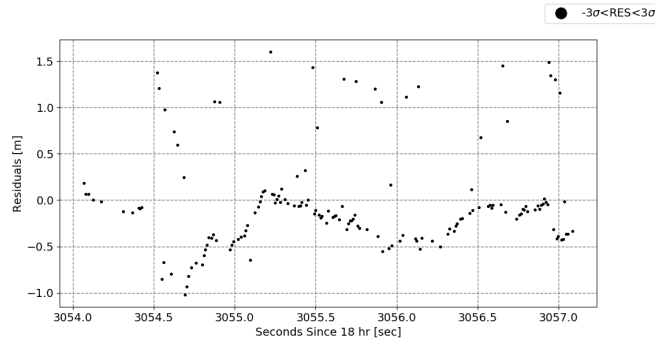


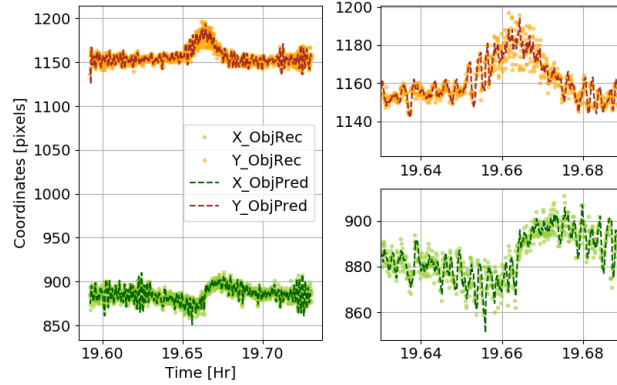
Figure 5.19: Residuals after a constraint-less orbit improvement using one observing station and an ultra-short arc. The bottom trace might correspond to the backscattered signal by a highly reflective element on board of the rocket body, which is a hypothesis supported by the relatively high return rate, while the upper trace might correspond to reflections from either the remaining irradiated portion of the body or a contribution provided by diffuse reflection of another highly reflective element on board of the rocket body.

5.5.3 Simultaneous Combined Observations

Through the current study, we have presented selected case studies showing capabilities to observe during daylight using either an active or passive electro-optical system. The outcome of each observation technique is not limited to measurements for orbit improvement, but provide a substantial contribution to the understanding of the attitude and attitude motion of the RSO of interest. Recent developments at the SwissOGS allow to retrieve measurements acquired by both passive and active systems simultaneously. One important technical challenge that we had to overcome, since we are using the same telescope for transmitting and receiving in both active and passive roles, was the temporal alignment between the starting signals for the emission of laser pulses and for exposing the scientific CMOS sensor, which is deemed critical to minimize the impact of laser straylight on the passive system. Furthermore, a narrowband filter mounted on the passive electro-optical system centred at the nominal operational wavelength of the laser further attenuates this signal. The time synchronization of the two triggering starting events between the two systems is done via the Field-Programmable-Gate-Array device, which adds a short delay for the starting triggering signal on the passive device. Additional challenges were addressed when implementing the Stare and Chase observation strategy reported in [58].

The next case study shows an example of a RSO observed simultaneously during daylight. The RSO is L-55 (YF24) (Long March (CZ) 2C) with Cospar identification number 2007-010B. Note that in spite of having the same name as the rocket body in Subsection 5.5.2, both correspond to different RSOs. This rocket body has an altitude of about 850 km and a radar cross section of 8 m². The date of observation was the 12th of June, 2020, at 19:30 UTC, when the Sun was close to setting. In Figure 5.20, we present

the angular, brightness and range measurements acquired while tracking the RSO. Each measurement type corresponds to horizontal angles of the RSO after the transformation of X_{cam} and Y_{cam} (top plot in Figure 5.20) – in the camera reference frame – into horizontal angular components by the known transformation [58], the brightness as a by-product of the active tracking in the bottom left plot in Figure 5.20, and the observed ranges minus computed from the predictions acquired with the active system in the bottom right plot in Figure 5.20. We highlight that the presented measurements are raw and were not further post-processed. We start the analysis by focusing on the results from the active tracking and the estimated changes in brightness. From the top plot in Figure 5.20, we can see the geometrical effects of the tracking in the camera reference frame; the scattering of the measurements is explained by the estimated centroid (see [58] for more details). Moreover, after inspecting the extracted light curve (bottom-left plot in Figure 5.20), we can see that there is low scattering in the estimated brightness with respect to time, which translates into good signal to noise ratio. The latter is deemed crucial for a successful RSO recognition on the acquired images in combination with the active tracking phase (see top plot in Figure 5.20) and to retrieve reliable changes in brightness from the RSO. The light curve depicts the influence of the geometrical factors, i.e. observation geometry between the RSO and the SwissOGS, the geometrical configuration Sun-RSO-station, and the impact of the air mass as a function of the elevation in the horizontal frame. A post-processing step may provide more insight into the tumbling state of the RSO since the raw measurements are dominated by the observation conditions. Regarding the observed ranges, we represented the difference between the observed light travel time to the predicted one and binned it 30 nanoseconds in the Y-axis and 1 second in the X-axis. Note that the previous operation was done to derive a figure of merit for the concentration of photoelectrons in time and in the observed-minus-computed domain, but is not considered a post-processing step per se.



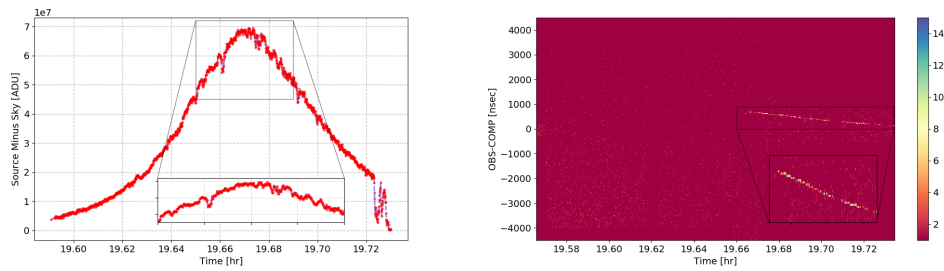


Figure 5.20: Top: resulting tracking measurements in the camera reference system for both X and Y after the RSO recognition on the acquired frames by the passive system *ObjRec* and the prediction *ObjPred* step estimated by the active tracking module. Bottom left: resulting light curve for the RSO of interest extracted in real time while tracking the RSO. The lack of scattering suggest a good signal to noise ratio between source and background. Bottom right: resulting active observations after a binning of 30 nanoseconds in the Y -axis and 1 sec in the X -axis to infer the concentration of photoelectrons in both domains.

On the right side in the bottom plot in Figure 5.20, we can see the highly concentrated photoelectrons depicting a concentration of up to five times larger than for the bins containing presumably noise only. Such concentration of photoelectrons might be expected for cooperative or pseudo-cooperative RSOs. Despite the high concentration of photoelectrons, there are variations on the consecutive bins along the trace suggesting most likely an influence on the attitude motion of the RSO. Finally, it is important to notice that for this case our real-time signal detection algorithm failed. One potential explanation for the failure was found to be the wrong binning size in the Y -axis, which corresponds to the estimated RSO depth.

5.6 Discussion

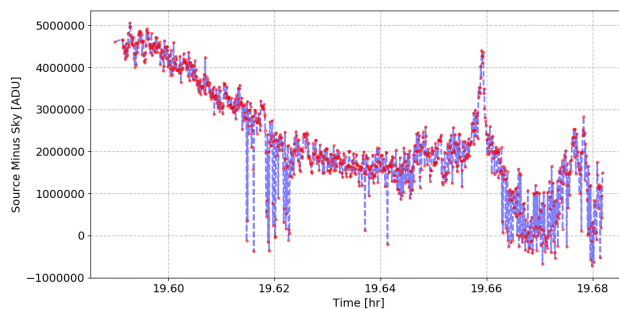
The central axis of the presented work was the study of daylight observations from the point of view of information gain in a space situational awareness context, and from the SwissOGS technical point of view as an optical ground-based observatory. We proved that existing observing and tracking observatories could provide either measurements to update the state vector of RSOs more regularly, or improved evidence of the attitude and attitude motion via light curves benefiting from different illumination conditions and different attitude states of the targeted RSO along the orbit. There is nevertheless, one important question to be addressed: will the simultaneous observation of a RSO by a passive and active system add indispensable information compared to the non-simultaneous observation of the RSO by either system? In order to answer the formulated question, we present a second pass of the RSO with Cospar identification number 2004-046B observed on July 8, 2020, at 19:33 UTC, where the simultaneous

measurement acquisition proved to partially disambiguate the interpretation of the attitude motion of the RSO.

In Figure 5.21, we present the real-time light curve (top plot) and one-way range residuals (bottom plot) after orbit improvement. The constraint-less orbit improvement was conducted using the measurements recognized as hits by the real-time laser ranging filter for this pass only. In Figure 5.19, we saw that the RSO was providing interesting features possibly related to attitude motion. With the observation of this new pass, we can further explore and propose hypotheses for the attitude and attitude motion, besides insights regarding optical properties of the RSO.

By inspection of the observed pass by both systems, we can distinguish at least two positions of the RSO with respect to the observing station. For the first part, starting at 19.59 until 19.64 hr, the distribution of the range residuals hardly permit to see a clear periodic pattern. From the point of view of the passive data, the light curve is dominated mainly by the observation geometry and air mass. For the second part, starting at 19.64 until 19.69, the RSO reveals a local maxima on the passive light curve. In addition, there is evidence of presence of more than one reflective element on the rocket body. The relative maxima on the passive light curve may indicate either the observation of the largest cross section of the rocket body, a favourable phase angle for some reflective parts on the body, or the combination of both.

It is interesting to note that the change in brightness does not happen instantaneously as may occur with RSOs that reflect intense glints or flashes, instead, we can see a progressive increase of the brightness until reaching the maximum and the corresponding decreasing behaviour in a symmetrical fashion. By the end of the pass, the observation conditions turn unfavourable hiding probably details that we could use for further analysis. From the point of view of the active measurements, we can distinguish at least two traces that might correspond to two highly reflective elements separated with an average distance of about 1 m, and a weak upper trace correlating in trend with the ones of the highly reflective elements, which might correspond to reflected photons by the remaining irradiated part of the body. Finally, the two main traces of the second part show a rotating pattern with variable amplitude that might correspond to the rotation of the rocket body with respect to the principal axis of moment of inertia.



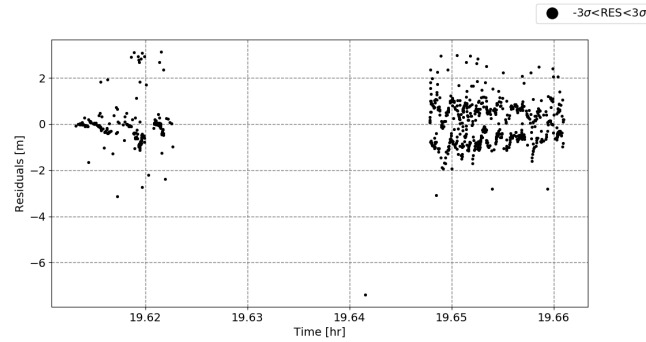


Figure 5.21: Top: real-time extracted light curve as a by-product of the active tracking; note that the signature shows a significant scatter coming from a suboptimal signal to noise ratio, however, the presence of relative critical points may add information to the understanding of the attitude and attitude motion of the RSO. Bottom: one-way laser ranges residuals after a constraint-less orbit improvement using all detected hits by our laser ranging real-time filter.

The experience acquired with the data collected for this particular RSO supports the claim that simultaneous observations, with optical passive and active observing systems, are a valuable asset for the correct understanding and disambiguation of the attitude and attitude motion of RSOs. We are positive that after gathering of enough passes by several optical ground-based observing stations, an attitude model for the RSO with Cospar identification number 2004-046B could be proposed with the final aim of showing an example for the future modelling of attitude states derived from the fusion of only optical data. Here a key point is the international collaboration between institutions and the joint observation of the RSO.

5.7 Summary and Outlook

The rapidly growing number of resident space objects is critical for the safe operation of current and future space missions, which together with the unbalanced ratio between functional and defunct RSO depict a scenario with high likelihood of collisions. The prevention of such collisions starts by building up RSO catalogues, which is not possible without the continuous acquisition of measurements by ground and space systems employing different observation techniques. The presented work aims at reducing an existing data gap in optical observations due to the technique being restricted to nighttime observations. We presented:

- **The impact of daylight observations within the context of space surveillance and tracking.** Current observation windows for optical sensors are constrained to the observation of RSOs during nighttime only. Those observation windows are further reduced for mid-latitude northern ground-stations between

equinoxes. We presented examples of light curves from ENVISAT acquired during daylight from which we could exploit different illumination and viewing conditions. The defunct RSO was chosen conveniently to point out that due to its orbital configuration, currently there are optical data gaps of months for stations that are not able to observe during daylight. We presented evidence that the contribution of daylight observations aid in reducing this observational gap. Furthermore, the observation during daylight can be optimized to adjust to challenging configurations between Sun-RSO-observer while maximizing the arc coverage and distribution of observed arcs along the orbit.

- **The impact of background noise and its mitigation in active and passive electro-optical systems.** The diffuse solar component on ground was used to derive the number of triggered photoelectrons on the receiver particularized for the systems available at the SwissOGS. Its impact on both active and passive electro-optical systems was analysed and modifications at the hardware level were presented with the final aim of enhancing existing ground-based optical stations to enable daylight observation capabilities. Furthermore, for the case of passive electro-optical systems an apparent magnitude of 7 was found to be the limiting magnitude when the brightness of the sky was quantified with an apparent magnitude of 2.9. The theoretical estimates were corroborated with real observations of reference stars. Finally, the use of the near- and short-wave infrared spectral regions for active and passive optical sensors, would be the preferred choice due to the lower sky background contribution. The efficiency of the transmitting system was analysed on the near infrared reinforcing the idea of further exploiting that specific spectral region for the optical sensors available at the SwissOGS.
- **The estimation of the minimum observable RSO with active and passive electro-optical systems.** In the case of passive systems we derived a formula (Equation 5.5), from which we can estimate the radius of a geometrical cross section as a function of the apparent magnitude of the RSO, the slant range and assuming a certain phase angle and optical properties of the RSO such as the albedo and the reflectivity function. In the case of an active system, we used the link budget equation with the technical specifications of our active system, together with a large set of observations to LAGEOS-1, to derive the minimum observable cross section of defunct RSOs varying the altitude of the RSO and fixing a minimum number of photoelectrons per second at the receiver.
- **Active and passive observations from the enhanced systems at the SwissOGS.** Passive observations were acquired to the RSOs TanDEM-X and TerraSAR-X, both within the same frame, stressing the fact that the monitoring of relative formation flying will gain interest rapidly due to on-orbit servicing and active debris removal initiatives. Additionally, observations to the second stage Zenit-2 were acquired and analysed. From the active observations, we focused on providing examples that indicate current challenges being in particular the rather low signal to noise ratio when observing non-cooperative RSOs using low power active

systems, the tumbling motion and the quality of the ephemerides of the RSO. Finally, an example proving the capabilities of the simultaneous daylight acquisition was presented.

- **Usefulness of simultaneous combined active and passive electro-optical observations.** We presented a case study where the combination of only optical simultaneous observations allowed us to partially disambiguate the tumbling motion of the RSO during the observed pass. The results showed that potentially simultaneous observations by several sensors of a network will further contribute to the better understanding of the attitude dynamics of one of the Long March rocket bodies.

Within future foreseeable activities, we plan a campaign for the daylight observation, using the passive system, of different reference stars evenly distributed along the sky. During this campaign, we will attempt the tracking of selected RSOs. We aim at deriving conclusions regarding the limiting magnitude of the system accounting for more variability in the observation conditions, and vicariously, after the reduction of the data, estimate geometrical cross-sections from daylight observations. Incoming further developments in our active system comprise the usage of the fundamental frequency of the laser system, i.e. 1,064 nm, which will not only reduce the diffuse solar background at the receiver level, but will increase the energy of the emitted pulse by at least a factor of 2 compared to the power in our current system.

WE conclude this dissertation summarizing the contribution of the current work within the context explained in Chapter 1. We highlight the achieved milestones, which may provide the basis for a follow-on work.

6.1 Achievements

Within the presented work we were able to:

- Assess our up-to-date footprint in the outer space. Latest reports, such as the yearly space environment report issued by the European Space Agency, support the rather worrisome fact that our current use of the outer space is not only unsustainable, but regularly threatens active functional missions or space activities. Mitigation guidelines are already being implemented to improve the situation through measures comprising e.g. prevention of on-orbit collisions, active debris removal, in-orbit servicing and others. To prevent collisions, knowledge from the defunct RSO population must be gained in terms of updated extended state vectors, helping to build catalogs, from which close conjunctions can be estimated. The role of the laser ranging technique benefits not only from all the legacy available from its use in the geodetic domain, but from the intrinsic characteristics of the technique itself. There are, however, several challenges that must be solved to provide with a fully operational capability to an Space Surveillance and Tracking observing network. Within all potential challenges, the current work focused on the development of a target acquisition and tracking subsystem, which will compensate for the lack of accurate ephemerides when observing exclusively with the laser, the optimization of a laser ranging system by enabling the operation of the fundamental wavelength of 1,064 nm, mitigating mainly for the losses occurring as a consequence of frequency doubling, and finally the acquisition of measurements during daylight, which allows to extend current observation windows for ground-based optical observing stations.

- Design and implement a target acquisition and tracking subsystem. We studied current approaches using a passive electro-optical system with a wide field of view – compared to the beam width of the laser in our system. The subsystem comprises two main modules, namely the stare and chase. During the stare phase, images are collected and, by using a tailored digital image processing workflow, the object is identified. Once a minimum number of detections occur, an active tracking phase begins aiming at locking the targeted RSO within the laser beam of the system. After studying and comparing different strategies available for both modules, we implemented in a real-time system the aperture photometry procedure for detecting the object within the stare module, besides the active tracking estimating a trajectory given a certain number of elements within a temporal sliding window, which is able to distinguish between outliers and changes in the trajectory reliably by using robust estimators. As a by-product of the newly target acquisition and tracking module, within our laser ranging system, ranges, horizontal angular measurements and brightness measurements could be retrieved simultaneously.
- Implement operationally the fundamental wavelength of the existing laser system at the SwissOGS. Once the target is locked within the laser beam, an increase of energy, about a factor of 2 if compared to the nominal energy after frequency doubling, strengthen the optical link, thus the number of expected backscattered returns from the irradiated RSO at the receiver. The full process consisted on the study of the theoretical system performance using the 532 nm wavelength, and comparing it to a performance figure of merit derived from a statistically representative set of data. In addition, the same theoretical system performance done for the 532 nm wavelength was done for the 1,064 nm, to provide the motivation for its non-trivial installation. We describe all necessary steps needed to align the fundamental wavelength to the operational one, first observations to available calibration targets, single shot root-mean-square for both wavelengths using an external calibration target located at about 600 m from the reference point of the laser system, and preliminary results to selected targets from the ILRS active RSO catalog.
- Acquired first daylight combined optical observations utilizing a passive and active electro-optical system. For achieving this milestone, we did a comprehensive study of all factors involved in the acquisition chain, both for passive and active electro-optical systems. Specifically, we analyzed the impact of an extension of observation windows for current observing optical networks, the solar photon budget, the mitigation of the solar backscattered photons in each system, besides implementing specific new hardware components, which help to minimize the impact of the backscattered solar photons. In addition, daylight observations to selected defunct RSOs were presented, e.g. to ENVISAT and a rocket body, proving that in selected cases we could extract confidently changes in brightness, horizontal angular measurements and ranges. The importance of fusing different types of observations, e.g. range residuals and changes in brightness, was further analyzed using a de-

funct RSO, from which there are presumably highly reflective elements on-board. Likewise, we were able to get preliminary observations to non-cooperative RSOs, even though the number of detected events, associated presumably to backscattered photons from the target, occur mainly at the epoch of closest approach and the trace of the detected signal is rather short. However, even in some cases where the observed arc, using laser ranging only, was significantly short, if compared to the revolution period of the RSO, we successfully conducted a constraint-less orbit improvement.

6.2 Follow-on Work

As a continuation of the previous work, we foresee the following blocks, which may continue and further extend all the work presented within this dissertation.

- With the advent of the new dynamical models for orbit propagation and determination of defunct RSOs, e.g. The SGP4-XP, the collected measurements, i.e. angular measurements from the target acquisition and tracking subsystem together with laser ranges, may be merged, employing those models, and the quality of the estimates assessed, using e.g. precise ephemerides, to derive a figure of merit of their accuracy. An improvement in the accuracy of the ephemerides have a direct impact in the width of the range gate besides the shape of the trace depicted by the backscattered photons from the target in the observed-minus-computed domain affecting directly their identification.
- Signal processing algorithms based on Poissonian statistics may be derived, analyzed, implemented and tested. During the extensive experimentation sessions, it became obvious that current algorithms used when ranging to cooperative targets are not fully optimized for the detection of backscattered signal from defunct RSOs. First results show the potential of selected algorithms for successfully detecting signal from passes where the depicted trace is completely embedded in background noise. Nevertheless, an extended testing phase comprising different target RSOs, and even different systems may be conducted to derive the limits of their applicability.
- The near-infrared transmitting and receiving optical chains, in the laser system at the SwissOGS, may be further inspected. From the experimental phase presented in Chapter 4, there are several features that up-to-date, we have not been able to completely understand and therefore correct. One example is given by the multiple traces observed in the observed-minus-computed domain, which is present in several passes shown in Chapter 4. Other features include understanding why the received return rate is significantly lower than the theoretical figure of merit for the return rates using the near-infrared wavelength. In addition, successful observations to LAGEOS like RSOs may be acquired as a verification of the alignment of the beam in the far field, which hitherto have not been acquired.

Bibliography

- [1] Abercromby, K. J., Seitzer, P., Rodriguez, H. M., Barker, E. S., and Matney, M. J. (2009). Survey and chase: A new method of observations for the Michigan Orbital DEbris Survey Telescope (MODEST). *Acta Astronautica*, 65(1-2):103–111.
- [2] Andrenucci, M., Pergola, P., and Ruggiero, A. (2011). *Active removal of space debris-expanding foam application for active debris removal*. ESA Final Report, Pisa.
- [3] Anz-Meador, P. D., Opiela, J., Shoots, D., and Liou, J. (2018). History of on-orbit satellite fragmentations. *National Aeronautics and Space Administration Johnson Space Center Orbital Debris Program Office*. Available from: <https://orbitaldebris.jsc.nasa.gov/library/20180008451.pdf> [Accessed 26 August 2020].
- [4] Aviv, D. G. (2006). *Laser Space Communications*. Artech House Publishers.
- [5] Becker, D. and Cain, S. (2018). Improved space object detection using short-exposure image data with daylight background. *Applied optics*, 57(14):3968–3975.
- [6] Beutler, G. (2005). *Methods of celestial mechanics. Vol. I: Physical, mathematical, and numerical principles*. Springer, Astronomy and Astrophysics Library.
- [7] Born, M. and Wolf, E. (1999). *Principles of optics: electromagnetic theory of propagation, interference and diffraction of light*. Elsevier.
- [8] Box, G. E., Jenkins, G. M., and Reinsel, G. C. (2011). *Time series analysis: forecasting and control*. John Wiley & Sons.
- [9] Burns, J. A. (1976). Elementary derivation of the perturbation equations of celestial mechanics. *American Journal of Physics*, 44(10):944–949.
- [10] Chromey, F. R. (2010). *To measure the sky: an introduction to observational astronomy*. Cambridge University Press.

- [11] Clark, R. N. (1990). *Visual astronomy of the deep sky*. CUP Archive.
- [12] Coddington, O., Lean, J. L., Pilewskie, P., Snow, M., and Lindholm, D. (2016). A solar irradiance climate data record. *Bulletin of the American Meteorological Society*.
- [13] Collins, K. A., Kielkopf, J. F., Stassun, K. G., and Hessman, F. V. (2017). Astroimagej: Image Processing and Photometric Extraction for Ultra-Precise Astronomical Light Curves. *The Astronomical Journal*, 153(2):77.
- [14] Condon, J. J. (1992). Gbt Pointing Equations. Technical Report Memo Series, NRAO.
- [15] Cordelli, E., Lauber, P., Prohaska, M., Rodriguez, J., Schlatter, P., and Schildknecht, T. (2019a). Recent developments at the swiss optical ground station and geodynamics observatory zimmerwald. In *1st NEO and Debris Detection Conference, 20 - 23 April 2021, Darmstadt, Germany*.
- [16] Cordelli, E., Rodriguez, J., Schlatter, P., Lauber, P., and Schildknecht, T. (2019b). Use of a night-tracking camera during daytime. Presented at the 21 - 25 October International Laser Ranging Technical Workshop, Stuttgart, Germany.
- [17] Cordelli, E., Rodriguez-Villamizar, J., Schlatter, P., and Lauber, P. (2018). Real time improvement of orbits of space debris by fusing SLR and astrometric data acquired by a night-tracking camera. In *21st International Workshop on Laser Ranging, 5. - 9. November, Canberra, Australia*.
- [18] Cordelli, E., Vananti, A., and Schildknecht, T. (2020). Analysis of laser ranges and angular measurements data fusion for space debris orbit determination. *Advances in Space Research*, 65(1):419–434.
- [19] Courde, C., Torre, J., Samain, E., Martinot-Lagarde, G., Aymar, M., Albanese, D., Exertier, P., Fienga, A., Maréchal, H., Métris, G., et al. (2017). Lunar laser ranging in infrared at the grasse laser station. *Astronomy & Astrophysics*, 602:A90.
- [20] Cuevas, E., Osuna, V., and Oliva, D. (2017). Template matching. *Studies in Computational Intelligence*.
- [21] Degnan, J. J. (1993). Millimeter accuracy satellite laser ranging: a review. *Contributions of space geodesy to geodynamics: technology*, 25:133–162.
- [22] Degnan, J. J. (2008). Impact of Receiver Deadtime on Photon-Counting SLR and Altimetry during Daylight Operations. In *16th International Workshop on Laser Ranging, 12-17 October, Poznan, Poland*.
- [23] Estell, N., Ma, D., and Seitzer, P. (2019). Daylight imaging of leo satellites using cots hardware. In *Advanced Maui Optical and Space Surveillance Technologies (AMOS) Conference, Maui (HI), USA*.

- [24] Everett, M. and Howell, S. (2001). A Technique for Ultrahigh Precision CCD Photometry. *Publications of the Astronomical Society of the Pacific*.
- [25] Flohrer, T. (2012). *Optical Survey Strategies and Their Application to Space Surveillance*, volume 83. Schweizerischen Geodtischen Kommission.
- [26] Gibson, D., Pearce, E., Blythe, M., and Trujillo, P. (1993). Orbital debris characterization: ETS staring survey [1951-02]. *Astronomy and Astrophysics -Berlin-*, 1(1951):11–11.
- [27] Green, J. L., Welch, B. W., and Manning, R. M. (2019). *Optical Communication Link Atmospheric Attenuation Model*. National Aeronautics and Space Administration STI program.
- [28] Greene, B., Gao, Y., and Moore, C. (2002). Laser Tracking of Space Debris. In *13th International Workshop on Laser Ranging, 22. October 2002, Washington, D.C, USA*.
- [29] Groenewegen, G. L. M. and van Rooij, A. C. M. (2016). *The Stone-Weierstrass Theorem*. Atlantis Press, Paris.
- [30] Gurtner, W., Pop, E., and Utzinger, J. (2002). Zimmerwald dual-wavelength observations: first experiences. In *The 13th international workshop on laser ranging instrumentation. Washington DC, USA*.
- [31] Hampf, D., Riede, W., Bartels, N., Schafer, E., and Wagner, P. (2021). A path towards low-cost, high-accuracy orbital object monitoring. In *8th European Conference on Space Debris, 20.-23. Apr 2021, Darmstadt, Germany*.
- [32] Hasenohr, T., Hampf, D., Wagner, P., Sproll, F., Rodmann, J., Humbert, L., Herkommer, A., and Riede, W. (2016). Initial detection of low earth orbit objects through passive wide angle imaging systems. *Deutscher Luft- und Raumfahrtkongress 2016*, pages 1–7.
- [33] Hemmati, H. (2009). *Near-earth laser communications*. CRC press.
- [34] Henize, K. and Stanley, J. (1990). Optical observations of space debris. In *AIAA/NASA/DID Orbital Debris Conference: Technical Issues and Future Directions, 16-19 April, 1990, Baltimore, Maryland*, page 1340.
- [35] Howell, S. B. (1989). Two-dimensional aperture photometry - Signal-to-noise ratio of point-source observations and optimal data-extraction techniques. *Publications of the Astronomical Society of the Pacific*.
- [36] Howell, S. B. (2006). *Handbook of CCD astronomy*, volume 5. Cambridge University Press.

- [37] Imaida, T., Yokokohji, Y., Doi, T., Oda, M., and Yoshikawa, T. (2004). Ground-space bilateral teleoperation of ets-vii robot arm by direct bilateral coupling under 7-s time delay condition. *IEEE Transactions on Robotics and Automation*, 20(3):499–511.
- [38] Inter-Agency Space Debris Coordination Committee (2020). *Space Debris Mitigation Guidelines, Rev 2*. IADC Steering Group and Working Group 4.
- [39] Jelalian, A. V. (1992). *Laser radar systems*. Artech House.
- [40] Jenn, D. (2005). *Radar and laser cross section engineering*. American Institute of Aeronautics and Astronautics, Inc.
- [41] Karttunen, H., Kröger, P., Oja, H., Poutanen, M., and Donner, K. J. (2007). *Fundamental astronomy*. Springer.
- [42] Kay, S. M. (1993). *Fundamentals of statistical signal processing: estimation theory*. Prentice-Hall, Inc.
- [43] Klein, B. J. and Degnan, J. J. (1974). Optical Antenna Gain 1: Transmitting Antennas. *Applied Optics*.
- [44] Kneizys, F., Shettle, E., Gallery, W., Jr, C., and Abreu, L. (1983). Atmospheric transmittance/radiance: Computer code lowtran 6. supplement: Program listings. In *Environmental Research Papers*.
- [45] Kneizys, F. X., Shettle, E., Abreu, L. W., Chetwynd, J. H., and Anderson, G. P. (1988). User guide to LOWTRAN 7. In *Environmental Research Papers*.
- [46] Liou, J.-C. (2011). An active debris removal parametric study for leo environment remediation. *Advances in space research*, 47(11):1865–1876.
- [47] Marsillach, D. A., Virani, S., and Holzinger, M. J. (2017). Real-time hardware-in-the-loop hand-off from a finder scope to a larger telescope. In *1st IAA Conference on Space Situational Awareness (ICSSA) Orlando, FL, USA IAA-ICSSA-17-0X-XX*, volume 0X, pages 1–18.
- [48] Masias, M., Freixenet, J., Lladó, X., and Peracaula, M. (2012). A review of source detection approaches in astronomical images. *Monthly Notices of the Royal Astronomical Society*.
- [49] Moré, J. J. (1978). The levenberg-marquardt algorithm: implementation and theory. In *Numerical analysis*, pages 105–116. Springer.
- [50] National Research Council (2011). *Limiting Future Collision Risk to Spacecraft: An Assessment of NASA’s Meteoroid and Orbital Debris Programs*. The National Academies Press.
- [51] Pearlman, M., Arnold, D., Davis, M., Barlier, F., Biancale, R., Vasiliev, V., Ciuffolini, I., Paolozzi, A., Pavlis, E. C., Sośnica, K., et al. (2019). Laser geodetic satellites: a high-accuracy scientific tool. *Journal of Geodesy*, 93(11):2181–2194.

- [52] Pearlman, M. R., Degnan, J. J., and Bosworth, J. M. (2002). The International Laser Ranging Service. *Advances in Space Research*.
- [53] Peldszus, R. and Faucher, P. (2020). European union space surveillance & tracking (eu sst)—state of play and perspectives. In *71st International Astronautical Congress, IAC 2020, as a Cyberspace Edition, Session E*, volume 3.
- [54] Phipps, C. R. (2014). A laser-optical system to re-enter or lower low Earth orbit space debris. *Acta Astronautica*.
- [55] Pittet, J. N., Šilha, J., and Schildknecht, T. (2018). Spin motion determination of the Envisat satellite through laser ranging measurements from a single pass measured by a single station. *Advances in Space Research*.
- [56] Ploner, M., Cordelli, E., Bodenmann, D., Schildknecht, T., Schlatter, P., and Jaeggi, A. (2015). Gns observations for calibration tasks at the zimmerwald observatory. In *International Symposium on GNSS, November, Kyoto, Japan*.
- [57] Rodriguez-Villamizar, J., Cordelli, E., and Schildknecht, T. (2019). The new stare & chase procedure at the swiss optical ground station and geodynamics observatory zimmerwald. In *Proceedings 1st NEO and Debris Detection Conference, 20 - 23 April 2021, Darmstadt, Germany*. ESA Space Safety Programme Office.
- [58] Rodriguez-Villamizar, J., Cordelli, E., and Schildknecht, T. (2021). The stare and chase observation strategy at the swiss optical ground station and geodynamics observatory zimmerwald: From concept to implementation. *Acta Astronautica*.
- [59] Rodriguez-Villamizar, J. and Schildknecht, T. (2021). Daylight laser ranging of space debris with a geodetic laser from the swiss optical ground station and geodynamics observatory zimmerwald: First experiences. In *Proceedings 8th European Conference on Space Debris (virtual), 20.03.-23.03.2021, ESA/ESOC, Darmstadt, Germany*. ESA Space Debris Office.
- [60] Rork, E. W., Lin, S. S., and Yakutis, A. J. (1982). Ground-based electro-optical detection of artificial satellites in daylight from reflected sunlight. Technical report, Massachusetts Institute of Technology, Lexington Laboratory, Massachusetts.
- [61] Rousseeuw, P. J. and Croux, C. (1993). Alternatives to the median absolute deviation. *Journal of the American Statistical Association*.
- [62] Schnabel, R. B. and Eskow, E. (1999). A revised modified Cholesky factorization algorithm. *SIAM Journal on Optimization*.
- [63] Shaddix, J., Brannum, J., Ferris, A., Hariri, A., Larson, A., Mancini, T., and Aristoff, J. (2019). Daytime geo tracking with aquila: Approach and results from a new ground-based swir small telescope system. In *Advanced Maui Optical and Space Surveillance Technologies (AMOS) Conference, Maui (HI), USA*.

- [64] Shan, M. (2018). *Net deployment and contact dynamics of capturing space debris objects*. PhD thesis, Delft University of Technology.
- [65] Shepherd, L. C. G. and Command, A. F. S. (2006). Space surveillance network. In *Shared Space Situational Awareness Conference, Colorado Springs, CO*.
- [66] Šilha, J., Pittet, J. N., Hamara, M., and Schildknecht, T. (2018). Apparent rotation properties of space debris extracted from photometric measurements. *Advances in Space Research*.
- [67] Smith, C. H. (2006). The eos space debris tracking system and razorview demonstration. In *The Advanced Maui Optical and Space Surveillance Technologies (AMOS) Conference, Maui (HI), USA*, pages 799–807.
- [68] Smith, S. W. (1997). *The Scientist and Engineer's Guide to Digital Signal Processing*. California Technical Publishing.
- [69] Smullin, L. D. and Fiocco, G. (1962). Optical echoes from the moon. *Nature*, 194(4835):1267–1267.
- [70] Steindorfer, M., Kirchner, G., Koidl, F., and Wang, P. (2019a). Recent space debris related activities at the slr station graz. In *Proceedings 1st NEO and Debris Detection Conference, 20 - 23 April 2021, Darmstadt, Germany*. ESA Space Safety Programme Office.
- [71] Steindorfer, M., Koidl, F., Wang, P., and Kirchner, G. (2019b). Daylight space debris laser ranging. *LPI Contributions*, 2109:6002.
- [72] Steindorfer, M. A., Kirchner, G., Koidl, F., Wang, P., Antón, A., Fernández Sánchez, J., and Merz, K. (2017). Stare and chase of space debris targets using real-time derived pointing data. *Advances in Space Research*.
- [73] Stellingwerf, R. F. (1978). Period determination using phase dispersion minimization. *The Astrophysical Journal*.
- [74] Tapley, B. D., Schutz, B. E., and Born, G. H. (2004). *Statistical Orbit Determination*.
- [75] Thomas, S., Fusco, T., Tokovinin, A., Nicolle, M., Michau, V., and Rousset, G. (2006). Comparison of centroid computation algorithms in a Shack-Hartmann sensor. *Monthly Notices of the Royal Astronomical Society*.
- [76] United Nations (2002). *United Nations Treaties and Principles on Outer Space*. United Nations Publications.
- [77] Vananti, A., Schildknecht, T., and Krag, H. (2017). Reflectance spectroscopy characterization of space debris. *Advances in space research*, 59(10):2488–2500.

- [78] VanderPlas, J. T. (2018). Understanding the LombScargle Periodogram. *The Astrophysical Journal Supplement Series*.
- [79] Viard, E., Le Louarn, M., and Hubin, N. (2002). Adaptive optics with four laser guide stars: correction of the cone effect in large telescopes. *Applied optics*, 41(1):11–20.
- [80] Webb, C. E. (2020). *Handbook of Laser Technology and Applications: Volume 1: Principles*. CRC Press.
- [81] Williams, D. (2001). *Weighing the odds: a course in probability and statistics*. Cambridge University Press.
- [82] Yang, F., Xiao, C., Chen, W., Zhang, Z., Tan, D., Gong, X., Chen, J., Li, H., and Zhang, J. (1999). Design and observations of satellite laser ranging system for daylight tracking at shanghai observatory. *Science in China Series A: Mathematics*, 42(2):198–206.
- [83] Zdunkowski, W., Trautmann, T., and Bott, A. (2007). *Radiation in the atmosphere: A course in theoretical meteorology*. Cambridge University Press.

Declaration of consent

on the basis of Article 18 of the PromR Phil.-nat. 19

Name/First Name: Rodriguez Villamizar Julian

Registration Number: 17-144-205

Study program: Physik mit Schwerpunkt Astronomie

Bachelor Master Dissertation

Title of the thesis: Efficient Laser Ranging to Space Debris

Supervisor: Professor Dr. Thomas Schildknecht

I declare herewith that this thesis is my own work and that I have not used any sources other than those stated. I have indicated the adoption of quotations as well as thoughts taken from other authors as such in the thesis. I am aware that the Senate pursuant to Article 36 paragraph 1 litera r of the University Act of September 5th, 1996 and Article 69 of the University Statute of June 7th, 2011 is authorized to revoke the doctoral degree awarded on the basis of this thesis.

For the purposes of evaluation and verification of compliance with the declaration of originality and the regulations governing plagiarism, I hereby grant the University of Bern the right to process my personal data and to perform the acts of use this requires, in particular, to reproduce the written thesis and to store it permanently in a database, and to use said database, or to make said database available, to enable comparison with theses submitted by others.

Bern, 11.03.2022

Place/Date



Signature

Curriculum Vitae

Complete Name: Julian Camilo Rodriguez Villamizar

Date of Birth: 10 May 1991

Place of Birth: Bogota, Colombia

Education

03/2018 - present: Astronomical Institute University of Bern, Switzerland
PhD Candidate in Physics with special qualification in Astronomy

09/2015-10/2017: Technische Universität München, Germany
Earth Oriented Space Science and Technology Master of Science Program (120 ECTS)
Specialization in Remote Sensing and Navigation
Master Thesis: Dynamical Compensation Methods in Uncertain Systems

09/2010-01/2015: Universidad Politécnica de Madrid, Spain
Degree in Geodesy and Informatics (252 ECTS)
Specialization in Signal Processing
Diploma Thesis: Observation of the Earth via Remote Sensing: Application to Hydrocarbon Exploration

09/2003-09/2010: Instituto Alameda de Osuna, Madrid, Spain
Scientific-Technological High School Graduate
Specialization in Mathematics, Physics, Electronics and Technical Drawing